UNIVERSITY OF CALIFORNIA
RIVERSIDE

Colloidal Nanoparticle Assemblies: Synthesis, Surface-modification, and Applications

A Dissertation submitted in partial satisfaction
of the requirements for the degree of

Doctor of Philosophy

in

Chemistry

by

Zhenda Lu

September 2012

Dissertation Committee:

Dr. Yadong Yin, Chairperson
Dr. Francisco Zaera
Dr. Gregory Beran

The Dissertation of Zhenda Lu is approved:

_____

_____

_____

Committee Chairperson

University of California, Riverside

Acknowledgements

It would not be possible to write this doctoral thesis without the help and support of the kind people around me, to only some of whom it is possible to give particular mention here.

Above all, I would like to thank my advisor Dr. Yadong Yin for his academic advice and constant encouragement during my five years' PhD study. I learned tremendous experimental skills and well-organizing working styles from him. Most importantly, I really had fun in my research work under his guidance. I feel so lucky that I chose Dr. Yadong Yin as my graduate advisor. This is one of the wisest choices that I have made in my whole life.

I would like to thank Dr. Wenwan Zhang and Dr. Quan Cheng for our collaboration on nanoparticle application in Bioanalysis. They have always been very supportive and provided great suggestions throughout my projects. I am deeply grateful for their enthusiastic input and detailed guidance.

I would like to thank my committee members, Dr. Francisco Zaera and Dr. Gregory Beran for their time in my defense and valuable comments on my dissertation.

Also, I greatly appreciate my group members and my classmates in UCR for the wonderful time we spent together in the past five years. I would like to thank Dr. Jiangping Ge, Dr. Tierui Zhang, Dr. Xiaogang Han, Dr. Chuanbo Gao, Dr. Jibong Joo, Dr. Lei Sun, Dr. Gaoren Li, Yongxing Hu, Qiao Zhang, Le He, James Goebl, Michael Dahl, Mingsheng Wang, Yiding Liu, Chunguang Li, Yan Wang, Wenshou Wang, Miaomiao Ye, Hongxia, Yu, Qipeng Lu and Jiemei Lei in my group for their great help and support.

Last but not the least, I would like to thank my wife and parents for their unconditional love and substantial support during these years. Thanks to my wife, Ying Liu, who is also a graduate student in Chemistry Department in UCR. She is the one who always stands with me and shares my joy and sadness. I am also so grateful to my parents Lingmei Xi and Qiang Lu for bringing me up to this wonderful would and providing me the best education. Without their wholehearted support and unfailing understanding, the completion of this thesis would have been impossible.

Copyright Acknowledgements

ABSTRACT OF THE DISSERTATION

Colloidal Nanoparticle Assemblies: Synthesis, Surface-modification, and Applications

by

Zhenda Lu

Doctor of Philosophy, Graduate Program in Chemistry
University of California, Riverside, September 2012
Dr. Yadong Yin, Chairperson

Assembling nanoparticles into secondary structures not only allows the combination of properties of individual nanoparticles, but also takes advantage of the interactions between neighboring nanoparticles which result in new properties that cannot be found in the individual constituents. Moreover, the formation of secondary structures from primary nanoparticles is able to effectively address many challenges that are currently limiting the direct use of colloidal nanoparticles in practical applications.

Two general processes for assembling hydrophobic nanoparticles to colloidal clusters were developed in my thesis work. The first method is direct self-assembly of hydrophobic nanoparticles on host nanostructures containing high density surface thiol groups. Hydrophobic nanoparticles of various compositions and combinations can be directly assembled onto the host surface through the strong coordination interactions between metal cations and thiol groups. The resulting structures can be further conveniently overcoated with a layer of normal silica to stabilize the assemblies and render them highly dispersible in water for biomedical applications. As the entire fabrication process does not involve complicated surface modification procedures, the hydrophobic ligands on the nanoparticles are not disturbed significantly so that they

retain their original properties such as highly efficient luminescence. Multilayer structures can be achieved by repeating the mercapto-silica coating and nanoparticle immobilization processes.

Another universal strategy for direct assembly of hydrophobic nanopaticles is based on emulsion method. Nanoparticles confined in an oil droplet are self-assembled into spherical clusters upon evaporation of the low-boiling-point organic solvent. Hollow clusters can be formed when nanoparticles and polymers are confined together in the oil droplet. For the practical application of these clusters, I further developed a post-treatment method called protected calcination to achieve well-dispersed mesoporous cluster with clean surface. Due to the crystalline nature of the primary nanoparticles, they do not grow significantly during calcination, allowing the preservation of high surface area and formation of packing pores in the clusters. The pore sizes can be conveniently controlled by changing the size and shape of building blocks during assembly.

The as-synthesized mesoporous colloidal nanocrystal clusters are ready applied in bioseparation and photo catalysis due to their unique properties, including clean surface, high specific surface area, narrow pore size distribution, adjustable pore size and great water dispersity. As an example, mesoporous TiO_2 clusters are applied in the enrichment of phosphopeptides in phosphoproteome analysis. The superior features of these mesoporous structures have been fully tested by effective enrichment of phosphopeptides from digests of standard phosphoproteins, complex protein mixtures, natural non-fat milk and human serum samples. Phosphorylated proteins also can be effectively adsorbed on

these mesoporous clusters. Moreover, the different pore sizes, controlled by changing the size of building blocks, allow selective enrichment of phosphorylated proteins with various sizes based on size exclusion mechanism.

It is expected that these self-assembly strategies and post-treatment methods provide the research community a highly versatile, configurable, and reproducible process to prepare various multifunctional structures, which may have wide technical applications from photonics, separation, detection, multimodal imaging, energy storage and transformation, and catalysis.

Table of Contents

List of Figures

capped γ-Fe_2O_3 nanoparticles, (c) MPS spheres and (d) γ-Fe_2O_3 nanoparticles assembled on the surface of MPS spheres.

Figure 4.2 TEM images of various hydrophobic nanoparticles assembled on the surface of MPS spheres: left columns (column 1 and 3) show the different nanoparticles and right columns (column 2 and 4) represent the corresponding nanoparticle-capped MPS spheres. The ZrO_2, TiO_2 nanodots are originally protected by TOPO, $NaYF_4$:Yb,Er, TiO_2 nanorods by oleic acid, CdSe and NiO by TOPO and oleylamine, and both small and large Cu_2S nanodisks by 1-dodecanethiol.

Figure 4.3 (a) Low magnification TEM image of CdSe and γ-Fe_2O_3 nanoparticles co-assembled on the surface of MPS spheres. (b) SEM image and the corresponding EDX mapping of the elemental distribution of Si, Cd and Fe in a composite sphere of MPS@γ-Fe_2O_3&CdSe.

Figure 4.4 Effect of original capping ligands on nanoparticle assembly: (a) Molecular structures of the three protection ligands capped on Au nanoparticles (TOAB, C12N and C12S). (b) Digital photo of toluene dispersion of MPS spheres loaded with Au nanoparticles whose surfaces are capped with the three different protection ligands. (c) TEM images of the corresponding MPS spheres in photo b.

Figure 4.5 (a) Schematic diagram of the self-assembly of CdSe@CdZnS QDs on MPS spheres, showing how the PL spectra in (b) and TEM images in (c) were recorded. The original surface of QDs was covered by oleic acid. (b) PL spectra of the supernatant after adsorbtion of QDs by diffenert amount of MPS spheres. (c) TEM images of the precipitates (QD-capped MPS spheres) corresponding to the three points highlighted with numbers **1**, **2** and **3** in Figure b.

Figure 4.6 (a) Schematic illustration showing the approach for transferring nanoparticle-capped MPS spheres from oil to water phase by forming bilayer structure and subsquent silica coating. (b) TEM images of low and high magnification of silica coated γ-Fe_2O_3 nanoparticle-capped MPS spheres (MPS@γ-Fe_2O_3@SiO_2) synthesized in the presence of SDS. The γ-Fe_2O_3 nanoparticles were originally protected by oleic acid. (c) TEM images of MPS spheres capped with various nanoparticles and then surface coated with silica in the presence of SDS surfactant: (**1**) MPS@Au@SiO_2, (**2**) MPS@TiO_2 nanorods@SiO_2, and (**3**) MPS@ZrO_2@SiO_2. The Au nanoparticles were originally proteced by dodecylamine (C12N), TiO_2 nanorods by oleic acid, and ZrO_2 nanodots by TOPO.

Figure 4.7 (a) TEM images of of γ-Fe_2O_3 nanoparticle-capped MPS spheres prepared in the presence of CTAB: (1) before silica coating; (2) after SiO_2 coating with CTAB as the surfactant in aqueous NaOH solution; (3**)** after additional SiO_2 coating using the standard Stöber process. The γ-Fe_2O_3 nanoparticles were originally protected by oleic acid. Inset in (2) is the

corresponding TEM image at high magnification showing the presence of a thin silica layer (scale bar: 20 nm). (b) PL intensity as a function of time after storing the MPS@QD@SiO_2 composite spheres in water under ambient conditions; Inset is the TEM image of a portion of a typical MPS@QD@SiO_2 sphere. The original surface of CdSe@CdZnS QDs was covered by oleic acid. (c) Confocal optical microscopy image of 3.5-μm MPS spheres loaded with QDs of two different sizes. QDs of different colors were assembled on MPS spheres separately and then mixed together for imaging. The sample was excited with a focused 488 nm line of Ar^+ laser.

Figture 4.8 FTIR spectra of normal silica spheres before and after coating with an additional MPS layer. The relatively strong absorption of C-H and S-H stretching indicates the high loading of thiol groups introduced during the modification.

Figture 4.9 TEM images of (a) original Fe_3O_4@SiO_2 particles and (b) corresponding Fe_3O_4@SiO_2&MPS@CdSe@SiO_2 composite structures. The superparamagnetic Fe_3O_4 particles were synthesized using a high temperature precipitation reaction in the presence of polyacrylic acid (PAA), surface coated with normal silica using the Stöber process, modified with MPS layer, and then decorated with oleic acid-capped CdSe@CdZnS QDs, and then surface protected by another layer of normal SiO_2 with the assistance of CTAB surfactant. Insets are corresponding photographs of an aqueous dispersion of the composite particles excited by an ultraviolet lamp: the left sample is a normal dispersion while the right one is exposed to a magnetic field.

Figture 4.10 (a) TEM image of the Ag nanowire@SiO_2&MPS@CdSe&γ-Fe_2O_3 composite nanowires. The Ag nanowires were synthesized by using a polyol process in the presence of poly(vinyl pyrrolidone) (PVP), surface coated with normal silica using the Stöber process, modified with MPS layer, and then decorated with TOPO/oleylamine-capped CdSe and oleic acid-capped γ-Fe_2O_3 nanoparticles. Inset is a schematic illustration of the assembled structure. (b) SEM image and EDX mapping of the elemental distribution of Si, O, Fe, Cd and Se in the composite nanowire structures.

Figture 4.11 (a) Schematic illustration and TEM image of the MPS@γ-Fe_2O_3@SiO_2&MPS@CdSe multilayer composite, synthesized by sequential procedures including initial loading of oleic acid capped γ-Fe_2O_3 nanoparticles on MPS spheres, surface coated with normal silica using the Stöber process, modified with MPS layer, and then decorated with TOPO/oleylamine capped CdSe nanoparticles. (b) SEM images and EDX mapping of the elemental distribution of Si, S, Fe and Cd in the assembled structure.

Figture 5.1 (a) Schematic illustration showing the procedure of self-assembly of hydrophobic nanoparticles on MPS spheres. (b) TEM images of oleic acid

List of Tables

Chapter 1

Overview of Colloidal Nanoparticle Assembly

1.1 Introduction

Nanoparticles are usually defined as particles with size in the range of 1 to 100 nm at least in one of the three possible dimensions. In this size range, the nanoparticle possesses a large proportion of atoms on the particle surface, an immense specific surface area and a high possibility of quantum effects. For example, Figure 1.1 shows the percentage of surface atoms changes with palladium nanoparticle diameter.[1] For a spherical particle of 1 cm, the percentage of surface atoms would be only about 10^{-5}%, when the particle is divided into smaller ones with size of 5 nm, the percentage of the surface atoms would increase to 45%. In a nanoparticle of 1 nm, most of all atoms would be surface atoms. Such a dramatic increase in the ratio of surface atoms to interior atoms makes nanoparticles possess unexpected physical and chemical properties, as compared to their bulk counterparts. Therefore, nanoparticles are of great interest for researchers from a wide range of disciplines, including material science, chemistry, physics, and engineering

Significant progresses have been made in the development of robust synthesis protocols which allow precise control over composition, size, shape, surface property, and uniformity of colloidal nanoparticles.[2, 3] Recently, the focus of synthetic efforts has been directed to the creation of secondary structures of colloidal nanoparticles which holds great promise in the development of advanced materials with novel integrated functions.[4] Assembling nanoparticles into secondary structures not only allows the

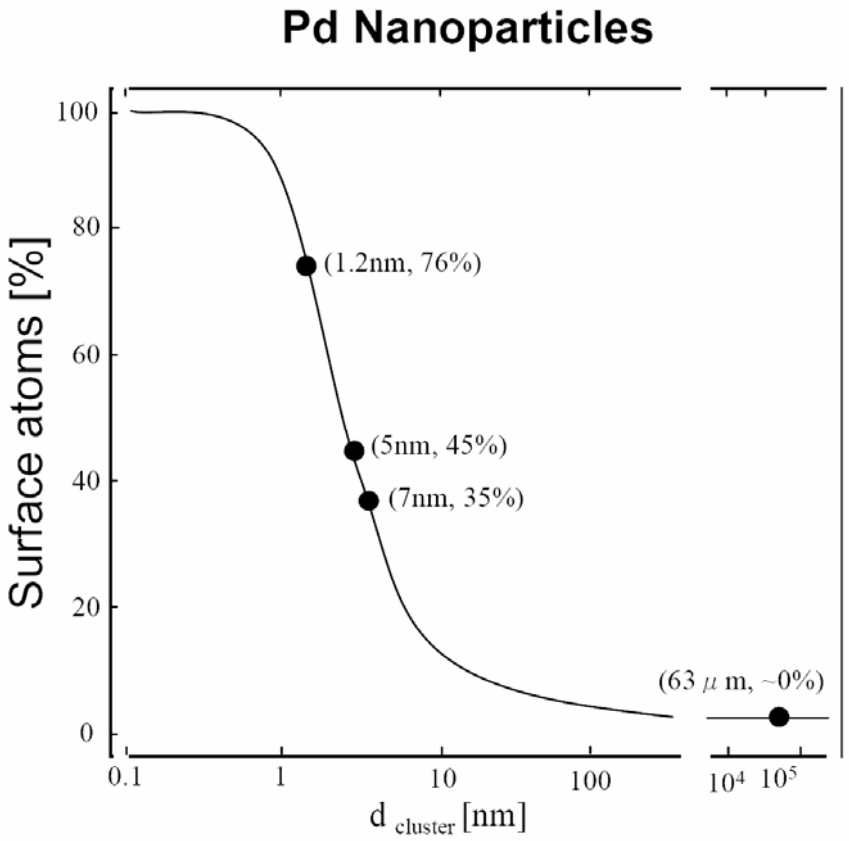

Figure 1.1 The percentage of surface atoms of Pd Nanoparticles changes with the cluster diameter.

combination of properties of individual nanoparticles, but also takes advantage of the interactions between neighboring nanoparticles which result in new properties that cannot be found in the individual constituents.[5] Considering the facts that the syntheses of large variety of nanoparticles have been enabled in the past two decades and that large number of different combinations can be made from these nanoparticles, one can easily see the great potential of assembly approaches in the creation of novel nanoparticle-based functional materials. Moreover, the forces involved in nanoparticle assembly, including both covalent and non-covalent interactions (e.g. hydrogen bonding, electrostatics and van de Walls interactions) can be tailored by the choices of solvents, surfactants, and reaction temperatures, providing exciting opportunities for controlling specific geometric configurations and consequently desired functions.

On the other hand, for most practical applications, the nanoparticles have to be assembled in one, two or three dimensions, similar to how atoms are assembled into molecules. For example, a sensing device may require nanoparticles to be arranged with specific inter-particle separation. The formation of secondary structures from nanoparticles is also able to effectively address many challenges that are currently limiting the direct use of colloidal nanoparticles in real applications. For example, owing to their high surface-to-volume ratio, small nanoparticles are believed to possess significantly enhanced catalytic activities, which however may quickly decay due to their sintering into large ones during reactions. In addition, the capping ligands, which are generally required to stabilize the nanoparticles during their initial synthesis, may prevent the access of the target molecules to the catalyst surface and therefore severally reduce

the catalytic activity. Organizing nanoparticle catalysts into clusters can circumvent these difficulties by allowing additional post-treatment to remove the capping ligands while maintaining the high surface area.[6, 7] Although more efforts are required to develop effective bottom-up assembly approaches for colloidal nanoparticle clusters, this strategy now opens up an nearly unlimited platform for designing and manufacturing functional materials with new physical and chemical properties.

In this overview, I will focus on the liquid-phase synthesis and preparation of various colloidal nanoparticle clusters (CNCs), which are typically composed of primary nanocrystallites of approximately several to tens of nanometers in size. I will also highlight a number of representative examples of their many potential technological applications, including catalysis, energy storage and conversion, magnetic separation, multimode imaging, detection and drug loading and release.

1.2 Assembly Methods

As shown in Figure 1.2, there are basically two strategies for the preparation of the CNC structures: i) one-step processes which integrate the synthesis of nanoparticles and their aggregation into clusters in a single step; and ii) multi-step processes which first produce nanoparticles with desired size, shape and surface functionality, and then assembly them into clusters of designed configurations in separate steps via methods such as solvent evaporation, electrostatic attraction, or interfacial tension. While the one-step processes are more efficient in producing CNC structures, the multi-step processes have the advantage of being more flexible and universal for organizing nanoparticles of a large variety of materials into CNCs with highly configurable structures.

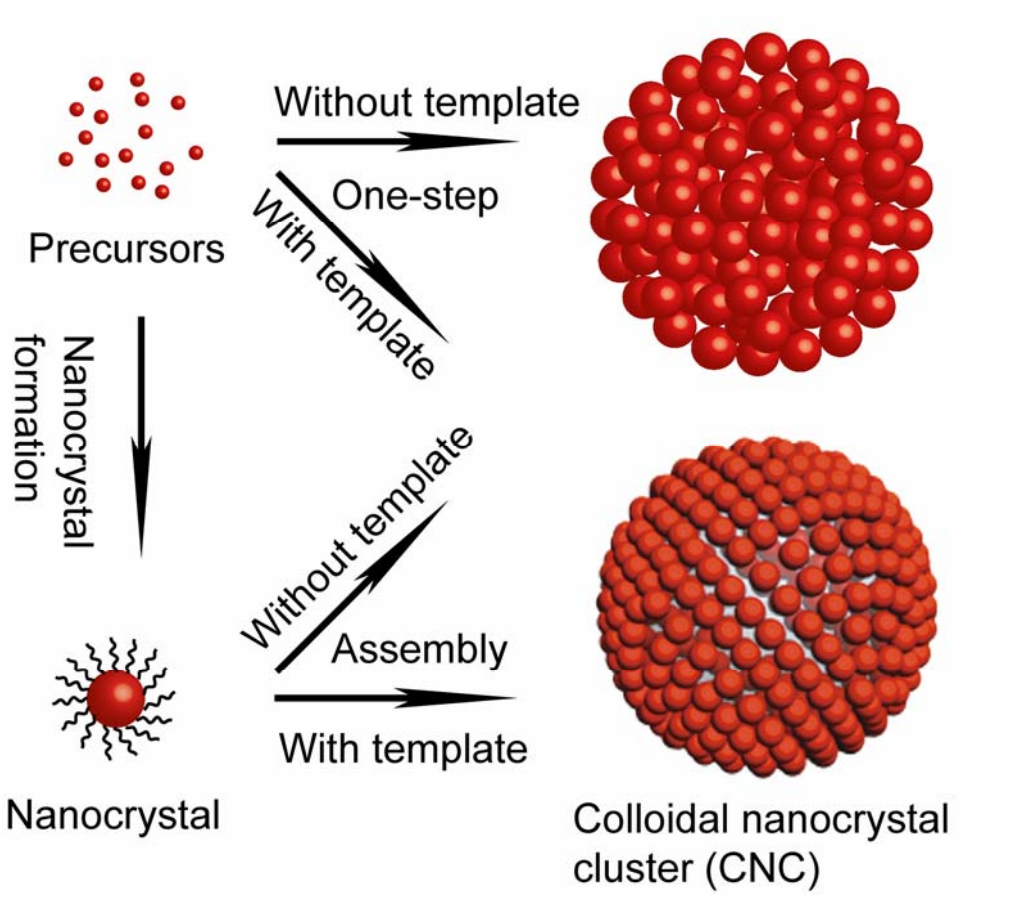

Figure 1.2 Schematic illustrations of the two preparation strategies of colloidal nanoparticle clusters (CNCs).

1.2.1 Direct Synthesis of Nanoparticle Clusters

Nanoparticle clusters can be produced through a number of different one-step methods, including thermolysis, solvothermal, and microwave methods. Table 1.1 summarizes various CNC syntheses reported in recent literature. Although the details in these methods are different from each other, they all involve two growth stages in which primary nanoparticles nucleate and grow first in a supersaturated solution and then aggregate into larger secondary particles.

1.2.1.1 Thermolysis Method

A typical thermolysis process refers to reacting precursors in solvent in the presence of a surfactant at high temperatures. The reaction typically consists of three critical components: precursors, organic capping ligands, and solvents. The capping ligands bind to the surfaces of nanoparticles, limit their growth, and prevent the interparticle agglomeration through steric interactions. With sufficient ligand protection, uniform nanoparticles with typically dot shapes are obtained. However, by reducing the degree of ligand protection to the domain of so called "limited ligand protection" (LLP), complex three dimensional (3D) nanostructures can be produced through the oriented attachment of primary nanoparticles. Peng et al. reported 3D nanoflower-like structures for metal oxides such as In_2O_3, CoO, MnO and ZnO by reducing the amount of stabilizing organic ligands to the point that the primary nanoparticles are insufficiently protected.[8, 9] Similar to the mainstream thermolytic syntheses, metal oxide nanoparticles nucleate upon the thermolysis of precursors. With increasing reaction temperature, the

Table 1.1 Summary of one-step approaches for CNC synthesis.

Cluster	Precursors	Solvent and Surfactant	Method	T (°C)	Size range (nm)	Ref.
In_2O_3, ZnO, CoO, MnO_2	Metal carboxylate (Ac, Mt or St)	ODE, OA or DA	Thermolysis	250-280		9
In_2O_3	Indium carboxylate (Ac, Mt or St)	ODE, DA	Thermolysis	250-290	15-60	8
Fe_3O_4	$FeCl_3$, NaOH	DEG, PAA	Thermolysis	220	30-180	10
PbS	$Pb(Ac)_2$, Thiourea	DEG, PAA	Thermolysis	215	155-240	11
ZnO	$Zn(Ac)_2$, NaOH	DEG, PAA	Thermolysis	210	60-180	12
MFe_2O_4 (M=Fe, Co, Mn, Zn)	$FeCl_3$, MCl_2, NaAc	EG, PEG	Solvothermal	200	200-800	13
Fe_3O_4	$Fe(acac)_3$	EG, PVP	Solvothermal	140-145	50-100	14
Fe_3O_4	$FeCl_3$, NaAc	EG, DEG, Sodium acrylate	Solvothermal	200	6-170	15
MFe_2O_4 (M=Fe, Mn, Zn, Co, Ni)	$FeCl_3$, MCl_2, NaAc	EG, DEG, PVP	Solvothermal	200	20-300	16
Fe_3O_4	$FeCl_3$, NaAc	EG, Na_3Cit	Solvothermal	200	170-300	17
α-Fe_2O_3	$FeCl_3$, urea	THF, ethanol, PVP	Solvothermal	180		18
ZnO	$Zn(Ac)_2$	DEG	Thermolysis (Microwave)		57-274	19

Abbreviations: Ac: acetate; Mt: myristate; St: stearate; ODE: 1-octadecene; OA: octadecyl alcohol; DA: decyl alcohol; EG: Ethylene glycol; DEG: diethylene glycol; PEG: polyethylene glycol; Cit: Citrate; PAA: Polyacyl acid; PVP: polyvinyl pyrrolidone.

dot-shaped nanoparticles grow further at 250 ^{o}C and eventually agglomerate into the flower-like clusters due to the lack of sufficient protection from ligands. The key to the formation of CNCs is to maintain an appropriate concentration of capping ligands which is not enough for protecting the primary nanoparticles against aggregation but sufficient in stabilizing the resulting 3D nanostructures. The formation of relatively large crystalline cluster structures proceeds through the 3D oriented attachment of primary nanoparticles.[20] By changing the reaction conditions such as the specific concentration of ligands and reaction time, the size of the clusters can be adjusted in a reasonably wide range, for example, 15-60 nm in the case of In_2O_3.[8] The LLP approach is believed to be a powerful strategy for the design of complex 3D CNCs, which can be applied to metal oxides with different compositions. It is also believed that the principle of LLP may be applicable to a broad spectrum of colloidal nanoparticles, without involving drastic alternation to the synthetic chemistry established for simple 0D and 1D nanoparticles in the past decades.

Recently, our group has developed a one-pot high-temperature polyol process for the synthesis of polyelectrolyte-capped superparamagnetic CNCs of magnetite (Fe_3O_4).[10] Briefly, Fe_3O_4 CNCs are prepared by hydrolyzing $FeCl_3$ with NaOH at ~220 °C in a diethylene glycol (DEG) solution with short-chain polyacrylic acid (PAA) as a surfactant. DEG was chosen as the polar solvent because of its high boiling point as well as its high permittivity, which enables high dissolving capacity for a variety of polar inorganic and many organic compounds. Under the reductive atmosphere provided by DEG at a high temperature, Fe^{3+} partially transforms into Fe^{2+} and finally forms Fe_3O_4 particles. The

particle size can be tuned from 30 to 180 nm with a relatively narrow distribution by changing the concentration of NaOH. The growth of CNCs follows the well-documented two-stage growth model in which primary nanoparticles nucleate first in a supersaturated solution and then aggregate into larger secondary particles. As shown in the transition electron microscopy (TEM) images in Figure 1.3, these magnetite CNCs have a well-developed cluster-like structure: each cluster is composed of many interconnected primary nanoparticles with size of ~ 10 nm. A crystallographic alignment of the primary crystals to the adjacent ones are observed in the high resolution imaging and electron diffraction studies, suggesting the possible formation mechanism of CNCs through oriented attachment and subsequent high-temperature sintering during synthesis. This synthesis method has been extended to the synthesis of CNCs of other materials, such as PbS[11] and ZnS.[12]

Microwave irradiation represents a very efficient heating method that can find unique advantages in the synthesis of colloidal inorganic nanomaterials. It is often believed that microwave dielectric heating can address the issues such as heating inhomogeneity and slow reaction kinetics in the conventional thermolysis reactions, which rely on thermal conduction to drive chemical reactions. As a result, it is becoming an increasingly popular heating method for nanomaterial synthesis. Hu et al. have employed a rapid microwave process to produce narrowly distributed ZnO CNCs in relatively large quantities by heating a zinc acetate solution in DEG using microwave irradiation.[19] The high polarizability of DEG makes this solvent an excellent microwave absorbing agent, thus leading to a high heating rate and significantly short reaction time,

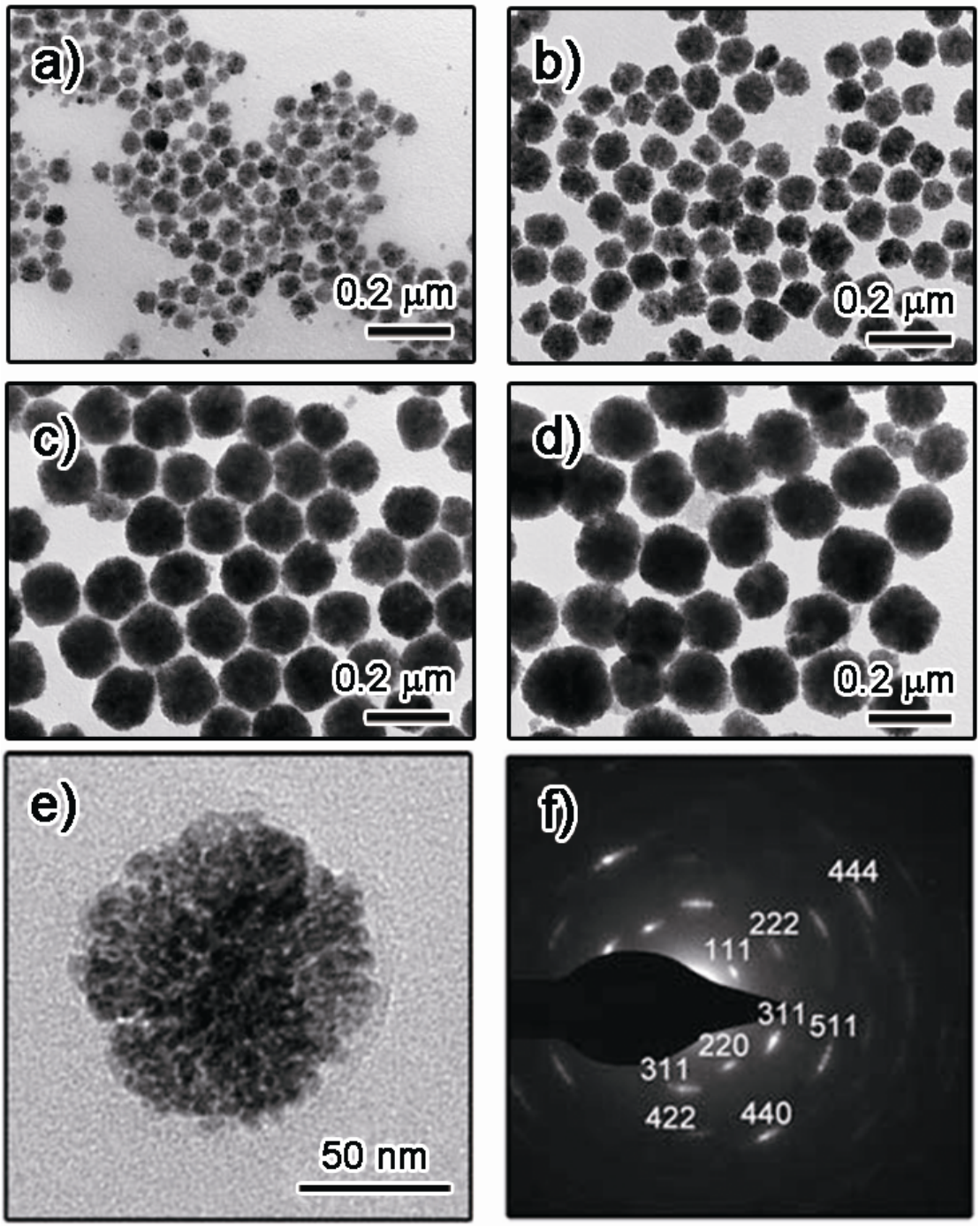

Figure 1.3 Representative TEM images of Fe_3O_4 CNCs. The average diameters of CNCs, obtained by measuring about 150 clusters for each sample, are (a) 53, (b) 93, (c) 141 and (d) 174 nm. (e) High magnification TEM images of 93 nm CNCs; (f) Typical SAED pattern of the cluster.

compared to existing solution-based synthetic route using conventional heating techniques. The size of the clusters that are composed of small primary nanoparticles can be tuned continuously and precisely from about 57 to 274 nm by simply varying the amount of zinc precursors.

1.2.1.2 Solvothermal Synthesis

Solvothermal synthesis refers to chemical reactions that are performed in a closed reaction vessel (autoclave) at temperatures higher than the boiling point of the solvent. This approach has become one of the widely used tools for nanoparticle synthesis due to the relatively easy steps, simple setups, and less energy requirement, although it suffers from several drawbacks such as limited scalability and the lack of opportunities for direct monitoring the reaction process. A number of examples of 3D CNCs composed of primary nanoparticles have been demonstrated through solvothermal methods.[13-18] In a typical process for the synthesis of Fe_3O_4 CNCs, a solution containing $Fe(acac)_3$ (precursor), polyvinylpyrrolidone (PVP, surfactant), and ethylene glycol (EG, solvent) was sealed in a Teflon-lined autoclave, heated to 140-145 ^oC and maintained at this temperature for 36 hrs.[14] The products were Fe_3O_4 CNCs containing disordered nanoscale pores formed by assembling the corresponding primary nanoparticles. Although the exact formation mechanism cannot be fully revealed due to the difficulty of sampling under high temperature and high pressure, it has been convenient to control the sizes of the Fe_3O_4 CNCs by changing the amount of precursor $Fe(acac)_3$. To further tune the sizes of primary nanoparticles and secondary Fe_3O_4 CNCs, Xuan et al. modified the solvothermal process by utilizing sodium acrylate as surfactant to synthesize a series of clusters.[15] The

average primary nanoparticle size can be continuously tuned from ~5.9 to about ~21.5 nm by simply changing the weight ratios of sodium acrylate/NaAc, while the overall size of the secondary structures can also be precisely controlled in a wide range (up to ~280 nm) by regulating the ratio of the two solvents (EG/DEG). Although this solvothermal method is believed to be general for constructing cluster structures from many other inorganic materials, the success has been mainly limited to iron related materials, such as Fe_3O_4, ferrite, and α-Fe_2O_3 (Table 1.1).

1.2.2 Clustering Pre-synthesized Nanoparticles

The utilization of pre-prepared nanoparticles as building blocks for the assembly of new materials such as 3D CNCs provides unique opportunities to combine the inherent functionality of the nanoparticles with potential collective properties from their interaction. Thanks to rapid progress in colloidal nanostructure synthesis, a great number of materials can now be routinely produced in form of nanoparticles with excellent control over size, shape and surface properties.[2] It can be easily appreciated that modular assembly approaches are highly attractive for the preparation of secondary structured nanomaterials with various configurations and programmable properties. Many nanoparticle assembly methods have been developed in the last decade. In this review, we focus on the liquid-phase strategies, which is very flexible in controlling the structure, composition and morphology of the final CNC structures.

1.2.2.1 Evaporation-induced Self-assembly (EISA)

Self-assembly of pre-synthesized nanoparticles through evaporation of solvents in the presence of block-copolymers as structure directing templates was initially designed

for preparing metal oxide mesoporous structures with high surface area, high thermal stability, and fully crystalline networks.[21, 22] Although mesoporous materials were extensively reported, the preparation of fully crystalline frameworks has remained a major challenge due to the fact that many oxide mesoporous structures collapse during the crystallization process. Compared to the well-known surfactant-templating method for mesoporous silica structures, EISA utilizes crystalline nanoparticles instead of molecular precursors as building blocks. As a typical example, tin oxide monodispersed nanoparticles of several nanometers were prepared first, and then dispersed in tetrahydrofuran (THF), forming transparent and stable dispersion with the addition of polybutadiene-block-poly(ethylene oxide) (PB-PEO) block copolymer.[23] The subsequent evaporation of the THF solvent induced the assembly of nanoparticles and PB-PEO block-copolymer micelles, finally leading to the formation of mesoporous structures with ordered 18-20 nm mesopores. The samples were further treated under air at high temperatures to completely remove polymer templates, producing high quality mesoporous structures.

EISA is a general method for the preparation of mesoporous structures containing different nanoparticleline components. When applied to nanoparticle dispersions confined in defined volumes, such as droplets in an emulsion, it becomes a powerful method to produce various mesoporous nanoparticle clusters with desired overall dimensions. However, it is difficult, and requires much effort to make these structures into colloidal form, smaller size and homogenous morphology in order to satisfy the needs of their specific applications, such as photonics and bioanalysis.

The Oil-in-water emulsion evaporation method can be divided into two steps as shown in Figure 1.4a: (i) Nonpolar dispersion of pre-synthesized nanoparticles emulsification into an aqueous solution containing emulsifier (i.e., SDS and CTAB), producing an oil-in-water emulsion with 'oil' droplets of a few micrometers. (ii) Concentration and condensation of the nanoparticles into CNC structures by evaporating the oil phase in the emulsion droplets. The assembly is driven by the hydrophobic van der Waals interaction of the capping ligands on the nanoparticle surface. The hydrophobic nature of the nanoparticles also keeps the clusters aggregated and prevents them from breaking up in the aqueous environment. The emulsifier is adsorbed onto the cluster surface through hydrophobic-hydrophobic interactions with the capping ligands on the nanoparticles, which also helps dispersion of the clusters in water. Bai et al. demonstrated this facile and universal bottom up assembly strategy for preparing CNCs from various nanobuilding blocks with different sizes and shapes, such as $BaCrO_4$, Ag_2Se, CdS, PBS, Fe_3O_4, ZrO_2, $NaYF_4$ nanodots, Bi_2S_3 and LaF_3 nanoplates and $PbSeO_3$ nanorods.[24] The TEM images of $BaCrO_4$ CNCs shown in Figure 1.4b clearly illustrate that the constituent nanoparticles retain their individual character and do not sinter into large units. The size of the CNCs can be controlled by the parameters of the emulsification process such as concentration of nanoparticles in oil phase and oil-to-water ratio. Specifically, smaller clusters were obtained by emulsification under sonication than by stirring; higher nanoparticle concentration and oil-to-water ratio led to larger clusters. More experimental details of this emulsion based nanoparticle assembly were provided by Simard and co-workers.[25] They concluded that: (1) the size and size distribution of the clusters are

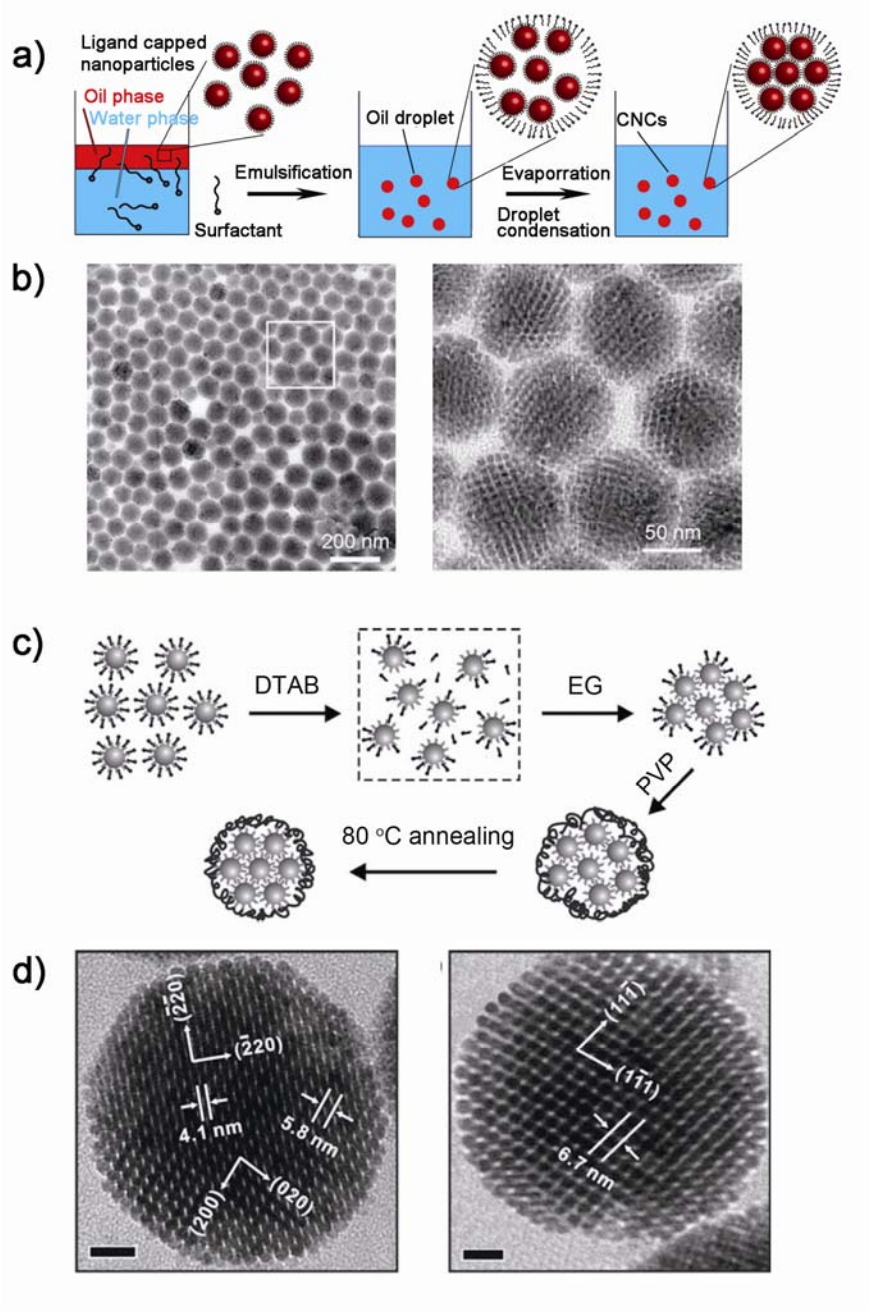

Figure 1.4 (a) Schematic illustration of oil-in-water emulsion solvent evaporation for CNC preparation. (b) TEM images of $BaCrO_4$ CNCs. (c) Schematic illustration of CNC preparation. (d) TEM images of CNCs made of Fe_3O_4 nanoparticles (5.8±0.2 nm in diameter) viewed along different zone axis. Scale bars: 20 nm.

defined by the droplets made during emulsification and, as a result, are determined by the emulsification conditions and emulsion composition; (2) The size of the clusters is most conveniently controlled by varying the concentration of nanoparticles in oil phase; (3) The size distribution can be narrowed by using a high volume fraction of droplet phase. This emulsion-based assembly process also brings the convenience of incorporation of multiple components to clusters to enable multi-functions. Composite nanoparticle clusters can be fabricated by simply starting with a mixture of different types of nanoparticles, such as γ–Fe_2O_3/TiO_2,[26] $NaYF_4$-Yb,Er/$NaYF_4$:Eu[27] and CeO_2/Pd[28] multiple component clusters. The nanoparticle packing characteristics in clusters can be determined by temperature, which determines the rate of solvent evaporation.[29] Well ordered nanoparticle superlattices with a body-centered cubic (bcc) structure form with slow evaporation at room temperature; while at higher evaporation temperature, multi-domain polycrystalline structures and eventually completely amorphous structures are produced.

To achieve more ordered packing of nanoparticles in clusters, Cao and co-workers developed a modified assembly approach as illustrated in Figure 1.4c. Pre-synthesized uniform nanoparticles are first transferred from nonpolar solvent to aqueous solution by using surfactants such as dodecyltrimethylammonium bromide (DTAB). Then, ethylene glycol (EG) is added to the nanoparticle dispersion, leading to the formation of CNC structures due to the weakened protection of DTAB in EG solution. Finally, the clusters are protected by adding PVP and annealed at 80 ^oC for 6 h.[4, 30, 31] The annealing treatment is important to increase the order of the nanoparticle packing in CNCs. TEM

images in Figure 1.4d clearly show superlattice fringes, suggesting that the nanoparticles were rearranged into a nearly perfect face-centered cubic (fcc) packing after annealing.

Several modifications to the emulsion evaporation method were reported for fabricating CNC structures. The Silica precursor tetraethylorthosilicate (TEOS) was mixed with hydrophobic nanoparticles in a nonpolar solvent and then emulsified in a DEG solvent by surfactant, as shown in Figure 1.5a.[32] This oil-in-DEG technique offers the following advantages: (1) TEOS is constrained in oil droplets together with nanoparticles, ensuring that the hydrolysis and condensation of TEOS only occur in the oil droplets and avoiding the formation of free silica spheres. Silica was directly coated on the CNCs after assembly. (2) The use of DEG effectively limits the hydrolysis and condensation of TEOS within the oil droplets, resulting in better control of the particle size and avoiding agglomeration. In another case, the biodegradable polymer (Poly(D,L-lactic-co-glycolic acid), PLGA) was introduced into the oil droplet containing nanoparticles to form an oil-in-water emulsion (Figure 1.5b).[33] After oil evaporation, nanoparticles were successfully embedded into the PLGA matrix to form CNC structures. With the same approach, QDs can be embedded in a matrix of polystyrene-co-methacrylic acid (poly-St-co-MAA) copolymer.[34] In these assemblies, polymers acted as glue for clustering nanoparticles and provided a matrix for loading drugs or other functional species, such as fluorescent probes. Instead of matrixes, polymers can also be used as templates for nanoparticle clustering.[29] When polymers are included in the emulsion formulation, monolayer- and multilayer-nanoparticle coated polymer beads and partially coated Janus beads are prepared. The nanoparticles are expelled by the polymer

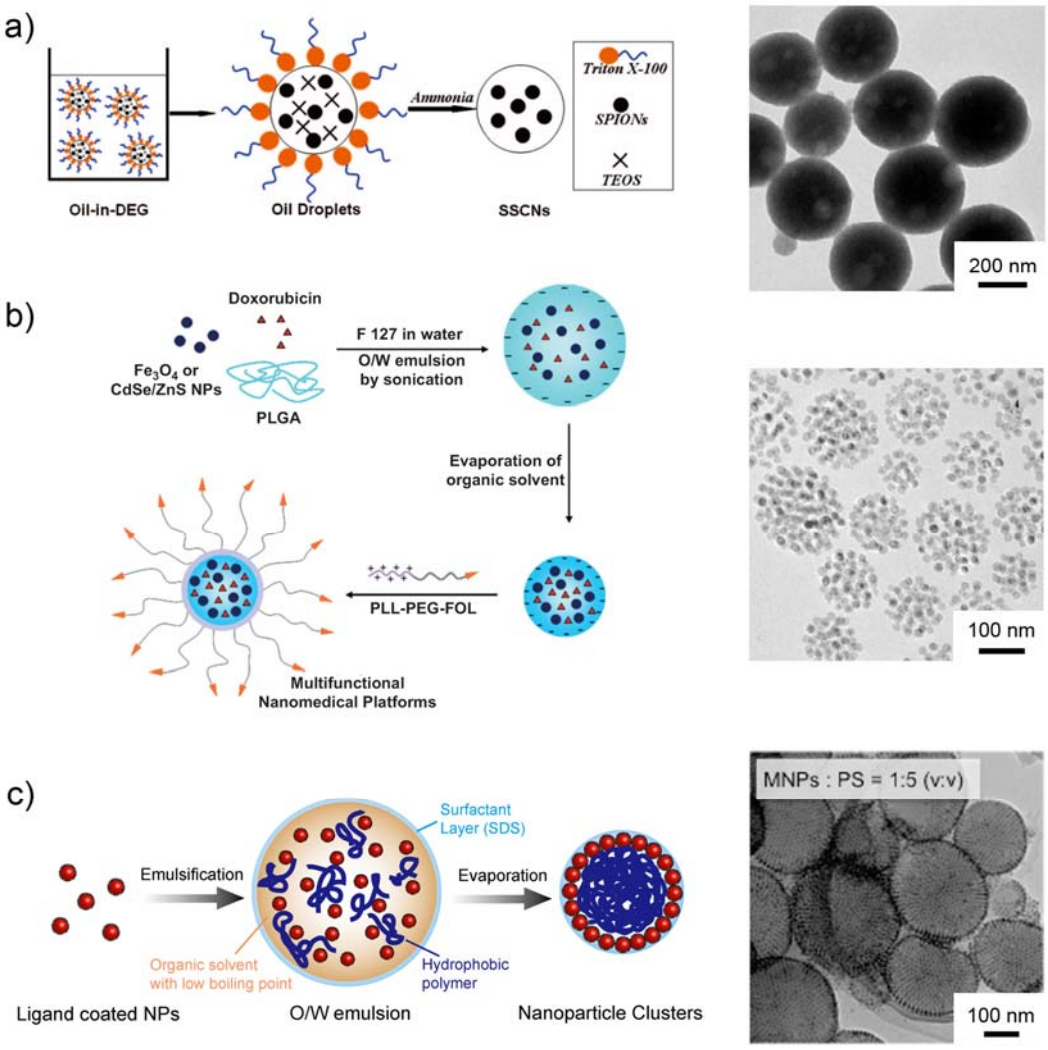

Figure 1.5 Schematic illustration of CNC preparation based on emulsion evaporation and typical TEM images of CNCs fabricated with corresponding method. (a) TEOS assisted clustering. (b) Polymer assisted clustering. (c) Polymer as templates.

as its concentration increases on evaporation of the solvent and accumulates on the surfaces of the polymer beads (Figure 1.5c). The number of nanoparticle layers depends on the polymer/nanoparticle ratio in the oil droplet phase.

1.2.2.2 Layer-by-layer (LBL) Assembly

A Layer by layer (LbL) assembly technique was originally used for producing thin polyelectrolyte films on solid surfaces. The assembly process involves sequential incubation of charged solid support in an oppositely charged polyelectrolyte solution. After its invention, the LBL process was quickly adopted as a versatile route to the creation of various nanoparticle shells by sequential adsorption of nanoparticles and polyelectrolyte onto the surface of submicrometer beads.[35-38] As shown in Figure 1.6a, in a typical process, submicrometer beads (e.g. silica or polystyrene) are first primed with several layers of polyelectrolyte film to provide uniform charged surfaces that assists subsequent uniform deposition of nanoparticles. Following nanoparticle adsorption, the beads are centrifuged and washed several cycles to remove unadsorbed species, and then used for the next cycle of adsorption of polyelectrolytes. The process is repeated until the desired number of layers is obtained. An apparent limitation of this LBL assembly method is that it mostly applies to hydrophilic nanoparticles only because they heavily rely on electrostatic interactions. Many technologically important high quality nanoparticles, especially semiconductors and metal oxides cannot be directly assembled using the LBL method because they are predominantly prepared and dispersed in organic solvents.

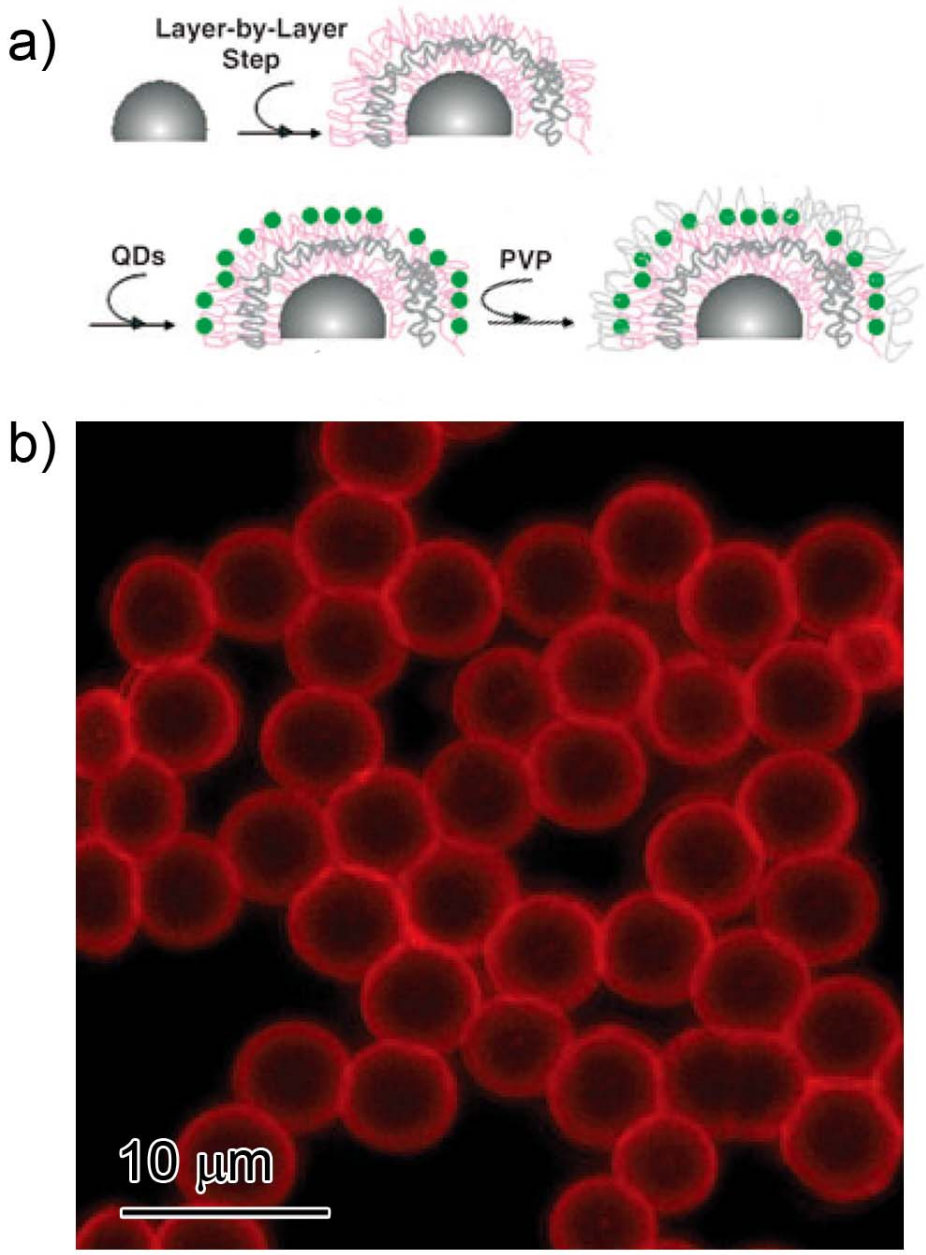

Figure 1.6 Schematic illustration of nanoparticle assembly on silica beads with layer by layer method. (b) Confocal optical microscopy image of QD-loaded silica spheres.

Yoon et al. recently developed a novel LBL method for nanoparticle assembly based on a nucleophilic substitution reaction between the bromo and amine groups in organic media.[39] They prepared 2-bromo-2-methylpropionic acid (BMPA) stabilized nanoparticles and amine-functionalized poly(amidoamine) (PAMA) dendrimers first, which are sequentially coated on silica colloidal beads. Analogous to the assembly induced by metal-thiol interaction, the direct adsorption of the nanoparticles in organic nonpolar solvent significantly increases the packing density of nanoparticles in the lateral dimensions because electrostatic repulsion between neighboring nanoparticles is absent. Moreover, the capping ligands on the nanoparticles are not disturbed so that they retain their original properties such as highly efficient luminescence.

1.2.2.3 Liquid-liquid Interface Assembly

The assembly of nanoparticles at liquid-liquid interface, analog to the case in pickering emulsions, generates a resistant film at the interface between two immiscible phases, inhibiting the coalescence of emulsion drops, as shown in Figure 1.7a. A typical example is CdSe nanoparticle assembly at the water-toluene interface to form kinetically stabilized water-in-oil emulsion.[40] This interfacial assembly is driven by the reduction in interfacial energy, which depends on the nanoparticle size, particle-particle interaction, particle-water and particle-oil interactions. Larger nanoparticles have a stronger stabilization effect for the assembly. For example, 4.6-nm CdSe nanoparticles can be assembled on the surface of an already stabilized droplet, displacing the smaller 2.8-nm ones.[41] To fabricate mechanically stable capsules and membranes from spherical nanoparticle assemblies, the nanoparticles need to be crosslinked at the interface, which

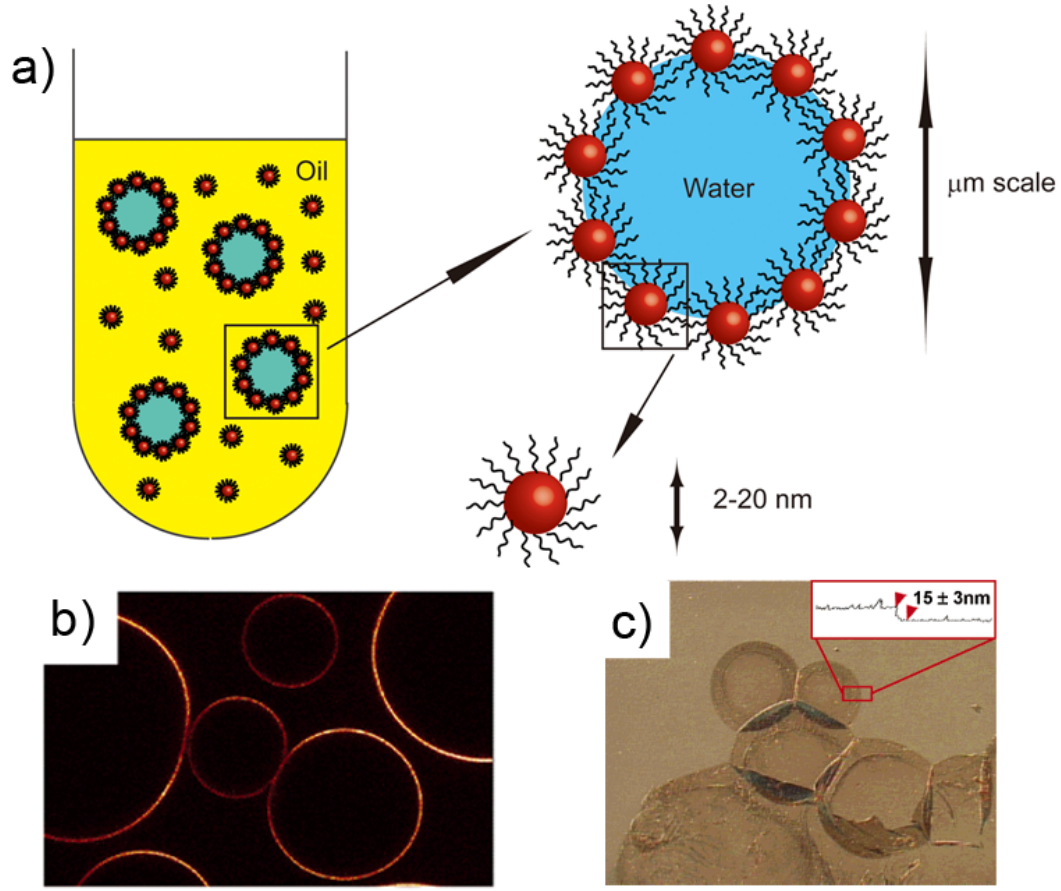

Figure 1.7 (a) Schematic of the self-assembly of solid nanoparticles at the oil–water interface. (b) Fluorescence confocal microscope image of water droplets dispersed in toluene, covered with CdSe nanoparticles. (c) Differential interference contrast optical microscopy image of dried droplets on a silicon substrate. Inset: AFM height section analysis.

requires pre-modification of the nanoparticle surface with reactive organic molecules.[42] Compared with layer-by-layer polyelectrolyte deposition, assembly at the liquid-liquid interface requires fewer steps, affords ultrathin nanoparticle shells, and may reduce structural defects due to the mobility of nanoparticles at the fluid interface. However, the emulsion droplet produced by the liquid-liquid interface assembly is generally larger than several micrometers, which may limit their potential applications.

1.2.3 Comparison of One-step and Multi-step Method

One-step synthesis of CNC structures is more convenient and time-saving than those involve multiple steps. Moreover, clusters obtained through this method typically have narrower size distribution, which is very important for some applications that require high uniformity, for example, in the construction of photonic crystals. However, literature only contains a limited number of examples for successful preparation of CNC structures because controlling the clusterization of nanoparticle during synthesis is usually even more challenging than that of simple isolated nanoparticles. The key issue is to identify the critical point of ligand protection for clusters formation. Above the critical point, isolated and non-agglomerated nanoparticles will form, whereas below the critical point, care has to be taken to avoid the formation of uncontrolled aggregations with random morphologies. Nanoparticle assembly through two or more consecutive steps represents a class of more general strategies for the preparation of CNC structures. Considering the number of various types of nanoparticles that have been prepared in the last decade, and the many possibilities to arrange them, such modular approaches are apparently advantageous for preparing materials with tailored properties. Among various

assembly approaches, EISA in combination with emulsion represents a general method which is very flexible in organizing various nanoparticles into cluster structures, although it remains a challenge to improve the uniformity of resulting clusters. Assembly of nanoparticles at liquid-liquid interfaces is unique in producing hollow shells which can be further stabilized by crosslinking the surface ligands. The challenge is, however, in controlling the size as well as the thickness of the shells. LBL assembly also provides a universal strategy to arrange the nanoparticles into clusters with uniform size and morphology, but the loading density of nanoparticle is relatively low due to single layer adsorption.

1.3 Surface Modification of Nanoparticle Assembly

The directly synthesized CNC structures are usually mechanically stable so they can be handled in the same way as typical colloidal nanoparticles, including multiple times of cleaning, surface modification, and further assembly into more complex structures. On the other hand, the CNCs produced through assembly approaches are generally protected by a layer of surfactants which render the particles good dispersity in solvents. The van der Waals interactions between the ligands capped on nanoparticles and the hydrophobic tails of the surfactant are generally weak and can be easily disturbed by changes in the chemical environment, sometimes leading to aggregation of the clusters in solution. The cluster structures may be destroyed when they are subjected to strong mechanical forces or when they are exposed to good solvents which can solvate individual nanoparticles. In addition, it is often required to link functional molecules to the surface of the CNCs, which however becomes difficult by connecting these molecules

to the weakly adsorbed surfactants. To address these issues, a more robust protecting layer is often required. For some applications, in particular catalysis, a clean surface is often required. Although calcination at high temperatures allows convenient removal of the surfactants/capping ligands, those are required to maintain the cluster form without producing big aggregates. In this case, it may also become necessary to introduce a sacrificial coating to the surface of clusters that can prevent the formation of large aggregation. Here we summarize three main surface treatment methods reported for nanoparticle cluster structures: direct calcination, silica coating, and polymer coating, as schematically illustrated in Figure 1.8a.

1.3.1 Direct Calcination

The application of nanostructured materials in bio-separation or catalysis generally requires a clean surface to ensure sufficient active surface sites. However, high quality nanoparticles, as well as CNCs assembled from them are typically covered with a layer of capping ligands, which prevent them from effectively accepting target molecules. Direct calcination is the most straightforward treatment to remove these organic ligands and completely clean the material surface. Han et al. calcined ion oxide clusters at 550 ^{o}C in air for 3h to yield mesoporous microspheres with a clean surface, as shown in Figure 1.8b. The calcination removes ligands adsorbed on the material surface and enhances the mechanical stability of the clusters. On the other hand, the primary nanoparticles still can be identified by TEM imaging, suggesting the interparticle fusion is modest.[43] However, as expected, the calcination can cause severe aggregation of the clusters, and their spherical morphology may not be well maintained during calcination.[26]

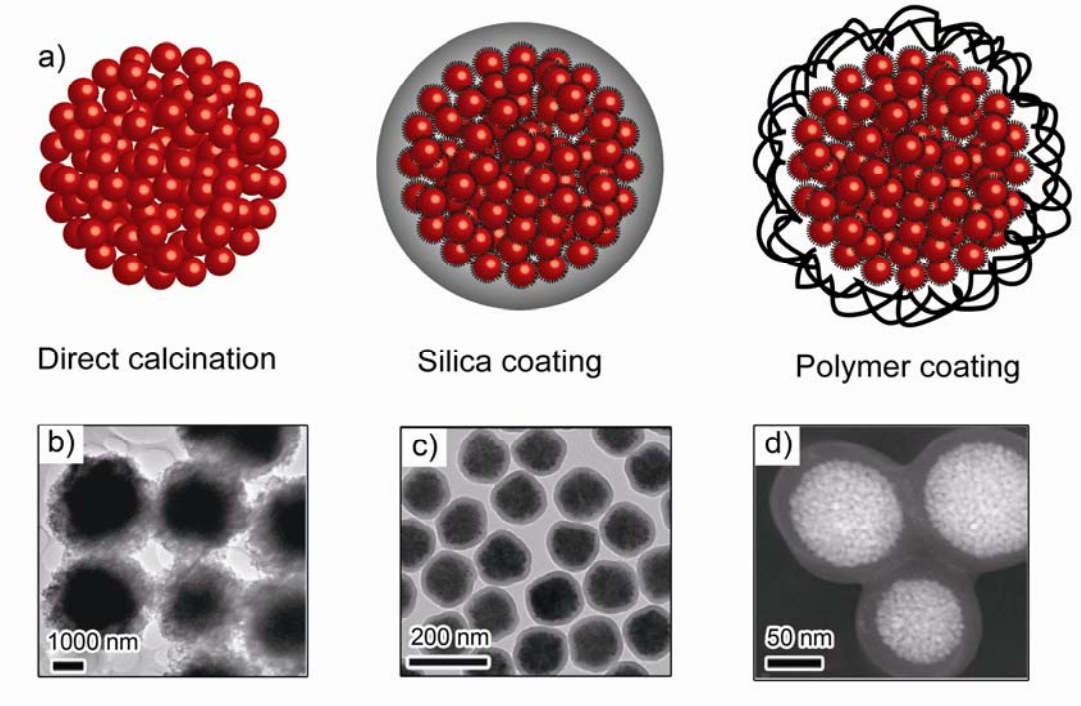

Figure 1.8 (a) Schematic illustration of surface modification of CNC structures. (b) TEM image of calcined mesoporous ferric oxide CNCs. (c) TEM image of silica coated Fe_3O_4 CNCs. (d) TEM image of iron oxide CNCs protected by copolymerization of GMA and EGDMA.

1.3.2 Silica Coating

The advantage of using silica as a coating material mainly lies in its high stability, easy regulation of the coating process, chemical inertness, controllable porosity, processability and optical transparency. In addition, silica coatings can endow the composites with biocompatibility and the possibility of subsequent functionalization. We have demonstrated silica coating on hydrophilic Fe_3O_4 CNCs by hydrolyzing tetraethoxysilane (TEOS) in a mixture containing ethanol, CNCs, and an ammonium ($NH_3 \cdot H_2O$) aqueous solution. The thickness of the silica shell can be tuned from ten to several hundred nanometers by simply controlling the concentration of precursor, TEOS.[44, 45] After silica coating, the CNCs can be well-dispersed in polar solutions such as water and alcohol solvents.

As an additional advantage, silica layers provides more possibilities for further surface modification through well-developed silane chemical reactions. For example, we have demonstrated that a monolayer of hydrophobic n-octadecyltrimethoxysilane (ODTMS) alkyl chains can be grafted to the silica surface through covalent -Si-O-Si- bonds, making the Fe_3O_4 CNC@SiO_2 colloids dispersible in most nonpolar solvents such as 1,2-dichlorobenzene, toluene, chloroform, and hexane.[46] In another demonstration, we have functionalized the Fe_3O_4 CNC@SiO_2 colloids with [3-(methacryloyloxy)propyl] trimethoxysilane (MPTMS) through the siloxane linkage. An aqueous phase precipitation polymerization process was then used to form a robust thermoresponsive polymer coating on the core surfaces by copolymerizing surface MPTMS with N-isopropylacrylamide (NIPAM, monomer).[47, 48]

Mesoporous silica shells can also be coated on the CNCs through a well-known surfactant-templating approach with cetyltrimethylammonium bromide (CTAB) as the templating surfactant.[49] An ordered mesoporous silica phase with cylindrical channels forms in the outer layer, as confirmed by TEM imaging. These unique mesoporous channels, which are perpendicular to the CNC core surface, offer high surface area for the derivation of various functional groups, provide large pore volume for the adsorption and encapsulation of biomacromolecules and even functional nanoparticles, and also enhance the accessibility to the CNC cores.

For CNCs assembled from preformed nanoparticles, the silica layer is critically important to keep their morphology during calcination. We have recently developed a protected calcination method to obtain well dispersible colloidal clusters by using hydrophobic TiO_2 CNCs as a model system.[6] In a typical process, TiO_2 CNCs are prepared by evaporation of the nonpolar solvent from an oil-in-water emulsion, and then coated with a silica layer, calcined at 500 ^oC for 2 h in air, followed by removal of SiO_2 layer through chemical etching in a dilute aqueous solution of NaOH. The silica coating and removal steps are essential for the successful fabrication of well-dispersible clusters. First, the silica layer protects the clusters from aggregation during calcination at high temperatures. Even though slight inter-cluster aggregation occurs due to silica fusion during calcination, the subsequent etching by NaOH removes the silica layer and releases the clusters from aggregation. Second, the etching process after calcination introduces a relatively high density of hydroxyl groups so that the cluster surface becomes negatively charged, making clusters dispersible in water. This silica coating – calcination - silica

removing method can be easily extended to other clusters with different components or prepared by different methods. For example, Fe_3O_4 CNCs prepared by one-step solvothermal synthesis are modified using this method and successfully applied in drug loading and magnetic resonance imaging.[50]

1.3.3 Polymer Coating

Polymer coating is an alternative method to render the clusters mechanically more robust. In addition, polymer coating has a number of other advantages: (1) the surface properties of clusters can be easily tuned by different polymer layers. For example, polyethylene glycol (PEG) may greatly enhance the water dispersity and biocompatibility of the clusters. (2) The large family of functional polymers offers many opportunities for building up multifunctional clusters. (3) New functionality may also be incorporated into polymer shell by copolymerizing a functional monomer or through a post-modification method. (4) The thickness of the polymer shell can be easily adjusted to several nanometers, which is important particularly when only a thin shell is required. Polymer coating can be achieved either by polymer adsorption or monomer polymerization on the CNC surface. For example, the positively charged poly(L-lysine)-poly(ethylene glycol)-folate (PLL-PEG-FOL) was adsorbed on the negatively charged cluster surfaces through an electrostatic interaction.[33] An amphiphilic hydrolized polymer poly(maleic anhydride-alt-1-octadecene) (PMAO) was selected to partially replace the SDS to coat on clusters through a coordination interaction between carboxylic acid and metal oxide surface.[51] Paquet et al. reported a direct polymer coating for clusters using seed-emulsion polymerization.[25] In this method, CNCs were first prepared by oil-in-water emulsion

evaporation method with SDS adsorbed on the surface. As the polymerization reaction was thermally initiated, monomers such as methyl methacrylate, styrene, and/or acrylic acid started to grow on the cluster surface. To achieve polymerization at the surface of the clusters and prevent nucleation and polymerization in micelles form by SDS, the concentration of the SDS in the dispersion of clusters must be below the critical micelle concentration of SDS, but high enough to maintain stability of the clusters.

1.4 Applications of Nanoparticle Assembly

CNCs represent a new class of materials that have broad applications in photonics, catalysis and bioanalysis due to their unique properties compared to the primary nanoparticle building blocks.

(1) CNCs can enhance the properties of the primary nanoparticles. For example, quantum dots (QDs) are especially attractive fluorescent materials for biological imaging due to their spectral tunability in the visible and infrared regions. Individual QDs, although with high quantum yields, sometimes are still not bright enough due to their small sizes. Therefore, CNC structures assembled by primary QDs can provide much stronger signals in biological imaging.[52] Another important case is superparamagnetic iron oxide nanoparticles, which have received most attention for biomedical applications, as they are not subject to strong magnetic interactions in dispersion. Several robust approaches have been developed for synthesizing magnetic iron oxide (e.g., γ-Fe_2O_3 or Fe_3O_4) nanoparticles with the size from several to ~20 nm. However, these as-synthesized nanoparticles have a low magnetization per particle, which limits their usage in many important applications such as separation, targeted

delivery or magnetic resonance imaging (MRI). Increasing the nanoparticle size increases the saturation magnetization, but also induces a superparamagnetic–ferromagnetic transition.[10] The unique and complex structure of CNCs allows materials to possess much higher saturated magnetization, while retaining the superparamagnetic behavior at room temperature even though their sizes exceed 30 nm. By taking advantage of this unique feature, many groups have successfully demonstrated the use of these superparamagnetic iron oxide CNCs with various sizes for magnetic separation.[53, 54] In addition, iron oxide CNCs have shown improved contrast in MRI due to high concentration of nanoparticles in the cluster structures.[55]

(2) Clusterization may enable multifunctionality by combining various building blocks. For example, clusters composed by magnetic iron oxide nanoparticles and fluorescent quantum dots have been widely studied as multiple-mode imaging contrast agents combining MRI and optical imaging.[33] Replacing QDs with noble metal nanoparticles in such composites creates multifunctional structures that are capable of MRI and photothermal therapy.[56] Superparamagnetic iron oxide nanoparticles were added to TiO_2 clusters to facilitate separation by external magnetic field in phosphopeptide enrichment.[26] Besides the building blocks of the clusters, capping ligands on nanoparticles and protection layer of the clusters such as silica and polymer can also act as functional materials. Clusters composed of oleic acid capped iron oxide nanoparticles were employed for enrichment of peptides and proteins based on the use of hydrophobic-hydrophobic interactions between the oleic acid and analytes.[57] Aligned mesoporous silica shell coated on clusters are used for removal of microcystins.[49]

(3) CNCs may exhibit collective properties not existing in individual nanoparticles. A classic example is the creation of “hotspots” by clustering the noble metal nanoparticles for generation of "hot spots" for enhancing Raman scattering. The assembly of plasmonic nanoparticles into secondary structures may induce near field electromagnetic coupling of surface plasmon between adjacent particles, thus creating "hotspots" which can significantly enhance the Raman signals from analytes.[58, 59]

(4) CNCs represent novel mesoporous structures with crystalline frameworks. Mesopores can be formed by packing primary nanoparticles into clusters. For primary nanoparticles containing capping ligands, they are typically calcined to remove the organic ligands to allow full access of the target molecular. Calcination at high temperatures may also enhance the mechanical stability of the clusters by bridging neighboring nanoparticles together through thermal fusion. Due to the crystalline nature of the primary particles, they do not grow significantly during calcination, allowing the preservation of high surface area and spherical morphology of the clusters. The pore sizes of the CNCs can be conveniently controlled by changing the size and shape of building blocks during assembly. The submicrometer size of the clusters and the three-dimensional pores enable fast diffusion and adsorption of target molecules. As a result of these great properties, the clusters can be employed for drug loading[60], bioseparation[6], sensing[19] and catalysis[7]. Furthermore, clustering method can be easily extended to the production of multicomponent structures such as QD/TiO_2 and QD/Au/TiO_2 hybrid mesoporous CNCs, which have been found to be highly efficient in photoelectrochemical (PEC) cell applications.[61, 62]

(5) Clusters make the surface modification much easier. Ligand exchange for individual nanoparticles usually involves several complex steps and in many cases is detrimental to the physical properties of the nanoparticles because the new hydrophilic ligands may not be able to effectively insulate the inorganic cores from chemical disturbance from the environment. On the other hand, surface modification of nanoparticle clusters can be considerably easier as many approaches including ligand attachment, silica encapsulation, and polymer coating have been well developed in the past for submicrometer objects.

These great features enable a number of interesting applications for CNC structures in the last few years. Since it is difficult to give a complete overview in this tutorial review, here we use three typical applications to highlight their unique advantages in designing structural and surface properties.

1.4.1 Magnetic Responsive Photonic Crystal Structures

The unique cluster structure allows Fe_3O_4 CNCs to retain the superparamagnetic property at room temperature even though their overall size exceeds the critical size (30 nm) distinguishing ferromagnetic and superparamagnetic magnetite. As shown in Figure 1.9a and 1.9b, the magnetization hysteresis loops of CNCs with various sizes display typical superparamagnetic characteristics with immeasurable remanence or coercivity at 300 K. The cluster-like structure renders the Fe_3O_4 CNC a much higher saturated magnetization and thereby a stronger magnetic response to external fields than the individual nanoparticles. The inset shows the magnetic moment per cluster increases with their overall size.

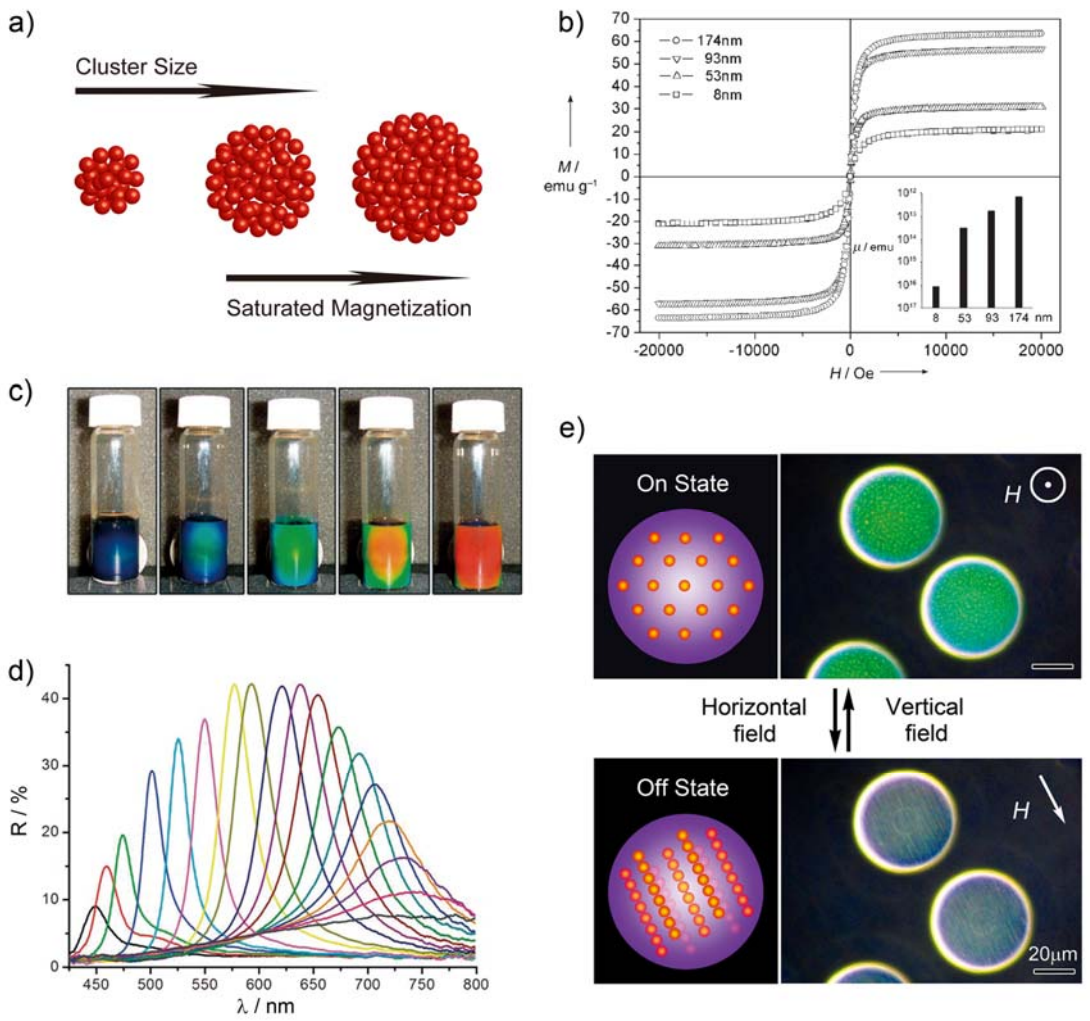

Figure 1.9 (a) Schematic illustration showing larger Fe_3O_4 CNCs have higher saturated magnetization. (b) Mass magnetization (M) as a function of applied external field (H) measured for 53-nm, 93-nm, 174-nm CNCs and a reference sample of 8-nm single crystalline nanoparticles of Fe_3O_4. Inset shows the magnetic moment (μ) per cluster (or particle) plotted in a logarithmic graph. (c) Photographs of aqueous solution of Fe_3O_4 CNCs in response to the changing magnetic field. The sample-magnet distance decreases gradually from left to right. (d) Reflection spectra of 120-nm Fe_3O_4 CNC aqueous solution in response to an external magnetic field with varying strength achieved by changing the magnet-sample distance. (e) Schematic illustrations and optical microscopy images for the magnetochromatic effect caused by rotating the chain-like photonic structures in magnetic fields.

With the successful synthesis of Fe_3O_4 CNCs featured with superparamagnetic properties, large and uniform sizes, and highly charged surfaces, we have demonstrated their assembly in aqueous solution into photonic crystal structures whose optical signals can be instantly tuned by using external magnetic fields. Under white light illumination, the colloidal photonic crystals in the solution show brilliant colors from red to blue when the strength of applied magnetic field is increased (Figure 1.9c). This visual effect, observable in direction parallel to the magnetic field, results from the Bragg diffraction of incident light by the periodically ordered structures assembled from Fe_3O_4 CNCs. A strong magnetic dipole-dipole interparticle attraction is induced instantly in the superparamagnetic particle dispersion in response to the application of external magnetic fields, which creates one-dimensional chains each containing a string of particles. The interparticle separation is defined by the balance between the magnetic attraction and the interparticle repulsions such as the electrostatic force. By employing uniform superparamagnetic CNCs of appropriate sizes and surface charges, one-dimensional periodicity may be created, which leads to strong diffraction in the optical regime. Magnetic forces, acting remotely over a large distance, not only drive the rapid formation of colloidal photonic arrays with a wide range of interparticle spacing, but also allow instant tuning of the photonic properties by changing the orientation of the colloidal assemblies or their periodicity through the manipulation of the interparticle force balance. Such optical response to the external magnetic field is instant and fully reversible, and the required field strength for realizing the ordering of CNCs and color tuning is merely 50-500 G.

By modifying the CNC surface properties, we have been able to extend such assembly process to solvents of various polarities, making it possible to fabricate photonic crystal microspheres whose orientation and consequently photonic behavior can be easily controlled by using external magnetic fields.[63] The magnetically responsive photonic microspheres are prepared through instant assembly of Fe_3O_4 CNC@SiO_2 colloidal particles inside emulsion droplets of a UV curable resin (poly(ethyleneglycol) diacrylate, PEGDA), followed by an immediate UV curing process to polymerize the droplets and fix the ordered structures (Figure 1.9e). Unlike the previously reported "opal balls" whose orientation can't be controlled, the embedded superparamagnetic chains make microspheres magnetically "polarized" so that their orientation becomes fully controllable because the superparamagnetic chains always tend to align along the external field direction. The diffraction of the "opal balls" can be conveniently switched "on" and "off" by rotating the external magnetic field. In a vertical field, the particle chains stand straight so that their diffraction is turned "on" and the corresponding color can be observed from the top. Each bright color dot in the dark-field optical microscopy image actually represents one vertically aligned particle chain. On the contrary, when the field is switched horizontally, the microspheres are forced to rotate 90° so that the particle chains are laid down and the diffraction is turned off.

1.4.2 Catalysis

Metal nanoparticles have been extensively studied as effective catalysts in many reactions. In catalysis, it is important to ensure that the dispersed metal nanoparticles retain their original structure in particular their size and shape, throughout their

pretreatment, activation, and catalytic use. However, metal nanoparticles tend to reconstruct, diffuse, coalesce, and sinter during the reaction process, which leads to significant reduction in catalytic activity. It is therefore highly desirable to develop ways to overcome this limitation. Nanoparticle clusters are ideal support materials because of their intrinsic porous structure, high surface area, rigid framework, short diffusion length for surrounding solutes, and easy inclusion of catalyst nanoparticles. For example, metal nanoparticles can be conveniently embedded in metal oxide CNCs to display high and stable catalytic activity, as shown in Figure 1.10. Metal particles are effectively separated from each other and trapped in the metal oxide matrix. Even after heat treatment, the metal nanoparticles are still well separated. In addition, the target molecules can easily access the metal nanoparticle surface through the mesopores of the CNC structures.[28] The hydrogenation of cyclohexene to cyclohexane and its dehydrogenation to benzene were used as probe reactions to study the catalytic performance of the prepared Pd-CeO_2 composite CNCs. The results in Figure 1.10 show excellent selectivity of the CNC catalyst, with products being exclusively cyclohexane at low reaction temperature (<185 °C) and benzene at high temperature (~350 °C). Conducting the hydroconversion reactions for three cycles shows no significant loss in catalytic activity, indicating good thermal stability and robust performance of the composite catalysts.

1.4.3 Bioseparation

Metal oxide affinity chromatography (MOAC), built upon a variety of metal oxide materials, have been intensively studied because of their high selectivity for bio-molecular trapping, such as TiO_2, ZrO_2, Fe_2O_3 for phosphopeptides and NiO for histidine

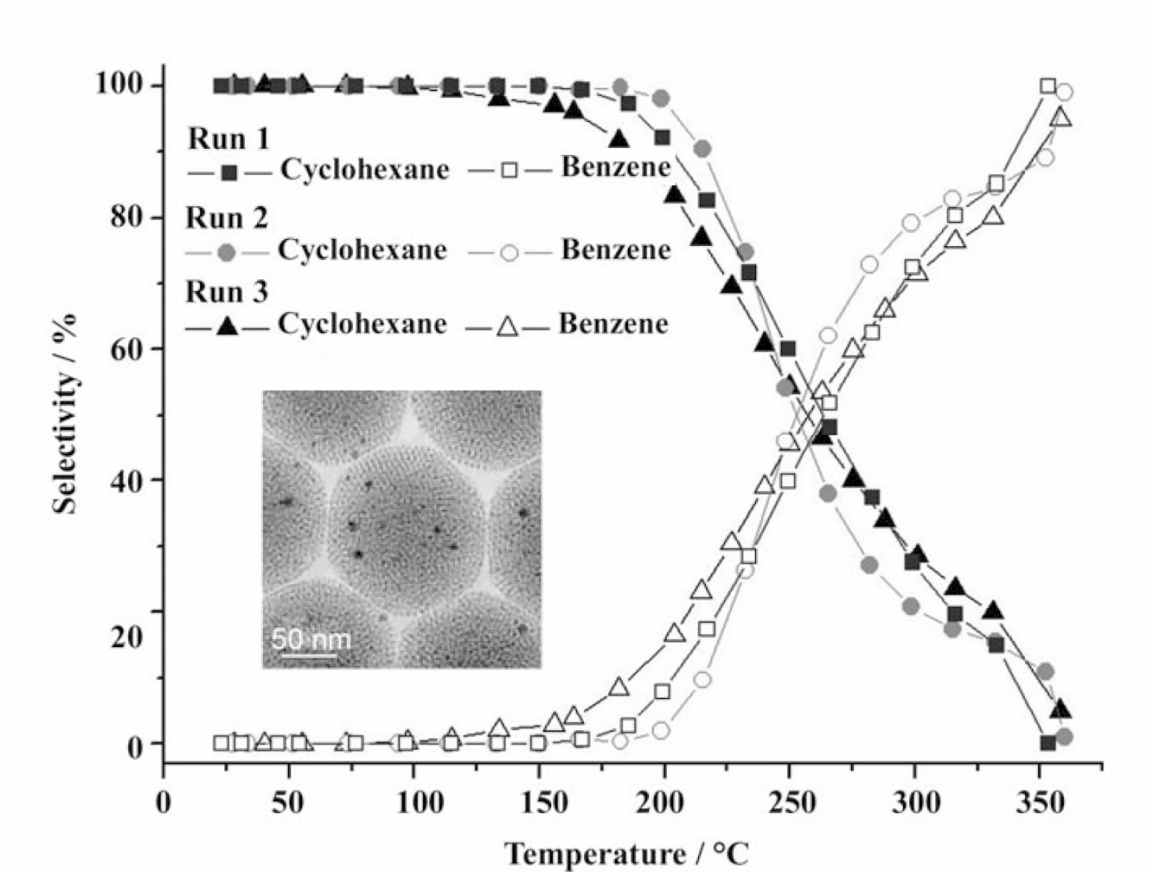

Figure 1.10 Selectivity of the cyclohexene hydrogenation to cyclohexane (filled symbols) and the dehydrogenation to benzene (empty symbols) with Pd–CeO_2 CNCs as catalysts. Inset is typical TEM image of hybrid CNC structures.

tagged proteins. In addition, nanoparticles have many superior characteristics for bioseparation compared to those of the conventional micrometer-sized resins or beads, including high capacity, fast and effective binding, and short diffusion length for biomolecules. However, there are several intrinsic difficulties in the application of nanoparticles for bio-separation. First, they cannot be conveniently separated from the solution mixture by conventional methods such as centrifugation because of their extremely small sizes. Second, high quality nanoparticles are typically synthesized in nonpolar solvents so that they are covered with a layer of hydrophobic ligands, which makes the particles non-water-soluble and greatly limits their direct use in aqueous environments. Third, the surfaces covered with hydrophobic ligands cannot effectively trap biomolecules. The mesoporous CNCs with clean surface by calcination can well address these challenges. The mesoporous Fe_2O_3 CNCs have demonstrated high sensitivity, selectivity and capacity to specifically enrich phosphopeptides from tryptic digest of complex proteins under mild treatment condition in short loading time, due to its large mesoporosity. Additionally, the preparation of mesoporous Fe_2O_3 microspheres is simple and low cost. Such Fe_2O_3 microspheres show great potential application in the rapid and effective isolation of phosphopeptides from complex sample prior to MS analysis.[43]

1.5 My Work in Nanoparticle Assembly

My PhD research focuses on the development of general processes that allow convenient production of functional colloidal particles by direct self-assembly of single or multiply hydrophobic nanoparticles, and then applying these assemblies in catalysis

and bioseparation field. Recently, most conventional fabrication methods for multifunctional structures are limited to the assembly of hydrophilic nanoparticles. However, a large portion of high quality nanoparticles, such as semiconductor quantum dots and metal oxide nanoparticles, are synthesized through high-temperature thermolysis reactions. By kinetically controlling the nucleation and growth process, I have been able to routinely produce nanoparticles with well-defined size, shape, composition, and surface properties. Many nanoparticles can be conveniently produced in our laboratory, including CdSe, ZrO2, Ag, γ-Fe2O3, and NaYF4:Yb,Er nanodots and CdSe nanorods. They are generally covered with hydrophobic surfactants such as oleic acid.

Two general processes for assembling hydrophobic nanoparticles to colloidal clusters were developed in my thesis work. The first method is direct self-assembly of hydrophobic nanoparticles on host nanostructures containing high density surface thiol groups. Briefly, mercapto-silica colloidal particles made from (3-mercaptopropyl)trimethoxysilane (MPS) are first synthesized as an adsorbent, hereafter as MPS spheres. As each MPS molecule contains one thiol group, the as synthesized silica spheres contain an extremely high density of thiol groups on their surfaces. Nanoparticles with desired functions are efficiently attached to the surface of MPS spheres by taking advantage of the high density of thiol groups. In order to improve the chemical/mechanical stability and water-dispersibility, the composites are further coated with another thin silica shell. Mercapto-silica can also be coated onto nonspherical objects to form new types of hosts that can immobilize nanoparticles and produce multifunctional nanorods, nanodisks, and nanowires. On the other hand, by forming

another layer of mercapto-silica coating on the normal silica surface, nanoparticles of different compositions and properties can be introduced onto the host particle surface in a layer-by-layer (LbL) manner. The details of this research are shown in Chapter 2, Chapter 3 and Chapter 4.

Another universal strategy for the assembly of hydrophobic nanopaticles is based on emulsion method. Typically, nanocrystals confined in an oil droplet are self-assembled into spherical clusters upon evaporation of the low-boiling-point organic solvent (the "oil"). Clusters of densely packed hydrophobic superparamagnetic γ-Fe_2O_3 nanocrystals have been prepared as a powerful adsorbent for enrichment of peptides and proteins based on the use of hydrophobic-hydrophobic interactions between the protection ligands of the nanocrystals and the analytes.

Then, I further developed a post-treatment method called protected calcination to achieve well-dispersed mesoporous cluster with clean surfaces. Typically, the clusters are first coated with a silica layer and then calcined at 500 ^{o}C to enhance the mechanical stability of the clusters, and at the same time to remove the organic surfactants and make the nanocrystal surface fully accessible to target molecules. By coating a layer of silica before calcination and removing it afterwards through chemical etching, we have been able to prevent the clusters from aggregating during heating, make the cluster surface hydrophilic and negatively charged, and eventually enhance the dispersibility of the clusters in aqueous solution.

The as-synthesized mesoporous colloidal nanocrystal clusters (CNCs) were ready applied in bioseparation and photo catalysis due to their unique properties, including their

clean surface, high specific surface area, narrow pore size distribution, adjustable pore size and great water dispersity. As an example, mesoporous TiO_2 clusters were applied in the enrichment of phosphopeptides from complex biosamples. The results confirmed the excellent enrichment power of the nanoparticle clusters compared to the TiO_2 solid spheres, which have been fully tested by effective enrichment of phosphopeptides from digests of standard phosphoproteins, complex protein mixtures, natural non-fat milk and human serum samples. Phosphorylated proteins can also be effectively adsorbed on these mesoporous clusters.

An inherent advantage of the self-assembly process is the convenient incorporation of multiple components into the clusters to further facilitate separation and detection. We showed that the addition of superparamagnetic iron oxide nanocrystals to the clusters allows not only selective phosphopeptide enrichment but also their efficient removal from the analyte solution by using an external magnetic field. Moreover, the pore sizes of the TiO_2 clusters could be conveniently controlled by changing the size and shape of the building blocks during assembly, thus making it possible to isolate the biomolecules such as intact phosphorylated proteins with different sizes based on the size-exclusion strategy.

Hollow colloidal nanocrystal clusters (HCNCs) could be formed if uniform nanocrystals and hydrophobic polymers are confined together in an oil droplet. Upon the evaporation of the low boiling point oil, the nanocrystals are expelled by the polymer as its concentration increases in the oil droplet and accumulates on the surface of polymers to form monolayer and multilayer assembly. The number of nanocrystals layers depends

on the original nanocrystal/polymer ratio in the oil droplet. The size and morphology of assemblies can be conveniently tuned by controlling the size and shape of nanocrystals, the chemical nature of protection ligands on nanocrystals and the type of polymers. The stable, clean and well-dispersed HCNCs also could be fabricated by the process of 'silica coating-calcinations-silica removed'.

Such assembly approaches and surface modification methods will provide the research community a highly versatile, configurable, and reproducible process to prepare various multifunctional structures, which may have many important technical applications. The detail results of this research is described in Chapter 5, Chapter 6 and Chapter 7.

Reference

(1) Nutzenadel, C.; Zuttell, A.; Chartouni, D.; Schmid, G.; Schlapbach, L., *Eur. Phys. J. D* **2000,** 8, 245-250.

(2) Yin, Y.; Alivisatos, A. P., *Nature* **2005,** 437, 664-670.

(3) Murray, C. B.; Norris, D. J.; Bawendi, M. G., *J. Am. Chem. Soc.* **1993,** 115, 8706-8715.

(4) Zhuang, J. Q.; Wu, H. M.; Yang, Y. G.; Cao, Y. C., *Angew. Chem. Int. Ed.* **2008,** 47, 2208-2212.

(5) Lu, Z.; Gao, C.; Zhang, Q.; Chi, M.; Howe, J. Y.; Yin, Y., *Nano Lett.* **2011,** 11, 3404-3412.

(6) Lu, Z.; Ye, M.; Li, N.; Zhong, W.; Yin, Y., *Angew. Chem. Int. Ed.* **2010,** 49, 1862-1866.

(7) Zhang, Q.; Joo, J.-B.; Lu, Z.; Dahl, M.; Oliveira, D.; Ye, M.; Yin, Y., *Nano Res.* **2011,** 4, 103-114.

(8) Narayanaswamy, A.; Xu, H. F.; Pradhan, N.; Kim, M.; Peng, X. G., *J. Am. Chem. Soc.* **2006,** 128, 10310-10319.

(9) Naravanaswamy, A.; Xu, H.; Pradhan, N.; Peng, X., *Angew. Chem. Int. Ed.* **2006,** 45, 5361-5364.

(10) Ge, J.; Hu, Y.; Biasini, M.; Beyermann, Ward P.; Yin, Y., *Angew. Chem. Int. Ed.* **2007,** 46, 4342-4345.

(11) Li, C.; Zhao, Y.; Li, F.; Shi, Z.; Feng, S., *Chem. Mater.* **2010,** 22, 1901-1907.

(12) Li, C.; Zhao, Y.; Wang, L.; Li, G.; Shi, Z.; Feng, S., *Eur. J. Inorg. Chem.* **2010**, 217-220.

(13) Deng, H.; Li, X.; Peng, Q.; Wang, X.; Chen, J.; Li, Y., *Angew. Chem. Int. Ed.* **2005,** 44, 2782-2785.

(14) Zhu, Y.; Zhao, W.; Chen, H.; Shi, J., *J. Phys. Chem. C* **2007,** 111, 5281-5285.

(15) Xuan, S.; Wang, Y.-X. J.; Yu, J. C.; Cham-Fai Leung, K., *Chem. Mater.* **2009,** 21, 5079-5087.

(16) Xuan, S. H.; Wang, F.; Wang, Y. X. J.; Yu, J. C.; Leung, K. C. F., *J. Mater. Chem.* **2010,** 20, 5086-5094.

(17) Liu, J.; Sun, Z. K.; Deng, Y. H.; Zou, Y.; Li, C. Y.; Guo, X. H.; Xiong, L. Q.; Gao, Y.; Li, F. Y.; Zhao, D. Y., *Angew. Chem. Int. Ed.* **2009,** 48, 5875-5879.

(18) Fang, X.-L.; Chen, C.; Jin, M.-S.; Kuang, Q.; Xie, Z.-X.; Xie, S.-Y.; Huang, R.-B.; Zheng, L.-S., *J. Mater. Chem.* **2009,** 19, 6154-6160.

(19) Hu, X. L.; Gong, J. M.; Zhang, L. Z.; Yu, J. C., *Adv. Mater.* **2008,** 20, 4845-4850.

(20) Penn, R. L.; Banfield, J. F., *Science* **1998,** 281, 969-971.

(21) Corma, A.; Atienzar, P.; Garcia, H.; Chane-Ching, J. Y., *Nat Mater* **2004,** 3, 394-397.

(22) Deshpande, A. S.; Pinna, N.; Smarsly, B.; Antonietti, M.; Niederberger, M., *Small* **2005,** 1, 313-316.

(23) Ba, J. H.; Polleux, J.; Antonietti, M.; Niederberger, M., *Adv. Mater.* **2005,** 17, 2509-2512.

(24) Bai, F.; Wang, D. S.; Huo, Z. Y.; Chen, W.; Liu, L. P.; Liang, X.; Chen, C.; Wang, X.; Peng, Q.; Li, Y. D., *Angew. Chem. Int. Ed.* **2007,** 46, 6650-6653.

(25) Paquet, C.; Pagé, L.; Kell, A.; Simard, B., *Langmuir* **2009,** 26, 5388-5396.

(26) Lu, Z.; Duan, J.; He, L.; Hu, Y.; Yin, Y., *Anal. Chem.* **2010,** 82, 7249-7258.

(27) Li, P.; Peng, Q.; Li, Y., *Adv. Mater.* **2009,** 21, 1945-1948.

(28) Chen, C.; Nan, C.; Wang, D.; Su, Q.; Duan, H.; Liu, X.; Zhang, L.; Chu, D.; Song, W.; Peng, Q.; Li, Y., *Angew. Chem. Int. Ed.* **2011,** 50, 3725-3729.

(29) Isojima, T.; Suh, S. K.; Sande, J. B. V.; Hatton, T. A., *Langmuir* **2009,** 25, 8292-8298.

(30) Zhuang, J. Q.; Wu, H. M.; Yang, Y. A.; Cao, Y. C., *J. Am. Chem. Soc.* **2007,** 129, 14166-14167.

(31) Zhuang, J.; Shaller, A. D.; Lynch, J.; Wu, H.; Chen, O.; Li, A. D. Q.; Cao, Y. C., *J. Am. Chem. Soc.* **2009,** 131, 6084-6085.

(32) Li, L.; Choo, E. S. G.; Yi, J.; Ding, J.; Tang, X.; Xue, J., *Chem. Mater.* **2008,** 20, 6292-6294.

(33) Kim, J.; Lee, J. E.; Lee, S. H.; Yu, J. H.; Lee, J. H.; Park, T. G.; Hyeon, T., *Adv. Mater.* **2008,** 20, 478-483.

(34) Zhao, Y.; Ma, Y.; Li, H.; Wang, L., *Anal. Chem.* **2012,** 84, 386-395.

(35) Kotov, N. A.; Dekany, I.; Fendler, J. H., *J. Phys. Chem.* **1995,** 99, 13065-13069.

(36) Gomez, D. E.; Pastoriza-Santos, I.; Mulvaney, P., *Small* **2005,** 1, 238-241.

(37) Caruso, F.; Spasova, M.; Salgueirino-Maceira, V.; Liz-Marzan, L. M., *Adv. Mater.* **2001,** 13, 1090-1094.

(38) Caruso, F.; Caruso, R. A.; Möhwald, H., *Science* **1998,** 282, 1111-1114.

(39) Yoon, M.; Kim, Y.; Cho, J., *ACS Nano* **2011,** 5, 5417-5426.

(40) Lin, Y.; Böker, A.; Skaff, H.; Cookson, D.; Dinsmore, A. D.; Emrick, T.; Russell, T. P., *Langmuir* **2005,** 21, 191-194.

(41) Lin, Y.; Skaff, H.; Emrick, T.; Dinsmore, A. D.; Russell, T. P., *Science* **2003,** 299, 226-229.

(42) Skaff, H.; Lin, Y.; Tangirala, R.; Breitenkamp, K.; Boker, A.; Russell, T. P.; Emrick, T., *Adv. Mater.* **2005,** 17, 2082-2086.

(43) Han, L.; Shan, Z.; Chen, D. H.; Yu, X. J.; Yang, P. Y.; Tu, B.; Zhao, D. Y., *J Colloid Interf Sci* **2008,** 318, 315-321.

(44) Ge, J. P.; Yin, Y. D., *Adv. Mater.* **2008,** 20, 3485-3491.

(45) Fu, R.; Jin, X.; Liang, J.; Zheng, W.; Zhuang, J.; Yang, W., *J. Mater. Chem.* **2011,** 21.

(46) Ge, J. P.; He, L.; Goebl, J.; Yin, Y. D., *J. Am. Chem. Soc.* **2009,** 131, 3484-3486.

(47) Luo, B.; Song, X.-J.; Zhang, F.; Xia, A.; Yang, W.-L.; Hu, J.-H.; Wang, C.-C., *Langmuir* **2009,** 26, 1674-1679.

(48) Ge, J.; Huynh, T.; Hu, Y.; Yin, Y., *Nano Lett.* **2008,** 8, 931-934.

(49) Deng, Y.; Qi, D.; Deng, C.; Zhang, X.; Zhao, D., *J. Am. Chem. Soc.* **2008,** 130, 28-29.

(50) Xuan, S.; Wang, F.; Lai, J. M. Y.; Sham, K. W. Y.; Wang, Y.-X. J.; Lee, S.-F.; Yu, J. C.; Cheng, C. H. K.; Leung, K. C.-F., *ACS Appl. Mater. Interfaces* **2011,** 3, 237-244.

(51) Zhang, Q.; Wang, X.; Zhu, Y., *J. Mater. Chem.* **2011,** 21, 12132-12138.

(52) Yan, X.; Cui, Y.; Qi, W.; Su, Y.; Yang, Y.; He, Q.; Li, J., *Small* **2008,** 4, 1687-1693.

(53) Ye, M. M.; Zhang, Q.; Hu, Y. X.; Ge, J. P.; Lu, Z. D.; He, L.; Chen, Z. L.; Yin, Y. D., *Chem-Eur J* **2010,** 16, 6243-6250.

(54) Ge, J. P.; Zhang, Q.; Zhang, T. R.; Yin, Y. D., *Angew. Chem. Int. Ed.* **2008,** 47, 8924-8928.

(55) Qiu, P. H.; Jensen, C.; Charity, N.; Towner, R.; Mao, C. B., *J. Am. Chem. Soc.* **2010,** 132, 17724-17732.

(56) Kim, J.; Lee, J. E.; Lee, J.; Jang, Y.; Kim, S. W.; An, K.; Yu, H. H.; Hyeon, T., *Angew. Chem. Int. Ed.* **2006,** 45, 4789-4793.

(57) Lu, Z.; He, L.; Yin, Y., *Chem. Commun.* **2010,** 46, 6174-6176.

(58) Yan, B.; Thubagere, A.; Premasiri, W. R.; Ziegler, L. D.; Dal Negro, L.; Reinhard, B. r. M., *Acs Nano* **2009,** 3, 1190-1202.

(59) Yuan, C.; Liu, R.; Wang, S.; Han, G.; Han, M.-Y.; Jiang, C.; Zhang, Z., *J. Mater. Chem.* **2011,** 21, 16264-16270.

(60) Luo, B.; Xu, S. A.; Luo, A.; Wang, W. R.; Wang, S. L.; Guo, J.; Lin, Y.; Zhao, D. Y.; Wang, C. C., *Acs Nano* **2011,** 5, 1428-1435.

(61) Liu, L.; Hensel, J.; Fitzmorris, R. C.; Li, Y.; Zhang, J. Z., *J. Phys. Chem. Lett.* **2010,** 1, 155-160.

(62) Liu, L.; Wang, G.; Li, Y.; Li, Y.; Zhang, J. Z., *Nano Res.* **2011,** 4, 249-258.

(63) Ge, J. P.; Lee, H.; He, L.; Kim, J.; Lu, Z. D.; Kim, H.; Goebl, J.; Kwon, S.; Yin, Y. D., *J. Am. Chem. Soc.* **2009,** 131, 15687-15694.

Chapter 2

One-Pot Synthesis of Mercapto-Silica Colloidal Spheres

2.1 Introduction

Surface functionalization provides a powerful means of tuning the properties of nanostructured materials for their application in catalysis, adsorption, separation, optics, and many other areas.[1-9] Colloidal silica has been one of the most popular materials suitable for introducing surface functionality to nanostructures because of its chemical inertness, controllable porosity, convenient processability, optical transparency and possibility of post-functionalization.[10-16] In addition to the conventional grafting method for introducing functional groups to the silica surface, recent efforts have been made to directly use organosilane precursors for producing organosilica nanostructures containing functional surfaces.[17-20] The unhydrolyzable organic group on a typical organosilane will be automatically incorporated into the silica network, rendering the silica surface a high density of functional groups that is difficult to achieve using conventional grafting methods. In particular, mercapto-silanes such as 3-mercaptopropyltrimethoxysilane (MPS) have been employed to produce thiol-functionalized silica,[21-24] and used for adsorbing highly toxic heavy metals ions, such as mercury, silver and lead in contaminated water and organic solvents.[25-28] The strong thiol-metal interaction also allows binding of various nanoparticles, including Au,[16, 29-31] CdS,[32, 33] and $CoFe_2O_4$ to silica supports.[34] Moreover, thiol-functionalized silica has been used for the immobilization of oligonucleotides and proteins for bioanalysis.[35-40]

In contrast to pristine silica that can be easily produced by sol-gel processes such as the well-known Stöber method,[41] the colloidal chemistry of organosilane as the sole precursor to organosilica has not been fully developed, although considerable efforts have been made along this direction. Trau et al. have explored a two-step procedure for the synthesis of mercapto-silica spheres of several to tens of micrometers in size.[17, 42, 43] Nakamura et al. further reported a number of one-pot procedures for the preparation of mercapto-silica spheres with sizes ranging from a few hundred nanometers to several micrometers.[40] They pointed out that mercapto-silica spheres of narrower size-distributions are favored in a base-catalyzed aqueous hydrolysis reaction rather than the Stöber process which takes place mainly in alcohol solutions.[18] However, the products suffer from high polydispersities, even when using recent procedures that involve colloidal synthesis at a high temperature (100 ^{o}C).[36] In addition, although various synthesis conditions have been explored, these prior studies have not been able to clarify the mechanisms for how these organosilica particles nucleate, grow, and ripen and how these processes are affected by the reaction conditions. This understanding is very important for producing organosilica particles of well-controlled morphology, size, and uniformity.

Here, we carry out systematic studies of the colloidal synthesis of mercapto-silica spheres by hydrolyzing MPS precursor in a basic aqueous solution, and propose that the mercapto-silica spheres form through an emulsion-based process. Understanding of the formation and ripening mechanism allows us to produce high quality mercapto-silica spheres of uniform size ranging from ~150 nm to ~3.5 μm. The emulsion-based

mechanism is consistent with the one proposed by Trau et al. for their two-step process (acid-catalyzed hydrolysis and condensation followed by base-catalyzed condensation) for the synthesis of large microspheres (>2.5 μm),[42] although our focus in this work is on the formation of submicrometer spheres through a one-pot base-catalyzed synthesis. We show that the size of mercapto-silica spheres can be tuned systematically by changing the amount of precursor, the concentration of ammonia and additional surfactant, and the reaction time. All these effects can be explained well by using the emulsion-based mechanism. We also demonstrate the change of sphere size at the later stages of the reaction is due to Ostwald ripening, and further point out that the key for preparing uniform mercapto-silica spheres in this reaction process is to separate the products from the reaction mixture right after their solidification to avoid ripening, and then disperse them in solvents that can prevent particle dissolution and materials transfer.

2.2 Experimental Section

2.2.1 Materials

MPS precursor, sodium hydroxide, ammonium hydroxide solution ($NH_3 \cdot H_2O$, ~28% NH_3 in water) and sodium dodecyl sulfate (SDS) were purchased from Aldrich. Ethanol was obtained from Fisher Scientific. All chemicals were used as received without further treatment.

2.2.2 Synthesis of Mercapto-silica Spheres

Mercapto-silica spheres were prepared by using a one-pot procedure. In a typical synthesis, MPS precursor in the amount of 0.05–2.00 mL (final concentration between 0.009 and 0.36 M) was added to 1% NH_4OH aqueous solution (0.05 M) to a total volume

of 30 mL and vigorously shaken for 1 minute using an IKA MS3 minishaker at a speed of 2500 rpm. The resulting mixture was then incubated at room temperature for several hours. The final products were washed with ethanol a few times. For spheres with sizes less than 200 nm, washing was performed with 0.01 M NaOH aqueous solution first to prevent aggregation and then with ethanol several times. The incubation time decreased with increasing precursor concentration: 2 hours for the concentration above 180 mM, 3–5 hours for the concentration between 36 and 90 mM, and 12 hours for the concentration less than 18 mM. We also prepared the particles by varying only the concentrations of catalyst (NH_3) and surfactant (SDS), and keeping the rest of the parameters unchanged to investigate their influence on product size and uniformity.

2.2.3 Characterization

The morphology of the nanostructures was investigated using a Philips Tecnai 12 transmission electron microscope (TEM) with a 120 keV beam energy. UV-Vis absorption spectra measurements were carried out using a Varian Cary 50 spectrophotometer. Dynamic light scattering (DLS) analysis was performed on a ZetaPALS system. Optical images were taken using a Zeiss AXIO Imager optical microscope.

2.3 Results and Discussion

2.3.1 Formation of Mercapto-Silica Spheres

Mercapto-silica spheres are prepared using a MPS precursor as the only silica source, similar to the way tetraethyl orthosilicate (TEOS) is used in the Stöber method. However, unlike the standard Stöber process, water instead of alcohol is used as the main

solvent. The precursor MPS is dispersed initially as large oil droplets in water so that the solution appears clear upon one minute of mixing. Within several minutes, the solution starts to appear milky, indicating the formation of emulsion droplets that can scatter visible light. After several hours, solid mercapto-silica spheres form which can be recovered by centrifugation. Nakamura et al. suspected that the growth process of mercapto-silica particles may differ from that of TEOS, however, no mechanism was clearly proposed.[40] Our observations suggest that the mercapto-silica particles form through a process similar to the emulsion polymerization process that has been widely employed for the preparation of polymer latex particles. The base-catalyzed hydrolysis of MPS precursor produces mercaptopropylsilicate monomers or oligomers which have an amphiphilic structure due to the presence of both hydrophilic silanol groups and relatively hydrophobic mercaptopropyl chains. At the early stage of the reaction, the hydrolyzed mercaptopropylsilicate species act as surfactants to emulsify the remaining precursor droplets, producing an oil-in-water emulsion.[17] Further hydrolysis and condensation of MPS lead to the formation of solid spheres through a mechanism analogous to the well-studied emulsion polymerization process. Interestingly, a similar self-emulsification process has been reported for the formation of polydimethylsiloxane (PDMS) colloidal particles through the hydrolysis of dimethyldiethoxysilane (DMDES) in water, which contains two nonhydrolyzable hydrophobic methyl groups.[44, 45]

Figure 2.1 further illustrates the proposed mechanism. It begins with the formation of precursor mini-droplets through the deformation of the interface of MPS precursor/aqueous phase due to the shear force provided by the quick shaking method.

With ammonia as a catalyst, MPS precursor is partially hydrolyzed to form monomers and oligomers of mercaptopropylsilicate, which emulsify the precursor to produce smaller oil-in-water emulsion droplets. Hydrolysis and condensation continue inside the emulsion droplets, which subsequently grow through coalescence of droplets and the mass transfer of more precursor from the mini-droplets. Analogous to the classic emulsion polymerization process, the mini-droplets are believed to act as reservoirs by providing MPS precursor to the growing emulsion droplets. After a certain reaction period, the precursor mini-droplets disappear and most of the MPS species are located in the emulsion droplets. At this point, the emulsion droplets can only grow through coalescence, which becomes more difficult as the condensation of the silica proceeds at the later stage. After extensive condensation, the emulsion droplets convert into a uniform population of MPS solid spheres, as shown in the highlighted step in Figure 2.1. It is worth noting that this is not the final state for the mercapto-silica spheres if they are kept in the reaction solution. As will be discussed later, the well-known Ostwald ripening process may occur, leading to the growth of larger spheres at the expense of the relatively smaller ones and thus gradually increasing the polydispersity of the mercapto-silica spheres.[46] Understanding of the formation and ripening mechanism of the mercapto-silica spheres has helped us to significantly improve the quality of the products and harvest size-controlled monodisperse spheres.

The growth of mercapto-silica spheres was monitored by DLS, as shown in Figure 2.2a, for a sample prepared with the MPS and ammonia concentrations of 0.036 and 0.50 M, respectively. Right after mixing, no droplets can be detected by DLS due to

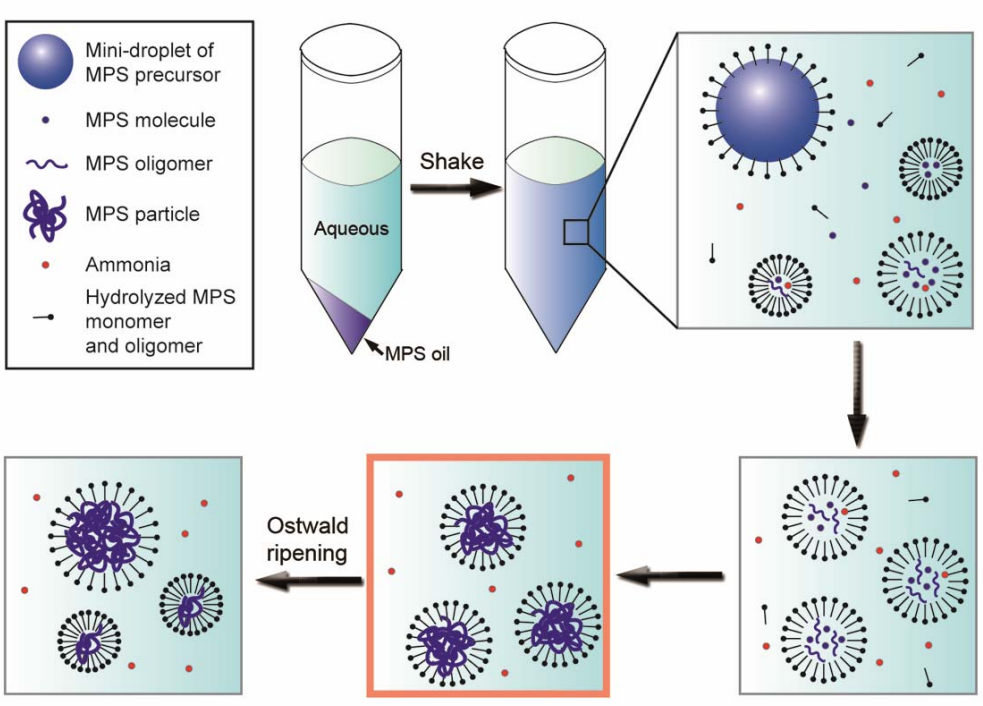

Figure 2.1 Schematic illustration showing the formation process of the mercapto-silica spheres.

the invisibility of the MPS precursor in water. Within 2 minutes, a small portion of the MPS precursor was hydrolyzed, yielding amphiphilic species that eventually allowed the emulsification of the system. As indicated in DLS measurements, emulsion droplets with an average size of ~180 nm started to form after 2 minutes, with size increasing gradually to about 600 nm in ~20 minutes and remaining constant afterwards. The growth of the emulsion droplets can be attributed to either the mass transfer from the precursor reservoir or inter-droplet coalescence, both of which are due to the liquid nature of the precursor and hydrolyzed monomer and oligomers at the initial stage of the reaction.[42] As the hydrolysis and condensation proceed in the presence of the base catalyst, a three-dimensional Si-O-Si network is gradually established which turns the emulsion droplets into rigid spheres. Because the coalescence becomes difficult, the particle size remains at ~600 nm after ~20 minutes of reaction. The formation of silica spheres can also be monitored by the optical transmittance of the solution because colloidal silica particles scatter visible and near IR light. As more liquid silane is converted to solid silica, the overall transmittance decreases accordingly. Figure 2.2b shows the evolution of the transmittance value at a wavelength of 900 nm during the reaction, while the inset shows the corresponding transmission spectra. Again, no obvious change in transmittance occurred in the first 2 minutes, which is consistent with DLS analysis. Then the transmittance decreased gradually due to the hydrolysis and polymerization of the MPS precursors. Interestingly, the transmittance continued decreasing as time elapsed. It suggests that hydrolysis and condensation still proceed inside the emulsion droplets even though their aggregation has effectively stopped.

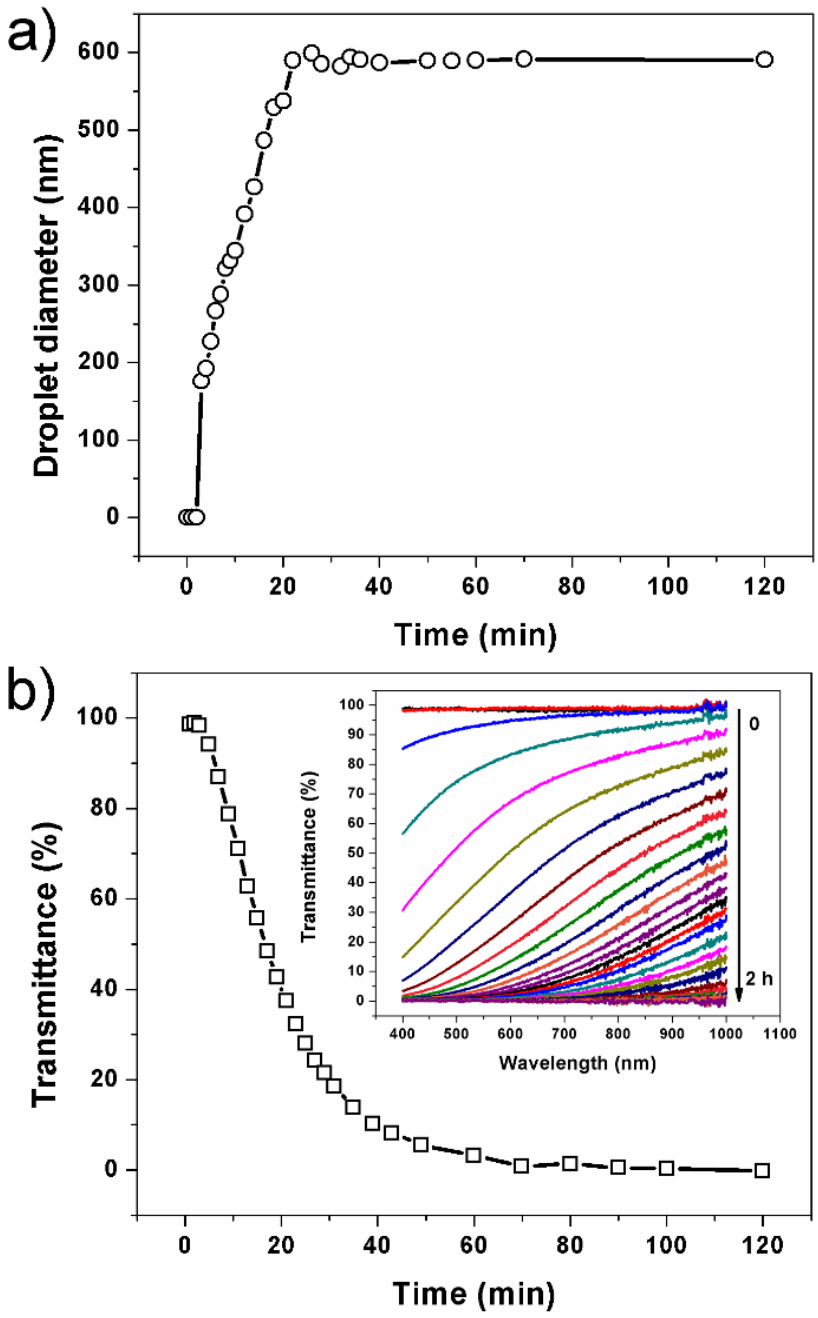

Figure 2.2 (a) Average diameter of mercapto-silica colloids characterized by DLS as a function of time; (b) Evolution in the transmittance of the solution at 900 nm during the colloid formation process. Inset is a plot showing the transmittance spectra of the aqueous solution. The concentrations of MPS and ammonia are 0.036 and 0.50 M, respectively.

2.3.2 Effect of the Precursor Concentration

To determine the critical factors that influence the mercapto-silica sphere formation, we carried out reactions by systematically varying the parameters, such as the concentrations of the precursor, catalyst ammonia, and the additional surfactant SDS, as well as the reaction time. A strong dependence of the size of mercapto-silica spheres on precursor concentration has been observed. In a series of syntheses, we varied only the concentration of the MPS precursor (0.009–0.36 M) but kept the rest of the parameters unchanged: 30 mL of total volume containing 0.50 M NH_3 prepared in a 50 mL centrifuge tube under shaking for 1 minute at 2500 rpm. Figure 2.3 plots the change of average droplet size at different precursor concentrations. The data were obtained by DLS after three hours of incubation to ensure that the spheres were fully grown. The sphere size increases as the precursor concentration increases, allowing a wide range of tuning from 170 nm to 3.5 μm. The larger sphere size at higher precursor concentrations is due to more extensive growth of emulsion droplets supported by the availability of more MPS precursor. No particles or droplets can be detected if the precursor concentration is lower than 0.005 M, suggesting that the hydrolyzed monomers or oligomers remain as soluble species in solution. At a precursor concentration of 0.72 M or even higher, mercapto-silica particles still can form but with a significantly greater polydispersity.

The size and morphology of mercapto-silica spheres were further characterized using optical and electron microscopy. As Figure 2.4 shows, the spheres with sizes larger than 500 nm can be clearly monitored using an optical microscope (OM) operated in dark field

mode. They can easily self-assembly into two dimensional close packed arrays on the glass substrate during the drying process, demonstrating a high degree of monodispersity. Insets are corresponding TEM images of the mercapto-silica spheres for the smaller samples, confirming their spherical morphology and narrow size distribution. Figure 2.4f summarizes the sphere sizes measured from microscopy images as a function of the precursor concentration, which is consistent with the results obtained from DLS analyses. Small mercapto-silica spheres (less than 300 nm) were evaluated only by TEM, as shown in Figure 2.5. The average diameter of spheres and the coefficient of variation (*cv*) measured from corresponding TEM images are listed in the figures. When low concentrations (0.018 and 0.009 M) of precursors were used, the average sphere size decreased to 210 nm and 151 nm and the size distribution was slightly broadened. This may be explained by the higher relative inhomogeneity associated with the fewer occasions of coalescence during the formation of smaller spheres. It is found that the sphere size from the images is slightly smaller than that measured by DLS characterization, especially in the case of the small spheres. This is due to the fact that DLS results account for the contribution of the solvation layer of the spheres extended in the solution, while such a layer has been removed under vacuum during TEM observations. Overall, the DLS, OM and TEM measurements show consistent results, which confirm that uniform mercapto-silica spheres with sizes ranging from 150 nm to 3.5 μm can be easily produced by controlling the concentration of the MPS precursor.

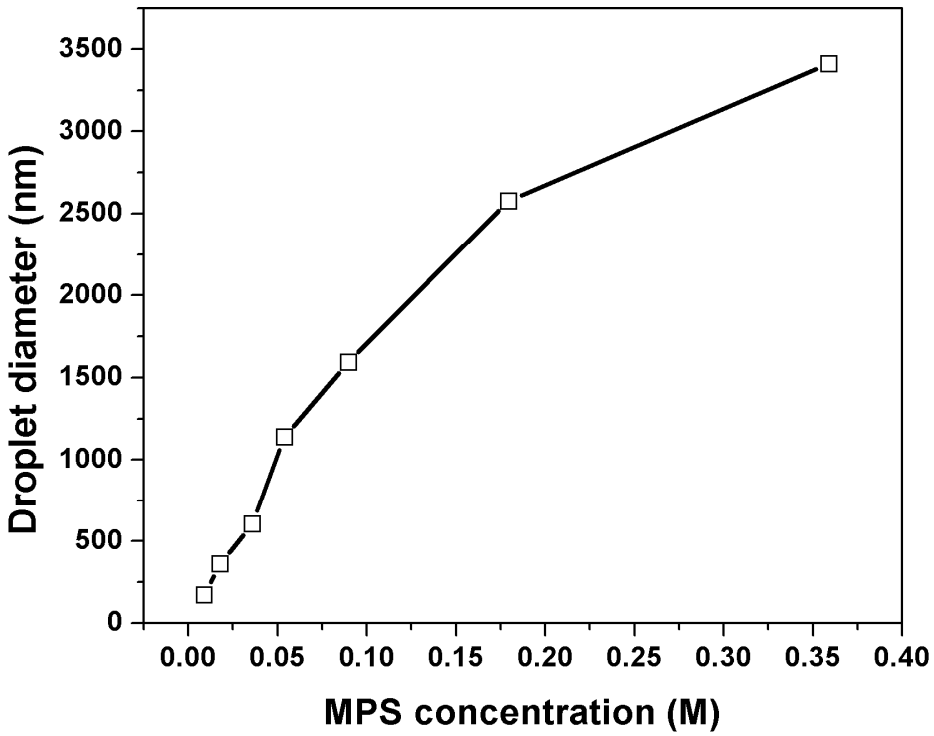

Figure 2.3 Average particle diameter (determined by DLS) as a function of MPS precursor concentration.

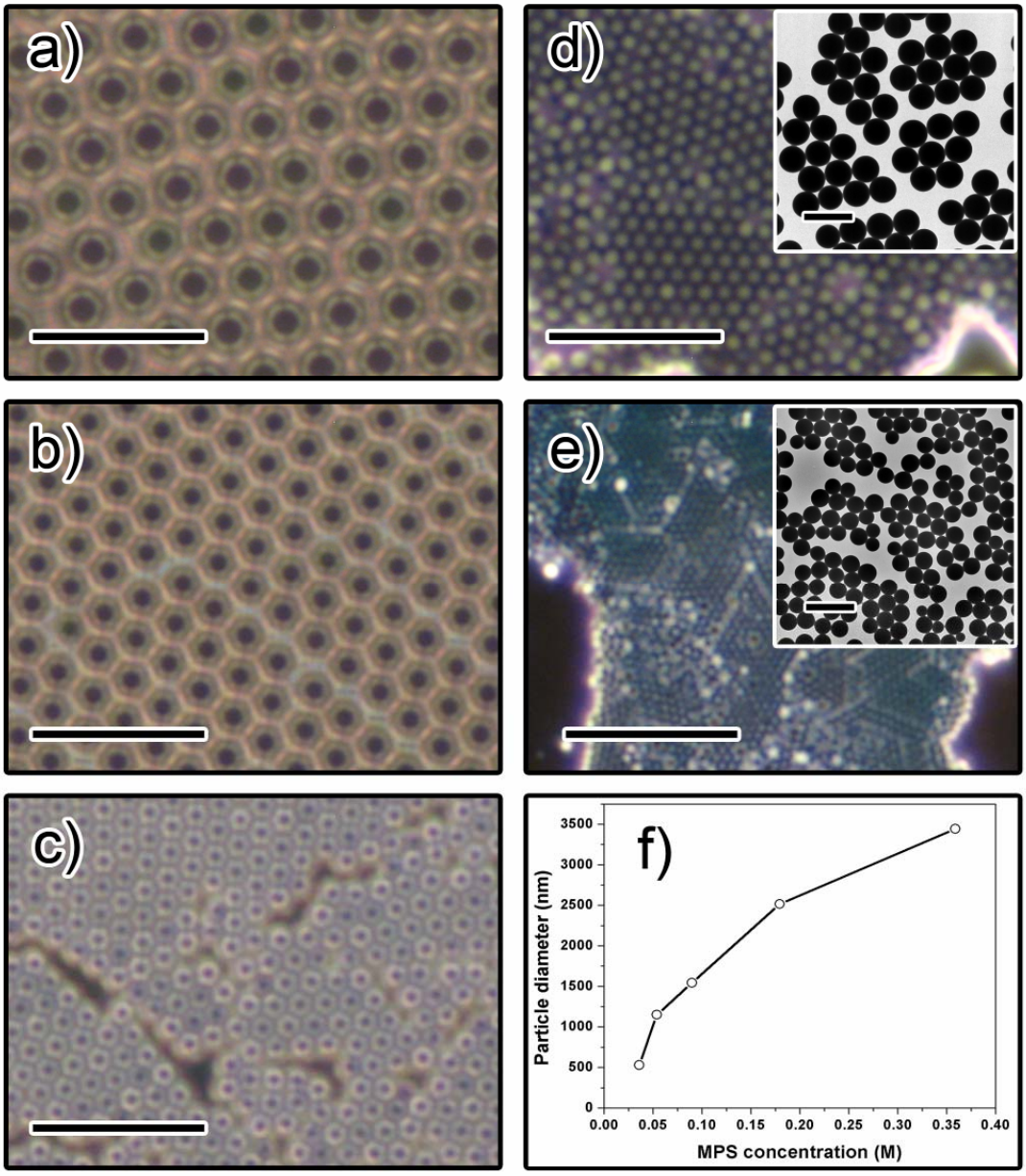

Figure 2.4 Dark-field optical microscopy images of mercapto-silica particles prepared at different MPS concentrations (a) 0.36 M; (b) 0.18 M; (c) 0.090 M; (d) 0.054 M; (e) 0.036 M. Scale bars are 10 μm. Insets are corresponding TEM images with scale bars of 2 μm. (f) Average sphere diameter as a function of MPS concentration measured from optical microscopy images.

2.3.3 Effect of Ammonia

Analogous to the classic sol-gel process, ammonia was used as a base catalyst for the hydrolysis of the MPS precursor. A higher concentration of ammonia produces more monomers and oligomers of silicates which emulsify the precursor more effectively, leading to a decrease in the size of emulsion droplets. On the other hand, ammonia also catalyzes the condensation reaction of the hydrolyzed species, promotes the formation of three-dimensional silica networks, and eventually accelerates the solidification of the mercapto-silica spheres. As shown in Figure 2.6, increasing the ammonia concentration indeed leads to a decrease in the size of mercapto-silica spheres. In a reaction system containing 0.054 M precursor, the sphere size can be tuned between 1.7 μm and 200 nm by changing the ammonia concentration from 0.1 M to 15 M. The *cv* values of the final spheres evaluated by DLS are relatively small when the ammonia concentration is in the range of 0.25–1 M. Out of this range, the polydispersity also increases. We note that an ammonia concentration of 0.5 M seems to be optimal for producing narrowly distributed mercapto-silica spheres for a wide range of precursor concentrations.

2.3.4 Effect of Additional Surfactant

To further understand the formation process and control the size of the mercapto-silica spheres, we added different amounts of additional surfactant, SDS, to a reaction mixture containing 0.036 M precursor and 0.5 M ammonia. SDS, as a typical surfactant, can be adsorbed on the surface of oil droplets to effectively lower the interfacial tension and introduce electrostatic repulsion. The growing process of mercapto-silica spheres with SDS is similar to that without SDS, as shown in Figure 2.7a. The emulsion droplets

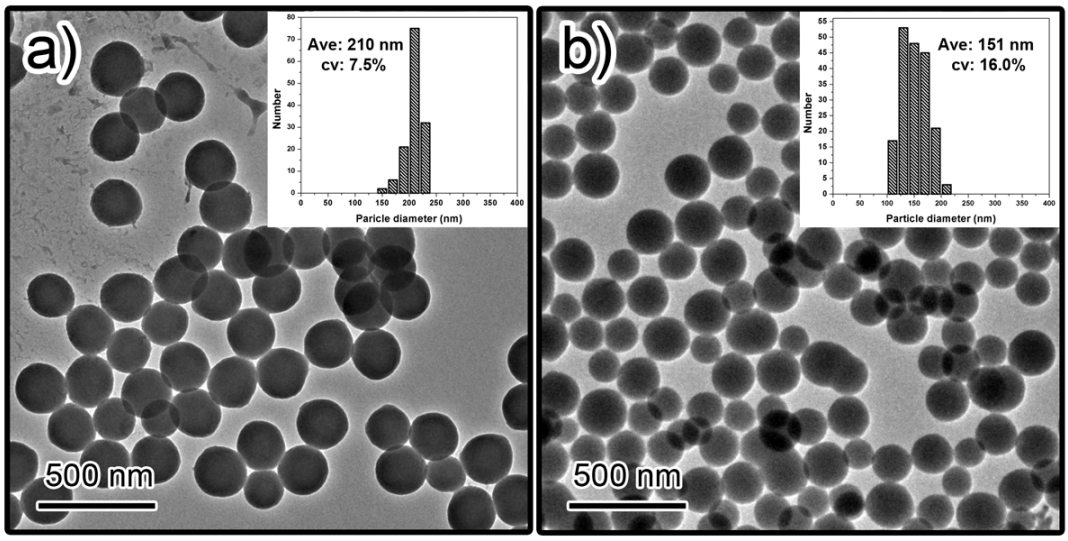

Figure 2.5 TEM images of mercapto-silica particles prepared at different MPS concentrations (a) 0.018 M; (b) 0.009 M. Insets are the measured size distributions of mercapto-silica particles from corresponding TEM images. (*cv*: coefficient of variation)

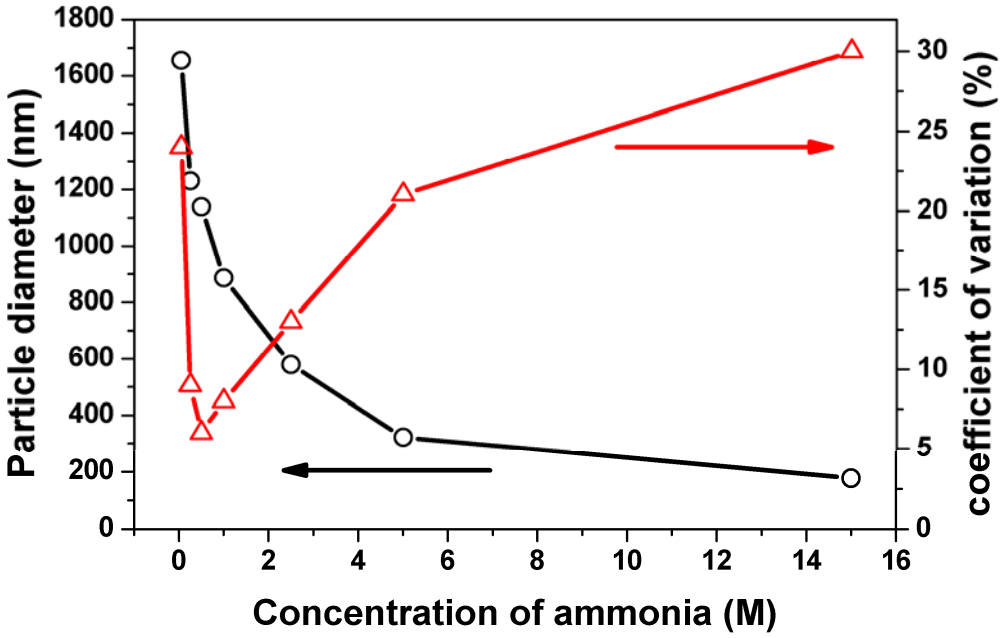

Figure 2.6 MPS droplet diameter as a function of ammonia concentration measured 4 h after initial mixing of the reactants. MPS concentration is 0.054 M.

can be detected at about 2 minutes after initial mixing. Unlike the reaction without SDS in which the particle size remained constant after 20 minutes, there was a slight size increase between 20 to 40 minutes for the reaction in the presence of SDS. Because the small size change is unlikely to be caused by coalescence, we believe the growth of droplets/spheres at the later stage of the reaction is mainly due to the uptake of the precursor from mini-droplet reservoirs or monomer/oligomer silicates dissolved in solution. Consistent with this understanding, we observed a decrease in the transmittance of the emulsion systems even after droplet/sphere diameter reached a maximum, and a slower change in the transmittance when a higher concentration of SDS was used (Figure 2.7b). More importantly, the final mercapto-silica spheres show average sizes of 590, 280 and 196 nm when prepared with different SDS concentrations (0, 0.003 and 0.067 mg/mL, respectively). The trend of decreasing sphere size with increasing SDS concentration has been further proven by a series of preparations containing 0.054 M precursor with various SDS concentrations. Figure 2.8 plots the average sphere diameter against the SDS concentration. Interestingly, we notice that the initial addition of tiny amounts of SDS can dramatically decrease the size of the mercapto-silica spheres, for example, from 1.1 μm to 620 nm only by adding 0.01 mg of SDS to 30 mL of reaction mixture. Further increasing the SDS concentration leads to a gradual decrease in the sphere size. When the concentration is higher than 3 mg/mL in the mixture, no droplets can be effectively detected by DLS: the mixture stayed clear even after 5 days of incubation. The reduction in product size can be easily understood as the result of the higher emulsification power of SDS than that of the hydrolyzed silicates. However, as

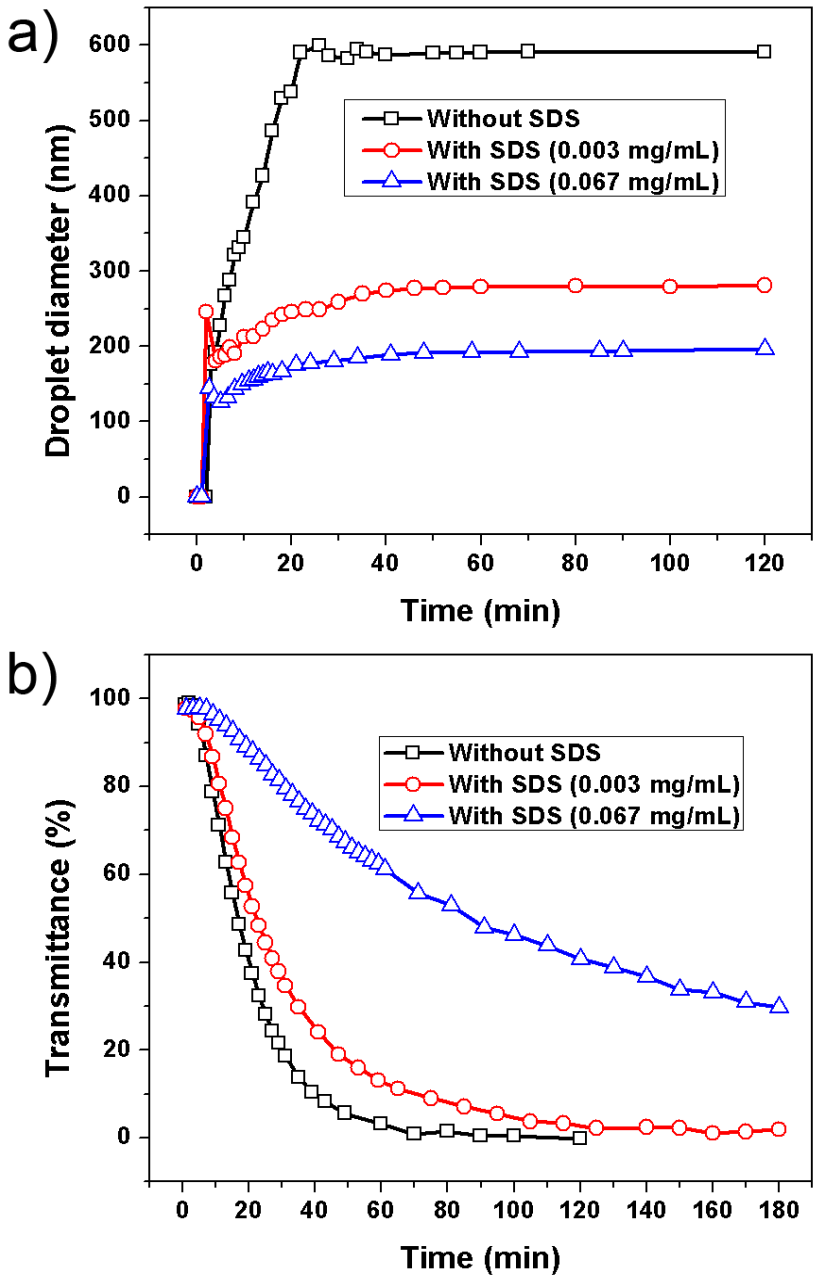

Figure 2.7 Surfactant effect on the mercapto-silica particle formation: (a) Average diameter of MPS droplets and (b) Transmittance at 900 nm of reaction solutions as a function of reaction time. The reactions were carried out in the presence of extra surfactant SDS at different concentrations. The concentration of MPS used here is 0.036 M.

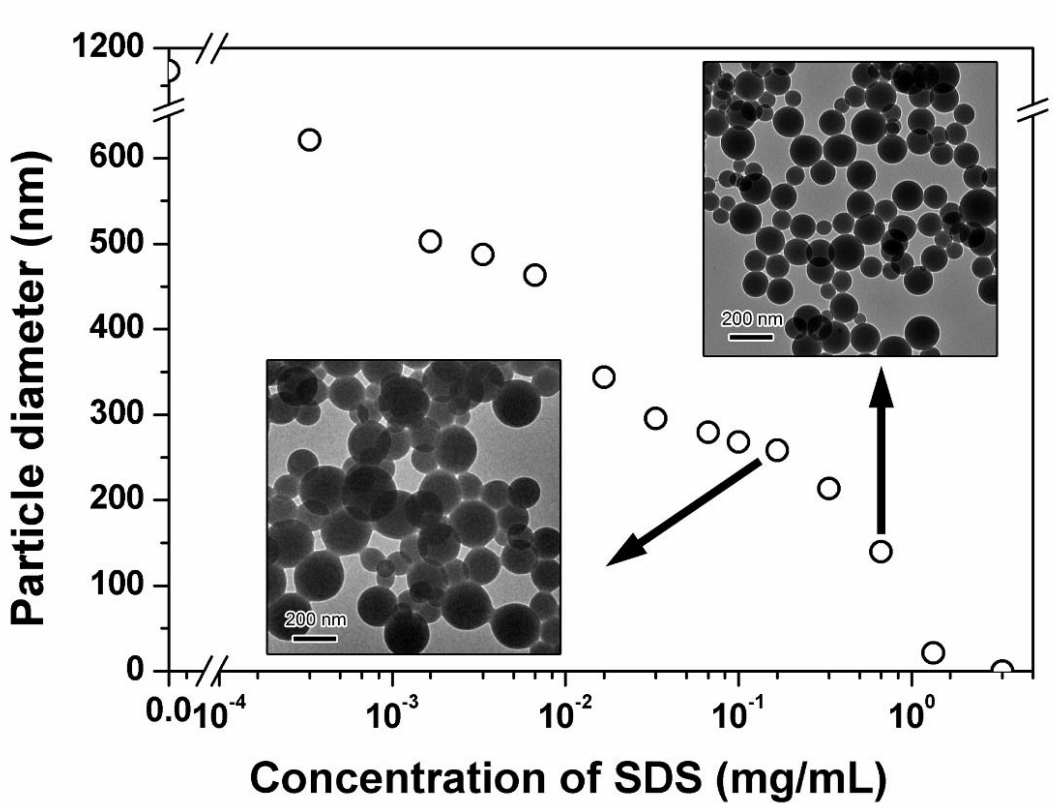

Figure 2.8 MPS droplet diameter as a function of surfactant concentration measured 4 h after initial mixing of the reactants. Insets show typical TEM images of mercapto-silica particles observed at SDS concentrations of 0.167 and 0.067 mg/mL. The MPS concentration is 0.054 M.

suggested in Figure 2.7b, the emulsion droplets prepared in the presence of SDS remained "soft" for a much longer time compared to the samples without SDS, giving more chances for inter-droplet coalescence and subsequently yielding particles with broader size distributions. The insets in Figure 2.8 show typical TEM images of mercapto-silica particles prepared at two SDS concentrations, both with *cv* higher than 30%. We therefore conclude here that adding additional surfactants allows a high degree of tuning of the size of mercapto-silica spheres, which is accompanied by an increase in size distribution.

2.3.5 Ostwald Ripening

The growth of mercapto-silica spheres has also been monitored by characterizing samples collected at different reaction times by using TEM and DLS. We first looked at the reaction containing 0.054 M of MPS precursor and 0.5 M ammonia. One hour after mixing, monodisperse spherical objects can be observed under optical microscope, but they collapse and fuse with each other when dried on the substrate. Also no isolated solid spheres can be recovered after washing. All these observations suggest that the condensation in the droplets/spheres at this stage is not extensive enough to reinforce them against the capillary forces experienced during drying or the mechanical treatment during washing, although they are rigid enough to prevent coalescence in the original solution. We find that a 4-hour period allows sufficient condensation in most cases. As can be seen in Figure 2.9a, after 4 hours of reaction, the product contains uniform solid spheres with a *cv* of ~1%. The spheres remain in the isolated form after washing for a few times and then drying on the carbon grids. Further prolonging the reaction time to 1

day leads to broader size distribution with the *cv* value increasing to 5%. The appearance of the smaller spheres in Figure 2.9b suggests the occurrence of the Ostwald ripening process, which cannot be ignored if the mercapto-silica spheres are left in the reaction mixture for one day. After 3 days, a large number of small spheres with diameters less than 200 nm can be observed through both TEM and DLS analysis, as shown in Figure 2.9c. Some of the original spheres grow larger to about 1.4 μm at the expense of the small ones. Therefore, a long incubation time is detrimental to the monodispersity of the products. In their earlier works, Nakamura et al. reported their synthesis of polydisperse thiol-organosilica particles which were collected from the reaction solution after one or three days.[18] We suspect the broad size distribution in their cases is probably due to the Ostwald ripening which occurred during the unnecessarily long incubation. To prevent ripening, it is necessary to separate the MPS spheres from the reaction mixture as soon as they become solidified, and then keep them in a solvent in which the spheres have a low solubility. Ethanol is a good candidate for this purpose because the mercapto-silica spheres can be well dispersed in ethanol but there is no significant solubility over time. Figure 2.9d shows a typical TEM image and corresponding DLS result of mercapto-silica spheres which were collected after 4 hours of incubation, then washed with ethanol several times, and finally re-dispersed and stored in ethanol for 3 days. The nearly unchanged diameter and size distribution clearly suggests the high stability of the spheres in ethanol. We therefore further conclude the requirements for preparing uniform mercapto-silica spheres: they need to be separated from the reaction mixture right after their solidification and before the occurrence of Ostwald ripening, and then stored in

ethanol or other solvents in which the mercapto-silica spheres have a good dispersibility but a low solubility.

We also studied the stability of smaller spheres prepared with an MPS precursor concentration of 0.018 M while keeping all other parameters unchanged. As shown in Figure 2.10, after 6 hours of incubation, uniform mercapto-silica spheres can be collected. Again, longer incubation time leads to a broader size distribution. Compared with the larger mercapto-silica spheres in Figure 2.9, the spheres with smaller sizes (~210 nm) need about 6 hours to solidify but obvious Ostwald ripening occurs in just 24 hours (Figure 2.10c). Therefore, the optimal incubation window for obtaining smaller mercapto-silica spheres is much narrower. When the mercapto-silica sphere is further reduced to below 200 nm, the solidification process and the ripening process may start to overlap, making it difficult to obtain stable particles with uniform sizes. This could explain why monodisperse mercapto-silica spheres with small sizes are generally much harder to produce.

2.4 Conclusion

In summary, high quality mercapto-silica spheres have been successfully synthesized through a one-pot process in which MPS was used as the single silica source. The formation of the spheres follows an emulsion based process in which the silicate species hydrolyzed at the early stage act as surfactants to emulsify the remaining MPS precursor in water, and further hydrolysis and condensation inside the emulsion droplets lead to the formation of solid mercapto-silica spheres. Based on the emulsion mechanism, we demonstrate systematic control over the size of mercapto-silica spheres

by changing the concentration of precursor, ammonia, additional surfactant, and the reaction time. We also revealed that Ostwald ripening may occur quickly if the spheres are kept in the reaction solution, which results in significant broadening of the size distribution of the products. As a final remark on preparing uniform and stable mercapto-silica spheres, we emphasize the importance of quenching the growth of the mercapto-silica spheres by separating them from the original reaction mixture and then storing them in solvents that can prevent further ripening.

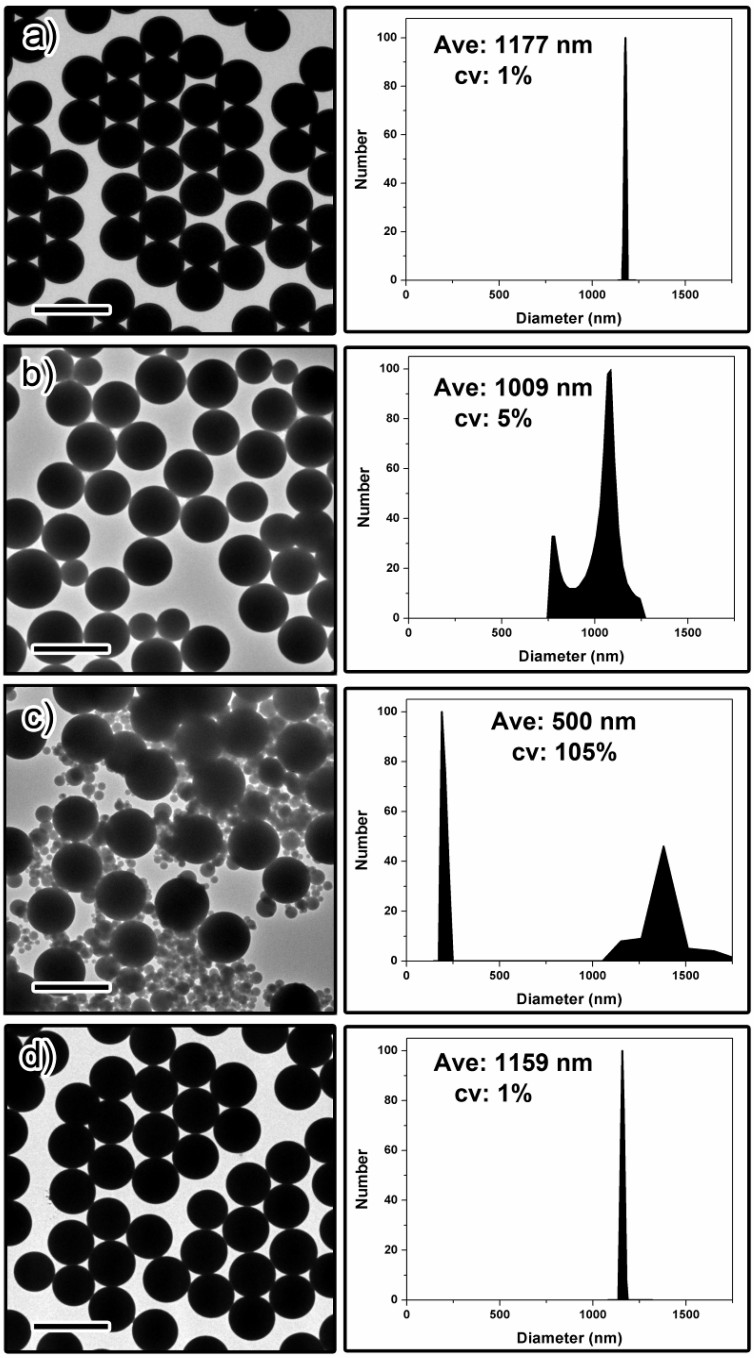

Figure 2.9 (a-c) TEM images and size measurements from DLS analyses of mercapto-silica particles collected after (a) 4 h, (b) 1 day, and (c) 3 days of reaction. (d) TEM image and size measurement of mercapto-silica particles collected 4 h after mixing, separated from the original reaction solution, then washed and re-dispersed in ethanol, and stored for 3 days. The concentration of MPS is 0.054 M. Scale bars are 2 μm.

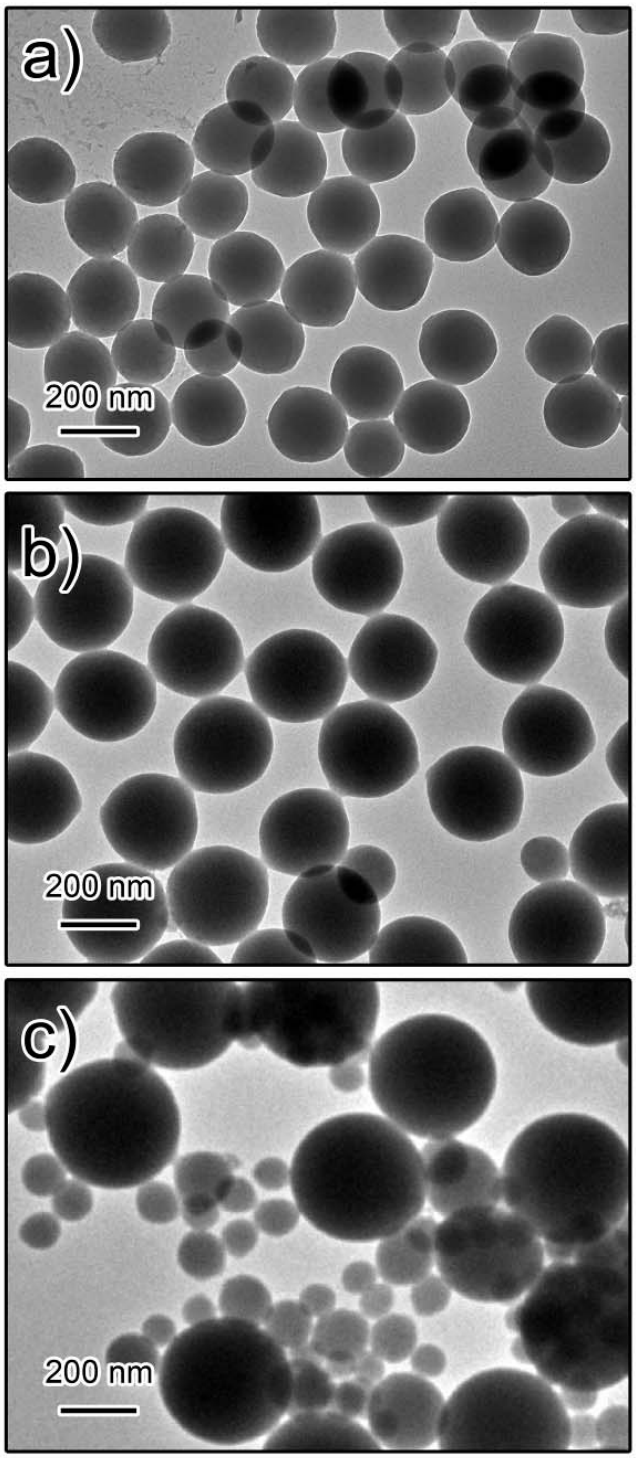

Figure 2.10 TEM images of mercapto-silica spheres collected after (a) 6 hrs, (b) 12 hrs, and (c) 24 hrs of reaction. The concentration of MPS is 0.018 M. Scale bars are 200 nm.

Reference

(1) Zayat, M.; Levy, D., *Chem. Mater.* **2003,** 15, 2122-2128.

(2) Graf, C.; van Blaaderen, A., *Langmuir* **2002,** 18, 524-534.

(3) Yang, C. M.; Sheu, H. S.; Chao, K. J., *Adv. Funct. Mater.* **2002,** 12, 143-148.

(4) Bruchez, M.; Moronne, M.; Gin, P.; Weiss, S.; Alivisatos, A. P., *Science* **1998,** 281, 2013-2016.

(5) Santra, S.; Bagwe, R. P.; Dutta, D.; Stanley, J. T.; Walter, G. A.; Tan, W.; Moudgil, B. M.; Mericle, R. A., *Adv. Mater.* **2005,** 17, 2165-2169.

(6) Hatton, B. D.; Landskron, K.; Whitnall, W.; Perovic, D. D.; Ozin, G. A., *Adv. Funct. Mater.* **2005,** 15, 823-829.

(7) Stein, A.; Melde, B. J.; Schroden, R. C., *Adv. Mater.* **2000,** 12, 1403-1419.

(8) Bagwe, R. P.; Hilliard, L. R.; Tan, W. H., *Langmuir* **2006,** 22, 4357-4362.

(9) Sayari, A.; Hamoudi, S., *Chem. Mater.* **2001,** 13, 3151-3168.

(10) Zhang, Q.; Ge, J.; Goebl, J.; Hu, Y.; Yin, Y., *Adv. Mater.* **2010,** 22, 1905-1909.

(11) Zhang, Q.; Lee, I.; Ge, J.; Zaera, F.; Yin, Y., *Adv. Funct. Mater.* **2010,** 20, 2201-2214.

(12) Ge, J.; Zhang, Q.; Zhang, T.; Yin, Y., *Angew. Chem. Int. Ed.* **2008,** 47, 8924-8928.

(13) Ge, J.; He, L.; Goebl, J.; Yin, Y., *J. Am. Chem. Soc.* **2009,** 131, 3484-3486.

(14) Ge, J.; Yin, Y., *Adv. Mater.* **2008,** 20, 3485-3491.

(15) Yin, Y.; Lu, Y.; Sun, Y.; Xia, Y., *Nano Lett.* **2002,** 2, 427-430.

(16) Lu, Z. D.; Goebl, J.; Ge, J. P.; Yin, Y. D., *J. Mater. Chem.* **2009,** 19, 4597-4602.

(17) Johnston, A. P. R.; Battersby, B. J.; Lawrie, G. A.; Trau, M., *Chem. Commun.* **2005**, 848.

(18) Nakamura, M.; Ishimura, K., *Langmuir* **2008,** 24, 5099-5108.

(19) Hatton, B.; Landskron, K.; Whitnall, W.; Perovic, D.; Ozin, G. A., *Acc. Chem. Res.* **2005,** 38, 305-312.

(20) Hoffmann, F.; Cornelius, M.; Morell, J.; Froba, M., *Angew. Chem.Int. Ed.* **2006,** 45, 3216-3251.

(21) Nooney, R. I.; Kalyanaraman, M.; Kennedy, G.; Maginn, E. J., *Langmuir* **2001,** 17, 528-533.

(22) Zhuang, X.; Zhao, Q. F.; Wan, Y., *J. Mater. Chem.* **2010,** 20, 4715-4724.

(23) Zhang, L. X.; Zhang, W. H.; Shi, J. L.; Hua, Z.; Li, Y. S.; Yan, J., *Chem. Commun.* **2003**, 210-211.

(24) Beaudet, L.; Pitre, R.; Robillard, L.; Mercier, L., *Chem. Mater.* **2009,** 21, 5349-5357.

(25) Volkan, M.; Ataman, O. Y.; Howard, A. G., *Analyst* **1987,** 112, 1409-1412.

(26) Arakaki, L. N. H.; Augusto, V. L. S.; Espinola, J. G. P.; da Fonseca, M. G.; de Oliveira, S. F.; Arakaki, T.; Airoldi, C., *J. Environ. Monit.* **2003,** 5, 366-370.

(27) Liu, A. M.; Hidajat, K.; Kawi, S.; Zhao, D. Y., *Chem. Commun.* **2000**, 1145-1146.

(28) Wu, H. Y.; Liao, C. H.; Pan, Y. C.; Yeh, C. L.; Kao, H. M., *Microporous Mesoporous Mater.* **2009,** 119, 109-116.

(29) Westcott, S. L.; Oldenburg, S. J.; Lee, T. R.; Halas, N. J., *Langmuir* **1998,** 14, 5396-5401.

(30) Slawinski, G. W.; Zamborini, F. P., *Langmuir* **2007,** 23, 10357-10365.

(31) Nakamura, T.; Yamada, Y.; Yano, K., *J. Mater. Chem.* **2007,** 17, 3726-3732.

(32) Hu, K.; Brust, M.; Bard, A. J., *Chem. Mater.* **1998,** 10, 1160-1165.

(33) Feng, G.; Qingyi, L.; Dongyuan, Z., *Chem. Phys. Lett.* **2002,** 360, 585-91.

(34) Claesson, E. M.; Philipse, A. P., *Colloids and Surfaces A: Physicochem. Eng. Aspects* **2007,** 297, 46-54.

(35) Hilliard, L. R.; Zhao, X. J.; Tan, W. H., *Anal. Chim. Acta* **2002,** 470, 51-56.

(36) Nakamura, M.; Ozaki, S.; Abe, M.; Doi, H.; Matsumoto, T.; Ishimura, K., *Colloid Surface B* **2010,** 79, 19-26.

(37) Qhobosheane, M.; Santra, S.; Zhang, P.; Tan, W. H., *Analyst* **2001,** 126, 1274-1278.

(38) Li, D.; Teoh, W. Y.; Gooding, J. J.; Selomulya, C.; Amal, R., *Adv. Funct. Mater.* **2010,** 20, 1767-1777.

(39) Corrie, S. R.; Vogel, R.; Keen, I.; Jack, K.; Kozak, D.; Lawrie, G. A.; Battersby, B. J.; Fredericks, P.; Trau, M., *J. Mater. Chem.* **2008,** 18, 523-529.

(40) Nakamura, M.; Ishimura, K., *J. Phys. Chem. C* **2007,** 111, 18892-18898.

(41) Stober, W.; Fink, A.; Bohn, E., *J. Colloid Interface Sci.* **1968,** 26, 62-69.

(42) Miller, C. R.; Vogel, R.; Surawski, P. P. T.; Jack, K. S.; Corrie, S. R.; Trau, M., *Langmuir* **2005,** 21, 9733-9740.

(43) Miller, C. R.; Vogel, R.; Surawski, P. P. T.; Corrie, S. R.; Ruhmann, A.; Trau, M., *Chem. Commun.* **2005**, 4783-4785.

(44) Obey, T. M.; Vincent, B., *J. Colloid Interface Sci.* **1994,** 163, 454-463.

(45) Zoldesi, C. I.; van Walree, C. A.; Imhof, A., *Langmuir* **2006,** 22, 4343-4352.

(46) Lifshitz, I. M.; Slyozov, V. V., *J. Phys. Chem. Solids* **1961,** 19, 35-50.

Chapter 3

Self-Assembly and Tunable Plasmonic Property of Gold Nanoparticles on Mercapto-Silica Microspheres

3.1 Introduction

Noble metal nanoparticles have been the subject of extensive studies in the past few decades primarily due to their unique optical property known as localized surface plasmon resonance (LSPR).[1-3] This dramatic optical effect is caused by the excitation of a collective oscillation of metal electrons in resonance with light of a certain frequency. Earlier efforts towards manipulating the plasmonic property have focused on controlling the composition, size, and shape of the nanoparticles, and the local dielectric constant of the surrounding medium.[4-9] Another parameter that plays an important role in the optics of metal nanoparticles is electromagnetic coupling to particles in close proximity.[10-15] Recently, considerable attention has been devoted to controlling interparticle separation, which determines the strength of the interparticle coupling and consequently the plasmon oscillation frequency, with the goal of developing functional structures for a wide variety of applications including electromagnetic energy transport at the subwavelength scale, signal enhancement of Raman scattering, and chemical and biological sensing and detection.[16-23] In addition to the lithographic techniques employed in the pioneer works, a number of self-assembly approaches have been explored to organize metal nanoparticles into simple aggregates in solution or thin films on flat substrates, both with the interparticle separation being controllable by the alkyl chain lengths of the capping agents.[20, 23-29] A practical challenge for nanoparticle aggregates is the precise control of

their size and internal particle arrangement, while thin films can only be used as solid substrates with limited applications. Here, we report the assembly of a monolayer of gold nanoparticles on mercapto-silica microspheres and show that the average interparticle separation and consequently the plasmonic property can be conveniently tuned by controlling both the length of the capping ligands and the molar ratio of gold nanoparticles to the supporting microspheres. The mercapto-silica spheres provide a quasi two-dimensional surface for nanoparticle assembly while at the same time retaining their well-defined and isolated colloidal form, making them useful for applications where both tailored plasmonic property and solution dispersibility are required.

3.2 Experimental Section

3.2.1 Materials

Hydrogen tetrachloroaurate ($HAuCl_4$), sodium borohydride ($NaBH_4$), (3-mercaptopropyl)trimethoxysilane (MPS), tetraoctylammonium bromide (TOAB), Dodecylamine (C12N), Hexadecylamine (C16N), 1-dodecanethiol (C12S) and ammonium hydroxide solution (NH_4OH, ~28% NH_3 in water) were purchased from Aldrich Chemical Co. Ethanol and toluene were of analytical grade and obtained from Fisher Scientific. All chemicals were used as received without further treatment.

3.2.2 Synthesis of Au Nanoparticles

Au nanoparticles capped with TOAB in toluene were synthesized by using a previously reported biphasic reduction procedure.[32] In a typical synthesis, a biphasic TOAB solution was prepared by dissolving TOAB (0.365 g) in toluene (13.3 ml), followed by the addition of 5 mL $HAuCl_4$ solution (0.01g/mL). After vigorous stirring for

10 minutes, the color of the toluene phase became orange. After that, sodium borohydride solution (56.8 mg dissolved in 2 mL water) was added dropwise. The color changed from orange to white to purple to eventually reddish. The resulting mixture was further stirred for 2 hours to ensure monodispersity. The final products were washed with dilute H_2SO_4 (1M) one time and distilled water several times.

3.2.3 Capping Ligand Exchange

200 mg C12N, C16N or C12S was added to 2 mL of the above Au nanoparticle solution. The mixture was stirred for 3 to 4 hours at room temperature. Then 5 mL ethanol was added to precipitate the Au nanoparticles. After centrifugation, the Au nanoparticles can be redispersed in 2 mL toluene. In order to fully replace the original capping agent, this step can be repeated several times.

3.2.4 Synthesis of Mercapto-Silica Microspheres

MPS microspheres were prepared by a one-pot procedure as described in Chapter 2. (3-mercaptopropyl)trimethoxysilane (MPS, 300 μL) was added to 30 mL of 1% NH_4OH water solution and vigorously shaken for 2 minutes using an IKA MS3 minishaker at a speed of 2500 rpm. The resulting mixture was then incubated at room temperature for 4 hours. The final products were washed with ethanol several times, and then one quarter of the sample was dispersed in 100 mL toluene.

3.2.5 Self-Assembly of Au Nanoparticles on MPS Spheres

Au nanoparticles with different capping agents can be assembled on the surface of MPS spheres by simply mixing their toluene solutions. Absorption spectra were measured to characterize the assembly. Specifically, 50 μL of the above Au nanoparticles

solution is diluted in 2500 μL toluene in a cuvette. To this solution, 50, 100, 150, 200, 300, 400 and 500 μL of the MPS sphere solution above was added, and then the absorption spectra were recorded using a UV-Vis spectrophotometer.

3.2.6 Characterization

The morphology of the nanostructures was investigated using a Philips Tecnai 12 transmission electron microscope (TEM) with a 120 keV beam energy. UV-Vis absorption spectra measurements were carried out using a Varian Cary 50 spectrophotometer.

3.3 Results and Discussion

Figure 3.1 schematically illustrates the assembled structure of Au nanoparticles on a mercapto-silica surface. The mercapto-silica spheres were synthesized by directly hydrolyzing (3-mercaptopropyl) trimethoxysilane (MPS) in an aqueous solution containing 1% NH_4OH. Although it is possible to vary the size of the microspheres by changing the synthetic conditions as described in previous reports,[30, 31] in this work we keep the sphere size at a constant value of 859 ± 24 nm. Interestingly, the MPS spheres cannot be re-dispersed in water after they have been dried in air. Instead, they can be well-dispersed in nonpolar solvents such as toluene, suggesting a high density coverage of thiol groups on the silica surface.

Au nanoparticles were prepared by using the well-known biphasic reduction process in which tetraoctylammonium bromide (TOAB) acts as both phase transfer catalyst and capping ligand.[32-34] A typical synthesis produces Au nanoparticles with narrow size distribution (5.0 ± 0.5 nm) and characteristic absorption band around 530 nm.

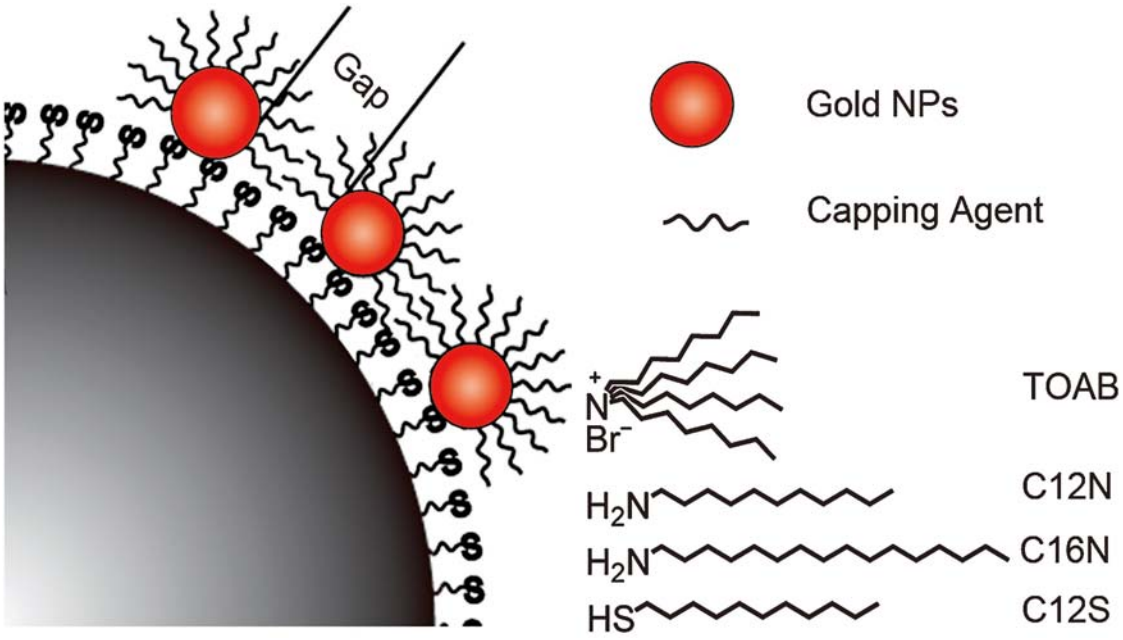

Figure 3.1 Schematic illustration of self-assembly of Au nanoparticles on MPS spheres.

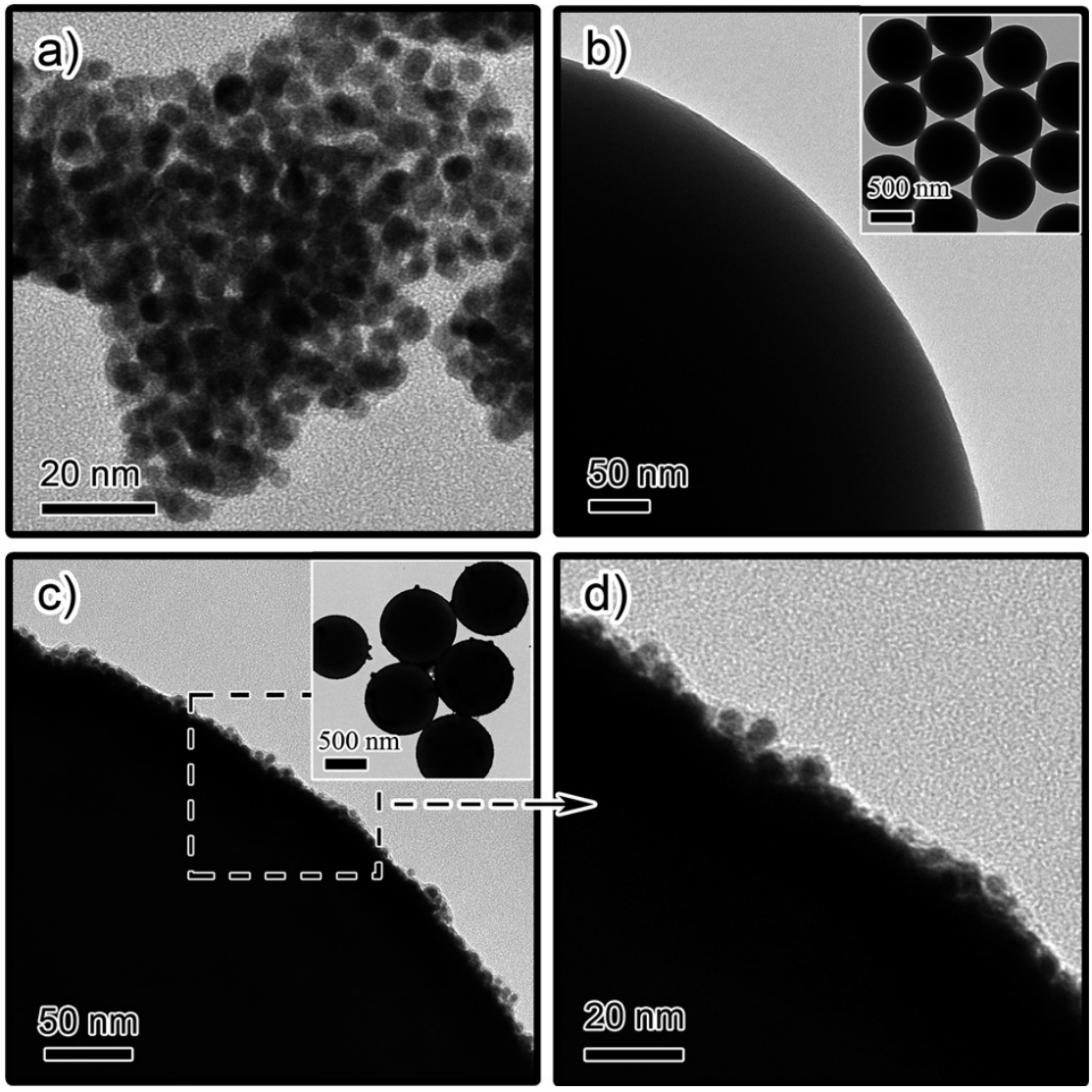

Figure 3.2 TEM images of (a) TOAB-capped Au nanoparticles; (b) MPS spheres; (c) TOAB-capped Au nanoparticles assembled on the surface of MPS spheres. Insets are TEM images at lower magnifications; and (d) High magnified image of the select area of figure 2c. Insets in (b) and (c) are TEM images of the microspheres at lower magnifications.

While dispersed in toluene, the nanoparticles form aggregations on carbon film during drying of the solution, as shown in the transmission electron microscopy (TEM) image in Figure 3.2a. This is consistent with the previous observation that TOAB can not fully protect the Au nanoparticles from contacting each other in the dried film.[34] The weak surface protection of TOAB also affects the long term stability of particles in solution phase: aggregates form after 3 days of storage at room temperature. The weak binding of TOAB on the Au surface, however, makes it convenient to exchange ligands with other capping agents such as dodecylamine (C12N), hexadecylamine (C16N), and 1-dodecanethiol (C12S).[34] As the amine and thiol groups bind to the Au surface strongly, the Au nanoparticles can remain stable after ligand exchange without obvious aggregation for several months.

The TOAB protected Au nanoparticles readily assemble on MPS surfaces by interacting with the high density thiol groups. Addition of excess Au nanoparticles into the toluene solution of MPS spheres at controlled concentration leads to a stable dispersion. Figures 3.2b and 3.2c compare the surface morphology of MPS spheres before and after adsorption of Au nanoparticles. Figures 3.2c and 3.2d reveal that a monolayer of Au nanoparticles has been attached to the MPS surface. Because the concentration of MPS spheres is kept low, their aggregation by Au nanoparticle bridging can be completely avoided so that the assembled structures retain their well-defined and isolated colloidal form (inset of Figure 3.2c). Similar monolayer assemblies have also been observed when alkylamine capped Au nanoparticles are used.

The assembly of Au nanoparticles on the MPS surface is accompanied by a shift of the surface plasmon resonance bands as a result of interparticle electromagnetic coupling. Figure 3.3 shows the absorption spectra of TOAB capped Au nanoparticles in a toluene solution (2.5 mL, 8×10^{-9} mol/L) following mixing with different amounts of MPS sphere solution (1.5×10^{-12} mol/L) for increasing time periods. Upon the addition of 100 μL MPS solution, the absorption band broadens and undergoes a gradual red-shift from the original value of 530 nm. The absorption intensity of the Au nanoparticles also decreases over time, with an accompanying development of a new band at ~630 nm. Apparently there is competition between two species with characteristic absorptions which can be attributed to the uncoupled Au nanoparticles and the monolayer of nanoparticles immobilized on MPS spheres. The strong Au-thiol interaction tends to closely pack the nanoparticles on the MPS surface, leading to significant electromagnetic interaction between the neighboring particles so that the plasmon resonance band shifts to higher wavelengths. The transition slows down significantly after ~ 10 min of reaction, suggesting a saturation of nanoparticle binding on the MPS surface. Since excess isolated nanoparticles remain in the solution, the absorption spectra show two plasmon bands. As revealed in Figure 3.3b, adding more MPS spheres (150 μL) to the solution depletes the isolated nanoparticles so that at the later stage of assembly the absorption spectra are dominated by the plasmon band of coupled particles. Interestingly, the maximum shift of the plasmon band is dependent on the molar ratio of Au nanoparticles to MPS spheres. As shown in Figure 3.3c, increasing the amount of MPS spheres to 200 μL can only shift the plasmon band to a maximum value of ~612 nm. The decreased red-

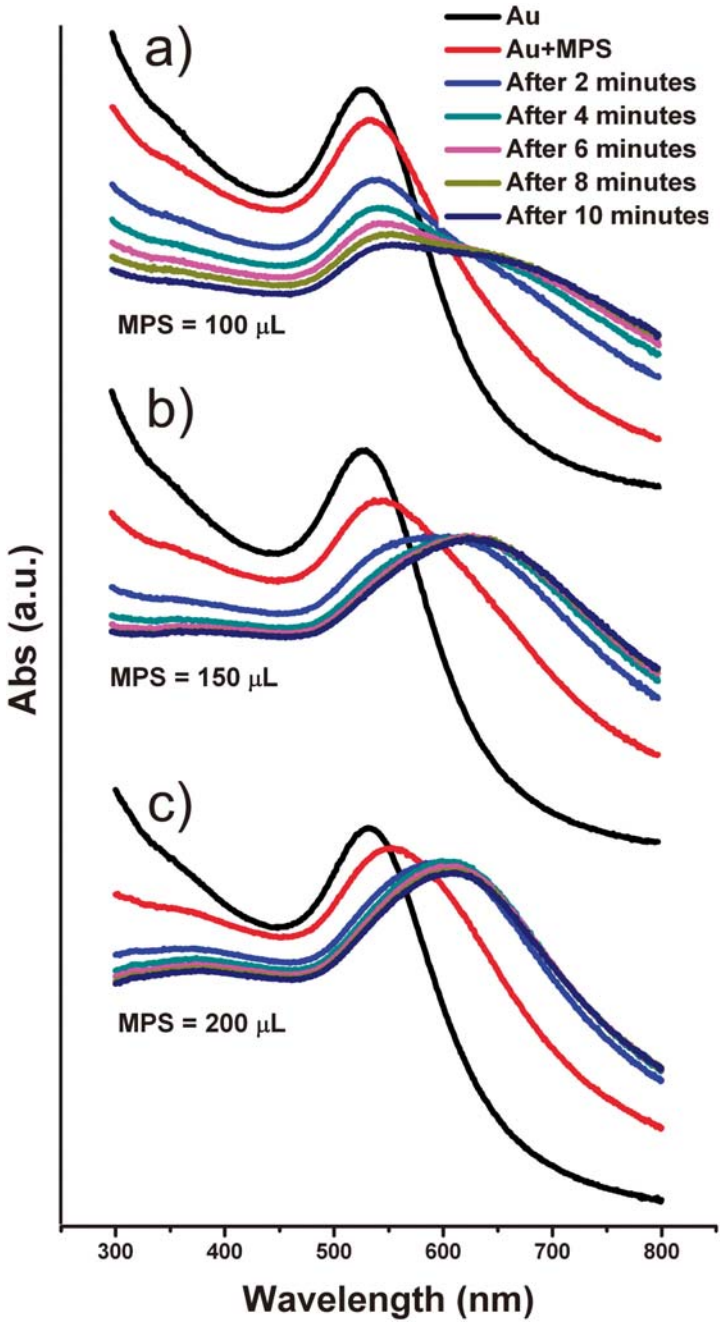

Figure 3.3 Absorption spectra of TOAB capped Au nanoparticles in toluene solutions (2.5 mL, 8×10^{-9} mol/L) after adding (a) 100 μL, (b) 150 μL, and (c) 200 μL MPS sphere solution. The concentration of MPS spheres is 1.5×10^{-12} mol/L.

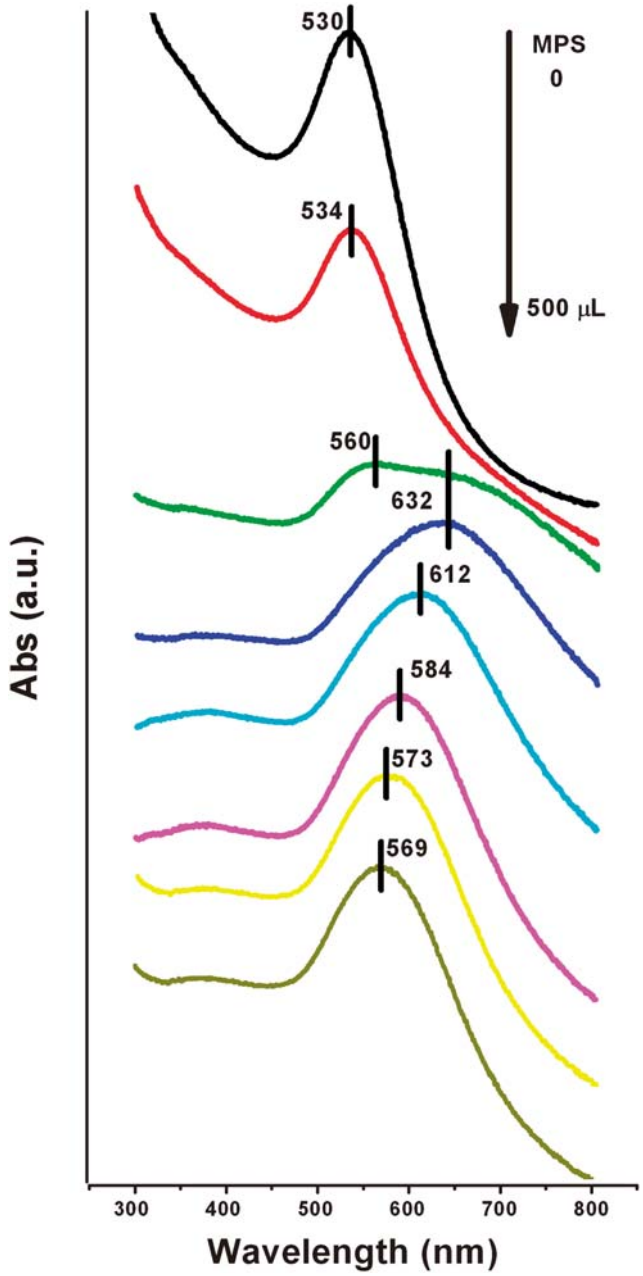

Figure 3.4 Absorption spectra of TOAB-capped Au nanoparticles in response to the addition of increasing amounts of MPS spheres. All spectra were taken after the assembly achieved equilibrium (>10 min). From top to bottom the volume of MPS solution is 0, 50, 100, 150, 200, 300, 400 and 500 μL.

shift of the plasmon band is due to the increased average interparticle separation when there are not enough Au nanoparticles to cover the MPS surface in the form of a close-packed monolayer. Note that in this paper "close-packing" is used to describe nanoparticle assemblies that have the closest possible interparticle distance which generally includes the steric contribution from capping ligands.

Figure 3.4 summarizes the maximum red-shifts in plasmon bands that can be obtained by introducing increasing amounts of MPS spheres into solutions of TOAB capped Au nanoparticles. The plasmon bands due to interparticle coupling enhance initially when the amount of MPS spheres is less than 150 μL, and then shift from the maximum value of ~632 nm gradually to ~569 nm when the volume of MPS solution is increased from 150 to 500 μL. A simple estimation of surface coverage confirms the close-packed assembly of Au nanoparticles when 150 μL MPS is present, with interparticle separation of ~ 0.5 nm. When more than 150 μL MPS solution is added, the Au nanoparticles assemble on the MPS surface in non-close-packed structures with increasing average particle separation as the number of MPS spheres increases. Because the total amount of Au nanoparticles remains the same, the intensities of the plasmon bands do not significantly change when the wavelengths shift from 632 to 569 nm.

Many reports have shown that coupling induced red-shift of the plasmon band is determined by the length of the capping ligands when the particles are assembled into close-packed films. We have observed a similar phenomenon when Au nanoparticles capped with the different ligands are utilized in the assembly. Figure 3.5 summarizes the

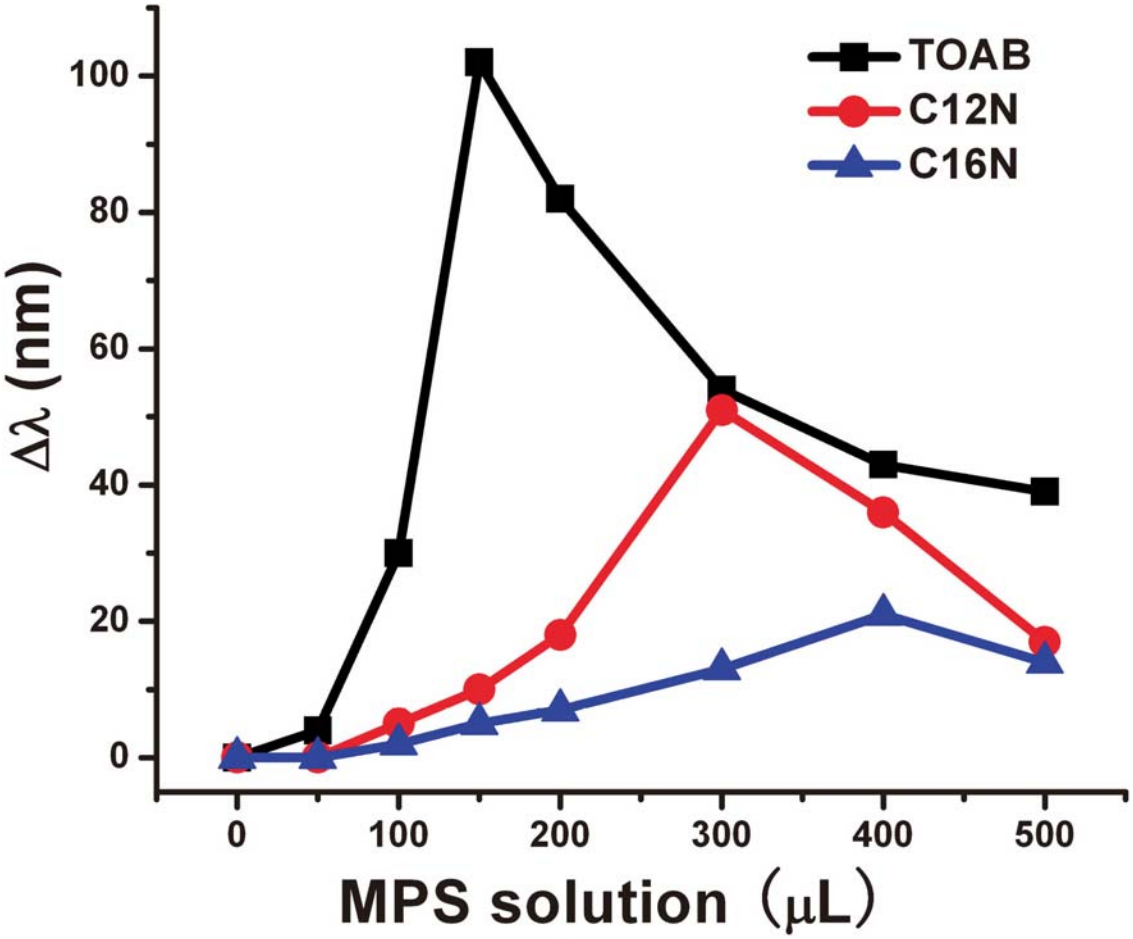

Figure 3.5 Summary of the red-shifts of plasmon bands due to interparticle coupling when increasing amounts of MPS spheres were added to the solutions of Au nanoparticles capped with different ligands: TOAB, C12N and C16N. The shifts were calculated relative to the plasmon band of the original isolated Au nanoparticles. All spectra were taken after the assembly achieved equilibrium (>10 min).

dependence of the red-shift of the plasmon bands on the amount of MPS spheres for the assembly of Au nanoparticles capped with three different ligands: TOAB, C12N, and C16N. Due to their relatively weak binding to the Au surface, TOAB molecules may partially detach from the Au particles during the assembly, making the average interparticle separation much smaller than expected for a dense monolayer of octyl chains. As a result, the maximum shift in plasmon resonance is found to be above 100 nm, a value which has been obtained in previous studies for close-packed Au particles capped by alkanethiols of three carbon atoms.[22] The structures assembled from Au particles capped with C12N and C16N show much smaller maximum plasmonic shifts, consistent with the previously studied cases with alkanethiols containing alkyl chains of the same length.[22] For the three capping ligands that we tested, the change of plasmon band follows the same trend: it shifts to longer wavelength initially, reaches the maximum value at certain amount of MPS spheres, and eventually shifts back when MPS is further increased. However, the amount of MPS spheres required to reach this transition point is different in each case. More MPS spheres are needed to reach the maximum red-shifts for assembling nanoparticles capped with longer ligands. This can be explained by the fact that fewer Au nanoparticles can be accommodated as a monolayer assembly on the surface of an MPS sphere when the interparticle separation is larger. Our estimation of surface coverage indicates that, when the maximum plasmonic shifts are reached, C12N and C16N capped Au nanoparticles assemble as monolayers with average interparticle separation of ~ 2.8 and ~4.0 nm, respectively. In both cases, the gap between neighboring Au nanoparticles is shorter than double the length of an

extended alkylamine chain, suggesting that the alkyl chains might interdigitate with the chains on neighboring particles.[26]

We have compared the absorption spectra and the corresponding photos of the Au nanoparticles before and after their assembly as a close-packed monolayer on MPS spheres. The isolated Au nanoparticles show very similar plasmon bands (~530 nm) even though they are capped with different ligands. This leads to the conclusion that the different shifts of the plasmon bands are due to variances in the assembly behavior of the nanoparticles and not the dielectric constants of the capping ligands.[26] As shown in Figure 3.6, the solution of TOAB capped nanoparticles changes from red to deep purple after adding enough MPS spheres, while for C12N and C16N capped nanoparticles, the solution color can only change to light purple after assembly.

The successful assembly of Au nanoparticles on the MPS surface is primarily due to the dominantly strong interaction between Au and the thiol groups. During the assembly process, the original capping ligands are believed to partially detach from the nanoparticle surface to allow for the formation of Au-S bonds. This is possible because the bindings of TOAB and amines on the Au surface are relatively weak compared to the Au-S bond. It is therefore expected that such preferential assembly would not occur if the Au nanoparticles were initially stabilized with capping ligands containing thiol groups. This is indeed the case when we switch the capping agent to 1-dodecanethiol (C12S). As shown in Figure 3.7, no changes in plasmon resonance are observed when C12S capped Au nanoparticles are mixed with various amounts of MPS spheres.

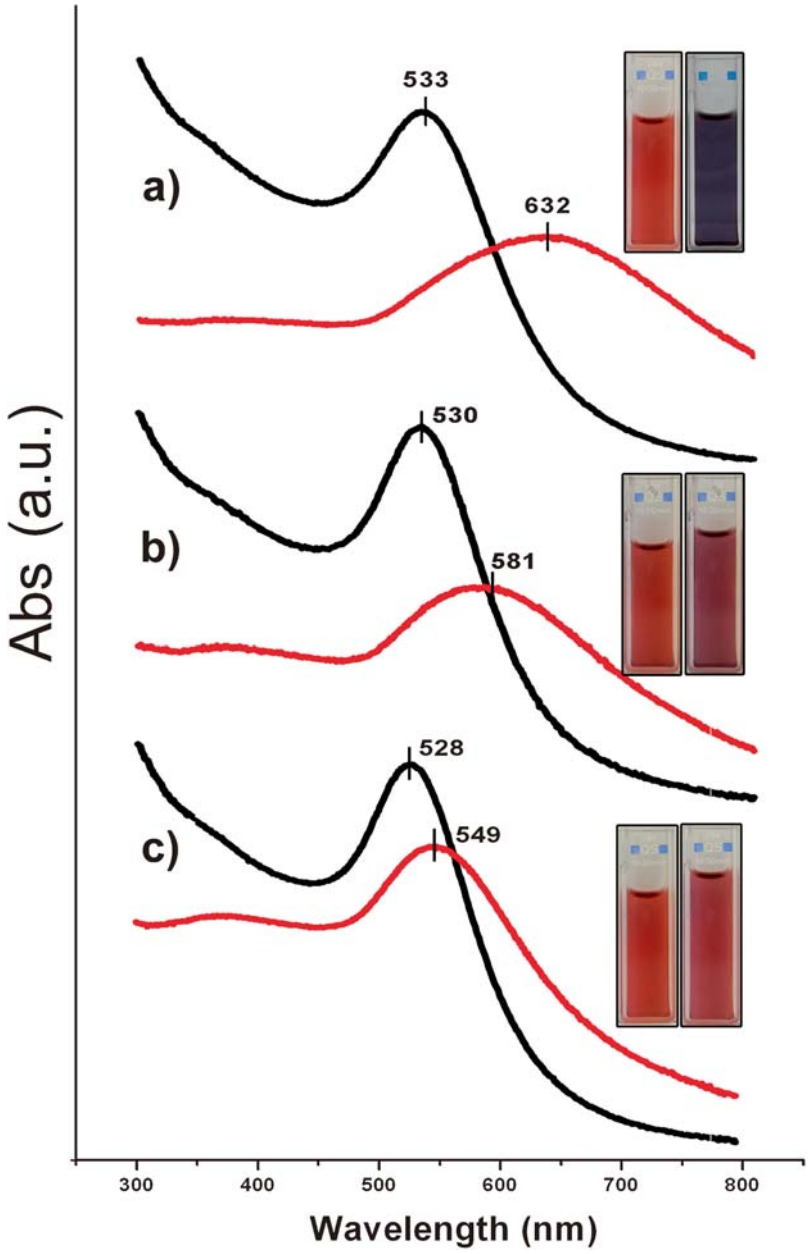

Figure 3.6 Absorption spectra and corresponding photos of the Au nanoparticles before and after their assembly as a close-packed monolayer on MPS spheres. The Au nanoparticles were capped with different capping agents: a) TOAB, b) C12N c) C16N. The volume of MPS sphere solution is 150, 300 and 400 μL for these three cases, respectively. All spectra were taken after assembly reached equilibrium (>10 min).

By monitoring the red-shift of the plasmon bands, we have been able to study the kinetics of assembly of Au nanoparticles on the surface of MPS spheres. As shown inFigure 3.8, the assembly of Au nanoparticles capped with different ligands reaches equilibrium after ~ 7 min, suggesting that the overall diffusion kinetics in these three cases is similar. The interaction between Au nanoparticles and thiol groups on the MPS surface is so strong that other interactions, such as Au-NH_2 coordination, do not effectively contribute to the dynamic binding process. To clarify the nature of the assembly kinetics, we plot the normalized data in Figure 3.8b. In all three cases, the assembly kinetics was proportional to the square root of elapsed time *t*, which is characteristic of a diffusion-limited process.

3.4 Conclusion

In summary, we describe the self-assembly of Au nanoparticles into a monolayer on the surface of mercapto-silica colloidal spheres by taking advantage of the strong interaction between Au nanoparticles and thiol groups. By controlling the interparticle separation and consequently the strength of the electromagnetic coupling, we have been able to conveniently tune the plasmon resonance property of the resulting composite microspheres. Unlike previous cases where nanoparticles were assembled into close-packed films through solvent evaporation so that the interparticle separation was solely determined by the length of the capping ligands, in this work we demonstrate that the interparticle separation can be tuned by controlling both the length of the capping ligands and the molar ratio of gold nanoparticles to the supporting MPS microspheres. In this case, the length of the capping agents only determines the maximum red-shift of the

plasmon bands that can be achieved at close-packed conditions. Within this limit of maximum shift, the plasmon band can be precisely tuned by controlling the relative concentration of the Au particles to the MPS support particles. The mercapto-silica spheres provide a quasi two-dimensional surface for nanoparticle assembly while at the same time retaining their isolated colloidal form. Compared to direct chemical synthesis methods for functional plasmonic nanostructures, the self-assembly process described here provides an alternative pathway which has the advantages of easy fabrication procedure, well-defined structures, and convenient tailoring of the optical properties.

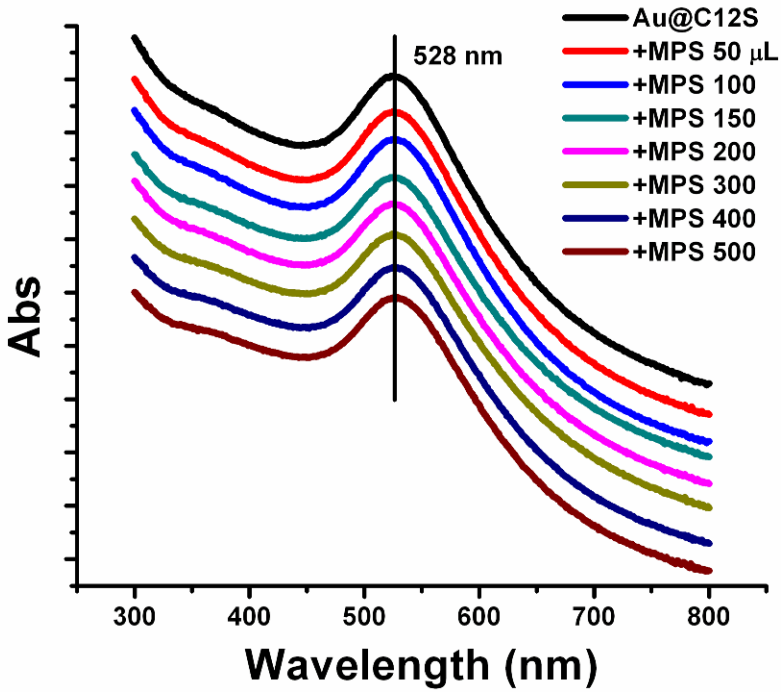

Figure 3.7 Concentration effect of MPS spheres on the absorption spectra of C12S-capped Au nanoparticles in toluene. From top to bottom the volume of MPS sphere solution is 0, 50, 100, 150, 200, 300, 400 and 500 mL. Each spectrum was taken after the assembly achieved equilibrium.

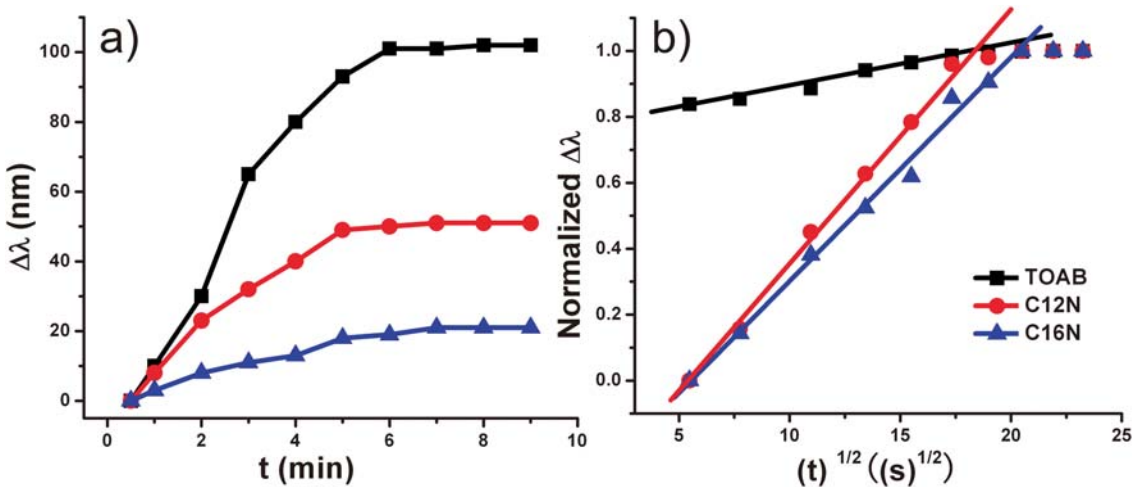

Figure 3.8 The kinetics (a) and normalized plot (b) of the assembly of Au nanoparticles capped with different ligands on the surface of MPS spheres. The amount of MPS spheres is 150, 300 and 400 μL for these three cases, respectively.

Reference

(1) Ozbay, E., *Science* **2006,** 311, 189-193.

(2) Halas, N., *MRS Bull.* **2005,** 30, 362-367.

(3) Haes, A. J.; Haynes, C. L.; McFarland, A. D.; Schatz, G. C.; Van Duyne, R. P.; Zou, S., *MRS Bull.* **2005,** 30, 368-375.

(4) Liz-Marzan, L. M., *Langmuir* **2006,** 22, 32-41.

(5) Templeton, A. C.; Pietron, J. J.; Murray, R. W.; Mulvaney, P., *J. Phys. Chem. B* **2000,** 104, 564-570.

(6) Taleb, A.; Petit, C.; Pileni, M. P., *J. Phys. Chem. B* **1998,** 102, 2214-2220.

(7) Underwood, S.; Mulvaney, P., *Langmuir* **1994,** 10, 3427-3430.

(8) Kelly, K. L.; Coronado, E.; Zhao, L. L.; Schatz, G. C., *J. Phys. Chem. B* **2003,** 107, 668-677.

(9) Wiley;, B.; Sun;, Y.; Chen;, J.; Cang;, H.; Li;, Z.-Y.; Li;, X.; Xia, Y., *MRS Bull.* **2005,** 30, 356-361.

(10) Rechberger, W.; Hohenau, A.; Leitner, A.; Krenn, J. R.; Lamprecht, B.; Aussenegg, F. R., *Opt. Commun.* **2003,** 220, 137.

(11) Su, K. H.; Wei, Q. H.; Zhang, X.; Mock, J. J.; Smith, D. R.; Schultz, S., *Nano Lett.* **2003,** 3, 1087-1090.

(12) Sih, B. C.; Wolf, M. O., *J. Phys. Chem. B* **2006,** 110, 22298-22301.

(13) Jain, P. K.; Huang, W.; El-Sayed, M. A., *Nano Lett.* **2007,** 7, 2080-2088.

(14) Gunnarsson, L.; Rindzevicius, T.; Prikulis, J.; Kasemo, B.; Kall, M.; Zou, S.; Schatz, G. C., *J. Phys. Chem. B* **2005,** 109, 1079-1087.

(15) Zhao, L.; Kelly, K. L.; Schatz, G. C., *J. Phys. Chem. B* **2003,** 107, 7343-7350.

(16) Maier, S. A.; Kik, P. G.; Atwater, H. A., *Appl. Phys. Lett.* **2002,** 81, 1714.

(17) Haynes, C. L.; McFarland, A. D.; Zhao, L.; Van Duyne, R. P.; Schatz, G. C.; Gunnarsson, L.; Prikulis, J.; Kasemo, B.; Kall, M., *J. Phys. Chem. B* **2003,** 107, 7337-7342.

(18) Bouhelier, A.; Bachelot, R.; Im, J. S.; Wiederrecht, G. P.; Lerondel, G.; Kostcheev, S.; Royer, P., *J. Phys. Chem. B* **2005,** 109, 3195-3198.

(19) Liu, G. L.; Yin, Y.; Kunchakarra, S.; Mukherjee, B.; Gerion, D.; Jett, S. D.; Bear, D. G.; Gray, J. W.; Alivisatos, A. P.; Lee, L. P.; Chen, F. F., *Nat. Nano.* **2006,** 1, 47.

(20) Kim, Y.; Johnson, R. C.; Hupp, J. T., *Nano Lett.* **2001,** 1, 165-167.

(21) Liu, J.; Lu, Y., *J. Am. Chem. Soc.* **2003,** 125, 6642-6643.

(22) Osterloh, F.; Hiramatsu, H.; Porter, R.; Guo, T., *Langmuir* **2004,** 20, 5553-5558.

(23) Lu, Y.; Liu, G. L.; Lee, L. P., *Nano Lett.* **2005,** 5, 5-9.

(24) Martin, J. E.; Wilcoxon, J. P.; Odinek, J.; Provencio, P., *J. Phys. Chem. B* **2000,** 104, 9475-9486.

(25) Malikova, N.; Pastoriza-Santos, I.; Schierhorn, M.; Kotov, N. A.; Liz-Marzan, L. M., *Langmuir* **2002,** 18, 3694-3697.

(26) Chen, C.-F.; Tzeng, S.-D.; Chen, H.-Y.; Lin, K.-J.; Gwo, S., *J. Am. Chem. Soc.* **2008,** 130, 824-826.

(27) Yu, A.; Liang, Z.; Cho, J.; Caruso, F., *Nano Lett.* **2003,** 3, 1203-1207.

(28) Agrawal, V. V.; Varghese, N.; Kulkarni, G. U.; Rao, C. N. R., *Langmuir* **2008,** 24, 2494-2500.

(29) Kim, B.; Tripp, S. L.; Wei, A., *J. Am. Chem. Soc.* **2001,** 123, 7955-7956.

(30) Nakamura, M.; Ishimura, K., *J. Phys. Chem. C* **2007,** 111, 18892-18898.

(31) Nakamura, M.; Ishimura, K., *Langmuir* **2008,** 24, 5099-5108.

(32) Brust, M.; Walker, M.; Bethell, D.; Schiffrin, D. J.; Whyman, R., *J. Chem. Soc., Chem. Commun.* **1994**, 801-802.

(33) Fink, J.; Kiely, C. J.; Bethell, D.; Schiffrin, D. J., *Chem. Mater.* **1998,** 10, 922-926.

(34) George Thomas, K.; Zajicek, J.; Kamat, P. V., *Langmuir* **2002,** 18, 3722-3727.

Chapter 4

Direct Assembly of Hydrophobic Nanoparticles to Multifunctional Structures

4.1 Introduction

Multifunctional particles in the micrometer or sub-micrometer scale that exhibit two or more different properties are highly desirable for many important technological applications, ranging from catalysis to energy harvesting and transformation, multimodal imaging, detection, and simultaneous diagnosis and therapy.[1-12] For example, microspheres embedded with magnetic iron oxide nanoparticles and fluorescent quantum dots have been widely studied as a multiple-mode imaging contrast agents combining magnetic resonance with optical detection and biological targeting.[13-15] By carefully controlling the loading of quantum dots, the obtained composite particles possess a dual function of optical encoding and magnetic separation.[11,16] Replacing quantum dots with noble metal nanoparticles in such composites results in new types of multifunctional structures that are capable of magnetic resonance imaging and photothermal therapy.[17,18] Magnetic materials have also been combined with nanocatalysts to form magnetically separable catalysts for the recovery and reuse of expensive catalysts after catalytic reactions, thus bridging the gap between heterogeneous and homogeneous catalysis.[19-23]

Nanoparticle assembly represents a powerful approach that has been actively explored recently for producing bi-, tri-, and multifunctional materials in contrast to their limited single-component counterparts. By organizing different types of nanoparticles together, it not only allows the utilization of the size- and shape-dependent properties of individual nanoparticles, but also takes advantage of new properties resulting from the

interactions between neighbors.[4-6,8,10,24-26] Conventional assembly processes for multifunctional structures such as the well-known layer-by-layer (LbL) methods are mostly limited to hydrophilic nanoparticle systems because they heavily rely on electrostatic interactions.[27-32] The Direct linking nanoparticles through chemical bonds between surface ligands has also been attempted,[33-35] but is limited to some special cases because most commonly used protecting ligands of nanoparticles do not contain additional active functional groups that allow further reactions.

Many technologically important high quality nanoparticles, especially semiconductors (such as CdSe, ZnSe, CdTe, and InP, InAs) and metal oxides (such as γ-Fe_2O_3, MnO, TiO_2, ZrO_2, $CoFe_2O_4$) are predominantly prepared through thermolytic routes by reacting inorganic precursors in organic solvents at high temperatures (typically 150-320 ºC).[36-43] The resulting nanostructures, however, retain the hydrophobic character of the organic ligands and, hence, are not soluble in water. As a result, it has been very difficult to assemble them directly into multifunctional nanostructures using means similar to those for water soluble particles. Typically, it is necessary to impose hydrophilic character on the nanoparticle surface and ensure water dispersibility (also bio-compatibility) by replacing the hydrophobic organic ligands with hydrophilic ones.[43-47] However, ligand exchange processes usually involve several extra steps and in many cases are detrimental to the physical properties of the nanoparticles because the new hydrophilic ligands may not be able to effectively insulate the inorganic cores from the aqueous environment. For example, ligand exchange of hydrophobic trioctylphosphine oxide (TOPO) on the surface of CdSe/ZnS quantum dots (QDs) with various hydrophilic

ligands causes a significant decrease in quantum efficiencies.[43,46] Furthermore, the new ligands tend to desorb gradually from the nanoparticles, leading to aggregation and precipitation of the nanoparticles. More importantly, if more than one type of nanoparticles is needed for achieving multiple functions, each must be surface-treated separately before assembly. Therefore, it is highly desirable to develop a simple and general approach that allows the fabrication of multifunctional nanostructures by direct assembly of hydrophobic nanoparticles of various compositions. As their major applications are in the biomedical fields,[23,35] it is also highly desired that these multifunctional systems be dispersible in water.

The strong coordinating interactions between alkanethiols and metal surfaces have been extensively studied and utilized in the formation of self-assembled monolayers (SAMs) on metal surfaces.[48] It has also been reported that alkanethiols can adsorb onto metal oxide surfaces (such as TiO_2,[49] ZnO,[50,51] and SnO_2[52]) and semiconductor substrates (such as InP,[53,54] InAs,[55,56] and GaAs,[57,58] and metal sulfides[59]). Recently, the thiol-metal interaction has been used to immobilize nanoparticles on alkanethiol-modified solid substrates,[60-64] and has been further extended to the colloidal substrates by assembling Au nanoparticles to thiol-functionalized silica colloids.[65,66] Philipse et al. have explored the attachment of magnetic particles to colloidal silica that was grafted with (3-mercaptopropyl)trimethoxysilane (MPS).[67,68] Their efforts, however, have been still limited to only water soluble γ-Fe_2O_3 and $CoFe_2O_4$ nanoparticles, probably due to the low density of thiol groups achievable during the surface modification of colloidal silica. Our

prior studies have shown that colloidal silica with a high surface loading of thiol groups can effectively harvest hydrophobic Au nanocrystals from nonpolar solutions.[69]

Here, we explore the use of thiol-terminated colloidal organosilica (mercapto-silica) particles to directly immobilize various types of hydrophobic ligand capped nanoparticles, and further develop a general and powerful self-assembly method for the fabrication of multifunctional composite nanostructures. Briefly, mercapto-silica colloidal particles made from MPS are first synthesized as adsorbent hosts, named as MPS spheres. Nanoparticles of desired functions are synthesized separately using well-established thermolysis methods, and then efficiently immobilized on the surface of MPS spheres by taking advantage of the high density thiol groups. In order to improve the chemical/mechanical stability and water-dispersibility, the composites can be further coated with a thin shell of normal silica. After demonstrating this simple assembly process, we generalize the procedure by immobilizing nanoparticles on mercapto-silica modified nanoscale objects, thus opening the door to the fabrication of more complex multifunctional composite structures.

4.2 Experimental Section

4.2.1 Materials

(3-mercaptopropyl)trimethoxysilane (MPS), tetraethyl orthosilicate (TEOS), sodium dodecyl sulfate (SDS), cetyl trimethylammonium bromide (CTAB), ammonium hydroxide solution (~28% NH_3 in water), oleylamine, and trioctylphosphine oxide (TOPO) were purchased from Aldrich Chemical Co. Ethanol, toluene, cyclohexane and

acetone were obtained from Fisher Scientific. All chemicals were used as received without further treatment.

4.2.2 Synthesis of Nanoparticles

Most of hydrophobic nanoparticles used in this work were synthesized via the well-established high-temperature thermolysis routes (oleic acid capped γ-Fe_2O_3,[36] TOPO and oleylamine capped CdSe,[70] TOPO capped ZrO_2,[71] oleic acid capped NaYF4:Yb,Er,[72] TOPO and oleylamine capped NiO,[73] 1-dodecanethiol capped Cu_2S disks,[74] TOPO capped TiO_2 dots,[75] oleic acid capped TiO_2 rods,[76] and oleic acid capped CdSe@CdZnS[77]). Au nanoparticles (5 ± 0.5 nm in diameter) were synthesized through the reduction of $HAuCl_4$ in a biphasic water-toluene mixture using $NaBH_4$ in the presence of TOAB.[69,78] 1-Dodecylamine and 1-dodecanethiol capped Au nanoparticles were prepared via ligand exchange.[69]

4.2.3 Synthesis of MPS Spheres

MPS spheres were prepared by using a one-pot procedure as described in Chapter 2.[79,80] Typically, 120 μL MPS precursor was added to 30 mL of 1% ammonia aqueous solution and vigorously shaken for 1 minute at a speed of 2500 rpm. The mixture was then incubated at RT for 12 hours. The final products were washed with 0.01 M NaOH aqueous solution and ethanol several times and then dispersed in 10 mL of toluene. The size of MPS spheres can be tuned systematically by changing the amount of precursor.

4.2.4 Assembly of Nanoparticles on MPS Spheres

Nanoparticles were assembled on the surface of MPS spheres by simply mixing them in nonpolar solvents such as toluene or cyclohexane. Typically, 500 μL of as-

synthesized nanoparticles were added to 10 mL toluene dispersion of MPS spheres. Then, the mixture was votexed for 20 minutes at a speed of 500 rpm, followed by washing with nonpolar solvents a few times to remove free nanoparticles. Generally, the amount of nanoparticles is in excess compared to that of the MPS spheres.

For quantifying the QD loading on MPS spheres, the concentration of as-synthesized QDs was calculated using the amount of limiting reagent selenium (2.4 mg), the density of CdSe, the final particle size and the volume of solvent toluene (5 mL).[77] After diluted 100 times, the concentration of QDs is about 10^{14} nanoparticles per mL, which is consistent with the results measured from UV-Vis adsorption spectrum by Leatherdale et al.[81] The concentration of the MPS spheres can be estimated at 2×10^{10} spheres per mL using the similar method. QD solution in toluene (500 μL) was mixed with different amount of MPS dispersion (0 to 500 μL) and pure toluene to obtain a total volume of 1 mL. After shaking 1 hour and subsequent centrifugation, PL of the supernatants was directly recorded and the precipitates were studied by TEM.

4.2.5 Silica Overcoating

For SDS assisted silica coating of γ-Fe_2O_3, Au, ZrO_2 and TiO_2 nanoparticle-capped MPS spheres, after washing and centrifugation, the precipitate was dissolved by 3 mL of aqueous solution of SDS (5.6 mg/mL) and sonicated for 10 minutes. The mixture was then heated to ~ 80 ^{o}C in a water bath for 1 hour to evaporate the remaining trace amount of toluene. The reaction solution was cooled down to room temperature and washed with water one time and re-dispersed in 3 mL of water. Then, ammonium hydroxide aqueous solution (1 mL, 28%), ethanol (20 mL), and TEOS (50 μL) were

added to the solution sequentially. After stirring for 20 min, the core/shell colloids were collected by centrifugation and washed with ethanol three times.

For CTAB assisted silica coating, γ-Fe_2O_3 capped or QD-capped MPS spheres were first washed and centrifuged after assembly. Then 3 mL of aqueous solution of CTAB (10 mg/mL) was used to mediate the transfer of nanoparticle-capped MPS spheres to water. The composite spheres were re-dispersed in 15 mL H_2O, mixed with aqueous NaOH solution (100 μL, 0.1 M), added 50 μL of methanol solution of TEOS (20% in volume) three times at 30-min intervals, reacted for 2 days under stirring, and then washed with ethanol three times. In order to grow a thicker silica layer, the thin-layer-silica coated composite particles were re-dispersed in water (3 mL), sequentially mixed with ammonia aqueous solution (1 mL, 28%), ethanol (20 mL), and TEOS (30 μL), and reacted for 20 min under vigorous stirring. The core/shell colloids were finally collected by centrifugation and washed with ethanol three times.

4.2.6 Coating of MPS Layer onto Normal Silica Surface

Nanostructures covered with normal silica such as normal silica beads prepared by Stöber method, Fe_3O_4@SiO_2,[82,83] Ag wire@SiO_2,[84] or MPS@γ-Fe_2O_3@SiO_2, with a typical amount of ~20 mg, was dispersed in 3 mL water, mixed with 1 mL of ammonia (28%) and 20 mL of ethanol, after which a mixture of MPS and TEOS (20 μL, volume ratio 1:1) was added, and reacted for 20 min. After that, 20 μL of MPS/TEOS mixture (volume ratio: 5:1) was injected and reacted for another 20 min. The final products were washed with ethanol three times and re-dispersed in nonpolar solvent for subsequent nanoparticle immobilization.

4.3 Results and Discussion

Figure 4.1a outlines the general self-assembly strategy for the fabrication of monodisperse, well-defined nanoparticle-silica multifunctional composites. The assembly involves two essential building blocks: mercapto-silica spheres and hydrophobic ligand-capped nanoparticles. In a typical process, MPS precursor is hydrolyzed rapidly in an ammonia solution to yield spherical colloids.[69,79,80] These mercapto-silica spheres are both structurally and functionally different from normal silica particles prepared from alkoxide precursors such as TEOS. The use of MPS grants the resulting spheres a layer of high density surface thiol groups, which are expected to tether a dense layer of nanoparticles through the strong thiol-metal interactions. On the other hand, the abundant mercaptopropyl groups make the MPS spheres dispersible in nonpolar solvents such as toluene, facilitating the approaching of mercapto-silica and hydrophobic nanocrystals during the assembly process. The narrowly distributed MPS spheres with controlled sizes ranging from ~150 nm to ~3.5 micrometers can be produced by simply changing the reaction conditions, for example, the amount of the silane precursor,[80] making it possible to produce uniform multifunctional nanocomposites with the desired dimensions. Hydrophobic ligand-capped nanoparticles are prepared through standard high-temperature thermolysis reaction.[38-40,43,85] Figure 4.1b and 4.1c show typical transmission electron microscopy (TEM) images of oleic acid-capped γ-Fe_2O_3 nanoparticles (diameter: 12 ± 0.7 nm)[36] and MPS spheres (diameter: 280 ± 30 nm).

Nanoparticles are assembled on the surface of MPS spheres by simply mixing them in nonpolar solvents such as toluene, hexane or cyclohexane. Generally, excess

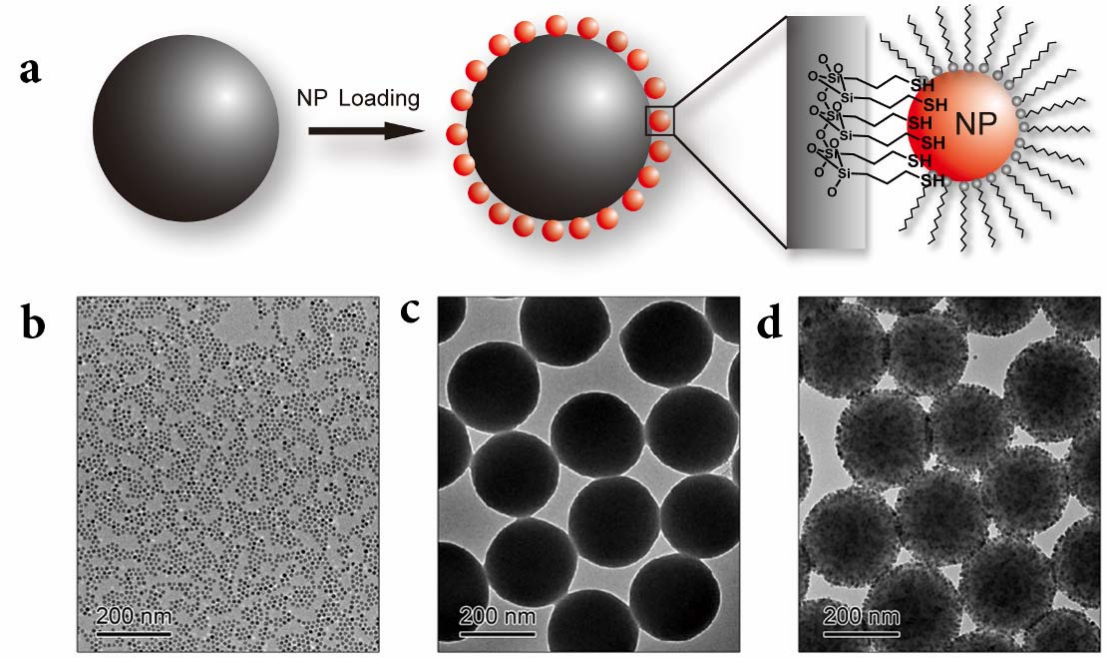

Figure 4.1 (a) Schematic illustration showing the procedure of self-assembly of hydrophobic nanoparticles on MPS spheres. (b) TEM images of oleic acid capped γ-Fe_2O_3 nanoparticles, (c) MPS spheres and (d) γ-Fe_2O_3 nanoparticles assembled on the surface of MPS spheres.

nanoparticles are used to ensure the dense coverage on the MPS spheres. Nanoparticle-capped MPS spheres are collected after washing several times with nonpolar solvent to remove free nanoparticles. As shown in Figure 4.1d, a monolayer of γ-Fe_2O_3 nanoparticles can be clearly observed on the originally smooth surface of MPS spheres. No free nanoparticles can be observed, suggesting a strong attraction between the nanoparticles and MPS spheres. It is believed that during the assembly process, the thiol groups can partially replace the original surface ligands (oleic acid) and coordinate to the metal sites on the nanoparticle surface.

Thiols form stable bonds with most metal cations except alkali and alkaline earth ions.[14] To test the versatility of the assembly process, various hydrophobic metal compound nanoparticles including TOPO and oleylamine capped CdSe,[70] TOPO capped ZrO_2,[71] oleic acid capped NaYF4:Yb,Er,[72] TOPO and oleylamine capped NiO,[73] 1-dodecanethiol capped Cu_2S discs,[74] TOPO capped TiO_2 dots[75] and oleic acid capped rods[76] were assembled on the surface of the MPS spheres, as shown in Figure 4.2. A layer of nanoparticles can be easily identified on the surface of each MPS sphere, indicating the generality of the assembly strategy for hydrophobic metal compound nanoparticles. Note that Cu_2S discs with different diameters (8 nm and 20 nm) show a similar high affinity for the MPS spheres, indicating a minimal size effect on the binding process. This has been also confirmed by the dense coverage of γ-Fe_2O_3 nanoparticles of 5 nm, 12 nm and 20 nm on MPS spheres. The similar adsorption behavior of TiO_2 nanodots and nanorods on MPS spheres also suggests that the shape of nanoparticles has no significant effect on assembly efficiency.

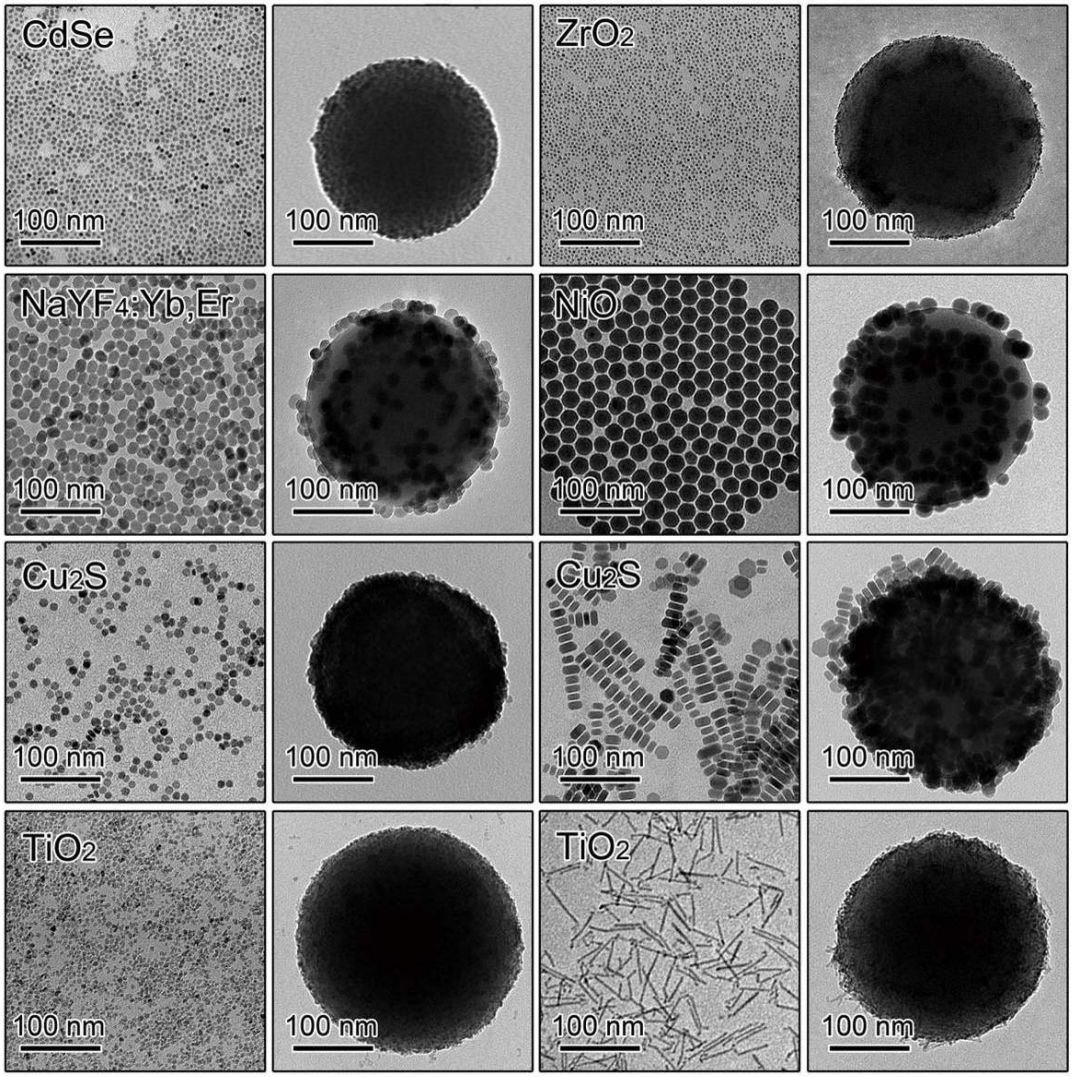

Figure 4.2 TEM images of various hydrophobic nanoparticles assembled on the surface of MPS spheres: left columns (column 1 and 3) show the different nanoparticles and right columns (column 2 and 4) represent the corresponding nanoparticle-capped MPS spheres. The ZrO_2, TiO_2 nanodots are originally protected by TOPO, $NaYF_4$:Yb,Er, TiO_2 nanorods by oleic acid, CdSe and NiO by TOPO and oleylamine, and both small and large Cu_2S nanodisks by 1-dodecanethiol.

The simple assembly process allows great flexibility in incorporating multiple nanoparticle components. A competition for immobilization on the surface of MPS spheres would appear among various types of nanoparticles due to their different affinity to thiol groups, which generally follows the Hard Soft Acid Base (HSAB) theory. Nanoparticles containing soft-acid cations such as Pt(II), Cu(I), Cd(II) and Au(I) bind to thiol groups much more strongly compared with those made of hard-acid cations such as Fe(III) and Ti(IV). In a nanoparticle mixture, it is necessary to increase the relative concentration of those with low-affinity to ensure sufficient loading. As an example shown in Figure 4.3, we demonstrate here the assembly of γ-Fe_2O_3 nanoparticles and CdSe QDs on MPS spheres by mixing their dispersions at a particle number ratio of 10:1. The simultaneous capture of nanoparticles of γ-Fe_2O_3 and QD on the MPS surfaces has been confirmed by using scanning electron microscopy (SEM) imaging and energy dispersive X-ray (EDX) elemental mapping of a typical composite sphere. The strong Si signal across the sphere confirms the organosilica core, while the Fe and Cd signals both detected in the surface region clearly suggests the co-adsorption of these two types of particles.

In order to reach the metal sites on the nanoparticle surface, the thiol groups of MPS spheres may partially replace the original capping ligands on the surface of the nanoparticles. To evaluate this ligand replacement, hydrophobic Au nanoparticles capped with three different protection ligands, tetraoctylammonium bromide (TOAB), dodecylamine (C12N) and 1-dodecanethiol (C12S) are used for assembly.[69] The molecular structures of these ligands are shown in Figure 4.4a. After mixing with Au

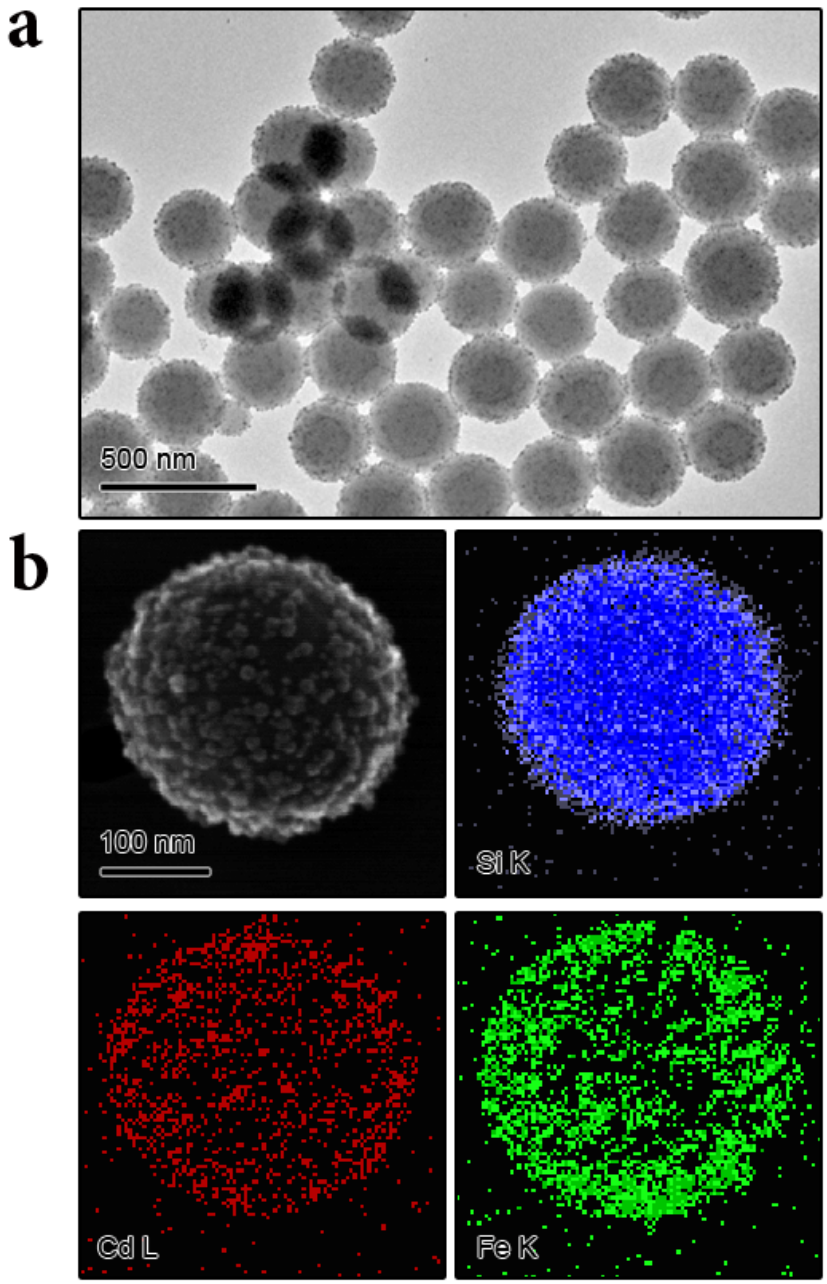

Figure 4.3 (a) Low magnification TEM image of CdSe and γ-Fe_2O_3 nanoparticles co-assembled on the surface of MPS spheres. (b) SEM image and the corresponding EDX mapping of the elemental distribution of Si, Cd and Fe in a composite sphere of MPS@γ-Fe_2O_3&CdSe.

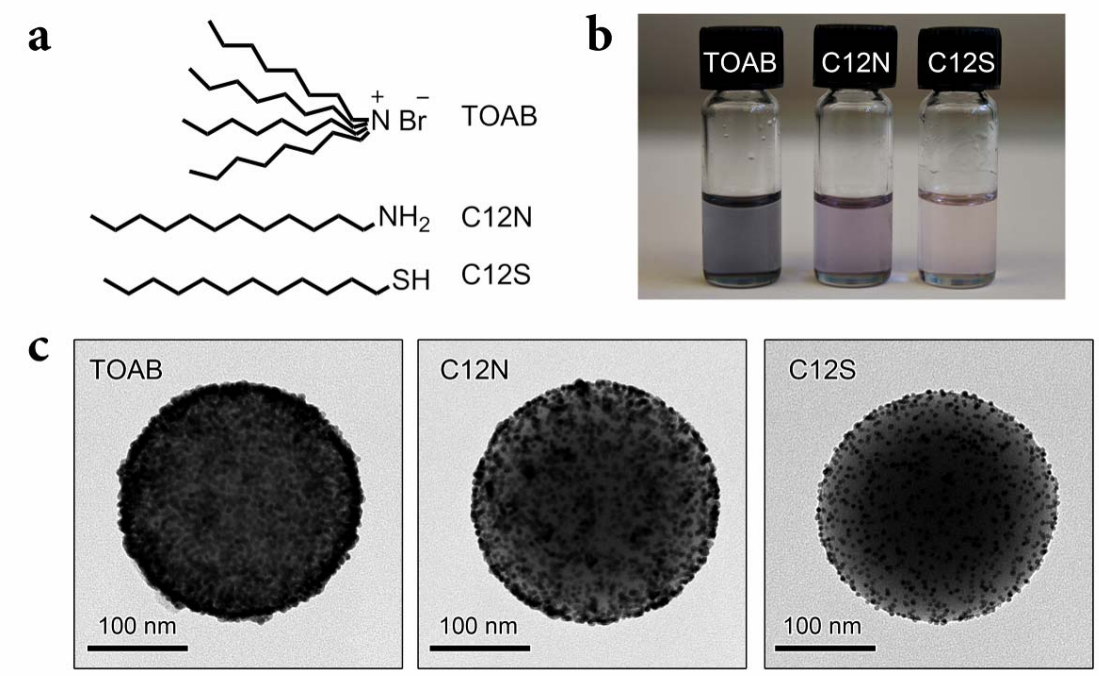

Figure 4.4 Effect of original capping ligands on nanoparticle assembly: (a) Molecular structures of the three protection ligands capped on Au nanoparticles (TOAB, C12N and C12S). (b) Digital photo of toluene dispersion of MPS spheres loaded with Au nanoparticles whose surfaces are capped with the three different protection ligands. (c) TEM images of the corresponding MPS spheres in photo b.

nanoparticles in toluene for ~20 minutes, the MPS spheres were separated from the mixture and washed a few times to remove free Au nanoparticles. Figure 4.4b presents the digital photos of toluene dispersions of Au nanoparticle-immobilized MPS spheres, with TOAB, C12N, and C12S capped spheres exhibiting blue, purple, and light red colors, respectively. The shift of the surface plasmon resonance bands (color change) is the result of interparticle electromagnetic coupling: MPS spheres attract more TOAB capped Au nanoparticles, resulting in smaller interparticle distance and consequently a larger blue shift.[69] The color intensity also indicates the loading of nanoparticles on MPS spheres. Due to the stability order of bonding Au-TOAB < Au-C12N <Au-C12S, the weaker capping ligands are believed to detach easily from the Au surface to allow for the formation of Au–S bonds, leading to higher nanoparticle loading, as confirmed in Figure 4.4c. The interesting fact that some C12S capped Au nanoparticles can still be captured by MPS spheres indicates that the thiol groups on MPS spheres can still replace some of the original alkanethiols to form new Au-S bonds even though the new bonds are similar to the original bonds in strength. This is consistent with our understanding of the dynamic nature of the ligand adsorption on nanoparticle surface.[38] As ligand replacement will eventually reach dynamic equilibrium, we predict that nanoparticle immobilization can always occur even if the new thiol-nanoparticle bond is weak compared to the original ligand-nanoparticle interaction, but the actual loading may be significantly affected by the relative bond strength.

The loading density of nanoparticles on the MPS spheres is related to their number ratio during assembly. If we assume the nanoparticles on the MPS spheres

arrange in a hexagonal close-packing structure, the number of nanoparticles per MPS sphere, N, can be estimated by $N = 4\alpha(1 + R/r)^2$, where α=0.906 is the density of the circular hexagonal arrangement, and R and r are the radii of MPS spheres and nanoparticles, respectively. This equation allows us to estimate the amount of nanoparticles that is needed for a required loading density, for example, one MPS sphere with diameter of 300 nm can immobilize ~5×10^3 8-nm nanoparticles. Experimentally, we can quantify the nanoparticle loading by measuring their optical absorption or photoluminescence (PL), as shown in Figure 4.5a by using CdSe/CdZnS QDs as an example.[77] QDs ~8 nm in diameter in a toluene solution (500 μL, ~10^{14} particles per mL) were mixed with different amounts of MPS sphere solution (~2×10^{10} spheres per mL) for 1 hour under vigorous shaking, followed by centrifugation at 11000 rpm for 10 min (free QDs remain in supernatant at this speed). Supernatant was collected for fluorescence measurement to monitor the amount of the free QDs left in the solution, and the precipitates were harvested for qualitative analysis of QD loading using TEM. As shown in Figure 4.5b, the fluorescence intensity of the supernatant decreased as more MPS solution was added to the system. When only a small amount of MPS solution (< 100 μL) was added, QDs remained in excess so that the decrease in fluorescence was nearly proportional to the added amount of MPS solution. The corresponding TEM image (Figure 4.5c) confirms that the surface of every MPS sphere is fully occupied by QDs. Adding more MPS spheres (200 μL and 300 μL) led to a decrease in fluorescence intensity because more QDs were captured by MPS spheres and then removed from the supernatant. No free QDs were left in supernatant when 300 μL MPS spheres was added.

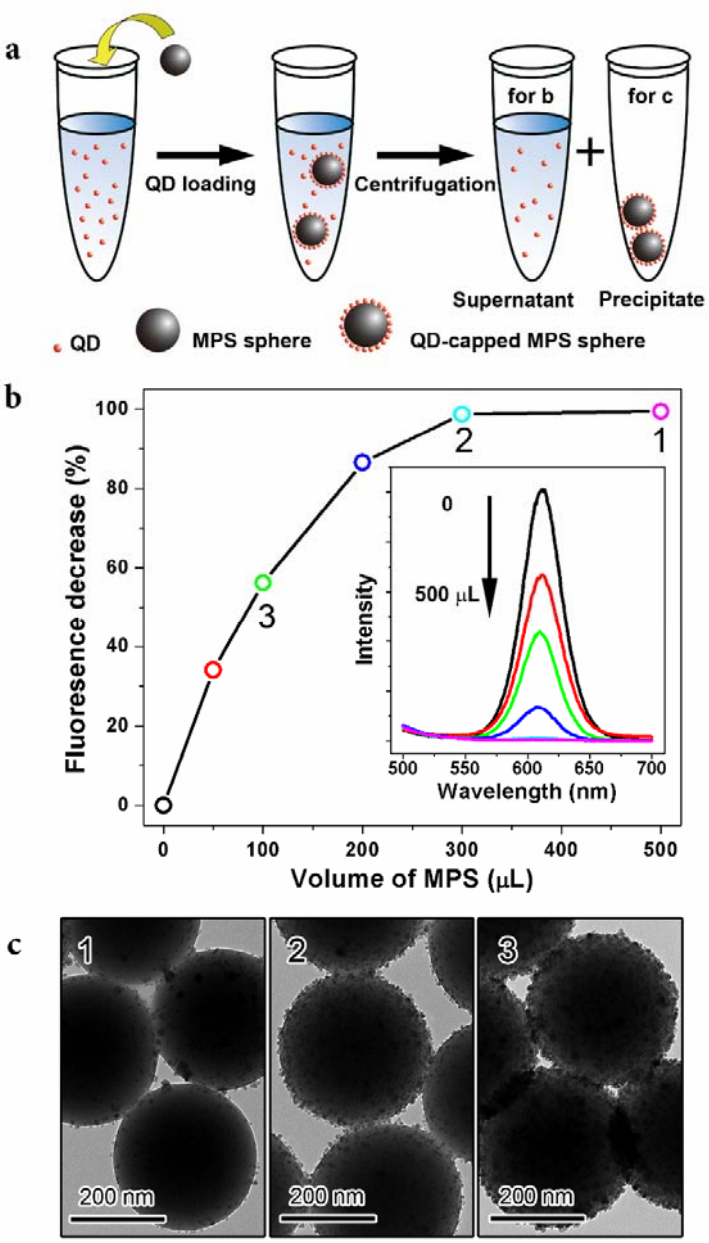

Figure 4.5 (a) Schematic diagram of the self-assembly of CdSe@CdZnS QDs on MPS spheres, showing how the PL spectra in (b) and TEM images in (c) were recorded. The original surface of QDs was covered by oleic acid. (b) PL spectra of the supernatant after adsorbtion of QDs by diffenert amount of MPS spheres. (c) TEM images of the precipitates (QD-capped MPS spheres) corresponding to the three points highlighted with numbers **1**, **2** and **3** in Figure b.

At this stage there are not enough QDs to cover all the MPS surfaces in the form of a close-packed monolayer, as indicated in the TEM image in Figure 4.5c. When 500 μL of MPS solution was added, even fewer QDs were adsorbed on each MPS sphere. If we assume that 200 μL of MPS solution is the amount needed for a close-packed monolayer of QDs, each MPS sphere can capture 10^4 QDs as estimated from the concentration and volume of MPS spheres and QDs that are used. This value is consistent with the result calculated based on geometric considerations (5×10^3).

The adsorption of hydrophobic nanoparticles onto MPS spheres results in composite particles that are non-dispersible in water, thus preventing their direct application in environmental and biomedical applications. This limitation can be conveniently addressed by overcoating the composite particles with an additional layer of normal silica. Silica coating can endow the composites with biocompatibility and the possibility of subsequent functionalization.[86-88] The additional advantages of using silica as a coating material mainly lie in its chemical stability, easy regulation of the coating process, controllable porosity, processability, and optical transparency.[1]

The nanoparticle-capped MPS composites are first transferred to aqueous phase by using additional surfactants to adsorb onto the surface of composite spheres through the formation of bilayer structures, as illustrated in 4.6a. The phase transfer makes it convenient to subsequently grow a silica layer using the well-known Stöber method.[89] The formation of a bilayer through hydrophobic-hydrophobic interaction also helps preserve the original ligands on the nanocrystal surface. As an example, we use an anionic surfactant, sodium dodecyl sulfate (SDS), to mediate the silica coating of oleic

acid capped MPS@γ-Fe_2O_3 composite spheres. After SDS adsorption, the MPS@γ-Fe_2O_3 composites were transferred into an ammonia/water/ethanol mixture and directly coated with uniform silica shells upon careful addition of TEOS. Figure 4.6b displays typical images of SiO_2 overcoated MPS@γ-Fe_2O_3 spheres. The thickness of the silica shell can be tuned from ten to several hundred nanometers by simply changing the amount of TEOS precursor. Interestingly, silica seems to initially nucleate on the individual nanoparticle surface and then grow independently before they eventually merge into a single layer. As a result, the silica coating possesses a rough surface until it reaches a thickness of ~100 nm. SDS has been demonstrated to be very effective in assisting the silica coating of composite spheres capped with various nanoparticles. This silica coating method assisted by SDS surfactant is universal for other hydrophobic nanoparticles-capped MPS spheres. In fact, the process has little to do with the compositions of nanoparticles and can be applied to passivate various nanoparticle/MPS systems as long as the additional surfactants can disperse these nanoparticles in the mixture of Ethanol/H_2O/NH_3, which is the chemical environment required for the Stöber method for silica coating. Figure 4.6c demonstrates a few more examples of normal silica passivated MPS@nanoparticle assemblies, with the nanoparticles being Au dots, TiO_2 rods, and ZrO_2 dots. Due to their small size compared to that of the MPS spheres, the nanoparticles cannot be individually identified in the TEM images and only a dark ring can be observed within the silica coating. Other typical surfactants, such as CTAB, can also be used to mediate silica coating on composite spheres. As shown in Figure 4.7a with MPS@γ-Fe_2O_3 as an example, we adapted a previously reported method to first

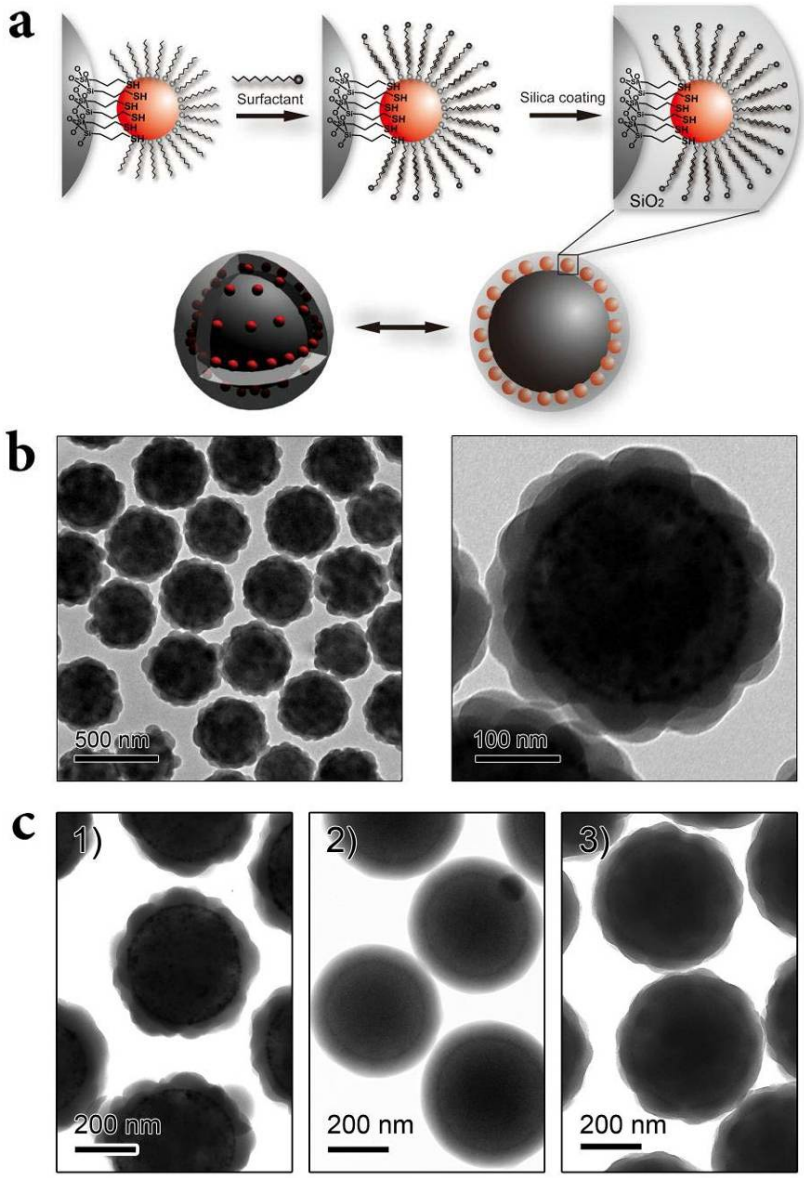

Figure 4.6 (a) Schematic illustration showing the approach for transferring nanoparticle-capped MPS spheres from oil to water phase by forming bilayer structure and subsquent silica coating. (b) TEM images of low and high magnification of silica coated γ-Fe_2O_3 nanoparticle-capped MPS spheres (MPS@γ-Fe_2O_3@SiO_2) synthesized in the presence of SDS. The γ-Fe_2O_3 nanoparticles were originally protected by oleic acid. (c) TEM images of MPS spheres capped with various nanoparticles and then surface coated with silica in the presence of SDS surfactant: (**1**) MPS@Au@SiO_2, (**2**) MPS@TiO_2 nanorods@SiO_2, and (**3**) MPS@ZrO_2@SiO_2. The Au nanoparticles were originally proteced by dodecylamine (C12N), TiO_2 nanorods by oleic acid, and ZrO_2 nanodots by TOPO.

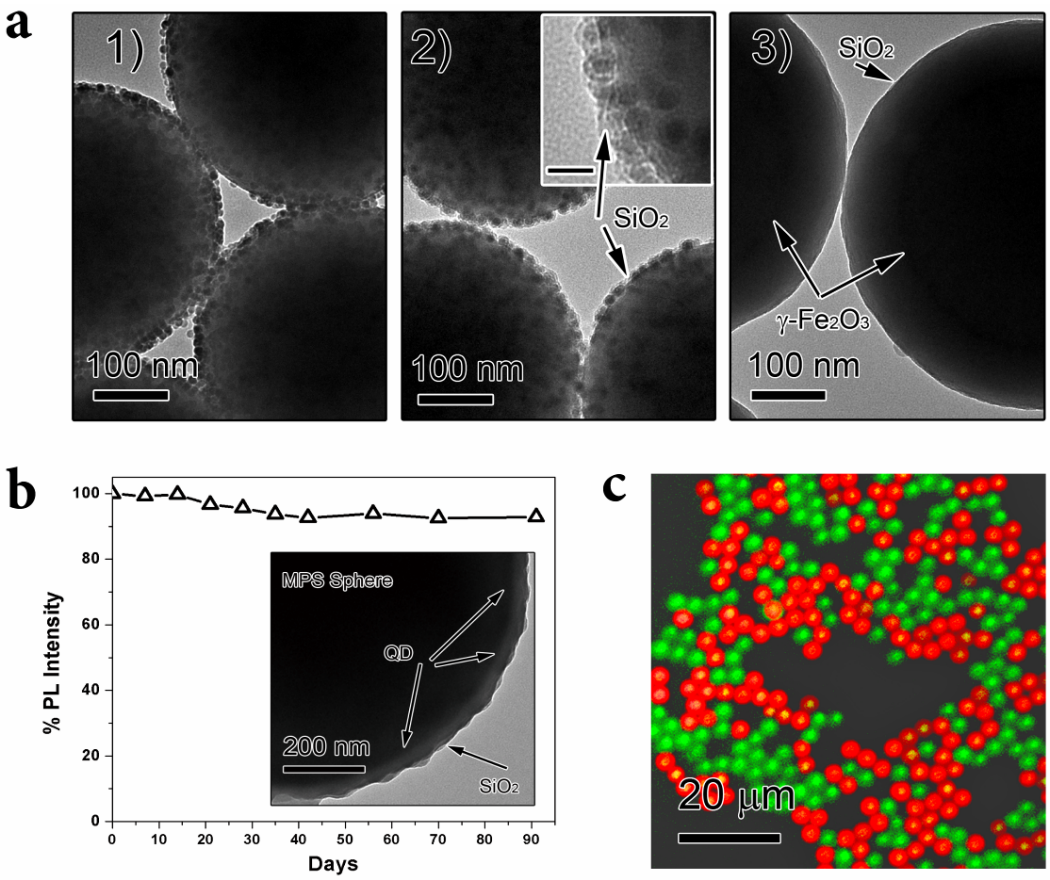

Figure 4.7 (a) TEM images of of γ-Fe_2O_3 nanoparticle-capped MPS spheres prepared in the presence of CTAB: (1) before silica coating; (2) after SiO_2 coating with CTAB as the surfactant in aqueous NaOH solution; (3**)** after additional SiO_2 coating using the standard Stöber process. The γ-Fe_2O_3 nanoparticles were originally protected by oleic acid. Inset in (2) is the corresponding TEM image at high magnification showing the presence of a thin silica layer (scale bar: 20 nm). (b) PL intensity as a function of time after storing the MPS@QD@SiO_2 composite spheres in water under ambient conditions; Inset is the TEM image of a portion of a typical MPS@QD@SiO_2 sphere. The original surface of CdSe@CdZnS QDs was covered by oleic acid. (c) Confocal optical microscopy image of 3.5-μm MPS spheres loaded with QDs of two different sizes. QDs of different colors were assembled on MPS spheres separately and then mixed together for imaging. The sample was excited with a focused 488 nm line of Ar^+ laser.

deposit a thin silica coating of a few nanometers on the composite surface by hydrolyzing TEOS in aqueous solution of CTAB with dilute NaOH solution as catalyst.[90] The thickness of the silica layer can be further increased by an additional step of standard Stöber process. Unlike the case using SDS, this two step procedure produces a very smooth silica surface even at a relatively small thickness. This procedure is especially useful for coating TOPO-capped MPS@QD spheres because CTAB causes smaller disturbance to the luminescence of QDs than SDS. Figure 4.7b demonstrates the high stability of the PL of MPS@QD@SiO_2 composites, with the TEM image of a portion of a typical sphere shown in the inset. The decrease of PL intensity is only about 10% even after 3 months of storage in water, which is significantly better than that of typical ligand-exchanged QDs. Surface passivation provided by silica and the intact ligand protection are believed to be the two main reasons for this excellent optical stability. Figure 4.7c shows a multicolor fluorescence microscopy image of a mixture of two types of "monochromatic" MPS@QD@SiO_2 spheres with an average diameter of 3.5 μm. These green and red spheres were prepared separately by using single-color quantum dots with emission wavelengths at 545 and 610 nm, respectively, and then mixed and imaged under a single wavelength light. All the spheres are observed with clearly distinguishable emission colors.

The necessity of MPS for high density thiol groups may appear as a limitation because MPS has only been produced in the form of microspheres and the functional nanoparticles can only be attached to the external surface of the spheres in the form of a monolayer. On the other hand, normal colloidal silica is well-known for its ability to

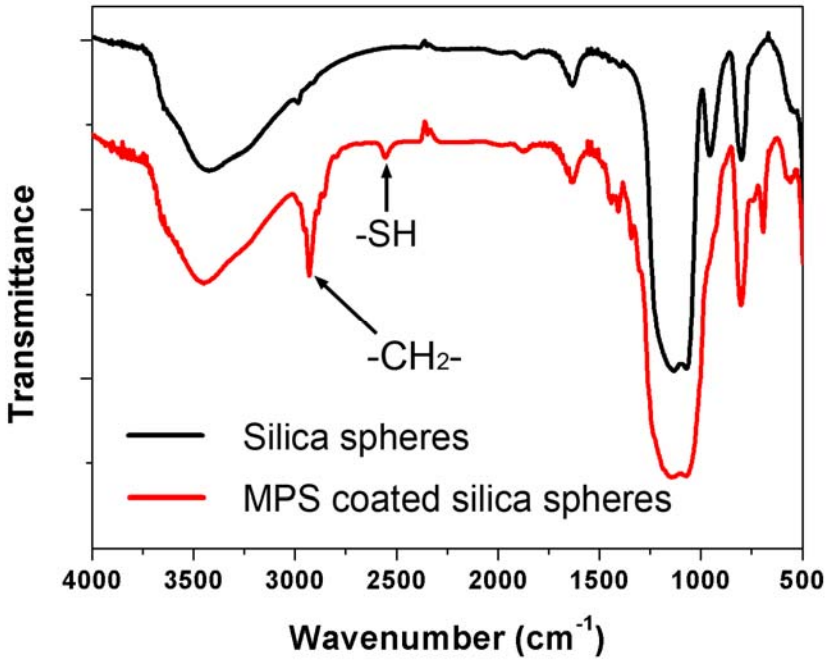

Figure 4.8 FTIR spectra of normal silica spheres before and after coating with an additional MPS layer. The relatively strong absorption of C-H and S-H stretching indicates the high loading of thiol groups introduced during the modification.

form a conformal coating on various nanostructures with a high degree of control over the thickness. Here we generalize the assembly process by coating mercapto-silica onto the surface of other nanoscale objects so that further nanoparticle assembly can occur on hosts with more complex morphologies than spheres. Our strategy is to first coat nano-objects such as dots, rods and wires with normal silica, and then introduce mercapto-silica to the surface through a co-condensation method. In the second step, multiple injections of the precursors were applied. The ratio of MPS to TEOS gradually increased for every injection to ensure a high density of thiol groups on the surface. The thiol-functionalized layer had been characterized by FTIR spectroscopy, as shown in Figure 4.8. After coating the normal silica spheres with an MPS layer, two bands in the ranges of 2950-2850 cm^{-1} and 2600-2500 cm^{-1} appeared, which can be attributed to the C-H and S-H stretching of the attached propanethiol groups.[91] The relatively strong absorption of C-H and S-H stretching in the IR spectrum indicates that the loading of thiol groups is significantly higher than that of colloidal silica spheres modified with MPS silane using conventional grafting methods (where only a sub-monolayer of MPS can be attached).

The ability to form MPS coatings on normal silica surfaces opens the door to the fabrication of a large variety of multifunctional composite nanostructures. Functional materials can now be incorporated as cores inside normal silica, whose surface can be modified with high density thiol groups for attaching other types of functional nanoparticles. Here, we have demonstrated a Fe_3O_4@SiO_2&MPS@QD@SiO_2 multilayer structure by using the simple solution phase assembly processes. First, superparamagnetic Fe_3O_4 particles with a diameter of ~100 nm were coated with SiO_2

using a procedure developed previously in our group.[18,19] After coating with a MPS layer, QDs were assembled on the surface, and subsequently another layer of SiO_2 was coated to make the composites water dispersible. Figure 4.9a and 4.9b show the TEM images of original Fe_3O_4@SiO_2 particle and the multilayer structure of the resulting Fe_3O_4@SiO_2&MPS@QD@SiO_2 composites, respectively. The inset demonstrates the strong fluorescence of the products under UV excitation and the superparamagnetic property that allows fast magnetic separation using an external magnet.

The process also allows the functionalization of nonspherical objects. As a demonstration, we have prepared Ag@SiO_2&MPS@γ-Fe_2O_3&QD multilayer composite nanowires by using this simple assembly processes. Silver nanowires were synthesized using a polyol process, coated with normal silica,[84] modified with MPS, and surface-immobilized with mixed nanoparticles of γ-Fe_2O_3 and QDs. Figure 4.10b shows the elemental distribution of Si, O, Fe, Ag, Cd, and Se, as analyzed by EDX mapping. Ag@SiO_2 cable-like structure can be easily identified by the strong Ag signal at the core and Si, O signals at the shell regions. The weaker but evenly distributed signals from Fe, Cd and Se prove the thin layer of immobilized γ-Fe_2O_3 and QDs. The uniform attachment of nanoparticles can be also clearly observed in the SEM image in Figure 4.10b and the TEM image in Figure 4.10a. This example demonstrates that multifunctional composites with nonspherical morphologies can be produced by coating nonspherical functional nanostructures with a mercapto-silica layer and then immobilizing nanoparticles on the surface. The expansion to nonspherical morphologies makes this assembly process truly unique in comparison to conventional methods.

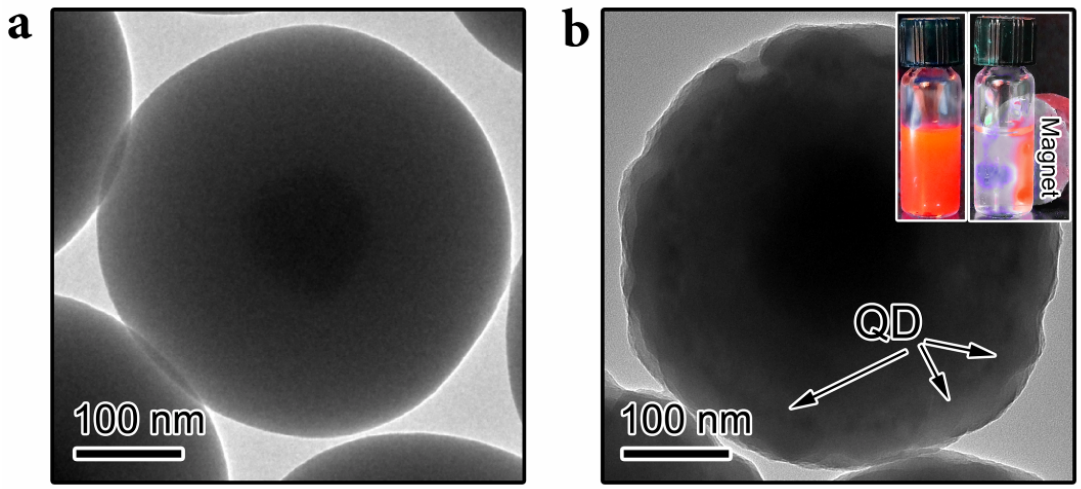

Figure 4.9 TEM images of (a) original Fe_3O_4@SiO_2 particles and (b) corresponding Fe_3O_4@SiO_2&MPS@CdSe@SiO_2 composite structures. The superparamagnetic Fe_3O_4 particles were synthesized using a high temperature precipitation reaction in the presence of polyacrylic acid (PAA), surface coated with normal silica using the Stöber process, modified with MPS layer, and then decorated with oleic acid-capped CdSe@CdZnS QDs, and then surface protected by another layer of normal SiO_2 with the assistance of CTAB surfactant. Insets are corresponding photographs of an aqueous dispersion of the composite particles excited by an ultraviolet lamp: the left sample is a normal dispersion while the right one is exposed to a magnetic field.

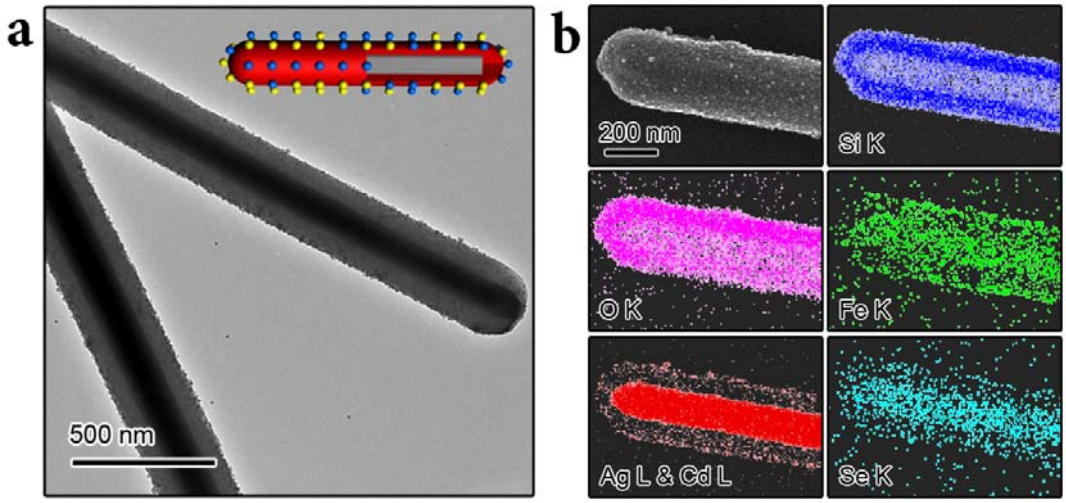

Figure 4.10 (a) TEM image of the Ag nanowire@SiO_2&MPS@CdSe&γ-Fe_2O_3 composite nanowires. The Ag nanowires were synthesized by using a polyol process in the presence of poly(vinyl pyrrolidone) (PVP), surface coated with normal silica using the Stöber process, modified with MPS layer, and then decorated with TOPO/oleylamine-capped CdSe and oleic acid-capped γ-Fe_2O_3 nanoparticles. Inset is a schematic illustration of the assembled structure. (b) SEM image and EDX mapping of the elemental distribution of Si, O, Fe, Cd and Se in the composite nanowire structures.

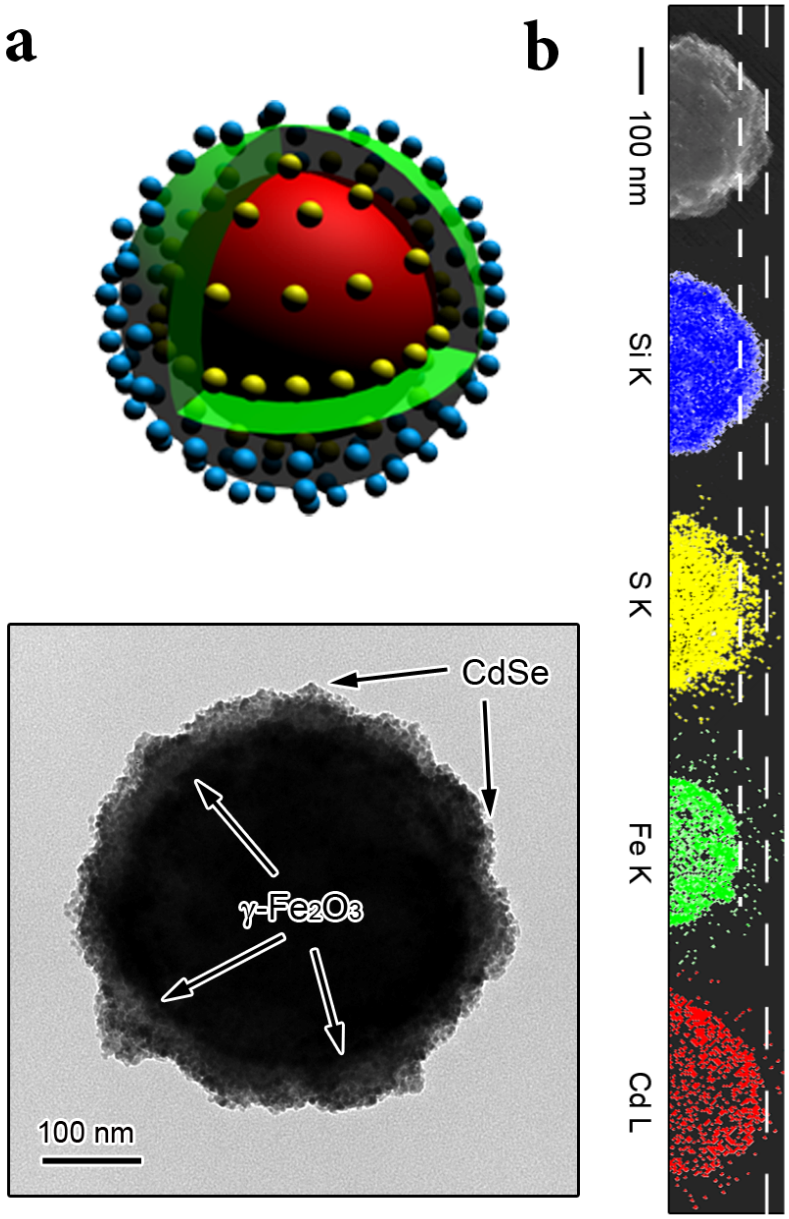

Figure 4.11 (a) Schematic illustration and TEM image of the MPS@γ-Fe_2O_3@SiO_2&MPS@CdSe multilayer composite, synthesized by sequential procedures including initial loading of oleic acid capped γ-Fe_2O_3 nanoparticles on MPS spheres, surface coated with normal silica using the Stöber process, modified with MPS layer, and then decorated with TOPO/oleylamine capped CdSe nanoparticles. (b) SEM images and EDX mapping of the elemental distribution of Si, S, Fe and Cd in the assembled structure.

Analogous to the LbL approach,[27-30] the assembly process here also allows multilayer assembly by repeating the nanoparticle immobilization, silica coating, and MPS modification procedures. As a demonstration, we started with MPS spheres (~300 nm in diameter), immobilized γ-Fe_2O_3 nanoparticles on the surface, overcoated with a thin SiO_2/MPS layer, and immobilized QDs on the surface again. Figure 4.11a shows a typical TEM image of the multilayer structure MPS@γ-Fe_2O_3@SiO_2&MPS@QD. The dark ring marked with the arrows is the layer of γ-Fe_2O_3 nanoparticles. The gray area outside this ring is the SiO_2&MPS layer with thickness of ~50 nm. QDs can be clearly seen on the sphere surface. This complex structure was further characterized by EDX elemental mapping, with results shown in Figure 4.11b. As indicated by the two dotted lines, the different locations of Fe and Cd (150 nm for Fe, 200 nm For Cd from the sphere's center) clearly suggests that the γ-Fe_2O_3 nanoparticles and QDs are distributed within different layers of the composite. The gap between these two nanoparticle layers is 50 nm which corresponds to the thickness of SiO_2&MPS layer. Interestingly, a strong S signal is also observed in this gap, indicating high loading of thiol groups in this layer. All these observations confirm the complex structure with multiple types of nanoparticles positioned at different layers. This multilayer assembly strategy not only provides the means to improve the loading capacity, but also makes it convenient to increase the number of functions while maintaining the loading density of each component.

4.4 Conclusion

We have developed a general process that allows convenient production of multifunctional colloidal particles by direct self-assembly of hydrophobic nanoparticles

on host nanostructures containing mercapto-silica surfaces. Although our focus here has been on the immobilization of hydrophobic nanoparticles as this has been a major challenge in the field, the developed process can be easily extended to the assembly of hydrophilic nanoparticles with minimal modifications. This universal, highly configurable, scalable and reproducible assembly process will help to produce various multifunctional structures for many important technological applications.

Reference

(1) Piao, Y.; Burns, A.; Kim, J.; Wiesner, U.; Hyeon, T. *Adv. Funct. Mater.* **2008**, *18*, 3745.

(2) Jun, Y.-W.; Lee, J.-H.; Cheon, J. *Angew. Chem., Int. Ed.* **2008**, *47*, 5122.

(3) Wu, S.-H.; Lin, Y.-S.; Hung, Y.; Chou, Y.-H.; Hsu, Y.-H.; Chang, C.; Mou, C.-Y. *ChemBioChem* **2008**, *9*, 53.

(4) Salgueiriño-Maceira, V.; Correa-Duarte, M. A. *Adv. Mater.* **2007**, *19*, 4131.

(5) Kim, J. S.; Rieter, W. J.; Taylor, K. M. L.; An, H.; Lin, W.; Lin, W. *J. Am. Chem. Soc.* **2007**, *129*, 8962.

(6) Rieter, W. J.; Kim, J. S.; Taylor, K. M. L.; An, H.; Lin, W.; Tarrant, T.; Lin, W. *Angew. Chem., Int. Ed.* **2007**, *46*, 3680.

(7) Liong, M.; Lu, J.; Kovochich, M.; Xia, T.; Ruehm, S. G.; Nel, A. E.; Tamanoi, F.; Zink, J. I. *ACS Nano* **2008**, *2*, 889.

(8) Suh, W. H.; Suh, Y.-H.; Stucky, G. D. *Nano Today* **2009**, *4*, 27.

(9) Yezhelyev, M. V.; Qi, L.; O'Regan, R. M.; Nie, S.; Gao, X. *J. Am. Chem. Soc.* **2008**, *130*, 9006.

(10) Han, M. Y.; Gao, X. H.; Su, J. Z.; Nie, S. *Nat. Biotechnol.* **2001**, *19*, 631.

(11) Sathe, T. R.; Agrawal, A.; Nie, S. M. *Anal. Chem.* **2006**, *78*, 5627.

(12) Shi, D. *Adv. Funct. Mater.* **2009**, *19*, 3356.

(13) Koole, R.; Mulder, W. J. M.; van Schooneveld, M. M.; Strijkers, G. J.; Meijerink, A.; Nicolay, K. *Wiley Interdiscip. Rev.: Nanomed. Nanobiotechnol.* **2009**, *1*, 475.

(14) Selvan, S. T.; Patra, P. K.; Ang, C. Y.; Ying, J. Y. *Angew. Chem., Int. Ed.* **2007**, *46*, 2448.

(15) Kim, J.; Lee, J. E.; Lee, J.; Yu, J. H.; Kim, B. C.; An, K.; Hwang, Y.; Shin, C.-H.; Park, J.-G.; Kim, J.; Hyeon, T. *J. Am. Chem. Soc.* **2006**, *128*, 688.

(16) Wilson, R.; Spiller, D. G.; Prior, I. A.; Veltkamp, K. J.; Hutchinson, A. *ACS Nano* **2007**, *1*, 487.

(17) Kim, J.; Park, S.; Lee, J. E.; Jin, S. M.; Lee, J. H.; Lee, I. S.; Yang, I.; Kim, J.-S.; Kim, S. K.; Cho, M.-H.; Hyeon, T. *Angew. Chem., Int. Ed.* **2006**, *45*, 7754.

(18) Spasova, M.; Salgueirino-Maceira, V.; Schlachter, A.; Hilgendorff, M.; Giersig, M.; Liz-Marzan, L. M.; Farle, M. *J. Mater. Chem.* **2005**, *15*, 2095.

(19) Shylesh, S.; Schuenemann, V.; Thiel, W. R. *Angew. Chem., Int. Ed.* **2010**, *49*, 3428.

(20) Ge, J.; Zhang, Q.; Zhang, T.; Yin, Y. *Angew. Chem., Int. Ed.* **2008**, *47*, 8924.

(21) Xuan, S.; Wang, Y.-X. J.; Yu, J. C.; Leung, K. C.-F. *Langmuir* **2009**, *25*, 11835.

(22) Lee, K. S.; Woo, M. H.; Kim, H. S.; Lee, E. Y.; Lee, I. S. *Chem. Commun.* **2009**, 3780.

(23) Ge, J.; Huynh, T.; Hu, Y.; Yin, Y. *Nano Lett.* **2008**, *8*, 931.

(24) Cho, M.; Lim, K.; Woo, K. *Chem. Commun.* **2010**, *46*, 5584.

(25) Kim, J.; Piao, Y.; Hyeon, T. *Chem. Soc. Rev.* **2009**, *38*, 372.

(26) Cheon, J.; Lee, J. H. *Acc. Chem. Res.* **2008**, *41*, 1630.

(27) Kotov, N. A.; Dekany, I.; Fendler, J. H. *J. Phys. Chem.* **1995**, *99*, 13065.

(28) Caruso, F.; Spasova, M.; Salgueirino-Maceira, V.; Liz-Marzan, L. M. *Adv. Mater.* **2001**, *13*, 1090.

(29) Caruso, F.; Susha, A. S.; Giersig, M.; Mohwald, H. *Adv. Mater.* **1999**, *11*, 950.

(30) Hong, X.; Li, J.; Wang, M.; Xu, J.; Guo, W.; Li, J.; Bai, Y.; Li, T. *Chem. Mater.* **2004**, *16*, 4022.

(31) Stoeva, S. I.; Huo, F.; Lee, J.-S.; Mirkin, C. A. *J. Am. Chem. Soc.* **2005**, *127*, 15362.

(32) Kim, J.; Lee, J. E.; Lee, J.; Jang, Y.; Kim, S.-W.; An, K.; Yu, J. H.; Hyeon, T. *Angew. Chem., Int. Ed.* **2006**, *45*, 4789.

(33) Wang, Z.; Zhao, Z.; Zhang, J.; Li, Z.; Gao, Y.; Wang, C.; Zhang, H.; Yang, B. *J. Colloid Interface Sci.* **2009**, *339*, 83.

(34) Lee, J.-H.; Jun, Y.-w.; Yeon, S.-I.; Shin, J.-S.; Cheon, J. *Angew. Chem., Int. Ed.* **2006**, *45*, 8160.

(35) Wang, C. G.; Chen, J.; Talavage, T.; Irudayaraj, J. *Angewandte Chemie-International Edition* **2009**, *48*, 2759.

(36) Hyeon, T.; Lee, S. S.; Park, J.; Chung, Y.; Na, H. B. *J. Am. Chem. Soc.* **2001**, *123*, 12798.

(37) Sun, S.; Zeng, H.; Robinson, D. B.; Raoux, S.; Rice, P. M.; Wang, S. X.; Li, G. *J. Am. Chem. Soc.* **2004**, *126*, 273.

(38) Yin, Y.; Alivisatos, A. P. *Nature* **2005**, *437*, 664.

(39) Murray, C. B.; Norris, D. J.; Bawendi, M. G. *J. Am. Chem. Soc.* **1993**, *115*, 8706.

(40) Park, J.; An, K.; Hwang, Y.; Park, J.-G.; Noh, H.-J.; Kim, J.-Y.; Park, J.-H.; Hwang, N.-M.; Hyeon, T. *Nat. Mater.* **2004**, *3*, 891.

(41) Talapin, D. V.; Rogach, A. L.; Kornowski, A.; Haase, M.; Weller, H. *Nano Lett.* **2001**, *1*, 207.

(42) Jun, Y.-w.; Huh, Y.-M.; Choi, J.-s.; Lee, J.-H.; Song, H.-T.; Kim, S.; Yoon, S.; Kim, K.-S.; Shin, J.-S.; Suh, J.-S.; Cheon, J. *J. Am. Chem. Soc.* **2005**, *127*, 5732.

(43) Bruchez, M., Jr.; Moronne, M.; Gin, P.; Weiss, S.; Alivisatos, A. P. *Science* **1998**, *281*, 2013.

(44) Chan, W. C. W.; Nie, S. *Science* **1998**, *281*, 2016.

(45) Mattoussi, H.; Mauro, J. M.; Goldman, E. R.; Anderson, G. P.; Sundar, V. C.; Mikulec, F. V.; Bawendi, M. G. *J. Am. Chem. Soc.* **2000**, *122*, 12142.

(46) Talapin, D. V.; Rogach, A. L.; Mekis, I.; Haubold, S.; Kornowski, A.; Haase, M.; Weller, H. *Colloids Surf., A* **2002**, *202*, 145.

(47) Xie, J.; Huang, J.; Li, X.; Sun, S.; Chen, X. *Curr. Med. Chem.* **2009**, *16*, 1278.

(48) Schreiber, F. *Prog. Surf. Sci.* **2000**, *65*, 151.

(49) Liu, G.; Rodriguez, J. A.; Chang, Z.; Hrbek, J.; Gonzalez, L. *J. Phys. Chem. B* **2002**, *106*, 9883.

(50) Perkins, C. L. *J. Phys. Chem. C* **2009**, *113*, 18276.

(51) Sadik, P. W.; Pearton, S. J.; Norton, D. P.; Lambers, E.; Ren, F. *J. Appl. Phys.* **2007**, *101*, 104514.

(52) Liu, F.; Quan, B.; Liu, Z.; Chen, L. *Mater. Chem. Phys.* **2005**, *93*, 301.

(53) Lim, H.; Carraro, C.; Maboudian, R.; Pruessner, M. W.; Ghodssi, R. *Langmuir* **2003**, *20*, 743.

(54) Yamamoto, H.; Butera, R. A.; Gu, Y.; Waldeck, D. H. *Langmuir* **1999**, *15*, 8640.

(55) Petrovykh, D. Y.; Smith, J. C.; Clark, T. D.; Stine, R.; Baker, L. A.; Whitman, L. J. *Langmuir* **2009**, *25*, 12185.

(56) Tanzer, T. A.; Bohn, P. W.; Roshchin, I. V.; Greene, L. H.; Klem, J. F. *Appl. Phys. Lett.* **1999**, *75*, 2794.

(57) Voznyy, O.; Dubowski, J. J. *J. Phys. Chem. C* **2008**, *112*, 3726.

(58) McGuiness, C. L.; Diehl, G. A.; Blasini, D.; Smilgies, D.-M.; Zhu, M.; Samarth, N.; Weidner, T.; Ballav, N.; Zharnikov, M.; Allara, D. L. *ACS Nano* **2010**, *4*, 3447.

(59) Buckley, A. N.; Goh, S. W.; Lamb, R.; Fan, L.-J.; Yang, Y.-W. *ECS Trans.* **2006**, *2*, 107.

(60) Hu, K.; Brust, M.; Bard, A. J. *Chem. Mater.* **1998**, *10*, 1160.

(61) Colvin, V. L.; Goldstein, A. N.; Alivisatos, A. P. *J. Am. Chem. Soc.* **1992**, *114*, 5221.

(62) Mann, J. R.; Watson, D. F. *Langmuir* **2007**, *23*, 10924.

(63) Lee, Y. L.; Huang, B. M.; Chien, H. T. *Chem. Mater.* **2008**, *20*, 6903.

(64) Pichon, B. P.; Demortiere, A.; Pauly, M.; Mougin, K.; Derory, A.; Begin-Colin, S. *J. Phys. Chem. C* **2010**, *114*, 9041.

(65) Nakamura, T.; Yamada, Y.; Yano, K. *J. Mater. Chem.* **2007**, *17*, 3726.

(66) Westcott, S. L.; Oldenburg, S. J.; Lee, T. R.; Halas, N. J. *Langmuir* **1998**, *14*, 5396.

(67) Claesson, E. M.; Philipse, A. P. *Langmuir* **2005**, *21*, 9412.

(68) Claesson, E. M.; Philipse, A. P. *Colloids Surf., A* **2007**, *297*, 46.

(69) Lu, Z. D.; Goebl, J.; Ge, J. P.; Yin, Y. D. *J. Mater. Chem.* **2009**, *19*, 4597.

(70) Peng, Z. A.; Peng, X. *J. Am. Chem. Soc.* **2002**, *124*, 3343.

(71) Joo, J.; Yu, T.; Kim, Y. W.; Park, H. M.; Wu, F.; Zhang, J. Z.; Hyeon, T. *J. Am. Chem. Soc.* **2003**, *125*, 6553.

(72) Li, Z. Q.; Zhang, Y.; Jiang, S. *Adv. Mater.* **2008**, *20*, 4765.

(73) Park, J.; Kang, E.; Son, S. U.; Park, H. M.; Lee, M. K.; Kim, J.; Kim, K. W.; Noh, H. J.; Park, J. H.; Bae, C. J.; Park, J. G.; Hyeon, T. *Adv. Mater.* **2005**, *17*, 429.

(74) Wang, Y.; Hu, Y.; Zhang, Q.; Ge, J.; Lu, Z.; Hou, Y.; Yin, Y. *Inorg. Chem.* **2010**, *49*, 6601.

(75) Trentler, T. J.; Denler, T. E.; Bertone, J. F.; Agrawal, A.; Colvin, V. L. *J. Am. Chem. Soc.* **1999**, *121*, 1613.

(76) Joo, J.; Kwon, S. G.; Yu, T.; Cho, M.; Lee, J.; Yoon, J.; Hyeon, T. *J. Phys. Chem. B* **2005**, *109*, 15297.

(77) Carion, O.; Mahler, B.; Pons, T.; Dubertret, B. *Nat. Protocols* **2007**, *2*, 2383.

(78) Brust, M.; Walker, M.; Bethell, D.; Schiffrin, D. J.; Whyman, R. *Chem. Commun.* **1994**, 801.

(79) Nakamura, M.; Ishimura, K. *J. Phys. Chem. C* **2007**, *111*, 18892.

(80) Lu, Z.; Sun, L.; Nguyen, K.; Gao, C.; Yin, Y. *Langmuir* **2011**, *27*, 3372.

(81) Leatherdale, C. A.; Woo, W. K.; Mikulec, F. V.; Bawendi, M. G. *J. Phys. Chem. B* **2002**, *106*, 7619.

(82) Ge, J. P.; Yin, Y. D. *Adv. Mater.* **2008**, *20*, 3485.

(83) Ge, J. P.; Hu, Y. X.; Biasini, M.; Beyermann, W. P.; Yin, Y. D. *Angewandte Chemie-International Edition* **2007**, *46*, 4342.

(84) Yin, Y.; Lu, Y.; Sun, Y.; Xia, Y. *Nano Lett.* **2002**, *2*, 427.

(85) Sun, S.; Murray, C. B.; Weller, D.; Folks, L.; Moser, A. *Science* **2000**, *287*, 1989.

(86) Insin, N.; Tracy, J. B.; Lee, H.; Zimmer, J. P.; Westervelt, R. M.; Bawendi, M. G. *ACS Nano* **2008**, *2*, 197.

(87) Guerrero-Martinez, A.; Perez-Juste, J.; Liz-Marzan, L. M. *Adv. Mater.* **2010**, *22*, 1182.

(88) Yi, D. K.; Selvan, S. T.; Lee, S. S.; Papaefthymiou, G. C.; Kundaliya, D.; Ying, J. Y. *J. Am. Chem. Soc.* **2005**, *127*, 4990.

(89) Stober, W.; Fink, A.; Bohn, E. *J. Colloid Interface Sci.* **1968**, *26*, 62.

(90) Gorelikov, I.; Matsuura, N. *Nano Lett.* **2008**, *8*, 369.

(91) Caregnato, P.; Forbes, M. D. E.; Soria, D. B.; Martire, D. O.; Gonzalez, M. C. *J. Phys. Chem. C* **2010**, *114*, 5080.

Chapter 5

Nanocrystal Clusters for Enrichment of Low-Abundance Peptides and Proteins

5.1 Introduction

Peptide mapping by matrix-assisted laser desorption/ionization time-of-flight (MALDI-TOF) mass spectrometry is a powerful tool in current protein analysis.[1] The MALDI technique, however, is still insufficient for the detection of low-abundance peptides or proteins extracted from biosamples because its performance deteriorates markedly for samples containing multiple components and excessive amounts of salts.[2, 3] To address this issue, a number of affinity probes have been developed to separate and enrich low-abundance peptides/proteins from the sample solution prior to mass analysis, such as mesoprous silica particles,[4] zeolite nanocrystals,[5] diamond nanoparticles,[3] C_{60}-fuctionalized silica microspheres,[6] polymer beads,[7] and n-alkyl (C4, C8 and C18) modified column materials.[8, 9] Reverse-phase chromatographic techniques, typically using n-alkyl bonded silica microbeads as adsorbents, can enrich peptides/proteins through hydrophobic-hydrophobic interactions. In principle, higher separation efficiency can be achieved by employing smaller particles especially nanoparticles as the stationary phase in the column, however, this has been extremely challenging as the required pressure increases by the inverse of the particle diameter squared.[10, 11] As a result, although nanoparticles can now be routinely prepared in high quality for materials with various compositions,[12-14] their merits such as high specific surface area and fast binding to biomolecules have not been fully taken advantage of in conventional chromatographic methods.[15] On the other hand, magnetic materials used as affinity probes have received

increasing attention recently due to the ease of isolation of the magnetic material-target conjugates from the sample solution based on their magnetic properties.[16-19] For example, n-alkyl chain modified magnetic microspheres have been demonstrated for the facile enrichment of peptides and proteins from solutions.[20] However, direct use of n-alkyl functionalized nanometer sized magnetic particles for bio-separation has been seldom reported, probably due to the complicate processes involved for modifying the pre-synthesized nanoparticles with a high density coverage of n-alkyl chains, the insolubility of the nanoparticles in water due to their hydrophobic surfaces, and the inefficient magnetic separation as the result of their small magnetic moment.

Herein we demonstrate a novel cluster structure for highly efficient enrichment of peptides and proteins based on hydrophobic-hydrophobic interactions between the protection ligands of the nanocrystals and the analytes. As schematically illustrated in Figure 5.1, superparamagnetic iron oxide (γ-Fe_2O_3) nanocrystals are prepared using the well-known thermolysis reaction in a hot organic solvent,[12] then assembled into clusters with diameters ranging from 50-200 nm in an oil-in-water emulsion, and finally used for hydrophobic-interaction-based affinity separation. No additional steps are required to bind n-alkyl chains to the magnetic nanoparticles because a layer of protection ligands containing alkyl chains is naturally formed around the nanocrystals during the synthesis process. After assembly in emulsion droplets, the clusters containing hydrophobic nanocrystals are well-dispersed in water and thus suitable for applications in bio-separation. The submicron size of the clusters and the three dimensional particle networks inside enable fast diffusion and adsorption of target protein and peptides.[21] In

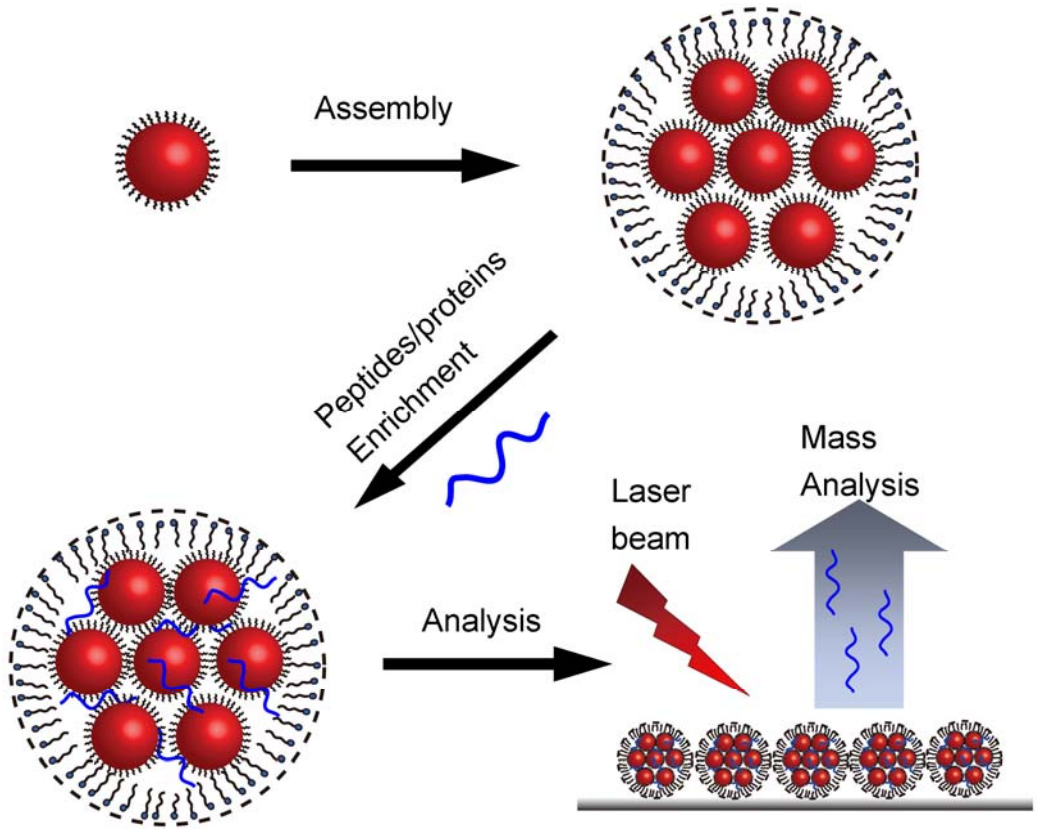

Figure 5.1 (a) Schematic illustration showing the procedure of self-assembly of hydrophobic nanoparticles on MPS spheres. (b) TEM images of oleic acid capped γ-Fe_2O_3 nanoparticles, (c) MPS spheres and (d) γ-Fe_2O_3 nanoparticles assembled on the surface of MPS spheres.

addition, the clustering of nanocrystals results in a higher saturation magnetization and significantly stronger magnetic responses than individual ones, allowing their efficient removal from the analyte solution after selective adsorption by using an external magnetic field.[22]

5.2 Experimental Section

5.2.1 Materials

Oleic acid, iron pentacarbonyl ($Fe(CO)_5$), dioctyl ether, sodium dodecyl sulfate (SDS), trifluoroacetic acid (TFA), α-cyano-4-hydroxycinnamic acid (CHCA), cytochrome c, bovine serum albumin (BSA, fraction V) and trypsin were purchased from Aldrich Chemical Co. Angiotensin II was obtained from VWR. Ethanol, cyclohexane, acetonitrile and HyperSep^{TM} C18 Tip (TipC18) were obtained from Fisher Scientific. All solutions were prepared in deionized water (18 MΩ) from a Milli.Q^{TM} water purification system (Millipore, Billerica, MA, USA).

5.2.2 Synthesis of γ-Fe_2O_3 Nanocrystals

Superparamagnetic γ-Fe_2O_3 nanocrystals were synthesized using a thermolysis process. $Fe(CO)_5$ (0.2 mL, 1.52 mmol) was added to a mixture containing 10 mL of octyl ether and 1.28 g of oleic acid at 100 ^oC. Then the solution was heated to 290 °C under an argon atmosphere and maintained at this temperature for 1 h. After being cooled down to 200 ^oC, the solution was bubbled with air for 2 hours. After cooling down to room temperature, the solution was added ethanol to precipitate γ-Fe_2O_3 nanoparticles, which were then separated by centrifugation and redispersed in 10 mL cyclohexane.

5.2.3 Self-assembly of Nanocrystals to Colloidal Clusters

In a typical experiment, a cyclohexane solution of γ-Fe_2O_3 nanocrystals (1 mL) was mixed with an aqueous solution of SDS (56 mg in 10 mL H_2O) under sonication for 5~10 minutes. The mixture was then heated to 70 – 72 ^oC in a water bath for 4 hours. A clear nanoparticle "micelle" solution was obtained after evaporation of cyclohexane. The final products were washed with water three times and re-dispersed in 2 mL of water.

5.2.4 Tryptic Digests of Proteins

BSA (1 mg/mL, 1 mL) was mixed with trypsin (1 mg/mL, 20 μL) in aqueous ammonium bicarbonate (50 mM, pH = 8) and incubated at 37 ^oC for 24 hours. The resulting peptide mixtures were stored at -20 ^oC until further use.

5.2.5 Selective Enrichment of Peptides/Proteins Using the Clusters

In a typical process, a suspension of nanocrystal clusters (10 μL, 10 mg/mL) was added into 500 μL of standard peptide, protein or protein digest at varied concentrations. (Angiotensin II (8 nM), cytochrome C (500 nM) and peptide mixture originating from tryptic digestion of BSA (6 nM)). Then the mixture was shaken at room temperature for 30 minutes. The peptide or protein-loaded clusters were collected by external magnet and washed with 100 μL of water three times. After that, 1 μL of CHCA aqueous solution (1 mg/mL, 50% acetonitrile and 0.1% TFA) was mixed with the obtained clusters. Finally, 0.5 μL of above slurry was deposited on the MALDI plate and applied for MALDI-TOF MS analysis.

5.2.6 Sample Preparation Using Commercial TipC18

The sample preparation of peptides using commercial Hypersep^{TM} C18 pipette tips was performed according to the standard procedure provided by the technical note from Thermo Scientific Corporation.

5.2.7 Structure Characterization

The morphology of the nanostructures was investigated using a Philips Tecnai 12 transmission electron microscope (TEM). Dynamic light scattering (DLS) and zeta potential analysis were performed on a ZetaPALS system.

5.2.8 MALDI-TOF MS

Matrix assisted laser desorption/ionization mass spectra were obtained by using a Voyager-DE STR MALDI-TOF mass spectrometer (Applied Biosystems, Framingham, MA, USA) operating in positive reflector mode. The spectrometer is equipped with a pulsed nitrogen laser operated at 337 nm with 3 ns duration pulses. Mass spectra were acquired as an average of 100 laser shots. Peptide mass mapping was carried out by comparing the mass spectra with the protein sequence database in ExPASy.

5.3 Results and Discussion

Superparamagnetic γ-Fe_2O_3 nanocrystals with an average diameter of ~15 nm were prepared by a thermolysis process (Figure 5.2).[23] The resulting nanocrystals were covered with a monolayer of protection ligands of oleic acid which made the particles hydrophobic and dispersible in nonpolar solvents such as toluene, chloroform and

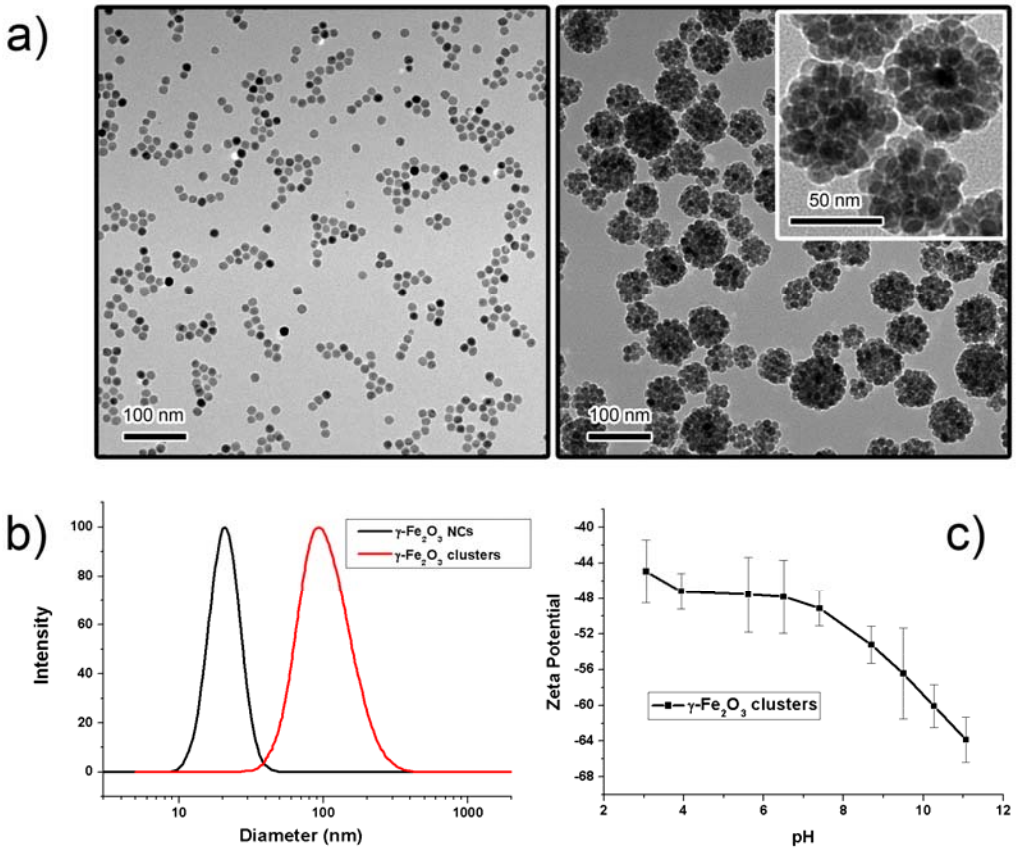

Figure 5.2 (a) TEM images of γ-Fe_2O_3 nanocrystals and corresponding clusters of assembled nanocrystals. Inset is a high magnification TEM image. (b) Size distributions of γ-Fe_2O_3 nanocrystals and clusters analyzed by dynamic light scattering. (c) Zeta-potential of γ-Fe_2O_3 clusters at different pH values.

cyclohexane. Following a previously reported method,[21, 24] densely packed clusters of the γ-Fe_2O_3 nanocrystals were prepared using oil-in-water emulsion droplets as templates followed by evaporation of the volatile solvent. The surfactant sodium dodecyl sulfate (SDS), which was used as the emulsifier in the process, was adsorbed onto the cluster surface through the hydrophobic-hydrophobic interactions between the SDS tails and the protection ligands (oleic acid) on the packed γ-Fe_2O_3 nanocrystals. The negatively charged head of SDS ($–SO_3^-$) helps the clusters disperse stably in water. After incubation with the nanocrystal clusters in water solution, peptides and proteins could be effectively enriched on these clusters, which subsequently could form a homogeneous layer on a MALDI plate with the matrix and did not hinder cocrystallization of the matrix and peptides/proteins. Therefore, the significance of our material lies in its utilization of the high affinity between the tails of oleic acid and peptides/proteins, the good water dispersability of the clusters, the facility of the magnetic separation, and the direct MALDI-TOF mass analysis to avoid unnecessary loss of sample during the process.

Typical transmission electron microscopy (TEM) images of γ-Fe_2O_3 nanocrystals and their corresponding clusters are shown in Figure 5.2a. The high-magnification image in the inset clearly shows that the clusters are composed of densely packed γ-Fe_2O_3 nanocrystals. Due to the non-uniformity of the emulsion droplets, the sizes of the clusters range from 50 nm to 200 nm, as confirmed by both TEM observations and dynamic light scattering (DLS) analyses (Figure 5.2b). Because clusters of superparamagnetic nanocrystals possess a higher saturation magnetization than individual particles,[22] the clusters can easily be isolated from solution within several minutes using an external

magnetic field. Zeta-potential analyses were performed to understand the surface charge characteristics of the clusters and to optimize the conditions of the enrichment method. As pH value is one of the primary factors influencing the surface property of the clusters, the zeta potential was examined by varying pH between 3 and 11. As shown in Figure 5.2c, the surface of the nanocrystal clusters was always negatively charged because of the presence of SDS around the clusters. With decreasing pH, the negative charge also decreased. When the pH rose from 8 to 11, the negative charge increased dramatically to the point that it might generate a high enough electrostatic force to prevent analytes from being adsorbed onto the clusters. Therefore, a pH range between 4 and 7 was selected for use during peptide and protein enrichment.

The enrichment efficiency of the γ-Fe_2O_3 nanocrystal clusters for protein/peptide analysis was studied using angiotensin II and cytochrome c as models. In a typical experiment, the clusters were incubated with the peptide or protein solution for 30 min at room temperature and then separated from the supernatant by applying a NdBFe magnet, followed by water rinsing three times. Then the peptide-loaded clusters were mixed with the matrix solution of α-cyano-4-hydroxycinnamic acid (α-CHCA) and applied to the MALDI target directly. Figure 5.3 shows the MALDI-TOF mass spectra for 8 nM Angiotensin II and 500 nM cytochrome c before and after enrichment with the clusters. For comparison, the peptide solution after treatment with individual γ-Fe_2O_3 nanocrystals and commercial HyperSep^{TM} C18 pipette tip (TipC18) were also analyzed by MALDI-TOF mass under the same experimental conditions. Angiotensin II consists of a linear chain composed of eight amino acids (DRVYIHPF), most of which are hydrophobic.[20]

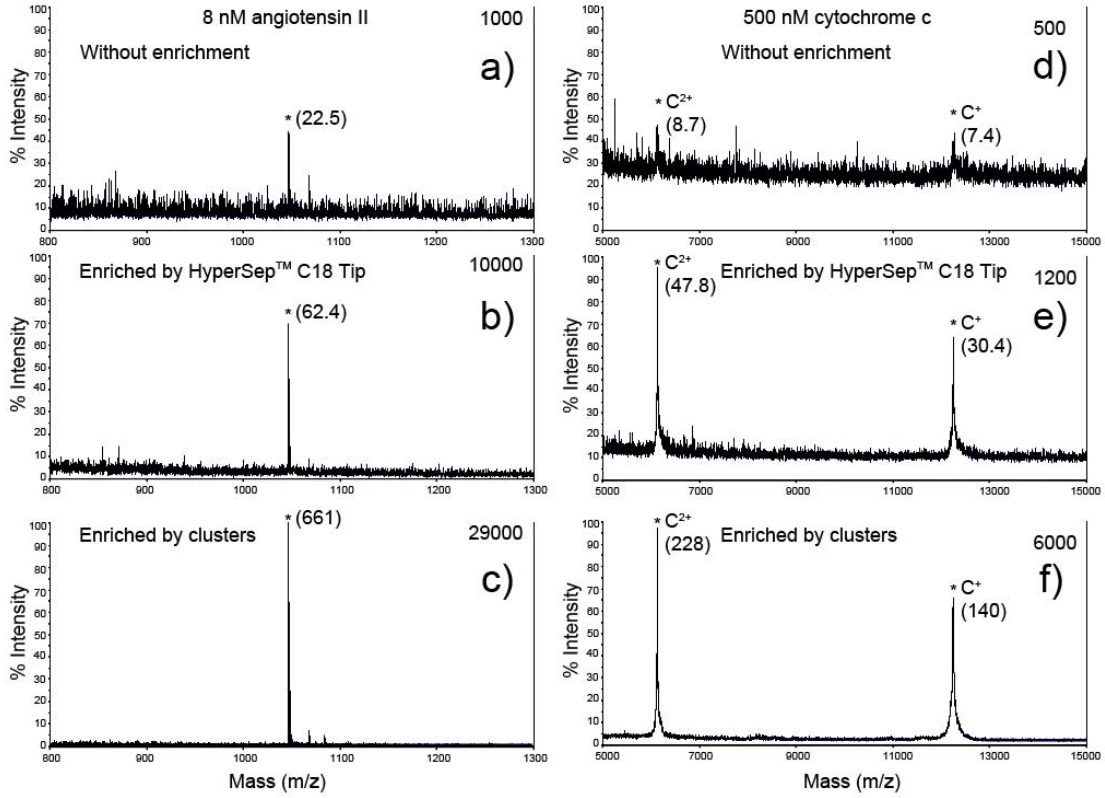

Figure 5.3 MALDI-TOF mass spectra of angiotensin II (left column) and cytochrome c (right column) before (a,d) and after enrichment by commercial HyperSep™ C18 Tip (b,e) and γ-Fe_2O_3 nanocrystal clusters (c,f). The peaks marked with asterisks represent angiotensin II (Mw: 1046.2); C^+ (Mw: 12242) and C^{2+} (Mw: 6121) correspond to the singly and doubly charged peaks of cytochrome c. The S/N ratios are indicated in parentheses.

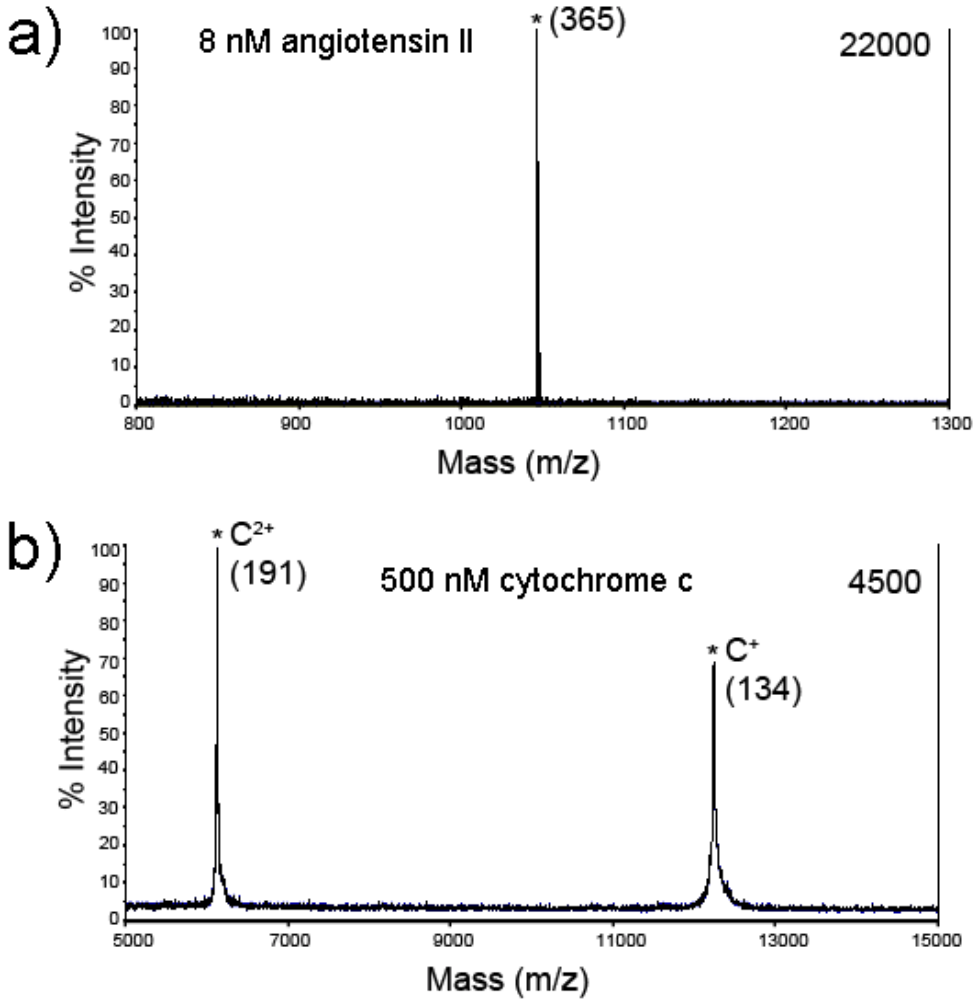

Figure 5.4 MALDI-TOF mass spectra of (a) angiotensin II (8 nM solution containing 100 mM of $CaCl_2$) and (b) cytochrome c (500 nM solution containing 100 mM of $CaCl_2$) after enrichment with the γ-Fe_2O_3 nanocrystal clusters.

As shown in Figure 5.3a, without enrichment the mass intensity was weak and the S/N ratio was only 22.5. Commercial TipC18 could also concentrate the peptide, but the overall signal was low and the S/N ratio of the peak was only 62.4 (Figure 5.3b). This could be ascribed to the relatively low adsorption capacity of the packing materials in the pipette tip. No obvious peaks could be observed after enrichment with primary γ-Fe_2O_3 nanocrystals because the γ-Fe_2O_3 nanocrystals were covered with a monolayer of oleic acid and thus not dispersible in water. After enrichment with the γ-Fe_2O_3 nanocrystal clusters, the peak of the peptide became clearly apparent with a very high intensity and the S/N ratio increased to 661. This indeed indicates that the clusters do have excellent enrichment effects for the hydrophobic peptides. In a naturally obtained biosample, desalting steps are normally required for a satisfactory analysis because the presence of salts can severely upset the MALDI process and result in poor mass spectra. The influence of salt on enrichment with the clusters was investigated in a peptide solution containing 100 mM $CaCl_2$. (Figure 5.4) The mass spectra results show that after enrichment with the clusters, strong signals with high S/N ratio could be still observed even of the original sample contained a high concentration of salt.

The clusters were also successfully used to enrich cytochrome c. The peak intensity and S/N ratio of cytochrome c increased by about two orders of magnitude after enrichment with the clusters (Figure 5.3d, f). For comparison, TipC18 could also increase the signal, but not as effectively as the clusters (Figure 5.3e). These tests demonstrate that the γ-Fe_2O_3 nanocrystal clusters are excellent candidates for the enrichment of hydrophobic peptides and proteins.

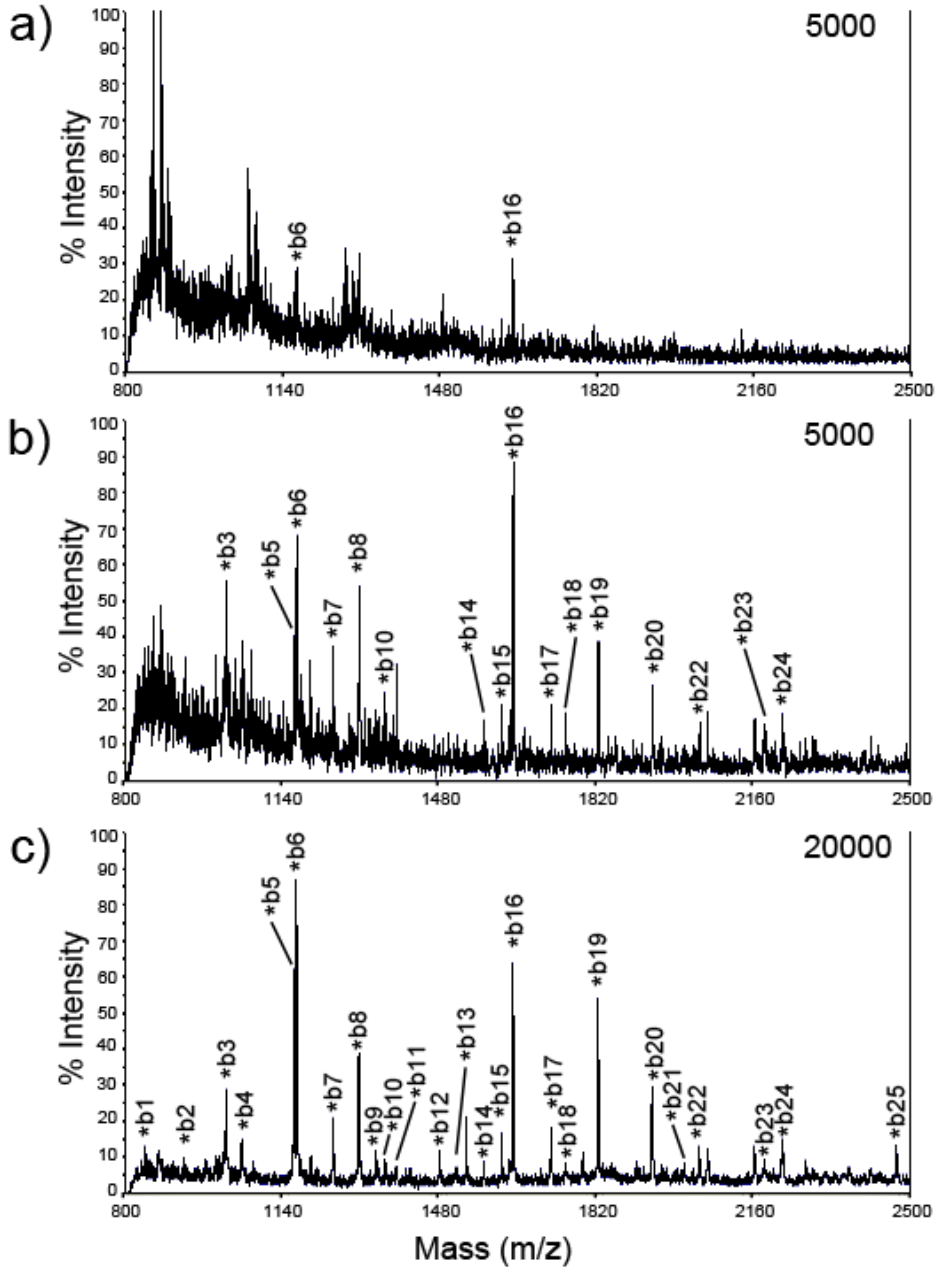

Figure 5.5 MALDI-TOF mass spectra of: (a) a normal BSA digest (6 nM), (b) BSA digest (60 nM), and (c) BSA digest (6 nM) enriched with γ-Fe_2O_3 nanocrystal clusters. Asterisks mark the peaks of the observed BSA fragments.

Table 5.1 Peptide peaks of detected peptides from tryptic digests of BSA by MALDI-TOF mass analysis.

Peak No	Theroretical mono $[M+H]^+$	Theroretical av. $[M+H]^+$	Observed $[M+H]^+$	Sequence
b1	841.5	842.0	841.9	LCVLHEK
b2	927.5	928.1	927.8	YLYEIAR
b3	1015.5	1016.2	1018.0	SHCIAEVEK
b4	1052.5	1053.2	1052.9	CCTKPESER
b5	1163.6	1164.3	1164.0	LVNELTEFAK
b6	1069.5	1070.2	1171.0	EACFAVEGPK
b7	1249.6	1250.4	1250.0	FKDLGEEHFK
b8	1305.7	1306.5	1306.1	HLVDEPQNLIK
b9	1349.5	1350.5	1349.7	TCVADESHAGCEK
b10	1362.7	1363.6	1363.0	SLHTLFGDELCK
b11	1388.6	1389.5	1388.0	EYEATLEECCAK
b12	1479.8	1480.7	1482.2	LGEYGFQNALIVR
b13	1511.8	1512.7	1513.4	VPQVSTPTLVEVSR
b14	1578.6	1579.7	1577.1	ECCHGDLLECADDR
b15	1616.7	1617.8	1616.1	QEPERNECFLSHK
b16	1640.0	1640.9	1640.4	KVPQVSTPTLVEVSR
b17	1723.8	1724.9	1722.2	DAFLGSFLYEYSRR
b18	1756.7	1758.0	1756.3	CCAADDKEACFAVEGPK
b19	1823.9	1825.1	1825.4	RPCFSALTPDETYVPK
b20	1942.8	1944.2	1942.3	VHKECCHGDLLECADDR
b21	2003.8	2005.2	2003.3	ETYGDMADCCEKQEPER
b22	2045.0	2046.3	2044.3	RHPYFYAPELLYYANK
b23	2174.0	2175.5	2173.4	ECCDKPLLEKSHCIAEVEK
b24	2220.1	2221.6	2223.5	LFTFHADICTLPDTEKQIK
b25	2472.2	2473.8	2471.9	QNCDQFEKLGEYGFQNALIVR

To further evaluate the effectiveness of the nanocrystal clusters for general peptide analysis, tryptic BSA digests were enriched using these clusters and then analyzed by MALDI-TOF mass. Figure 5.5 compares the MALDI-TOF MS spectra of the protein digests before and after enrichment by the clusters. Without pre-enrichment, only two peptides could be detected in BSA digests at a concentration of 6 nM (Figure 5.5a), and about sixteen peptides could be marked when the concentration was increased to 60 nM (Figure 5.5b). After enrichment using the γ-Fe_2O_3 nanocrystal clusters, twenty-five peptides could be identified from 6 nM BSA digests with sequence coverage of 47%, clearly showing the effectiveness of the peptide enrichment (Figure 5.5c). The detailed information of the detected phosphopeptides is listed in the Table 5.1. Again, these comparisons confirm the nanocrystal clusters' excellent enrichment power for peptides at trace levels.

5.4 Conclusion

In conclusion, we have demonstrated the highly efficient enrichment of peptides and proteins using γ-Fe_2O_3 nanocrystal clusters prepared through a general self-assembly process. Thanks to the high coverage of oleic acid ligands on primary nanocrystals and the high saturation magnetization of the clusters, the enrichment process is very simple, fast and efficient. In addition, the cluster structures show several other merits for protein/peptide enrichment: 1) they can be well dispersed in water; 2) their submicron size (50~200 nm) enables fast diffusion and adsorption of target peptides; 3) the cluster structure does not hinder cocrystallization of the matrix and peptides/proteins; 4) the co-concentration of salts can be avoided; 5) the surfactant and protection ligands in the

cluster are all small molecules, so that their mass signals do not disturb the analysis of peptides and proteins. As a result, peptide-loaded clusters can be directly deposited on the MALDI plate to avoid unnecessary loss of sample during the mass process. With all of these features, the nanocrystal clusters indeed represent a new class of materials that may find broad applications in biological sample preparation and detection.

Reference

(1) Fields, S., *Science* **2001,** 291, 1221-1224.

(2) Xu, Y. D.; Bruening, M. L.; Watson, J. T., *Mass Spectrom. Rev.* **2003,** 22, 429-440.

(3) Kong, X. L.; Huang, L. C. L.; Hsu, C. M.; Chen, W. H.; Han, C. C.; Chang, H. C., *Anal. Chem.* **2005,** 77, 259-265.

(4) Zuo, C.; Yu, W. J.; Zhou, X. F.; Zhao, D. Y.; Yang, P. Y., *Rapid Commun. Mass Spectrom.* **2006,** 20, 3139-3144.

(5) Zhang, Y. H.; Wang, X. Y.; Shan, W.; Wu, B. Y.; Fan, H. Z.; Yu, X. J.; Tang, Y.; Yang, P. Y., *Angew. Chem. Int. Ed.* **2005,** 44, 615-617.

(6) Chen, H. M.; Qi, D. W.; Deng, C. H.; Yang, P. Y.; Zhang, X. M., *Proteomics* **2009,** 9, 380-387.

(7) Xiong, H. M.; Guan, X. Y.; Jin, L. H.; Shen, W. W.; Lu, H. J.; Xia, Y. Y., *Angew. Chem. Int. Ed.* **2008,** 47, 4204-4207.

(8) Rochat, B.; Bolay, S.; Pascual, A.; Calandra, T.; Marchetti, O., *J. Mass Spectrom.* **2007,** 42, 440-449.

(9) Pettersson, S. W.; Persson, B. S.; Nystrom, M., *Journal of Chromatography B-Analytical Technologies in the Biomedical and Life Sciences* **2004,** 803, 159-165.

(10) Xiang, Y.; Liu, Y.; Lee, M. L., *J. Chromatogr. A* **2006,** 1104, 198.

(11) Horvath, C. G.; Preiss, B. A.; Lipsky, S. R., *Anal. Chem.* **1967,** 39, 1422.

(12) Yin, Y.; Alivisatos, A. P., *Nature* **2005,** 437, 664.

(13) Tao, A. R.; Habas, S.; Yang, P., *Small* **2008,** 4, 310-325.

(14) Park, J.; Joo, J.; Kwon, S. G.; Jang, Y.; Hyeon, T., *Angewandte Chemie International Edition* **2007,** 46, 4630-4660.

(15) Penn, S. G.; He, L.; Natan, M. J., *Curr. Opin. Chem. Biol.* **2003,** 7, 609-615.

(16) Chen, H. M.; Deng, C. H.; Zhang, X. M., *Angew. Chem. Int. Ed.* **2010,** 49, 607-611.

(17) Li, J. D.; Zhao, X. L.; Shi, Y. L.; Cai, Y. Q.; Mou, S. F.; Jiang, G. B., *J. Chromatogr. A* **2008,** 1180, 24-31.

(18) Lee, I. S.; Lee, N.; Park, J.; Kim, B. H.; Yi, Y. W.; Kim, T.; Kim, T. K.; Lee, I. H.; Paik, S. R.; Hyeon, T., *J. Am. Chem. Soc.* **2006,** 128, 10658-10659.

(19) Gu, H. W.; Xu, K. M.; Xu, C. J.; Xu, B., *Chem. Commun.* **2006**, 941-949.

(20) Chen, H. M.; Deng, C. H.; Li, Y.; Dai, Y.; Yang, P. Y.; Zhang, X. M., *Adv. Mater.* **2009,** 21, 2200-2205.

(21) Lu, Z. D.; Ye, M. M.; Li, N.; Zhong, W. W.; Yin, Y. D., *Angew. Chem. Int. Ed.* **2010,** 49, 1862-1866.

(22) Ge, J. P.; Hu, Y. X.; Yin, Y. D., *Angew. Chem. Int. Ed.* **2007,** 46, 7428-7431.

(23) Hyeon, T.; Lee, S. S.; Park, J.; Chung, Y.; Bin Na, H., *J. Am. Chem. Soc.* **2001,** 123, 12798-12801.

(24) Bai, F.; Wang, D. S.; Huo, Z. Y.; Chen, W.; Liu, L. P.; Liang, X.; Chen, C.; Wang, X.; Peng, Q.; Li, Y. D., *Angew. Chem. Int. Ed.* **2007,** 46, 6650-6653.

Chapter 6

Self-Assembled TiO_2 Nanocrystal Clusters for Selective Enrichment of Phosphorylated Peptides and Proteins

6.1 Introduction

Mesoporous oxides have been recently used for selective separation and adsorption of biomolecules.[1-10] Inorganic oxide materials such as silica can be synthesized into highly ordered mesoporous structures featuring high in-pore surface areas, narrow pore size distributions, adjustable pore sizes, and modifiable surface properties.[10-14] Such unique properties favor the selective enrichment of protein or peptide based on the size-exclusion mechanism. Classic mesoporous silica structures with narrow pore size distributions such as MCM-41 and SBA-15 have been used to selectively enrich peptides from human plasma and exclude other proteins by an accurate molecular weight (MW) cutoff.[1, 3-9] However, this type of enrichment method is mainly limited to silica and alumina because currently it is still difficult to broadly extend the surfactant-templating method to the synthesis of mesoporous structures of many other oxides in a convenient, controllable, and scalable manner (although literature does contain some relevant procedures.[15-17]) The limited choice of materials makes it difficult to further enhance the selectivity by taking advantage of both the size exclusion effect and the specific binding between many oxides and protein/peptides.

Here, we develop a general strategy for the fabrication of novel porous nanostructured materials for efficient separation of biomolecules such as proteins,

peptides, and DNA. Briefly, nanoparticles of various nanostructured materials with uniform sizes and shapes are first synthesized, and then self-assembled into three-dimensional submicrometer clusters containing uniform mesoscale pores. Thanks to rapid progress in colloidal nanostructure synthesis, a great number of materials can now be routinely produced in the form of nanoparticles with excellent control over size, shape, and surface properties,[18-21] making it possible to utilize specific material-peptide interactions to enhance the selectivity in peptide enrichment.[22, 23] Additionally, size exclusion can also be achieved by controlling the dimension of the pores produced by the packing of constituent nanoparticles,[24, 25] allowing selective enrichment of biomolecules based on their sizes. The outer surface of each colloidal nanoparticle cluster (CNC) can be made highly hydrophilic so that nonspecific binding of many hydrophobic protein/peptides can be avoided. The self-assembly process also brings the convenience of incorporation of multiple components into the clusters to further facilitate the separation and detection. For example, incorporation of fluorescent nanocrystals such as quantum dots during the assembly process may produce multifunctional microspheres that are able to not only selectively enrich but also easily identify the targeted biomolecules. Also, adding superparamagnetic iron oxide nanocrystals to the clusters allows their efficient removal from the analyte solution after selective adsorption by using an external magnetic field.

On the other hand, The efficient separation and accurate analysis of phosphorylated proteins are highly demanded in biomedical applications because phosphorylation of proteins is a key event in most cellular processes, including signal

transduction, gene expression, cell cycle, cytoskeletal regulation, and apoptosis.[26, 27] The combination of peptide mapping by matrix-assisted laser desorption/ionization time-of-flight mass spectrometry (MALDI-TOF MS) with the methods of phosphopeptide enrichment represents an efficient tool for characterization of the phosphorylated proteins after digestion. The most widely used approaches for specific enrichment of phosphopeptides are immobilized metal affinity chromatography (IMAC) and metal oxide affinity chromatography (MOAC).[22, 28-31] In IMAC, phosphopeptides can be selectively retained because of the affinity of metal ions for the phosphate groups; while in MOAC, the specific adsorption results from bridging bi-dentate bindings formed between the phosphate anions and the surface of a metal oxide, such as TiO_2, ZrO_2, Fe_2O_3, and Al_2O_3.[32]

We report here the fabrication of mesoporous TiO_2 colloidal nanoparticle clusters (CNCs) and demonstrate their use for selective enrichment of phosphorylated peptides and proteins from complex biosamples by taking advantage of specific affinity offered by the metal oxide. We describe in detail how the outer surface of each TiO_2 cluster can be made highly hydrophilic. And the superior features of these mesoporous structures have been fully tested by effective enrichment of phosphopeptides from digests of standard phosphoproteins, complex protein mixtures, natural non-fat milk and human serum samples.

In addition, we also demonstrate the selective enrichment of phosphorylated proteins by using these mesoporous TiO_2 CNCs. In literature, the direct enrichment of phosphorylated proteins by IMAC or MOAC is rarely reported due to the low adsorption

efficiency and significant losses of phosphorylated proteins during washing steps.[33, 34] Therefore, despite the intense interest in studying phosphorylation events, the direct enrichment of phosphorylated protein remains a technical challenge. We show that phosphorylated proteins also can be effectively adsorbed on these mesoporous clusters. Moreover, the different pore sizes, controlled by changing the size of building blocks, allow selective enrichment of phosphorylated proteins with various sizes based on size exclusion mechanism. All these unique properties of porous TiO_2 structures make them ideal adsorbents for enrichment of phosphorylated proteins in phosphoproteome analysis.

6.2 Experimental Section

6.2.1 Materials

Oleic acid, trioctylphosphine oxide (TOPO), hydroxypropyl cellulose (HPC), iron pentacarbonyl ($Fe(CO)_5$), sodium dodecyl sulfate (SDS), trifluoroacetic acid (TFA), phosphoric acid, ammonium hydroxide solution (NH_4OH, ~28% NH_3 in water) , dithiothreitol (DTT), iodoactamide (IAA), 2,5-dihydroxybenzoic acid (DHB), β-casein and α-casein from bovine milk, trypsin, bovine serum albumin (BSA) and human serum were purchased from Aldrich Chemical Co. Tetrabutyl orthotitanate (TBOT), titanium tetrachloride ($TiCl_4$) and urea were obtained from Fluka. Ethanol, toluene, cyclohexane, acetone and acetonitrile were obtained from Fisher Scientific. Nonfat milk was purchased from local grocery store.

6.2.2 Synthesis of TiO_2 Spheres

TiO_2 spheres with an average diameter of about 200 nm were synthesized by hydrolysis of TBOT. In a typical process, HPC (0.1 g) and H_2O (120 μL) were added to

25 mL of anhydrous ethanol. After stirring for 5 minutes, a TBOT solution (1 mL of TBOT dissolved in 5 mL of anhydrous ethanol) was added dropwise to the mixture, followed by refluxing with magnetic stirring for 1.5 hours. The final products were washed with ethanol several times. Figure S1 shows a typical TEM image of the TiO_2 spheres.

6.2.3 Synthesis of TiO_2 Nanodots

TiO_2 nanodots were prepared by a nonhydrolytic reaction. TOPO (5 g) was heated at 150 ^oC for 5 minutes in vacuum. After increasing the solution temperature to 200 ^oC under N_2 atmosphere, TBOT (1.4 mL) was injected into the hot solution. The resulting mixture was then heated to 320 ^oC, followed by rapidly adding 0.55 mL of $TiCl_4$. The solution was further heated for 20 minutes at 320 ^oC to ensure the complete reaction. After cooling the system down to 80 ^oC, 10 mL of acetone was added to yield a white precipitate, which was isolated by centrifugation and subsequently washed with a cylcohexane/acetone mixture to remove extra surfactant. The resulting powder was re-dispersed in 10 mL of cyclohexane. The larger TiO_2 nanodots were obtained using a seeded growth method by starting with a solution of TiO_2 nanodots in cyclohexane (0.5 mL) and then repeating the above synthesis procedure.

6.2.4 Synthesis of TiO_2 Nanorods

TiO_2 nanorods were synthesized using a high-temperature pyrolysis reaction. Oleic acid (22 mL) was heated at 150 ^oC under vacuum for 1 hour. Then titanium isopropoxide (7 mL) was injected after the solution was cooled to room temperature under N_2 flow. The mixture was then heated to 270 ^oC and kept at this temperature for 2

hours. Ethanol (40 mL) was added after the solution was cooled down to 80 ^{o}C. The white precipitate was collected by centrifugation and washed with cyclohexane/ethanol mixture several times. The final product was re-dispersed in 20 mL of cyclohexane.

6.2.5 Synthesis of γ-Fe_2O_3 Nanocrystals

Superparamagnetic γ-Fe_2O_3 nanocrystals were synthesized using a thermolysis process reported previously. $Fe(CO)_5$ (0.2 mL, 1.52 mmol) was added to a mixture containing 10 mL of octyl ether and 1.28 g of oleic acid at 100 ^{o}C. The solution was then heated to 290 °C under an argon atmosphere and maintained at this temperature for 1 h. After cooling down to 200 ^{o}C, the solution was bubbled with air for 2 hours. After cooling down to RT, ethanol was added to the solution to form precipitation, which were then separated by centrifugation and re-dispersed into 10 mL cyclohexane.

6.2.6 Self-assembly of Nanocrystals into Clusters

The clusters were formed by assembling nanocrystals in emulsion oil droplets by evaporating the low-boiling-point solvent (the oil phase).[35] Typically, 1 mL of cyclohexane solution of nanocrystals was mixed with an aqueous solution of sodium dodecyl sulfate (SDS) (56 mg in 10 mL H_2O) under sonication for 5 minutes. The mixture was then heated to 70 – 72 ^{o}C in a water bath for 4 hours. A clear nanoparticle "micelle" solution was obtained by evaporating cyclohexane. The final products were washed with water three times and re-dispersed in 3 mL of water.

6.2.7 Surface Modification of the Clusters

TiO_2 nanocrystal clusters were coated with a layer of SiO_2 by using a modified Stöber process. Typically, the above aqueous solution of TiO_2 clusters (3 mL) was first

mixed with ethanol (20 mL) and ammonium hydroxide (1 mL, 28%) aqueous solution. Then TEOS (0.1 mL) was injected into the solution and reacted for 20 min under vigorous stirring. The core/shell colloids were collected by centrifugation and washed with ethanol three times. After drying under vacuum overnight, the precipitate was heated to 500 ^{o}C for 2 hours in air to remove organic agents. Then the calcined particles were dispersed in aqueous NaOH solution (5 ml, 0.5 M) for 3~4 hours under stirring to dissolve the silica shell. The particles were collected by centrifugation and washed with dilute acetic acid solution (0.1 M) three times and then distilled water several times. The final TiO_2 nanocrystal clusters were named TiO_2 CNC1, TiO_2 CNC2 and TiO_2 CNC3 according to the different building blocks (TiO_2 nanodots, larger nanodots, and nanorods, respectively, as shown in Figure 6.9).

6.2.8 Tryptic Digests of Proteins

α- (or β-) Caseins (2 mg/mL, 1 mL) were mixed with trypsin (1 mg/mL, 40 μL) in aqueous ammonium bicarbonate (50 mM, pH = 8) and incubated at 37 ^{o}C for 24 hours. The resulting peptide mixtures were stored at -20 ^{o}C until further use. The nonfat milk (1 mL) was first denatured by mixing with an aqueous solution (1 mL) containing ammonium bicarbonate (50 mM) and urea (8 M) and then incubated at 37 ^{o}C for 30 min. An aqueous solution of DTT (200 μL, 90 mM) was added and the mixture was kept at 55 ^{o}C for 1 hour. Then an IAA solution (200 μL, 200 mM) was added at room temperature and incubated for an additional 2 hours in the dark. The final mixture was reacted with trypsin (1 mg/mL, 200 μL) in 50 mM ammonium bicarbonate buffer at 37 ^{o}C for 24 hours. Prior to extraction, all the peptide mixtures were diluted to a certain concentration

with 50% (v/v) acetonitrile containing 0.1% TFA aqueous solution. The digested nonfat milk mixture was diluted 100-fold before further use. Human serum sample (20 μL) was directly diluted 5 times with 50% (v/v) acetonitrile containing 0.1% TFA before enrichment.

6.2.9 Selective Enrichment of Phosphopeptides Using the Clusters

In a typical process, a suspension of nanocrystal clusters (10 μL, 10 mg/mL) was added into 100 μL of peptide mixture originating from tryptic digestion. Then the mixture was vibrated at room temperature for 30 minutes. The phosphopeptides-loaded TiO_2 materials were collected by centrifugation (or by magnet if γ-Fe_2O_3/TiO_2 composite clusters) and washed with 100 μL of 50% acetonitrile and 0.1% TFA water solution three times. Then an aqueous solution of NH_4OH (50 μL, 10%) was added to elute the captured phosphopeptides. The elution was dried under vacuum. Finally, 1 μL of DHB aqueous solution (20 mg/mL, 50% acetonitrile and 1% H_3PO_4) was mixed with dried phosphopeptides and 0.5 μL of the resulting mixture was deposited on the MALDI target for mass analysis.

6.2.10 MALDI-TOF MS

Matrix assisted laser desorption/ionization mass spectra were obtained by using a Voyager-DE STR MALDI-TOF mass spectrometer (Applied Biosystems, Framingham, MA, USA) operating in positive reflector mode. The spectrometer is equipped with a pulsed nitrogen laser operated at 337 nm with 3 ns duration pulses. MS spectra were acquired as an average of 100 laser shots. Peptide mass mapping was carried out by comparing the mass spectra with the protein sequence database in ExPASy.

6.2.11 Selective Enrichment of Phosphorylated Protein by the TiO_2 CNCs

TiO_2 materials **(**2.0 mg) were added to 1 mL of diluted protein mixture (0.01 mg/mL each in 50% acetonitrile and 0.1% TFA water solution) to selectively enrich the phosphorylated proteins. The mixture was incubated under stirring for 2 hours, followed by centrifugation at 11000 rpm for 5 minutes. After the supernatant was decanted, the precipitate was washed with two portions of 200 μL of loading/washing buffer (50% acetonitrile and 0.1% TFA water solution). Then 20 μL of NH_4OH water solution (10%) was used to elute the adsorbed proteins. After centrifugation, 5 μL of supernatant was dried by vacuum and re-dispersed in 2 μL of matrix solution (10 mg/mL of sinapinic acid dissolved in 50% acetonitrile and 0.1% TFA water solution), and then 0.5 μL of the mixture was directly dropped onto a stainless steel MALDI plate for MS analysis. The remaining supernatant (~15 μL) was collected for CE analysis.

6.2.12 Capillary Electrophoresis

All capillary electrophoresis experiments were performed on a P/ACETM MDQ Glycoprotein Capillary Electrophoresis System (Beckman Coulter, Fullerton, CA, USA). A 40-cm fused-silica capillary (75 μL id, 365 μL od, Polymicro Technologies, Phoenix, AZ, USA) with an effective length of 30 cm was used. For CE separation, the capillary was treated by 0.1 N NaOH for 2 minutes and then water for 1 minute at 30 psi before being filled with the 10 mM borate buffer (pH 8.05). The sample was injected hydrodynamically at 0.5 psi for 5 s, and the separation was performed at +25 kV with UV-absorption detection at 200 nm.

6.2.13 Structure Characterization

The morphology of nanostructures was investigated using a Philips Tecnai 12 transmission electron microscope (TEM). The composition of the materials was confirmed by using powder X-ray diffraction on a Bruker D8-Advance powder diffractometer operating at 40 kV, 40 mA for Cu Kα radiation (λ=1.5406 Å). The EDX analyses were performed on a Philips FEI XL30 scanning electron microscope (SEM). Dynamic light scattering (DLS) and zeta potential analysis was performed on a ZetaPALS system. N_2 gas sorption experiments were carried out on a Micromeritics ASAP 2010 surface area and pore size analyzer. Before the measurement, the sample was dried by using the "degas" function of the surface area analyzer for 20 h at 250 °C. The N_2 adsorption measurement was performed at 77 K using liquid nitrogen.

6.3 Results and Discussion

6.3.1 TiO_2 Clusters for Enrichment of Phosphopeptides

The general procedure for the fabrication of mesoporous nanocrystal clusters has been schematically illustrated in Figure 6.1. We choose TiO_2 as the adsorbent material because of its specific affinity towards phosphopeptides. TiO_2 nanocrystals with an average diameter of ~ 5.1 nm (Sample **1**) were prepared by a nonhydrolytic solution-based reaction using trioctylphosphine oxide (TOPO) as both the solvent and capping ligand.[35] The resulting nanocrystals were covered with a monolayer of TOPO which made the particles hydrophobic and only dispersible in nonpolar solvents such as cyclohexane, chloroform, and toluene. Figure 6.2a shows a typical transmission electron microscopy (TEM) image of the TiO_2 nanocrystals that were used for building the

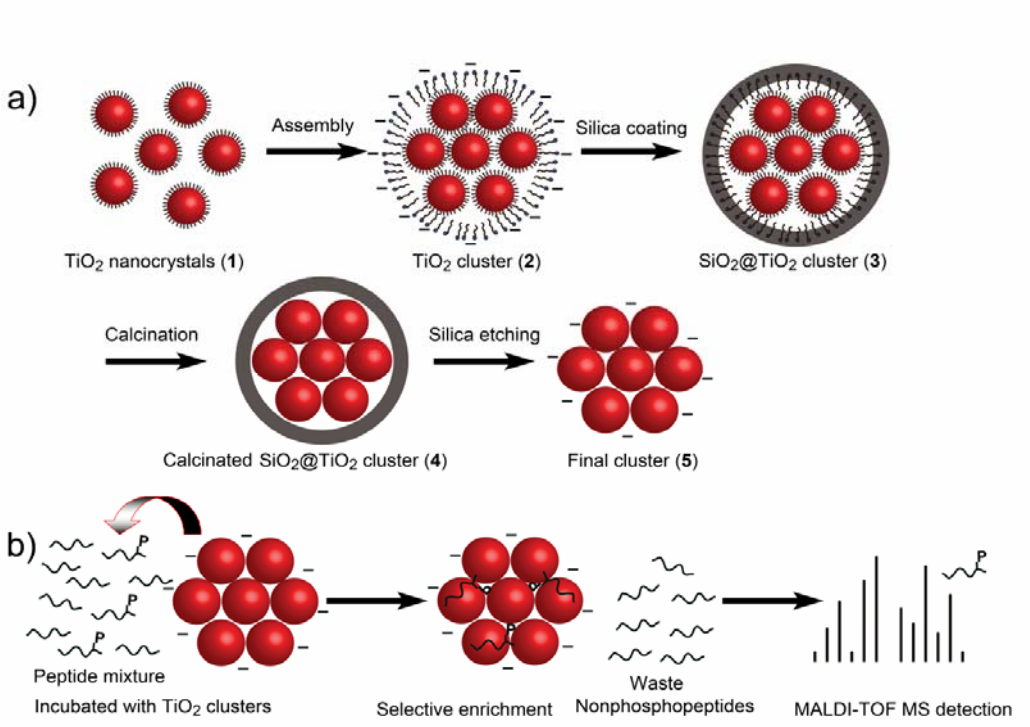

Figure 6.1 Schematic illustration of (a) the self-assembly procedure for the fabrication of the mesoporous TiO_2 nanocrystal clusters and (b) the selective enrichment process of phosphorylated peptides by taking advantage of the special affinity between the phosphate groups and titania surface of the mesoporous clusters.

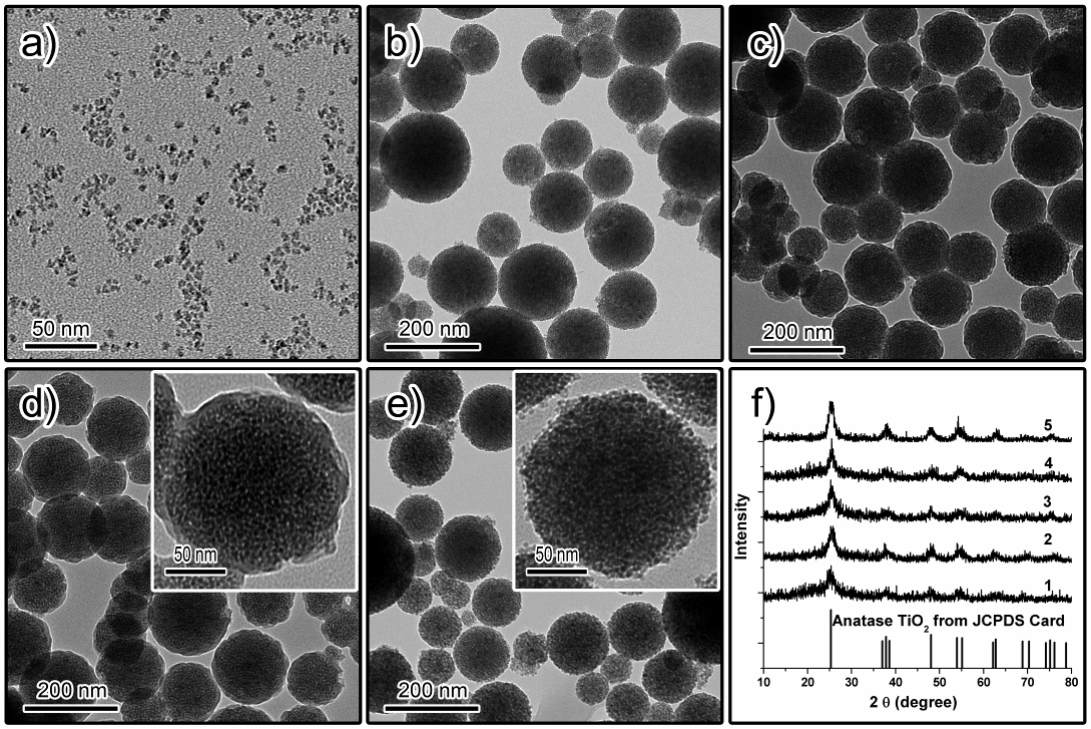

Figure 6.2 (a-e) TEM images of nanostructured TiO_2 materials produced during the fabrication steps: (a) TiO_2 nanocrystals (Sample **1**); (b) TiO_2 nanocrystal clusters obtained through self-assembly in emulsion droplets (Sample **2**); (c) Silica coated TiO_2 nanocrystal clusters (Sample **3**); (d) Calcined SiO_2@TiO_2 nanocrystal clusters (Sample **4**); (e) Calcined clusters after the silica layer has been removed by chemical etching (Sample **5**). Insets are TEM images of corresponding samples at higher magnifications. (f) Corresponding XRD patterns of the five samples (**1**-**5**).

clusters. In order to prepare cluster structures, a cyclohexane solution of TiO_2 nanocrystals was dispersed in water as oil-in-water emulsion droplets and followed by subsequent evaporation of the volatile solvent.[35, 36] The emulsification process was carried out in the presence of a surfactant of sodium dodecyl sulfate (SDS) under ultrasonication. After the organic solvent was evaporated at 70 ^{o}C with stirring and subsequent washing with deionized water, the spherical clusters of densely packed TiO_2 nanocrystals (Sample **2**, Figure 6.2b) were collected by centrifugation. The SDS, which was used as the emulsifier in the process, was adsorbed onto the cluster surface through the hydrophobic-hydrophobic interactions between the tails of the SDS and the protection ligands on the TiO_2 nanocrystals. The negatively charged heads of SDS ($–SO_3^-$) help the clusters disperse well in water and make the clusters ready for the next step of silica coating. The TiO_2 CNCs were further stabilized by coating their surfaces with a thin layer of silica through a sol-gel process. Figure 6.2c shows a typical sample of TiO_2 CNCs with ~ 10 nm surface coating (Sample **3**). For optimal adsorption of phosphopeptides, the organic ligands bound to the nanocrystal surface must be removed to allow full access of the peptides to the TiO_2 surface. This can be achieved by calcination at 500 ^{o}C in air (Sample **4**, Figure 6.2d). The calcination also enhances the mechanical stability of the clusters by bridging neighboring nanocrystals together through thermal fusing. As a result, stable TiO_2 clusters (Sample **5**, Figure 6.2e) can be obtained after the silica layer is etched away in a diluted NaOH aqueous solution. No apparent breakage of the clusters has been observed. For comparison, TiO_2 clusters without silica protection (Sample **2**) were directly calcined at 500 ^{o}C in air and the resulting product

was in the form of bulk powders (Sample **6)**. TEM measurements suggested that the clusters without protection became severely aggregated and could not maintain their spherical morphology after calcination.

The high-magnification TEM image in the inset of Figure 6.2d clearly shows the presence of a silica shell (~ 10 nm) which disappeared after etching in NaOH solution. As can be seen in the inset of Figure 6.2e, the surface of the TiO_2 clusters becomes rough after etching, revealing the particulate nature of the component. Due to the non-uniformity of the emulsion droplets, the sizes of the clusters range from 50 nm to 200 nm, as confirmed by both TEM observations and dynamic light scattering (DLS) analyses. X-ray diffraction measurements (Figure 6.2f) indicate that Samples **1**-**5** are pure anatase (JCPDS Card No. 21-1272) nanocrystalline materials with almost identical peak broadening. Calculations with the Debye-Scherrer formula for the strongest peak (101, $2\theta \sim 25.3^{o}$) gave grain sizes of 4.6, 4.9, 5.2 and 5.4 nm for cluster Samples **2**-**5** respectively, which are comparable to that of 5.1-nm original isolated TiO_2 nanocrystals. This implies that the primary nanocrystals did not grow significantly during the cluster formation and calcination. The slight increase in grain size of the calcined samples suggests modest interparticle fusion which contributes to the enhancement in mechanical stability of the final cluster structures.

The silica coating and removal steps are critically important for the successful fabrication of mesoporous clusters suitable for selective phosphopeptide enrichment. First, the thin silica coating protects the clusters from aggregation during calcination at high temperatures. Even though slight inter-cluster aggregation occurs due to silica

fusion during calcination, the subsequent etching by NaOH removes the silica layer and releases the clusters (Sample **5**) from aggregation. Second, the etching process introduces a relatively high density of hydroxyl groups so that the cluster surface becomes negatively charged. The charged surface renders the clusters highly dispersible in water. We have monitored the change of zeta potential during the removal of the silica layer in order to evaluate the surface charge of the clusters. Before etching, the silica coated clusters displayed a zeta potential of ~ -42.0 mV, suggesting a high density of silanol groups that cannot be completely eliminated by calcination at 500 ^{o}C in air. At the initial stage of etching, the zeta potential increased to ~ -47.5 mV due to the formation of more hydroxyl groups during the breakdown of Si-O-Si networks. This value is consistent with that measured for silica colloids freshly prepared through sol-gel processes. Further etching removed more silica so that the zeta potential gradually reduced in value, eventually stabilizing at ~ -22 mV. For comparison, we have also measured the zeta potentials of simple aggregations of TiO_2 nanocrystals and solid TiO_2 spheres prepared by sol-gel processes (Samples **6** and **7**, both calcined at 500 ^{o}C in air), which only give values in the range of -3 ~ -5 mV. It is therefore believed that the etching process left many hydroxyl groups on the TiO_2 cluster surface, and subsequently enhanced the surface charge to enable good water dispersibility.

Nitrogen adsorption/desorption isotherm measurements were conducted to further investigate the porous structure of the TiO_2 nanocrystal clusters (Sample **5**). TiO_2 solid spheres (Sample **7**) with an average diameter of ~200 nm were also included in measurements for comparison. the Barrett-Joyner-Halenda (BJH) pore size distribution

obtained from the isotherm suggests that Sample 5 contains pores with sizes ranging from 2 to 4 nm with an average value of 2.3 nm. The Brunauer-Emmett-Teller (BET) specific surface area has been estimated to be 240 m^2/g, a relatively high value achievable for porous TiO_2 materials. For Sample **7**, there are no obvious pores and the BET specific surface area is only 37 m^2/g. All these data strongly support the fact that the nanocrystal clusters produced by using this self-assembly method have a well-defined mesoporous structure. The composition information of sample **4**-**8** is listed in Table 1.

Bovine β-casein was used to evaluate the performance of the TiO_2 nanocrystal clusters for selective enrichment of phosphopeptides. A tryptic digest from 1 pmol of β-casein was incubated in the presence of the clusters. After separating the clusters from solution and thoroughly washing, the trapped phosphopeptides were eluted by an aqueous solution of NH_4OH (10%, pH: 12.2) for MALDI-TOF MS analysis. For comparison, direct analysis of β-casein digest was also performed by MS analysis, with the result presented in Figure 6.3a. The detailed information of detected phosphopeptides is listed in Table 6.2. Only two phosphopeptides (β1 and β5) derived from β-casein and some abundant non- phosphopeptides can be observed. The presence of large amounts of non-phospopeptides resulted in a severe diminishment of phosphopeptide characterization. The same amount of tryptic digest was also pretreated with simple aggregations of TiO_2 clusters (Sample **6**) and TiO_2 clusters with a silica coating (Sample **4**) using the same enrichment procedure, with the corresponding MALDI-TOF MS spectra illustrated in Figures 6.3b and 6.3c, respectively. The powders of simple

Table 6.1 Comparison of the TiO_2 material properties of sample **4-8.** [a] The particles size was from dynamic light scattering (DLS) results; [b] Surface area was determined by N_2 adsorption-desorption isotherm curves.

	Composition	Particle Size[a] (nm)	Surface area[b] (m^2/g)
Sample **4**	SiO_2@TiO_2 CNCs	50~200	-
Sample **5**	TiO_2 CNCs	50~200	240
Sample **6**	TiO_2 CNC aggregations	> 3000	130
Sample **7**	TiO_2 solid spheres	150~200	37
Sample **8**	TiO2&γ-Fe_2O_3 CNCs	50~200	-

Table 6.2. Peptide peaks of detected phosphopeptides from tryptic digests of α-casein, β-casein and human serum by MALDI-TOF mass analysis. [pS], phosphorylated site; [Mo], oxidation on methionine; Q*, pyroglutamylation on the N-terminal Gln. [a] Peptides S1-S4 from human serum are protein fibrinogen A fragments.

Peak No	Mw (Da)	Number of phosphorylation	Peptide sequence
			α-casein
α1	1237.5	1	TVDME[pS]TEVF
α2	1253.1	1	TVD[Mo]E[pS]TEVF
α3	1466.6	1	TVDME[pS]TEVFTK
α4	1538.6	2	EQL[pS]T[pS]EENSKK
α5	1660.8	1	VPQLEIVPN[pS]AEER
α6	1832.8	1	YLGEYLIVPN [pS]AEER
α7	1847.7	1	DIG[pS]ETEDQAMEDIK
α8	1927.7	2	DIG[pS]E[pS]TEDQAMEDIK
α9	1943.9	2	DIG[pS]E[pS]TEDQA^{18}EDIK
α10	1951.9	1	YKVPQLEIVPN[pS]AEER
α11	2618.7	4	NTMEHV[pS][pS][pS]EESII[pS]QETYK
α12	2678.0	3	VNEL[pS]KDIG[pS]E[pS]TEDQAMEDIK
α13	2703.8	5	Q*MEAE[pS]I[pS][pS][pS]EEIVPN[pS]VEAQK
α14	2719.9	5	QMEAE[pS]I[pS][pS][pS]EEIVPNPN[pS]VEQK
α15	2736.0	5	Q^{18}EAE[pS]I[pS][pS][pS]EEIVPNPN[pS]VEQK
α16	2747.1	4	NTMEHV[pS][pS][pS]EE[pS]IISQETYKQ
α17	2935.2	3	KEKVNEL[pS]KDIG[pS]E[pS]TEDQAMEDIKQ
α18	3008.0	4	NANEEEYSIG[pS][pS][pS]EE[pS]AEVATEEVK
α19	3087.9	5	NANEEEY[pS]IG[pS][pS][pS]EE[pS]AEVATEEVK
			β-casein
β1	2061.6	1	FQ[pS]EEQQQTEDELQDK
β2	2430.4	1	IEKFQ[pS]EEQQQTEDELQDK
β3	2556.5	1	FQ[pS]EEQQQTEDELQDKIHPF
β4	2965.7	4	ELEELNVPGEIVE[pS]L[pS][pS][pS]EESITR
β5	3122.9	4	RELEELNVPGEIVE[pS]L[pS][pS][pS]EESITR
			Human serum [a]
S1	1389.2	1	D[pS]GEGDFLAEGGGV
S2	1460.2	1	AD[pS]GEGDFLAEGGGV
S3	1545.3	1	D[pS]GEGDFLAEGGGVR
S4	1616.3	1	AD[pS]GEGDFLAEGGGVR
S5	1944.5		

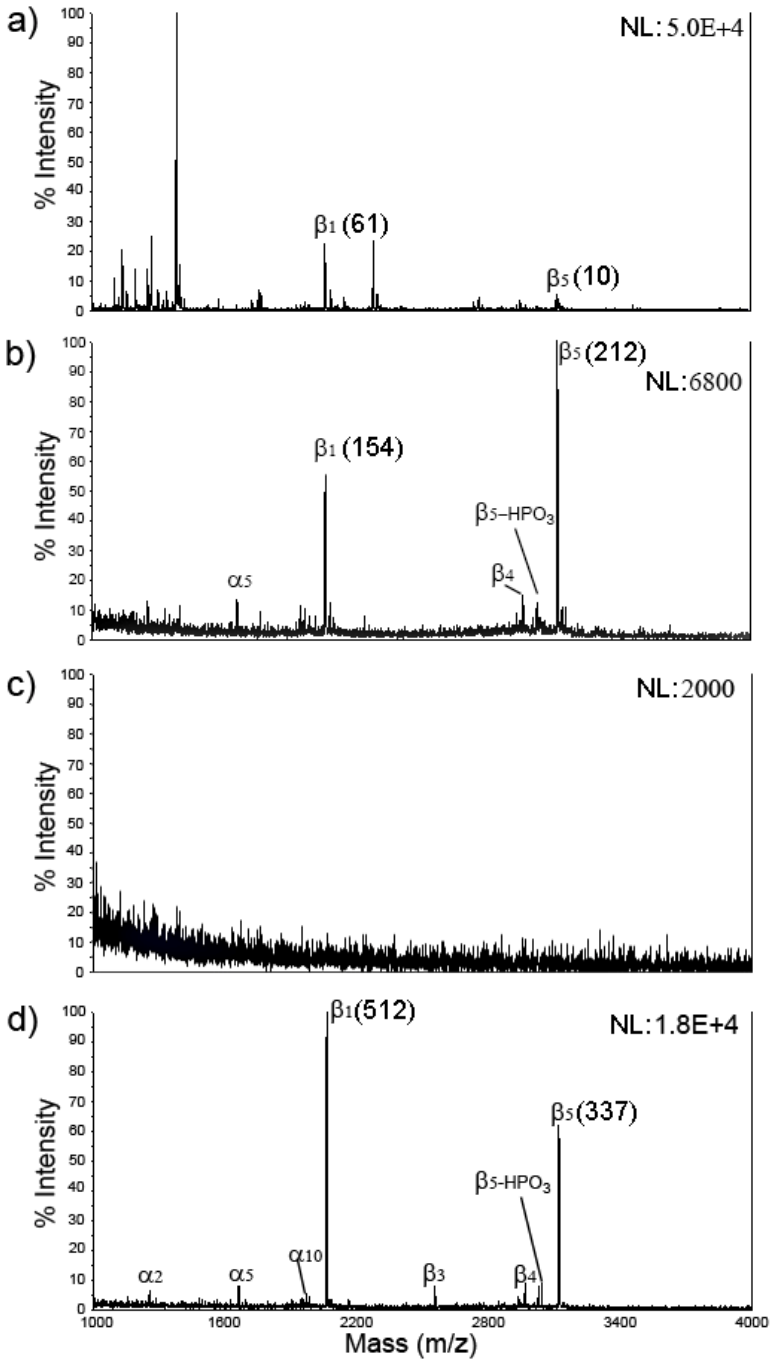

Figure 6.3 MALDI mass spectra of tryptic digest of β-casein (100 μL, 10^{-8} M): (a) direct analysis; (b-d) analysis after enrichment by Samples **6**, **4**, and **5**. The data in parentheses are S/N of the corresponding peaks. NL: normalized level.

nanoparticle aggregations (Sample **6**) clearly demonstrate the selective adsorption of phosphopeptides to the TiO_2 surface by showing the major peaks of phosphopeptides from β-casein (β1, β4, and β5). As the original protein sample contains a small amount of α-casein, phosphopeptide residue (α5) derived from this impurity has also been enriched and detected. However, the overall signal is low. No obvious peaks can be observed after enrichment with Sample **4**, indicating that there was no obvious specific or nonspecific adsorption of peptides onto the SiO_2 surface. Figure 6.3d displays the MS spectrum obtained after enrichment of the tryptic digest using Sample **5**. Four β-casein phosphopeptides (β1, β3, β4 and β5), along with dephosphorylated fragments of β5, which likely formed during the MALDI ionization process, were detected. In addition, a number of phosphopeptide residues due to α-casein have also been enriched and clearly identified, as demonstrated by the presence of peaks of α2, α5 and α10. The results indicate the high specificity of TiO_2 CNCs for phosphopeptides. Compared to Sample **6**, enrichment using the well-dispersed nanocrystal clusters (Sample **5)** yielded significantly higher signal intensity and S/N ratio, allowed unambiguous detection of lower abundance phosphopeptides such as β3, and displayed a very clean background. There are at least two reasons for the stronger signal. First, the good dispersibility of TiO_2 porous clusters makes material surface easy accessible to the phosphopeptides in comparison to the bulk aggregations of nanocrystals. Secondly, the fine-tuned cluster size (50~200 nm) enable the fast mass transfer and diffusion of the phosphopeptides.

To further evaluate the sensitivity and capacity of the mesoporous TiO_2 clusters for phosphopeptide enrichment, tryptic β-casein digests at different concentrations (10^{-6} to 10^{-10} M) with a fixed volume (100 μL) were enriched using the clusters (0.1 mg) and then analyzed by MALDI-TOF MS. For comparison, solid TiO_2 spheres (~ 200 nm, Sample **7**) were used as another affinity absorbent for selectively trapping phosphopeptides. As shown in Figure 6.4, after enrichment using Sample **5**, the intensities of two dominant peaks (β1 mono-phosphopeptide and β5 tetra-phosphopeptide) decreased as the amount of β-casein decreased from 100 pmol to 10 fmol. For Sample **7**, at small amounts of β-casein (less than 100 fmol), the intensities of the two peaks were about half of those obtained using Sample **5**. The intensity of the mono-phosphopeptide was higher than the tetra-phosphopeptide, which is similar to the case for Sample **5**. For the case of enriching a larger amount of β-casein (> 1 pmol) by Sample **7**, the intensity of mono-phosphopeptide became lower than the tetra-phosphopeptide and this trend was more obvious in the case of further increased amounts of β-casein (100 pmol). We believe this is due to the stronger chelating interaction between tetra-phosphopeptides and the TiO_2 surface than that for mono-phosphopeptides, which results in the preferential occupation of the TiO_2 surface by the tetra-phosphopeptide when there is a competition for TiO_2 surface.[18] Moreover, the intensities of the two peaks (β1 and β5) reached the maximum when the amount of β-casein increased to 10 pmol. When the amount of β-casein further increased to 100 pmol, the peak intensities declined because of the small surface area and consequently limited adsorption capacity of Sample **7** towards phosphopeptides. When the same mass of

Sample **5** was used, the intensity ratio of the mono-phosphopeptide and tetra-phosphopeptides changed very litter because the total TiO_2 surface area was high enough such that all the phosphopeptides could be enriched and there was no competition for adsorption sites. It was also observed that the solid microspheres of TiO_2 (Sample **7**) showed slightly better enrichment efficiency for tetra-phosphopeptides than the nanocrystal clusters (Sample **5**) at high peptide concentrations, probably because the peptides containing multiple phosphate groups had a higher tendency to be trapped in the mesopores during elution. As shown in the MS spectrum in the inset of Figure 6.4, three phosphopeptides could be easily enriched and detected even when the total amount of β-casein was decreased to only 10 fmol. These tests lead us to believe that the TiO_2 nanocrystal clusters are ideal adsorbents for phosphopeptides with high sensitivity and high capacity.

Superior enrichment efficiency and selectivity have also been demonstrated in the pretreatment of the tryptic digest of pure α-casein (10 pmol), which contains many more phosphorylated fragments than that of β-casein. Figure 6.5 compares the MALDI-TOF MS spectra of the protein digest before and after enrichment using Sample **5** and Sample **7**. Without pre-enrichment, direct analysis of the digested sample only shows six phosphopeptide peaks, along with many dominantly strong peaks due to non-phosphopeptides (Figure 6.5a). After enrichment using the mesoporous TiO_2 nanocrystal clusters (Sample **5**), nineteen phosphopeptides can be observed without any obvious peaks from non-phosphopeptides, clearly showing the effectiveness of the phosphopeptide enrichment (Figure 6.5b). In contrast, only eleven phosphopeptides have

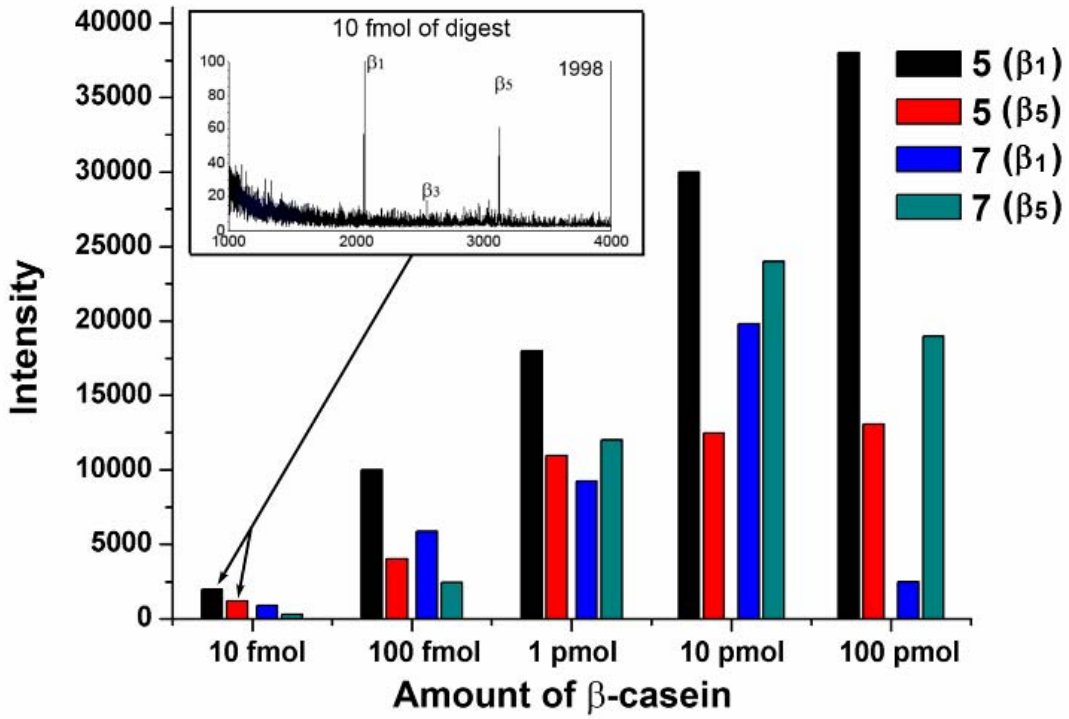

Figure 6.4 Comparison of the performance of TiO_2 nanocrystal clusters (Sample **5**, black and red bars) and solid TiO_2 spheres (Sample **7**, blue and green bars) for the selective enrichment of phosphorylated peptides with different amounts of tryptic digest of β-casein (100 μL, from 10^{-10} to 10^{-6} M). The MS spectra were analyzed by three trials, with the intensity averaged.

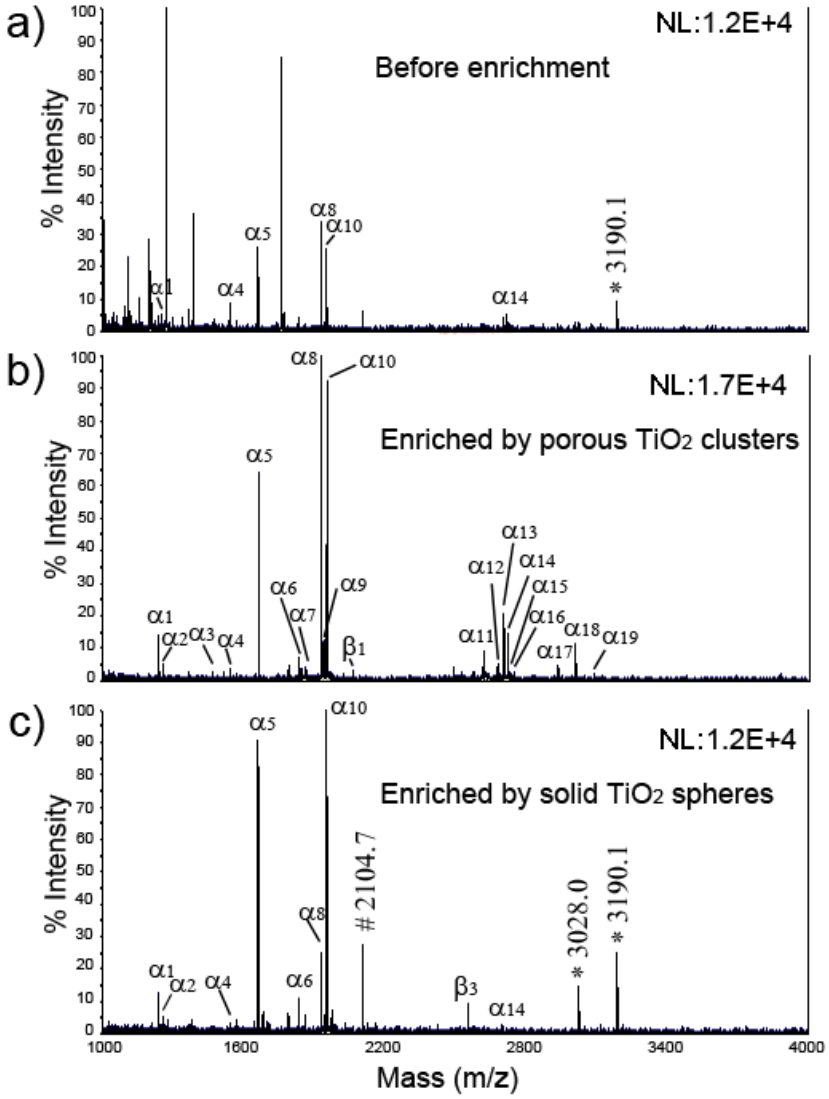

Figure 6.5 MALDI mass spectra of tryptic digest of α-casein (100 μL, 10^{-7} M): (a) direct analysis; (b, c) analysis after enrichment using Sample **5** and Sample **7**. NL: normalized level.

been detected after enrichment using the solid TiO_2 microspheres (Sample **7**), as shown in Figure 6.5c. The peaks at m/z of 3028.0 and 3190.1 have been proved to be multiphosphopeptides[37, 38] and the peak at m/z of 2104.7 represents nonphosphopeptide (TDAPSFSDIPNPIGSENSEK, pI = 3.92) derived from α-casein shows that acidic peptides may also bound to the TiO_2 solid spheres, which is a typical issue for normal IMAC or MOAC. These comparisons confirm the excellent enrichment power of the nanocrystal clusters which can be attributed to their high specific surface area due to the mesoporous structure and the clean TiO_2 surface that ensures high affinity to the phosphate groups.

To mimic a complex biological sample, BSA-derived tryptic peptides were added to the tryptic digest of β-casein at different molar ratios (β-casein:BSA = 1:10 and 1: 100). Figure 6.6 represents the mass spectra of the mixtures before and after enrichment by Sample **5**. At a molar ratio of 1:10 without enrichment, only one peak of phosphopeptide (β1) can be detected at abundance less than 1% compared to the nonphosphorylated peptides in the MS spectrum (Figure 6.6a). After enrichment with the TiO_2 clusters (Figure 6.6b), the signals of phosphopeptides from β-casein (β1, β3 and β5) as well as those from impurity α-casein (α2, α3, α5 and α10) can be detected in the mass spectrum, while no obvious non-phosphopeptides are observed. The S/N ratio of phosphopeptides is significantly improved. When the molar ratio decreases to 1:100, without enrichment no phosphopeptides from β-casein can be distinguished because of the presence of exceedingly more abundant non-phosphopeptides from BSA. However, selective enrichment with Sample **5** did not pick up any non-phosphopeptides but only

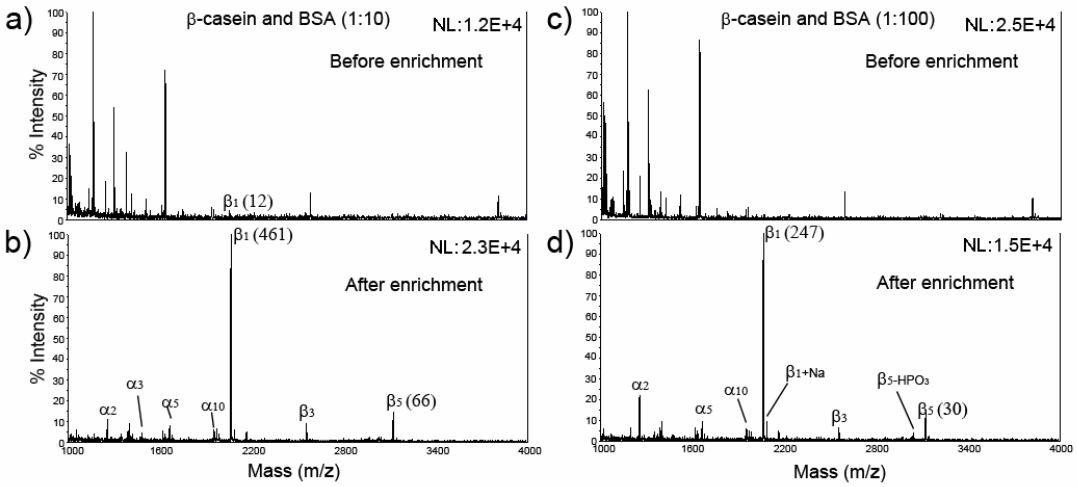

Figure 6.6 MALDI-TOF mass spectra of mixtures containing tryptic digest β-casein (100 μL, 10^{-8} M) and nonphosphorylated (bovine serum albumin, BSA) protein tryptic digests at varying ratios of (a,b) 1:10, and (c,d) 1:100 enriched with Sample **5**. The data in parentheses are S/N of the corresponding peaks. NL: normalized level.

phosphopeptides, leading to a very clean background in the MS spectrum. These results indicate that a trace amount of phosphopeptides can be effectively concentrated by the mesoporous TiO_2 clusters, even in the presence of a large amount of interfering peptides.

We have also used nonfat milk, which contains abundant phosphorylated proteins such as α- and β-casein, to further examine the effectiveness and selectivity of the TiO_2 nanocrystal clusters in the enrichment of phosphopeptides from a complex sample. The direct analysis of tryptic digest of nonfat milk is not shown here because of the significant suppression of ionization in MALDI due to the presence of extremely high concentrations of salts in the digest (Urea with a high concentration was used for protein denaturation).[39] After phosphopeptide enrichment using Sample **5**, the salt concentration was low enough for MALDI processing and a number of phosphopeptide peaks appeared in the mass spectrum. Most of these signals were derived from α- and β-casein as shown in Figure 6.7a. Peaks at m/z of 1993.9, 2103.6 and 2598.6 marked with asterisks may be attributed to acetylation or tri-methylation on the lysine side chain of corresponding phosphopeptides (α10, β1 and β3, mass difference of 42 Da) from the raw non-fat milk samples. Human serum sample was also used for testing the specificity of Sample **5**. As shown in Figure 6.7b, five peaks of phosphopeptides (S1-S5) can be clearly observed after enrichment. Compared with porous TiO_2 clusters (Sample **5**), the performance of solid TiO_2 spheres (Sample **7**) was not as good because fewer phosphopeptides could be detected and many the overall intensities of the peaks were much lower than those obtained by Sample **5**. These results suggest that porous TiO_2 clusters are capable of selectively trapping phosphopeptides from naturally obtained complex samples. In

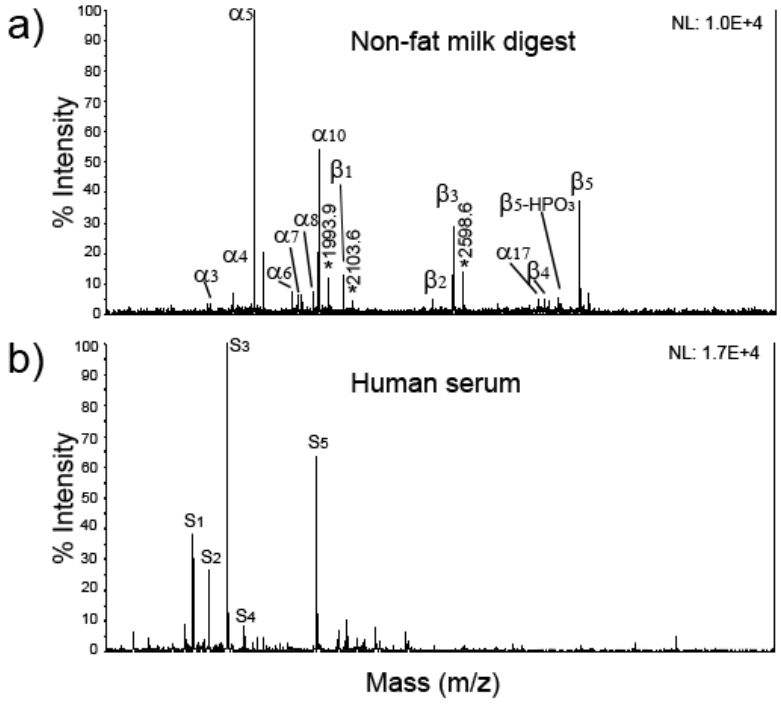

Figure 6.7 MALDI-TOF mass spectra of the tryptic digest of nonfat milk (100 μL, diluted 100-fold) and human serum (20 μL) after enrichment using Sample **5**. NL: normalized level.

addition, another obvious merit of the TiO_2 clusters-mediated enrichment process here is that concentration of salts can be avoided. The desalting properties of the TiO_2 clusters could be attributed to the calcined TiO_2 surface, which exhibits weak interactions with hydrophilic molecules such as salts.

The self-assembly process described here brings the convenience of incorporation of multiple components to the clusters to enable many additional functions beyond enrichment. Composite nanocrystal clusters can be fabricated by simply starting with a mixture of different types of nanocrystals. As an example, superparamagnetic iron oxide (γ-Fe_2O_3) nanocrystals were added to the clusters to facilitate separation. Representative TEM images of γ-Fe_2O_3/TiO_2 multiple component clusters (Sample **8**) and their corresponding primary γ-Fe_2O_3 nanocrystals (inset) are shown in Figure 6.8a. Individual TiO_2 (~ 5.1-nm) and γ-Fe_2O_3 (~12.0-nm) nanocrystals can be seen by carefully focusing at the edge of a single colloidal cluster. The XRD pattern of the clusters (Figure 6.8b) confirms the coexistence of anatase TiO_2 and γ-Fe_2O_3, and the peak broadening suggests that the nanocrystals retained their individual characters and did not sinter into larger units after calcination. The elemental composition was further confirmed with energy-dispersive X-ray spectroscopy (EDX), as shown in Figure 6.8d, which only displays strong peaks from Fe, Ti, and O. It is evident that TiO_2 and γ-Fe_2O_3 nanocrystals were successfully assembled together to form porous clusters.

We have reported previously that the clustering of superparamagnetic nanocrystals results in higher saturation magnetization and more rapid magnetic

responses than individual ones.[40] After enrichment with the multiple component clusters, it becomes easy to isolate the phosphopeptide loaded clusters from solutions using an external magnetic field. As the inset in Figure 6.8c shows, the multiple component clusters (Sample **8**) could be extracted from solution within 2 minutes upon the application of a NdBFe magnet. The tryptic digest of β-casein was used again to examine the performance of the phosphopeptide enrichment by Sample **8**. All the processes were the same as those discussed above, except that a magnetic field instead of centrifugation was used for separation. The MS result was similar to that obtained by Sample **5**. All the peaks could be attributed to the phosphopeptides from β-casein and impurity α-casein. As can be seen from this demonstration, the introduction of additional components to the clusters can further facilitate the enrichment process, and do not appear to deteriorate the enrichment capacity and selectivity.

6.3.2 TiO_2 Clusters for Enrichment of Phosphorylated Proteins

The self-assembly approach allows facile control over the pore dimensions by changing the size, shape or composition of the nanocrystal building blocks. For comparison, we have fabricated three samples of colloidal nanoparticle clusters (CNCs) by assembling TiO_2 nanodots and nanorods: CNC1 from ~5.1-nm nanodots, CNC2 from ~6.6-nm nanodots, and CNC3 from ~3.0-nm×28.1-nm nanorods. Representative transmission electron microscopy (TEM) images of clusters and corresponding primary TiO_2 nanocrystals are shown in Figure 6.9. One can easily observe the porous nature of the clusters by carefully inspecting the enlarged images in the insets. Sample CNC3,

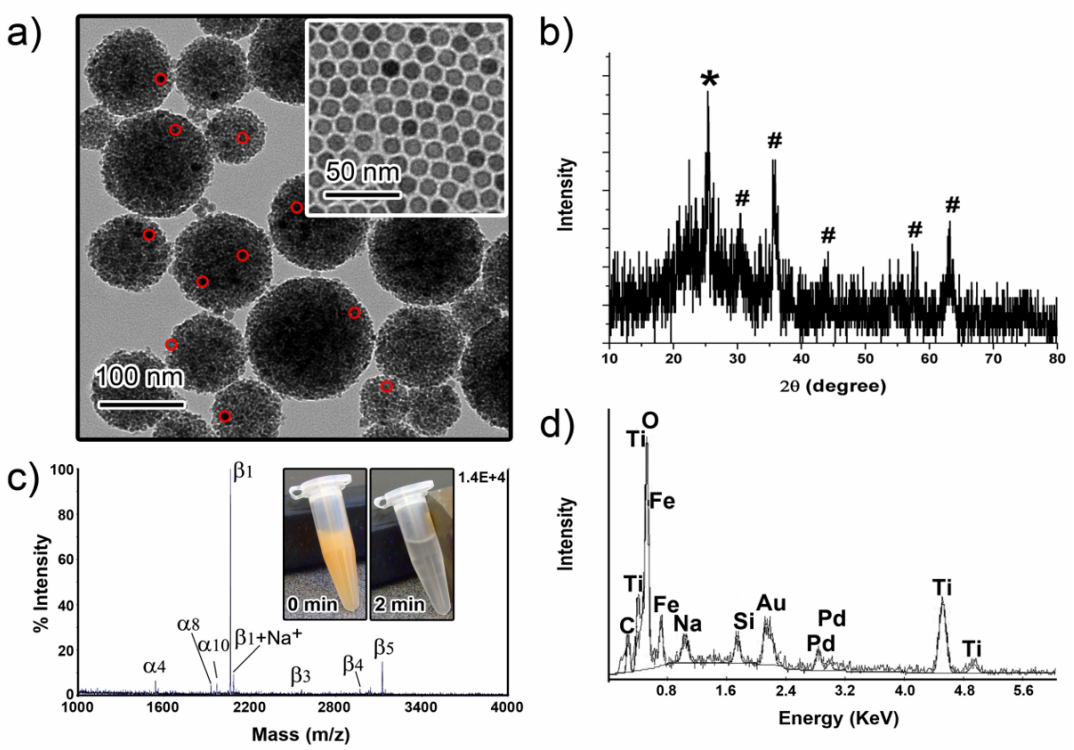

Figure 6.8 (a) TEM images of γ-Fe_2O_3/TiO_2 multiple component clusters (Sample **8**, red circles are used to highlight γ-Fe_2O_3 nanocrystals) and corresponding primary γ-Fe_2O_3 nanocrystals (Inset); (b) XRD pattern of Sample **8** (The peaks marked with '*' refer to anatase-phase TiO2, and '#' to maghemite-phase γ-Fe_2O_3); (c) MALDI mass spectra of tryptic digest of β-casein (100 μL, 10^{-8} M) after enrichment using Sample **8**; Insets are photos of Sample **8** dispersed in water before and after exposure to external magnetic fields; (d) EDX analysis of the as-synthesized Sample **8**.

composed of TiO_2 nanorods, has the largest pores. N_2 adsorption/desorption isotherms were used to examine the porous structures (Figure 6.9g). Solid TiO_2 spheres with an average diameter of ~200 nm were included in measurements for comparison. As shown in Figure 6.9h, the Barrett-Joyner-Halenda (BJH) pore-size distribution curves suggest that the three porous structures possess relatively uniform pores with average diameters of 2.3, 2.6, and 3.5 nm. Although the calculated average pore sizes of samples CNC1 and NCC2 do not differ significantly, it is apparent that CNC2 displays a broader size distribution and contains more relatively large pores with diameters in the range of 3~4 nm. Due to the random packing of TiO_2 nanorods, the pore size of sample CNC3 is much larger than the other two clusters, which is consistent with the TEM observations. The Brunauer-Emmett-Teller (BET) surface areas are 240, 324, and 441 m^2/g for the three porous samples, and 37 m^2/g for TiO_2 solid microspheres. The values for these clusters are relatively large in comparison to other recently reported TiO_2 porous structures, whose BET surface areas are typically around 100 m^2/g. Interestingly, the surface area of the porous clusters increases with the size of the primary nanocrystals, which seems to be inconsistent with simple geometric considerations as well as previous reports.[25] This may be explained by the fusion of the nanocrystals during calcination: smaller nanocrystals, which have larger contact area with neighboring particles and higher surface energy, are easier to fuse together at high temperatures, consequently leading to a smaller specific surface area.

To evaluate the efficiency of phosphorylated protein adsorption by as-obtained TiO_2 clusters, two approaches were used to analyze the amount of adsorbed proteins.

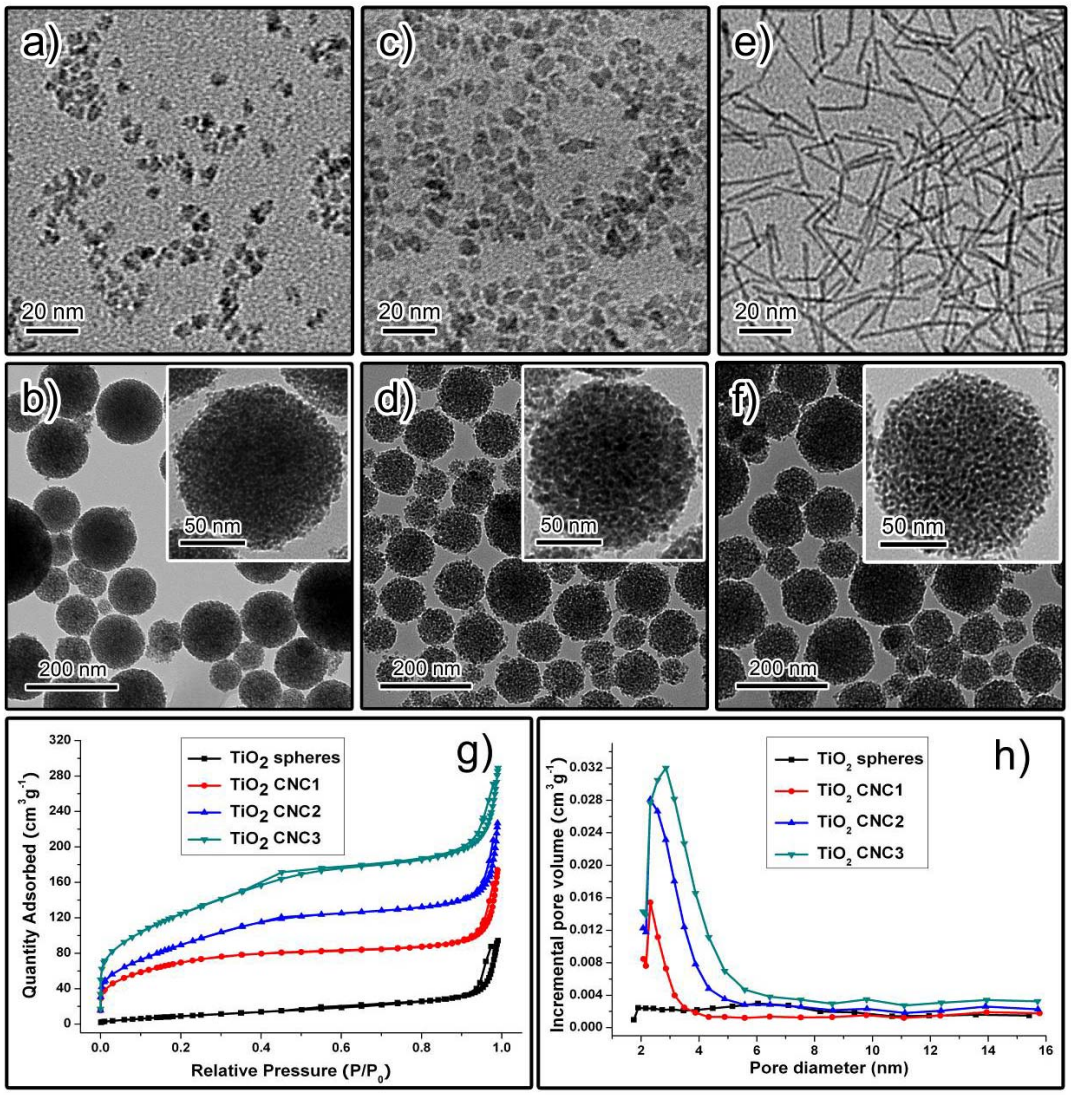

Figure 6.9 (a-f) TEM images of TiO_2 nanocrystals and corresponding clusters assembled from the nanocrystals: (a, b) nanodots of ~ 5.1 nm (CNC1); (c, d) nanodots of ~ 6.6 nm (CNC2); and (e, f) nanorods of ~ 3.0 nm× 28.1 nm (CNC3). Insets are TEM images at high magnifications. (g) N_2 adsorption-desorption isotherm curves for a sample of TiO_2 solid spheres and three samples of TiO_2 mesoporous clusters. (h) BJH pore size distribution curves for different TiO_2 materials.

One was measuring the difference of protein concentrations in supernatant before and after adsorption; the other was directly measuring the protein concentration in the elution fraction. Specifically, the TiO_2 clusters are added to a protein mixture containing β-casein, horseradish peroxidase and β-lactoglobulin (each 0.75 mg/mL) for 2 hours. After centrifugation, the supernatant was analyzed by capillary electrophoresis (CE) with UV detection at 200 nm; the precipitate was washed with washing buffer (50% acetonitrile, 0.1% TFA) two times and subsequently eluted with NH_4OH aqueous solution (10%). The elution was collected with centrifugation and also analyzed by CE. Here, only β-casein is a phosphate-containing protein and from the adsorption isotherm curve in Figure 6.10, the equilibrium adsorption of β-casein by CNC1 can be reached in about 1 hour even with a pore size of ~2.3 nm. Figures 6.11a and 6.11b show the CE results by comparing the protein concentration in the supernatant. The migration times of peroxidase, β-casein and β-lactoglobulin are 2.6, 3.1 and 3.5 min, respectively. For the different materials, ranging from solid TiO_2 spheres to CNC1, CNC2, and CNC3, the peak area of β-casein decreases obviously. The corresponding adsorption efficiencies of β-casein by these four structures are 6.5%, 30.7%, 47.6% and 62.4%. In contrast, the peak areas from peroxidase and β-lactoglobulin vary little after adsorption, and only less than 10% of these proteins were adsorbed by TiO_2 materials. These protein-adsorbed TiO_2 structures were washed with washing buffer and then eluted by NH_4OH aqueous solution. Figures 6.11c and 6.11d show the CE analysis of the elution. It is clear that no peak of peroxidase (at ~ 2.6 min) or β-lactoglobulin (at ~ 3.5 min) is observed, and only

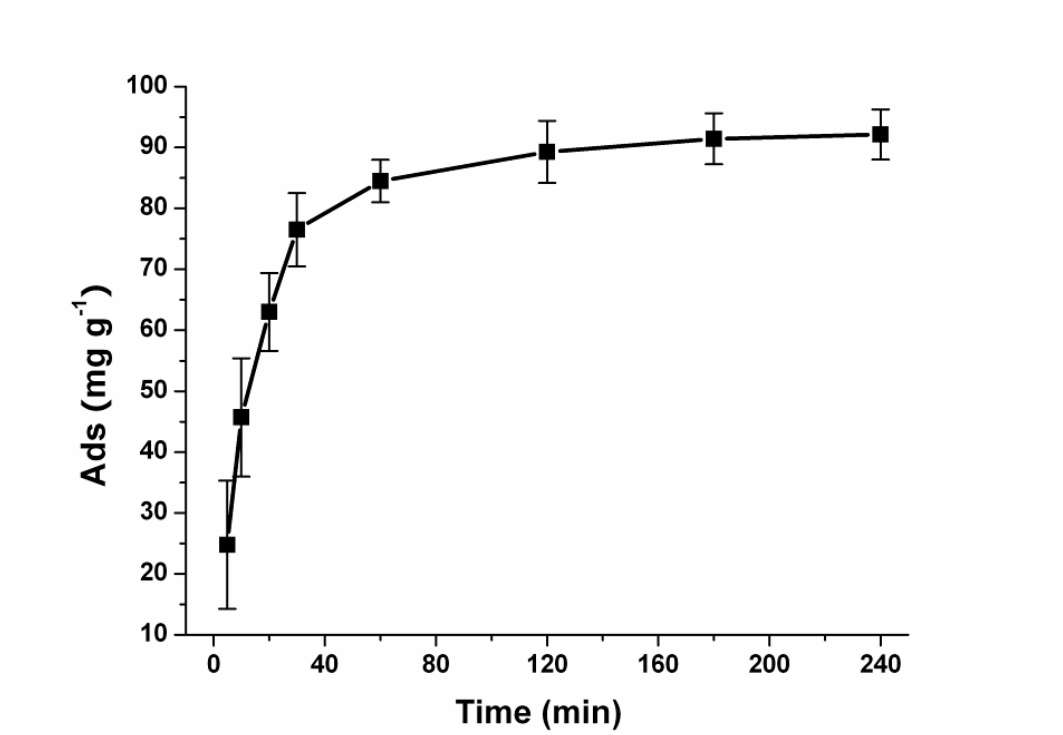

Figure 6.10 Equilibrium adsorption isotherm for β-casein on TiO_2 CNC1 determined by CE.

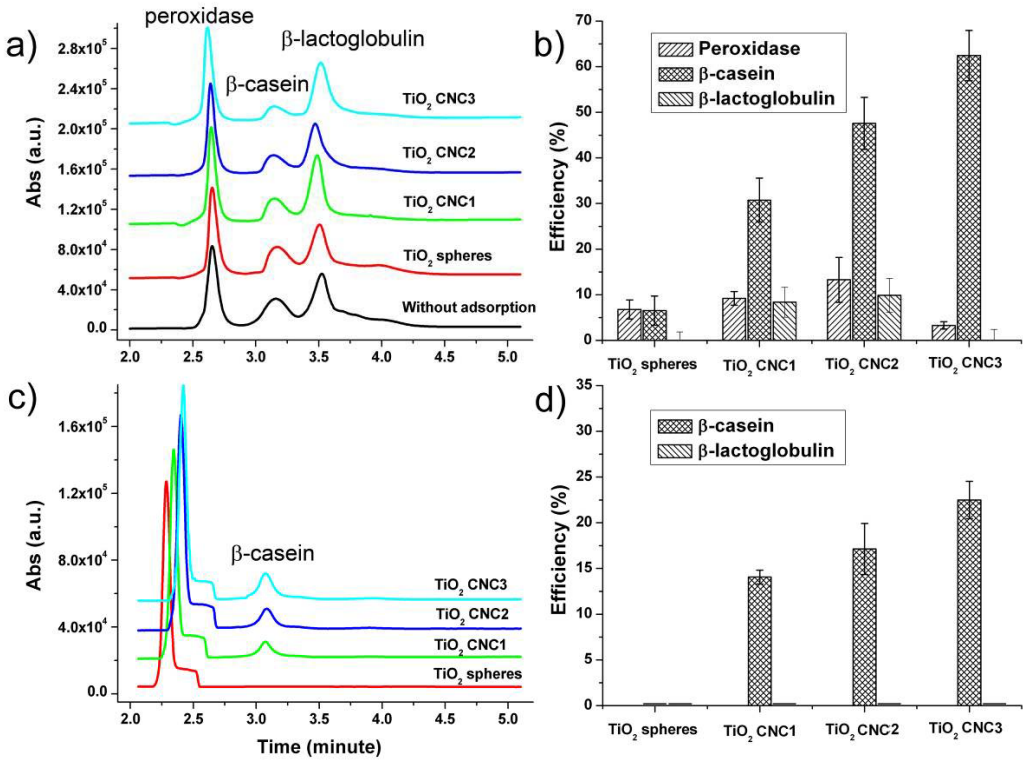

Figure 6.11 (a, c) Electropherograms of the protein mixture (peroxidase, β-casein and β-lactoglobulin): (a) supernatant and (c) elution after enriched by TiO_2 materials for 2 hours. (b, d) Corresponding adsorption efficiencies for proteins enriched by different TiO_2 materials.

β-casein can be detected. The strong peak at ~ 2.3 min can be attributed to the NH_4OH adsorption at 200 nm. TiO_2 CNC3 still shows the strongest adsorption for β-casein, which is consistent with the above results. After washing and eluting, the recovery efficiencies (the peak area after enrichment/the peak area before enrichment) for β-casein can reach ~50% for the three porous TiO_2 clusters. In contrast, TiO_2 solid spheres cannot retain any β-casein after washing two times, suggesting that the superior phosphorylated protein adsorption property of TiO_2 clusters may result from not only the affinity of the TiO_2 surface, but also the trapping effect of the mesoscale pores.

To test the size exclusion effect of the pores, we utilize a mixture of two phosphorylated proteins with different molecular weights, β-casein (Mw: 24 kDa) and fetuin (Mw: 48 kDa). As shown in Figure 6.12a, the peak area of β-casein decreases significantly after adsorption onto TiO_2 materials. In particular, the adsorption efficiency of β-casein by CNC3 is 52.9% calculated by the results from the supernatant and 25.8% from the eluted fraction. Because the molecular weight of fetuin is about twice that of β-casein, it is more difficult for fetuin to pass through the pores with sizes of 2~3 nm. Therefore, the amount of fetuin in the supernatant does not decrease much after adsorption by TiO_2 clusters (Figure 6.12a), while only about 6% of the fetuin was eluted after washing (Figures 6.12c and 6.12d). The adsorption of fetuin is believed to be only limited to the near surface regions of the clusters. From the comparison of adsorption efficiencies for the two proteins, it is clear that β-casein can be selectively adsorbed in the pores of the clusters, while fetuin is essentially excluded.

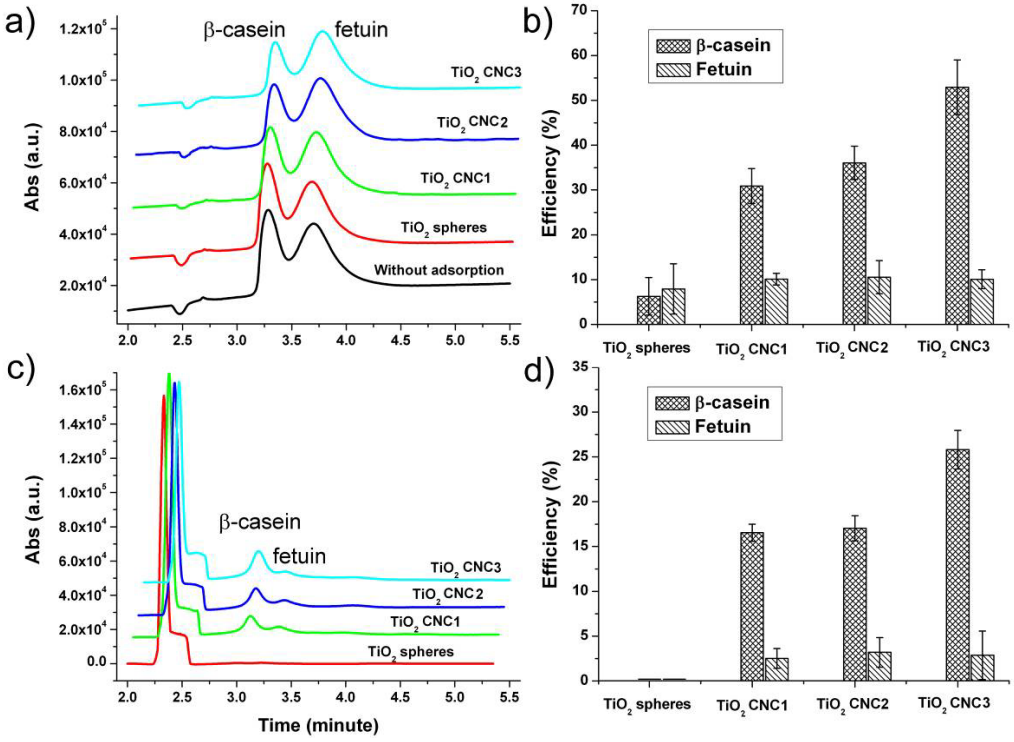

Figure 6.12 (a, c) Electropherograms of the protein mixture (β-casein and fetuin): (a) supernatant and (c) elution after enriched by TiO_2 materials for 2 hours. (b, d) Corresponding adsorption efficiencies for proteins enriched by different TiO_2 materials.

We also demonstrate the separation power of the TiO_2 nanocrystal clusters for low concentration proteins. In actual applications, it is a significant challenge to enrich low-abundance specific proteins in complex biosamples. A diluted protein mixture (β-casein, peroxidase, β-lactoglobulin and fetuin, 0.01 mg/mL) was incubated with TiO_2 materials for 2 hours. CE and MALDI-TOF MS were performed to analyze the eluted fraction for evaluating the enrichment efficiencies of the phosphorylated proteins. The CE analysis (Figure 6.13a) shows the enrichment efficiencies of β-casein by TiO_2 porous structures are 38.1%, 41.7% and 64.1% for three clusters, respectively. Nonporous TiO_2 spheres still cannot retain any phosphorylated proteins after being washed twice. The enrichment efficiencies for fetuin are much lower due to the size exclusion effect, while no peroxidase and β-lactoglobulin can be detected in the eluted fraction due to the lack of specific affinity. Figure 6.13b shows the MALDI-TOF MS spectra of the protein mixture before and after being treated by TiO_2 CNC3, clearly showing a high selectivity for enrichment of β-casein. When the mixture is directly analyzed without enrichment, the signal of β-casein is extremely poor and only peaks for β-lactoglobulin can be identified with a low signal/noise (S/N) ratio. After selective enrichment, the β-casein can be easily detected with a strong intensity and a high S/N ratio. Combining size-exclusion with high specific affinity, the mesoporous TiO_2 clusters hold great potential for the selective enrichment of phosphorylated proteins from complex biological samples.

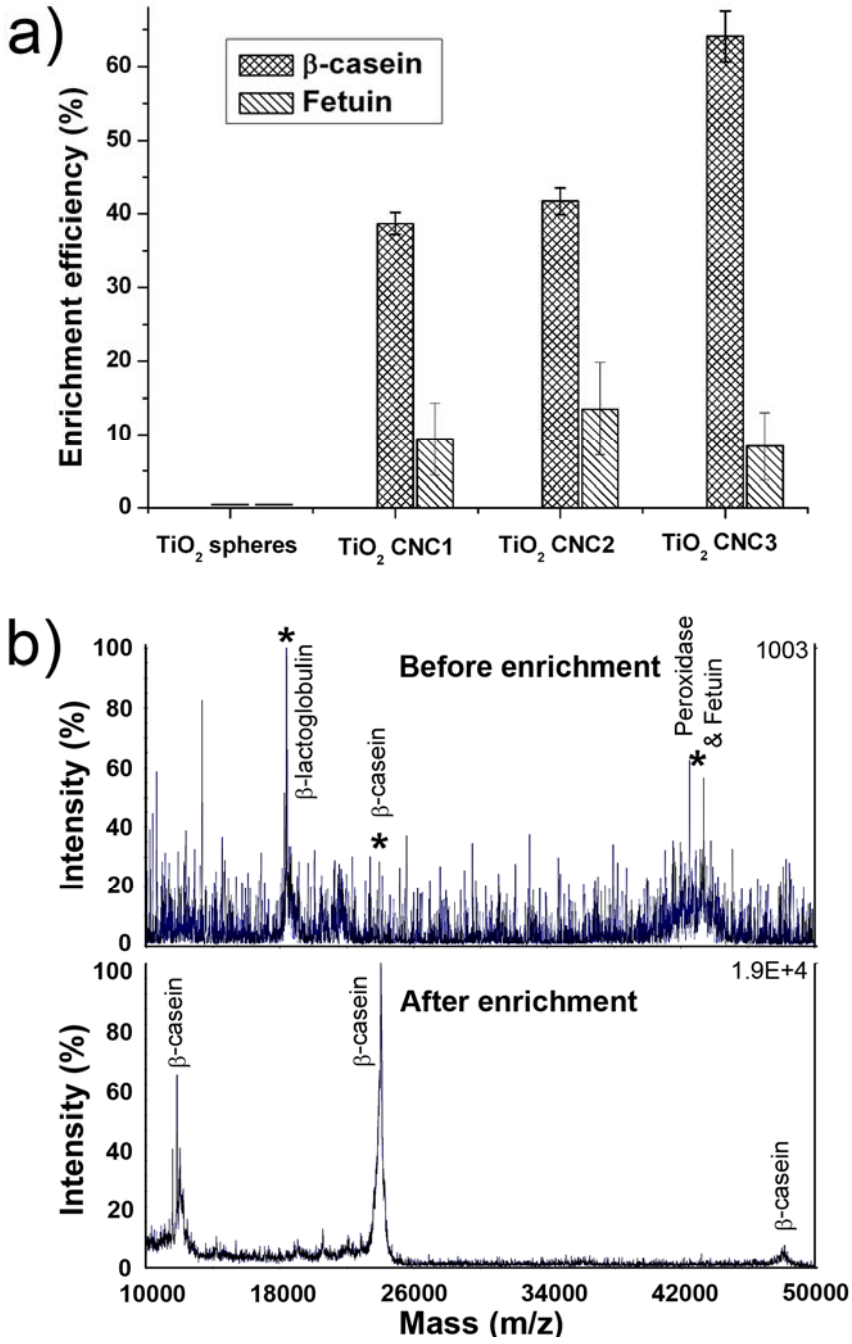

Figure 6.13 (a) Comparison of enrichment efficiencies of phosphorylated proteins by different TiO_2 materials from a mixture containing low concentrations of β-casein, peroxidase, β-lactoglobulin and fetuin; (b) MALDI-TOF MS spectra of protein mixture before and after enrichment by porous TiO_2 CNC3. Asterisks mark the peaks of the different proteins if they could be detected.

6.4 Conclusion

In summary, we have developed a general bottom-up assembly route to prepare porous nanocrystal clusters with specific surface affinity for biomolecules. The size and surface chemistry of the pores can be conveniently controlled by changing the properties of the building blocks during assembly. The demonstrated example of porous TiO_2 nanocrystal cluster structures shows ideal properties for the selective enrichment of phosphorylated proteins or phosphopeptides: 1) they can be dispersed stably in water; 2) their large specific surface area ensures a high capacity for capturing the target molecules; 3) because of the relatively large size of the clusters, they can be conveniently separated from the mixture by centrifugation; 4) the affinity of the TiO_2 surface for phosphate groups ensures the specific enrichment of biomolecules such as phosphorylated proteins and phosphopeptides. Elution can be easily performed by destroying the specific affinity using an alkaline solution. 5) the pore sizes are narrowly distributed and conveniently adjustable, promoting selective adsorption of proteins based on the size-exclusion mechanism. With all of these features, the porous TiO_2 clusters can effectively and selectively enrich low concentrations of phosphorylated proteins from protein mixtures. It is expected that the selective enrichment is not limited to phosphorylated proteins, but can also be extended to phosphate-containing peptides and DNA molecules. By properly selecting the oxide nanocrystals and their size and shape, this self-assembly strategy opens the door to a new class of mesoporous materials that may have wide applications in isolating biomolecules, in particular, low abundance proteomic biomarkers.

Reference

(1) Tian, R. J.; Zhang, H.; Ye, M. L.; Jiang, X. G.; Hu, L. H.; Li, X.; Bao, X. H.; Zou, H. F., *Angew. Chem. Int. Ed.* **2007,** 46, 962-965.

(2) Tian, R.; Ren, L.; Ma, H.; Li, X.; Hu, L.; Ye, M.; Wu, R. A.; Tian, Z.; Liu, Z.; Zou, H., *Journal of Chromatography A* **2009,** 1216, 1270-1278.

(3) Han, Y. J.; Stucky, G. D.; Butler, A., *J. Am. Chem. Soc.* **1999,** 121, 9897-9898.

(4) Terracciano, R.; Pasqua, L.; Casadonte, F. F.; S.; Preiano, M.; Falcone, D.; Savino, R., *Bioconjugate Chem.* **2009,** 20, 913-923.

(5) Rosa, T.; Marco, G.; Flaviano, T.; Luigi, P.; Pierosandro, T.; Mark Ming-Cheng, C.; Nijdam, A. J.; Emanuel, F. P.; Lance, A. L.; Giovanni, C.; Mauro, F.; Salvatore, V., *Proteomics* **2006,** 6, 3243-3250.

(6) Yiu, H. H. P.; Botting, C. H.; Botting, N. P.; Wright, P. A., *Phys. Chem. Chem. Phys.* **2001,** 3, 2983-2985.

(7) Hartmann, M., *Chemistry of Materials* **2005,** 17, 4577-4593.

(8) Katiyar, A.; Ji, L.; Smirniotis, P. G.; Pinto, N. G., *Microporous Mesoporous Mater.* **2005,** 80, 311.

(9) Katiyar, A.; Pinto, N. G., *Small* **2006,** 2, 644-648.

(10) Tanev, P. T.; Pinnavaia, T. J., *Science* **1995,** 267, 865-867.

(11) Kresge, C. T.; Leonowicz, M. E.; Roth, W. J.; Vartuli, J. C.; Beck, J. S., *Nature* **1992,** 359, 710-712.

(12) Davis, M. E., *Nature* **2002,** 417, 813-821.

(13) Dehong, C.; Fuzhi, H.; Yi-Bing, C.; Rachel, A. C., *Adv. Mater.* **2009,** 21, 2206-2210.

(14) Zhao, D.; Feng, J.; Huo, Q.; Melosh, N.; Fredrickson, G. H.; Chmelka, B. F.; Stucky, G. D., *Science* **1998,** 279, 548-553.

(15) Tang, J.; Wu, Y.; McFarland, E. W.; Stucky, G. D., *Chem. Comm.* **2004**, 1670-1671.

(16) Phonthammachaia, N.; Rumruangwonga, M.; Gularib, E.; Jamiesonc, A. M.; Jitkarnkaa, S.; Wongkasemjita, S., *Colloid Surf. A* **2004,** 247, 61-68.

(17) Hwang, Y. K.; Kwon, Y.-U.; Lee, K.-C., *Chem. Comm.* **2001**, 1738-1739.

(18) Yin, Y.; Alivisatos, A. P., *Nature* **2005,** 437, 664-670.

(19) Tao, A. R.; Habas, S.; Yang, P., *Small* **2008,** 4, 310-325.

(20) Wiley;, B.; Sun;, Y.; Chen;, J.; Cang;, H.; Li;, Z.-Y.; Li;, X.; Xia, Y., *MRS Bull.* **2005,** 30, 356-361.

(21) Kwon, S. G.; Hyeon, T., *Acc. Chem. Res.* **2008,** 41, 1696-1709.

(22) Li, Y.; Xu, X. Q.; Qi, D. W.; Deng, C. H.; Yang, P. Y.; Zhang, X. M., *J. Proteome Res.* **2008,** 7, 2526-2538.

(23) Zhang, Y. H.; Wang, X. Y.; Shan, W.; Wu, B. Y.; Fan, H. Z.; Yu, X. J.; Tang, Y.; Yang, P. Y., *Angew. Chem. Int. Ed.* **2005,** 44, 615-617.

(24) Klajn, R.; Bishop, K. J. M.; Fialkowski, M.; Paszewski, M.; Campbell, C. J.; Gray, T. P.; Grzybowski, B. A., *Science* **2007,** 316, 261-264.

(25) Wang, D. S.; Xie, T.; Peng, Q.; Li, Y. D., *J. Am. Chem. Soc.* **2008,** 130, 4016-4022.

(26) Hunter, T., *Cell* **2000,** 100, 113-127.

(27) Mann, M.; Jensen, O. N., *Nat. Biotechnol.* **2003,** 21, 255-261.

(28) Hu, L. H.; Zhou, H. J.; Li, Y. H.; Sun, S. T.; Guo, L. H.; Ye, M. L.; Tian, X. F.; Gu, J. R.; Yang, S. L.; Zou, H. F., *Anal. Chem.* **2009,** 81, 94-104.

(29) Feng, S.; Ye, M. L.; Zhou, H. J.; Jiang, X. G.; Jiang, X. N.; Zou, H. F.; Gong, B. L., *Mol. Cell. Proteomics* **2007,** 6, 1656-1665.

(30) Mazanek, M.; Mituloviae, G.; Herzog, F.; Stingl, C.; Hutchins, J. R. A.; Peters, J. M.; Mechtler, K., *Nat. Protoc.* **2007,** 2, 1059-U1.

(31) Cantin, G. T.; Shock, T. R.; Park, S. K.; Madhani, H. D.; Yates, J. R., *Anal. Chem.* **2007,** 79, 4666-4673.

(32) Rainer, M.; Sonderegger, H.; Bakry, R.; Huck, C. W.; Morandell, S.; Huber, L. A.; Gjerde, D. T.; Bonn, G. K., *Proteomics* **2008,** 8, 4593-4602.

(33) Dubrovska, A.; Souchelnytskyi, S., *Proteomics* **2005,** 5, 4678-4683.

(34) Adam, G. C.; Sorensen, E. J.; Cravatt, B. F., *Mol. Cell. Proteomics* **2002,** 1, 781-790.

(35) Trentler, T. J.; Denler, T. E.; Bertone, J. F.; Agrawal, A.; Colvin, V. L., *J. Am. Chem. Soc.* **1999,** 121, 1613-1614.

(35) Bai, F.; Wang, D. S.; Huo, Z. Y.; Chen, W.; Liu, L. P.; Liang, X.; Chen, C.; Wang, X.; Peng, Q.; Li, Y. D., *Angew. Chem. Int. Ed.* **2007,** 46, 6650-6653.

(36) Kim, J.; Lee, J. E.; Lee, S. H.; Yu, J. H.; Lee, J. H.; Park, T. G.; Hyeon, T., *Adv. Mater.* **2008,** 20, 478-483.

(37) Ye, J.; Zhang, X.; Young, C.; Zhao, X.; Hao, Q.; Cheng, L.; Jensen, O. N., *J. Proteome Res.* **2010,** ASAP, doi: 10.1021/pr100075x.

(38) Torta, F.; Fusi, M.; Casari, C. S.; Bottani, C. E.; Bachi, A., *J. Proteome Res.* **2009,** 8, 1932-1942.

(39) Brockman, A. H.; Dodd, B. S.; Orlando, R., *Anal. Chem.* **1997,** 69, 4716-4720.

(40) Ge, J. P.; Hu, Y. X.; Yin, Y. D., *Angew. Chem. Int. Ed.* **2007,** 46, 7428-7431.

Chapter 7

Controlled Assembly at Nanocrystal-Polymer Interface: A General Method for Hollow Colloidal Nanocrystal Clusters

7.1 Introduction

Controlled assembly of nanoparticles opens a new avenue to manufacture integrated materials with new physical and chemical properties, which are highly desirable in many important applications ranging from catalysis, biological labeling to drug encapsulation and delivery.[1-6] Ligand-stabilized colloidal nanoparticles, predominantly prepared through thermolytic routes by reacting inorganic precursors in organic solvents at high temperatures, are ideal building blocks for this assembly due to their narrow size distribution, uniform shape and tunable properties.[7, 8] Moreover, the resulting nanoparticles retain the hydrophobic capping ligands, which can be tailored the interactions between the particles and the surroundings.[9-11] The assembly of nanoparticles on flat surface has been reported for the synthesis of single or binary nanoparticle superlattices by spin, dip coating or the Langmuir-Blodgett technique.[12-14] However, the collective properties of these superlattices are still scarce, and their use as real materials in applications is still at the very beginning. Compared with the flat surface, liquid-liquid interface offers more surface area, greater access to the surrounding environment and easier surface modification for the assembly of the colloidal nanoparticles. Moreover, the assembly can be well dispersed in the solution, which makes the characterization much more efficient and continent.[15-20] Compared with layer-by-layer polyelectrolyte deposition,[21-24] assembly at the liquid-liquid interface requires fewer steps, affords

ultrathin nanoparticle shell, and may reduce structural defects due to the mobility of nanoparticles at the fluid interface.[25] Recently, nanoparticle assembly based on emulsion-evaporation method has also been investigated as a route for synthesis of three-dimensional superlattices[26] or mesoporous clusters[27, 28], which have been applied in bioseparation[29, 30] and photo catalysis[31]. More recently, Isojima et al. introduced polystyrene as solid template in this one-step solvent evaporation method to fabricate toroidal or Janus iron oxide nanoparticle clusters.[32]

Efficient encapsulation of active ingredients such as drugs, proteins, or even living cells is of increasing interest for a wide range of applications, such as drug delivery and biomedical applications.[33, 34] A very promising process so far was assembling submicrometer-size particles at liquid-liquid interfaces, followed by sintering to lock the particle together.[35] The resulting shell structure was built by quasi-hexagonal packing of the particles with narrow size distribution, which gave uniform pores in the range of several hundred nanometers. However, it remains a challenge to fabricate capsules with controlled pore size and pore size distribution on the nanometer scale, which is technologically important and a long-standing goal for drug delivery, cell encapsulation, cancer treatment and other applications.[36] Therefore, uniform nanoparticles with diameters ranging from 2 to 50 nm were naturally chosen as alternations to assemble at liquid-liquid interface to form capsules or membranes with nanoscale pores. To fabricate mechanically stable capsule and membranes from spherical nanoparticle assemblies, the particles have to be crosslinked at the interface by the surface modification with reactive organic molecules.[9, 25, 37, 38] However, most of these researches were still focused on the

proof-of-concept for the use of nanoparticles in the assembly, instead of the preparation of stable and applicable materials. Moreover, the liquid-liquid interface produced by emulsion droplet is generally larger than several micrometers, which may be a problem for some potential applications.

We develop a novel method for hollow colloidal nanocrystal clusters (HCNCs) within submicron meter size by clustering of nanoparticles at polymer-water interface in this work. As shown in Figure 7.1, ligand capped nanocrystals and liquid hydrophobic polymers are dispersed in an oil phase (cyclohexane), which is then mixed with SDS aqueous solution to form an oil-in-water emulsion system. Upon the evaporation of the low boiling point oil, the nanoparticles are expelled by the polymer as its concentration increases in the oil droplet and finally assembled at polymer-water interface to form a monolayer. In general, oleic acid or other organic ligands capped nanoparticles are hydrophobic and, therefore, water-in-oil emulsions are favored. In our experiment here, the surfactant SDS is adsorbed onto the cluster surface through the hydrophobic-hydrophobic interactions between the tails of the SDS and the capping ligands on the nanoparticles to form a bilayer structure, making the nanoparticles more hydrophobic and subsequently help to produce oil-in-water emulsions. The negatively charged heads of SDS ($-SO^{3-}$) help the clusters disperse well in water and make the clusters ready for the next step of silica coating.

7.2 Experimental Section

7.2.1 Materials

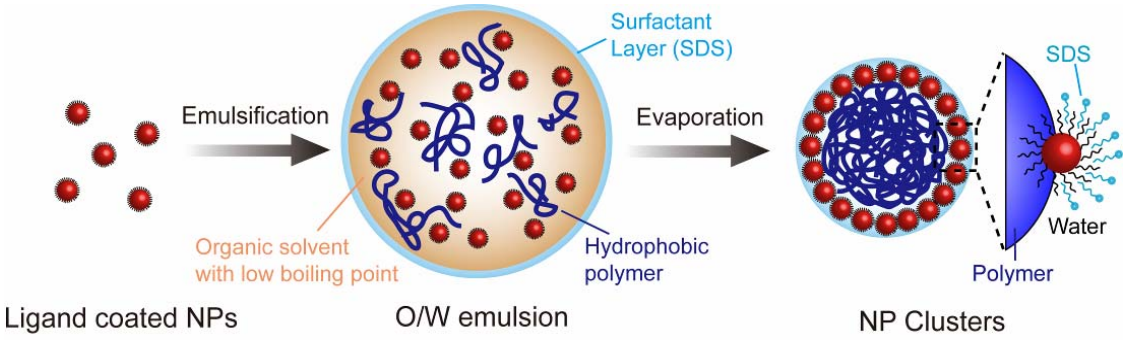

Figure 7.1 Schematic illustration of the preparation procedure of hollow colloidal nanocrystal clusters (HCNCs). Nanocrystals and hydrophobic polymers are dispersed in organic solvent and then emulsified with SDS aqueous solution. After the organic solvent was evaporated, the nanocrystals can self-assemble at the polymer-water interface.

Tetraethyl orthosilicate (TEOS), sodium dodecyl sulfate (SDS), ammonium hydroxide solution (~28% NH3 in water), oleylamine, trioctylphosphine oxide (TOPO), trioctylphosphine (TOP), iron pentacarbonyl ($Fe(CO)_5$), dioctyl ether, 1-octadecene (ODE, 90%), zirconium(IV) isopropoxide propanol complex, nickel(acetylacetonate)2, cadmium nitrate tetrahydrate, sodium myristate, selenium, zinc oxide, cadmium oxide, sulfur, oleic acid, oleylamine, triphenylphosphine, Ytterbrium chloride hexahydrate, Yttrium chloride hexahydrate, Erbium chloride hexahydrate, Poly(acrylic acid) (PAA, Mw=1,800), poly(1-decene) (viscosity: 50 cSt at 40 °C), hydrogenated poly(1-decene) (viscosity: 20 cSt at 40 °C) and Polystyrene (Mw=192K)were purchased from Aldrich Chemical Co. Ethyl alcohol (denatured), methanol, toluene (99.8%), cyclohexane, chloroform, acetone and sodium hydroxide (98.8%) were obtained from Fisher Scientific. All chemicals were used as received without further treatment.

7.2.2 Synthesis of γ-Fe_2O_3 Nanocrystals

Superparamagnetic γ-Fe_2O_3 nanocrystals were synthesized using a thermolysis process. $Fe(CO)_5$ (0.2 mL, 1.52 mmol) was added to a mixture containing 10 mL of octyl ether and 1.28 g of oleic acid at 100 ^oC. The solution was then heated to 290 °C under an argon atmosphere and maintained at this temperature for 1 h. After cooling down to 200 ^oC, the solution was bubbled with air for 2 hours. After cooling down to room temperature, ethanol was added to the solution to precipitate γ-Fe_2O_3 nanoparticles, which were then separated by centrifugation. Finally, the resulting black powder was re-dispersed into cyclohexane.

7.2.3 Synthesis of CdSe@CdZnS Nanoparticles (QD)

CdSe@CdZnS nanoparticles were prepared by a reproducible method reported by Dubertret group. First, four reagents were prepared exactly based on the reference (1) **Cadmium myristate** (2) **Cd(oleate)$_2$ 0.5 M in oleic acid** (3) **Zn(oleate)$_2$ 0.5 M in oleic acid** and (4) **TOPS 0.5 M solution in TOP**. Later, 1-octadecene (16 mL), Cadmium myristate (170 mg) and selenium (12 mg) were mixed in a flask, and kept at room temperature in vacuum for 1 hour. After that, the solution was heated up to 240 ^{o}C under Ar atmosphere and aged for 10 min, followed by injection of 1 mL oleic acid and wait a further 2 min. After cooling the solution down to room temperature, the CdSe nanoparticles were precipitated by adding excess ethanol and then harvested by centrifugation. The resulting powder was re-dispersed in 10 mL of chloroform as a CdSe stock solution. **CdZnS shell coating:** trioctylamine (8 mL), CdSe stock solution (2 mL), Zn(oleate)$_2$ stock solution (400 μL) and Cd(oleate)$_2$ stock solution (200 μL) were mixed in a flask. Then, the mixture was degassed under vacuum for 1 hour and heated to 300 ^{o}C under Ar atmosphere. Mixture of 4.4 mL trioctylamine and 0.6 mL TOPS was slowly added to the hot solution using a syringe pump at the rate of 10 mL/h. The final mixture solution was kept at 300 ^{o}C for 2 hours. The core/shell CdSe@CdZnS nanoparticles were precipitated by ethanol and finally dispersed in cyclohexane.

7.2.4 Synthesis of ZrO_2 Nanopartilces

ZrO_2 nanoparticles were prepared by a nonhydrolytic solution-based reaction. Trioctylphosphine oxide (10 g) was heated at 150 ^{o}C for 30 minutes in vacuum. After cool the solution temperature to 60 ^{o}C under N_2 atmosphere, zirconium(IV) isopropoxide propanol complex (1.56 g) and $ZrCl_4$ (1.16 g) were added into the solution. The resulting

mixture was then heated to 340 ^{o}C and further heated for 2 hours at 340 ^{o}C to ensure the complete reaction. After cooling the system down to 80 ^{o}C, 20 mL of acetone was added to yield a white precipitate, which was isolated by centrifugation and subsequently washed with a cylcohexane/acetone mixture to remove extra surfactant. The resulting powder was re-dispersed in cyclohexane.

7.2.5 Synthesis of $NaYF_4$:Yb,Er Nanocrystals

Upconversion fluorescent $NaYF_4$:18%Yb, 2%Er nanocrystals were synthesized according to the reference. $YCl_3 \cdot 6H_2O$ (242.7 mg), $YbCl_3 \cdot 6H_2O$ (70.0 mg) and $ErCl_3 \cdot 6H_2O$ (7.6 mg) were dissolved in 2 mL methanol first and then mixed with oleic acid (6 mL) and 1-octadecene (15 mL) in a 100 three-neck flask. The solution was degassed at 150 ^{o}C under Ar for 30 min, and then cooled down to room temperature. 10 mL of methanol solution containing NaOH (0.1 g) and NH_4F (0.1481 g) was added and stirred for 30 min. After that, the solution was slowly heated to 110 ^{o}C and kept at 110 ^{o}C for 0.5 h to remove methanol and small amount of water. During this period, one neck of the flask was left open under the flow of Ar gas. Then, the solution was quickly heated to 320 ^{o}C and aged for 1 h under Ar protection. After the solution as cooled down, acetone was added to precipitate the nanoparticles. The final $NaYF_4$:Yb,Er nanocrystals was redispersed cyclohexane after washing with cyclohexane/acetone two times.

7.2.6 Synthesis of NiO Nanoparticles

The NiO nanoparticles were synthesized by the hot injection method according to the previous report. Typically, triphenylphosphine (5 g) was heated at 120 ^{o}C for 30 minutes in vacuum, and then increase the temperature to 230 ^{o}C under Ar atmosphere. After that, a mixture of nickel(acetylacetonate)$_2$ (0.5 g) and oleylamine (2 mL) was

quickly injected and the solution was aged for 20 mins. After cooling down to 160 ^{o}C, the solution was bubbled with air for 1 hour. Ethanol was added to the solution to precipitate NiO nanoparticles, and then retrieved by centrifugation. The final black powder was redispersed in cyclohexane after washing two times.

7.2.7 Self-assembly of Nanocrystals on Polymer Surface

The nanocrystal/polymer hybrid clusters were assembled in emulsion oil droplets by evaporating low-boiling-point solvent (the oil phase). In a typical experiment, 1 mL of cyclohexane solution of nanoparticles (5 mg) was mixed with poly(1-decene) (3 mg) and then added into an aqueous solution of sodium dodecyl sulfate (SDS) (56 mg in 10 mL H_2O), followed by sonication for 4 minutes. The mixture was then heated to 65 ^{o}C in a water bath for 4 hours. After that, the reaction solution was cooled down to room temperature. The final products were washed with water one time and re-dispersed in 3 mL of water.

7.2.8 Silica Coating/Calcination/Silica Removing of Clusters

nanocrystal/polymer hybrid clusters were coated with a layer of SiO_2 by using a modified Stöber process. Typically, the above aqueous solution of clusters (3 mL) was first mixed with ethanol (20 mL) and ammonium hydroxide (1 mL, 28%) aqueous solution. Then TEOS (30 μL) was injected to the solution and reacted for 20 min under vigorous stirring. The core/shell colloids were collected by centrifugation and washed with ethanol three times. After dried in the vacuum over night, the precipitate was heated to 600 ^{o}C for 2 hours in air using a heating rate of 5 ^{o}C/min to remove organic agents. Then the calcined particles was dispersed in NaOH aqueous solution (1 M) for 3~4 hours

under stirring to remove the silica shell. The final hollow nanoparticle clusters were collect by centrifugation and washed with distilled water several times.

7.2.9 Characterization

The morphology of nanostructures was investigated using a Philips Tecnai 12 transmission electron microscope (TEM) and Philips FEI XL30 scanning electron microscope (SEM). The composition of the materials was confirmed by using powder X-ray diffraction on a Bruker D8-Advance powder diffractometer operating at 40 kV, 40 mA for Cu Kα radiation (λ=1.5406 Å). Dynamic light scattering (DLS) and zeta potential analysis was performed on a ZetaPALS system. Thermogravimetric analysis (TGA) was carried out under nitrogen atmosphere on a TA Instruments SDT Q500 thermal analyzer. All the samples were kept at 80 ^{o}C for 6 hours before the measurement. The magnetic properties were measured with a magnetic properties measurement system (MPMS) from Quantum Design, which utilities a superconducting quantum interference device (SQUID) magnetometer.

7.3 Results and Discussion

We chose γ-Fe_2O_3 nanoparticle as the model particles to study the assembly because of their uniform and tunable sizes, good stability, and unique magnetic properties. Uniform γ-Fe_2O_3 nanoparticles with the exact size range from 5 to 20 nm can routinely prepared by a thermolytic route using oleic acid as capping ligand.[39] In particular, 12.7-nm γ- Fe_2O_3 nanoparticles (5 mg) together with liquid hydrophobic poly(1-decene) (3 mg) were dispersed in cyclohexane, which was then emulsified in SDS aqueous solution to produce an O/W emulsion system. Upon the evaporation of the low

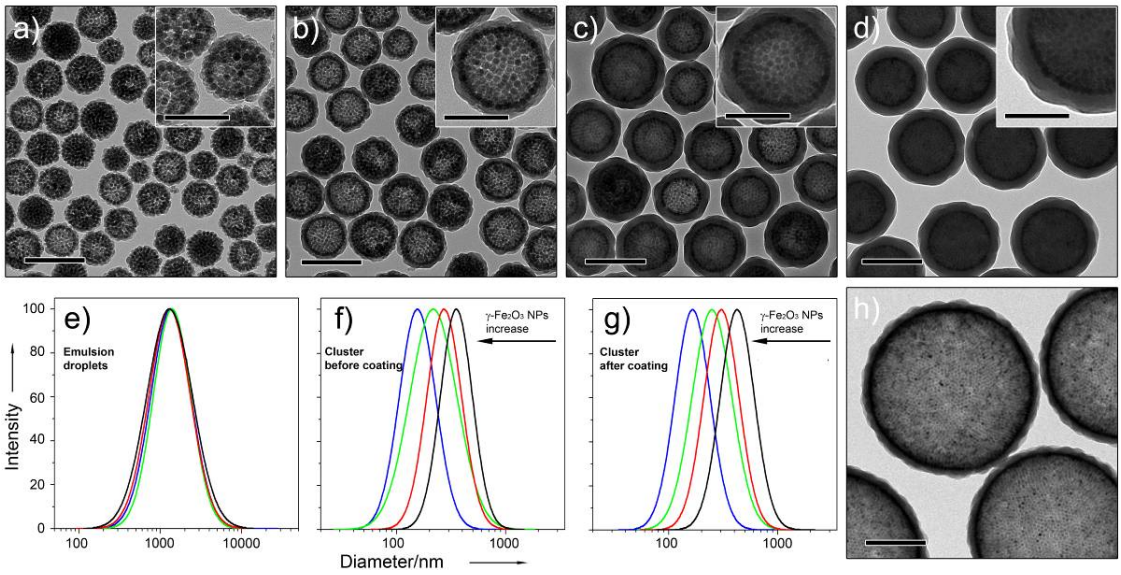

Figure 7.2 (a-d, h) TEM images of silica coated HCNCs assembled by poly(1-decene) (3mg) and different amount of 12.7-nm γ–Fe_2O_3: (a) 10 mg, (b) 5 mg, (c) 2.5 mg and (d) 1 mg. (h) 5 mg of γ–Fe_2O_3 and 30 mg poly(1-decene). Scale bar: 200 nm. Insets are high magnification TEM images with scale bar 100 nm. (e-g) Size distribution of the corresponding cluster structures analyzed by dynamic light scattering: (e) emulsion droplets before solvent evaporation; (f) γ–Fe_2O_3 HCNCs after solvent evaporation in water bath (65 ^{o}C) for 4 h; (g) silica coated γ–Fe_2O_3 HCNCs.

boiling point cyclohexane at about 65 ^{o}C, the γ-Fe_2O_3 nanoparticles were assembled at the polymer-water interface to form a nanoparticle monolayer clusters. Although the as-synthesized nanoparticle/polymer hybrids are relatively stable, which can be stored in the aqueous solution for several days without obvious changes, the hollow structures will collapse after drying on a substrate. To protect the assembly and enhance the mechanical strength of the hollow clusters, a thin layer of silica were coated using the well known stöber method.[40] As shown in Figure 7.2c, γ-Fe_2O_3 nanoparticle monolayer at the interface can be clearly seen and the silica layer was coated on each nanoparticle monolayer cluster. As monitored using dynamic light scattering (Figure 7.2e-g), the initial emulsion droplets were fairly polydispersed with a mean diameter around 1.2 μm. The average size of the emulsions was shrunk to several hundred nanometers after evaporation of cyclohexane based on the remaining of γ-Fe_2O_3 nanoparticles and poly(1-decene).

To study the critical factors that influence the formation of HCNCs, we carried out assemblies by systematically varying the parameters, such as the ratio of nanoparticle to polymer, the size of γ-Fe_2O_3 nanoparticles, as well as the type of polymers. The size of the assembled clusters can be tuned by controlling the amount ratio of γ-Fe_2O_3 nanoparticles to poly(1-decene). In a series of fabrication, we varied only the amount of γ-Fe_2O_3 nanoparticles (12.7 nm) ranged from 1 to 10 mg but kept the poly(1-decene) (3 mg) unchanged. The size difference of these assemblies was first monitored by dynamic light scattering. Figure 7.2e shows the average sizes and distributions of initial emulsion droplets are almost the same under different nanoparticle/polymer ratios. After

evaporation, the cluster size decreases as the γ-Fe_2O_3 nanoparticle increases, allowing a range of tuning from 420 to 160 nm (Figure 7.2f). Silica coating slightly increases the average size of the corresponding clusters in the DLS measurement. The size and morphology of silica coated clusters were further characterized using transmission electron microscope. As shown in Figures 7.2a-d, γ-Fe_2O_3 nanoparticles were clearly packed to form shell structures with silica layers outside. Small amount of γ-Fe_2O_3 nanoparticles leads to large colloidal cluster, which is consistent with the DLS analyses. In addition, relatively small amount of polymer can not evenly distribute to each emulsion droplet during the emulsification, and consequently multiple nanoparticle layers or solid nanoparticle clusters can be produced after evaporation of droplet solvent (Figure 7.2d). On the other hand, from Figure 7.2a to 7.2d, the thickness of silica layer decreases from 40 to several nanometers as γ-Fe_2O_3 nanoparticle increases under the same adding amount of TEOS, indicating more nanoparticle clusters per unit volume were produced before coating, which can be served as an indirect proof that more γ-Fe_2O_3 nanoparticles lead to smaller clusters. To prepare even larger clusters, we can simply extend the ratio of polymer to nanoparticle. As an example shown in Figure 7.2h, clusters with average diameter larger than 600 nm were produced by mixing 5 mg of γ-Fe_2O_3 nanoparticles with 30 mg of poly(1-decene). The γ-Fe_2O_3 nanoparticles on polymer droplets are clearly arranged in a hexagonal close-packing structure to form a nanoparticle shell with precisely controlled pore in several nanometers.

The interfacial assembly of nanoparticles here, which is similar to Pickering emulsions[41], is driven by a decrease of total free energy (ΔE). The three contributions to

the interfacial energy arise from the particle-oil interface ($\gamma_{P/O}$), the particle-water interface ($\gamma_{P/W}$) and the oil-water interface ($\gamma_{O/W}$). The energy difference (ΔE), due to the assembly of a single particle at the oil-water interface can be given by

$$\Delta E = -\frac{\pi r^2}{\gamma_{O/W}} \times (\gamma_{O/W} + \gamma_{P/O} - \gamma_{P/W}),$$

where r is the effective radius of the nanoparticle.[1, 15] On the basis of published values for $\gamma_{O/W}$ of 52 mN/m,[42] and on estimates for $\gamma_{P/O}$ of 40 mN/m (nanoparticles can not be dispersed in poly(1-decene) at all) and for $\gamma_{P/W}$ of 15 mN/m (after SDS adsorption, the particles can be well dispersed in water phase)[15], ΔE is about -3900 k_BT for 12.7-nm nanoparticles in our typical poly(1-decene)/water emulsion. The energy gain is much larger than thermal energy (a few k_BT), which leads to an effective confinement of nanoparticles at the interface. In a typical emulsion system, the total energy gain in assembly is determined by the square of the particle radius r due to energy $\gamma_{P/O}$, $\gamma_{P/W}$ and $\gamma_{O/W}$ are fixed. Therefore, the assembly should be less stable for smaller nanoparticles than for larger ones. To study the size dependence of nanoparticle on the assembly at polymer-water interface, we chose oleic acid capped γ-Fe_2O_3 nanoparticles with three sizes: 21.0, 12.7 and 5.9 nm. Due to the maximum cross section area of nanoparticle per mass unit is inverse proportion to the particle size, we used 10, 5, 2.5 mg nanoparticles for the three sizes 21.0, 12.7 and 5.9 nm respectively to ensure the same coverage ability of nanoparticles. Figure 7.3 presents the TEM images of the γ-Fe_2O_3 nanoparticles and corresponding silica-coated assembled clusters. Larger particles (21.0 and 12.7 nm) can be strongly held at the interface to a form a monolayer. The average size of the clusters

was smaller for 21.0-nm particles than that assembled by 12.7-nm ones, which indicates the larger particles have stronger stabilization effect for the assembly as the equation shows. However, 5.9-nm particles can not be effectively packed as a single layer at the interface due to the relatively lower energy gain for the smaller particles. As an alternation, the smaller particles form multiple layers at the interface to stablize the polymer droplet in the system.

In addition to the size of nanoparticles, the wettability of the particle surface is also related to the free energy, and subsequently affects the nanoparticle assembly at the interface. According to the equation above, values of $\gamma_{O/W}$ and $\gamma_{P/O}$ can be tuned by using different dispersion oil phases (hydrophobic polymers). Obviously, larger $\gamma_{O/W}$ and $\gamma_{P/O}$ values should produce a more stable interfacial assembly. 1-octadecene, hydrogenated poly(1-decene) and polystyrene (Mw=192000) were chosen to study the different assembly behaviors and the TEM results are shown in Figure 7.4. 1-octadecene and hydrogenated poly(1-decene), with lower $\gamma_{O/W}$ and $\gamma_{P/O}$ values than poly(1-decene), can not effectively hold a monolayer of nanoparticles at the interface; While polystyrene with a large molecular weight can be easily severed as a rigid template to form the nanoparticle single shell.

In our experiment, the polymer droplet surface was first completely covered by nanoparticles after evaporation of cyclohexane, and then a silica layer was coated to protect the assembled HCNCs. Once the nanoparticles were fixed, the polymers can easily penetrate from nanoparticle and silica shell in ethanol and be removed by washing with ethanol several times. Thermogravimetric analysis of initial γ-Fe_2O_3 nanoparticles,

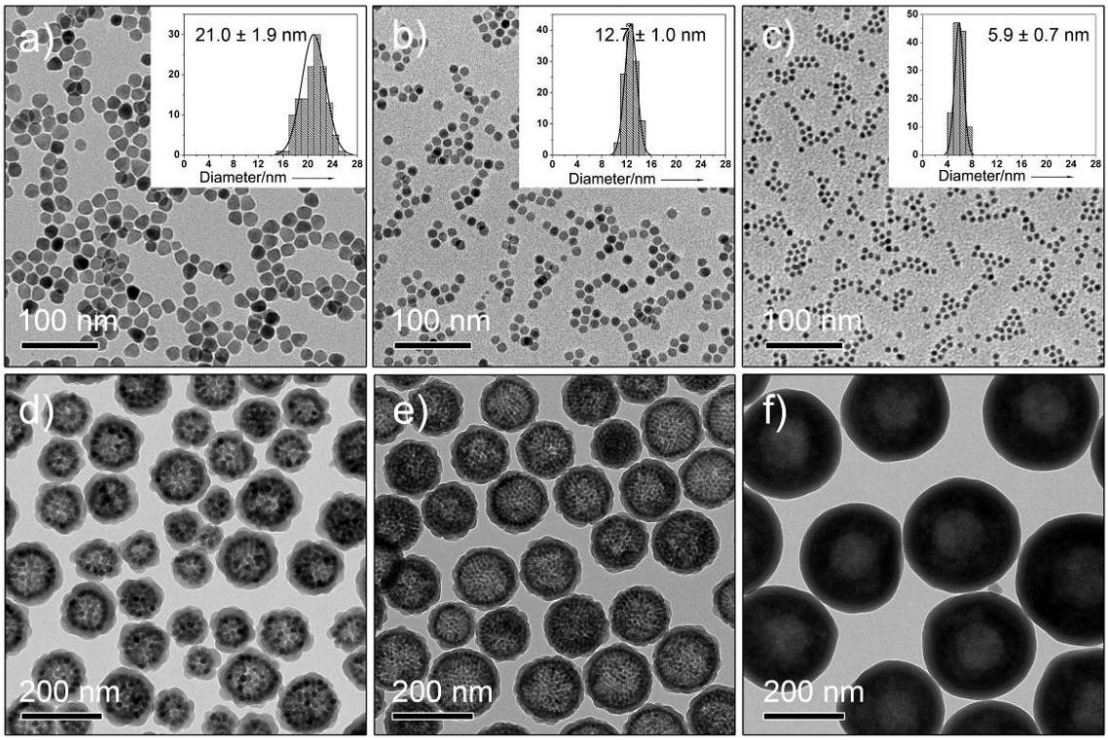

Figure 7.3 (a-c) TEM images of γ-Fe_2O_3 nanoparticles with different sizes and (d-f) TEM images of silica coated γ-Fe_2O_3 HCNCs assembled by poly(1-decene) (3mg) and nanoparticles with different size and amounts: (d) 21.0-nm, 10 mg; (e) 12.7-nm, 5 mg; (f) 5.9-nm, 2.5 mg.

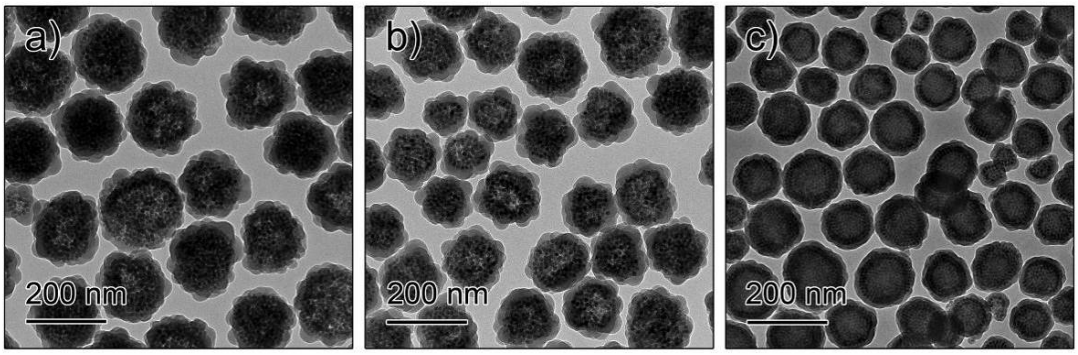

Figure 7.4 TEM images of 12.7-nm γ-Fe2O3 nanocrystals assembled at different dispersion oil/water interface: (a) ODE, (b) hydrogenated poly(1-decene) and (c) polystyrene.

corresponding HCNCs before and after silica coating shows the steps in weight loss (Figure 7.5). The evaporation of the low boiling point solvent or trapped moisture in nanoparticles leads to less than 5% loss in the temperature range from 20 to 200 ^{o}C for both initial nanoparticles and silica coated HCNCs. The percentage loss in these range reached to 22% for HCNCs without silica coating even after the sample was kept at 80 ^{o}C for 6 hours. The next weight loss steps in the temperature range 200-600 ^{o}C are mainly attributed to evaporation and decomposition of organic substances, such as oleic acid, SDS and poly(1-decene). The value of weight loss is about 10% in the coated HCNC sample, while before coating this value rises to 45% due to the presence of the poly(1-decene). Finally, 5% weight loss step above 600 ^{o}C can be explained by decomposition of hydroxyl groups on the iron oxide surface and followed by the release of chemically bound oleic acid, which is similar for all the three samples. The obvious difference of weight loss before and after silica coating in the middle step clearly proves the polymer penetration process during the ethanol washing. Even for high molecular weight polymers (polystyrene, Mw=192000), the leakage still can happen after the silica coated nanoparticle/PS structures were stored in ethanol for 1 week. All these results suggested the silica/nanoparticle shell is porous enough for the polymer penetration and the polymers can be conveniently removed by ethanol washing.

The assembled nanoparticles at the interface were locked together to form a stable shell by calcination. The silica coating before calcination is critically important for the successful fabrication of stable and dispersed HCNCs. First, the silica layer severs as a matrix to protect the nanoparticle layer from breaking at high temperatures. Second, the

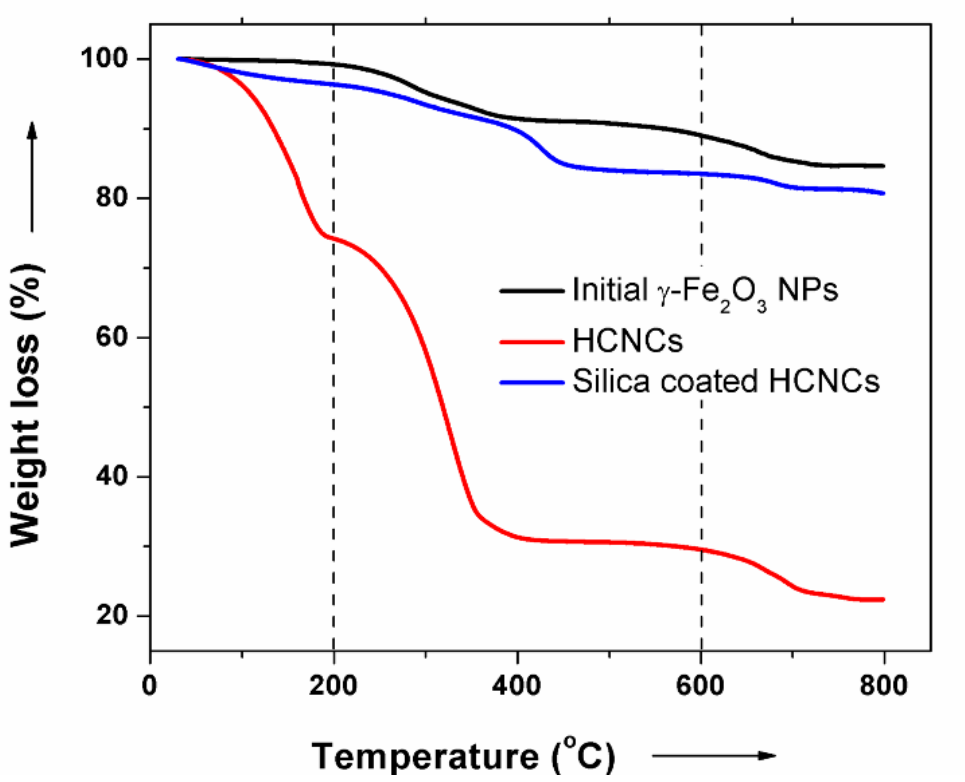

Figure 7.5 TGA curves of original γ-Fe_2O_3 NPs, γ-Fe_2O_3 HCNCs before and after silica coating.

silica coating protects the clusters from aggregation during calcination. Third, the etching process after calcination introduces a relatively high density of hydroxyl groups so that the cluster surface becomes negatively charged, making clusters dispersible in water. To make nanoparticles in the shell partially fused but keep the morphology and properties, different calcination temperatures ranged from 300 ^{o}C to 800 ^{o}C were tested. Without calcination or under low calcination temperature (below 500 ^{o}C), nanoparticle shells could not be efficiently locked together, and they were decomposed into single nanoparticles or some random aggregations. Calcination at 500 ^{o}C makes nanoparticle fused a little to form stable nanoparticle shells, but the yield is not very high. Temperatures above 600 ^{o}C are good choices for locking neighboring γ-Fe_2O_3 nanoparticles. An example is shown in Figure 7.6b, which are TEM images of γ-Fe_2O_3 HCNCs after calcination at 600 ^{o}C and silica removing. As a comparison, Figure 7.6a shows the original silica coated γ-Fe_2O_3 HCNCs. Upon heating, γ-Fe_2O_3 nanoparticles coalesced slightly, creating a bridge for the adjacent nanoparticles. The resultant nanoparticle shell packed by 12.7-nm γ-Fe_2O_3 nanoparticles, therefore, contains a precise array of uniform holes in the stable shell. Normally, γ-Fe_2O_3 nanoparticles will aggregate and be transformed to antiferromagnetic hematite α-Fe_2O_3 phase above certain temperature,[43] typically around 400 ^{o}C (Figure 7.7). The as-synthesized silica coated γ-Fe_2O_3 HCNCs demonstrated incredible thermal stability, which is characterized by XRD analysis and room-temperature magnetization measurement. All these samples were etched by NaOH solution to eliminate the influence of silica before characterizations. XRD measurements (Figure 7.6c) indicate that samples under different calcination

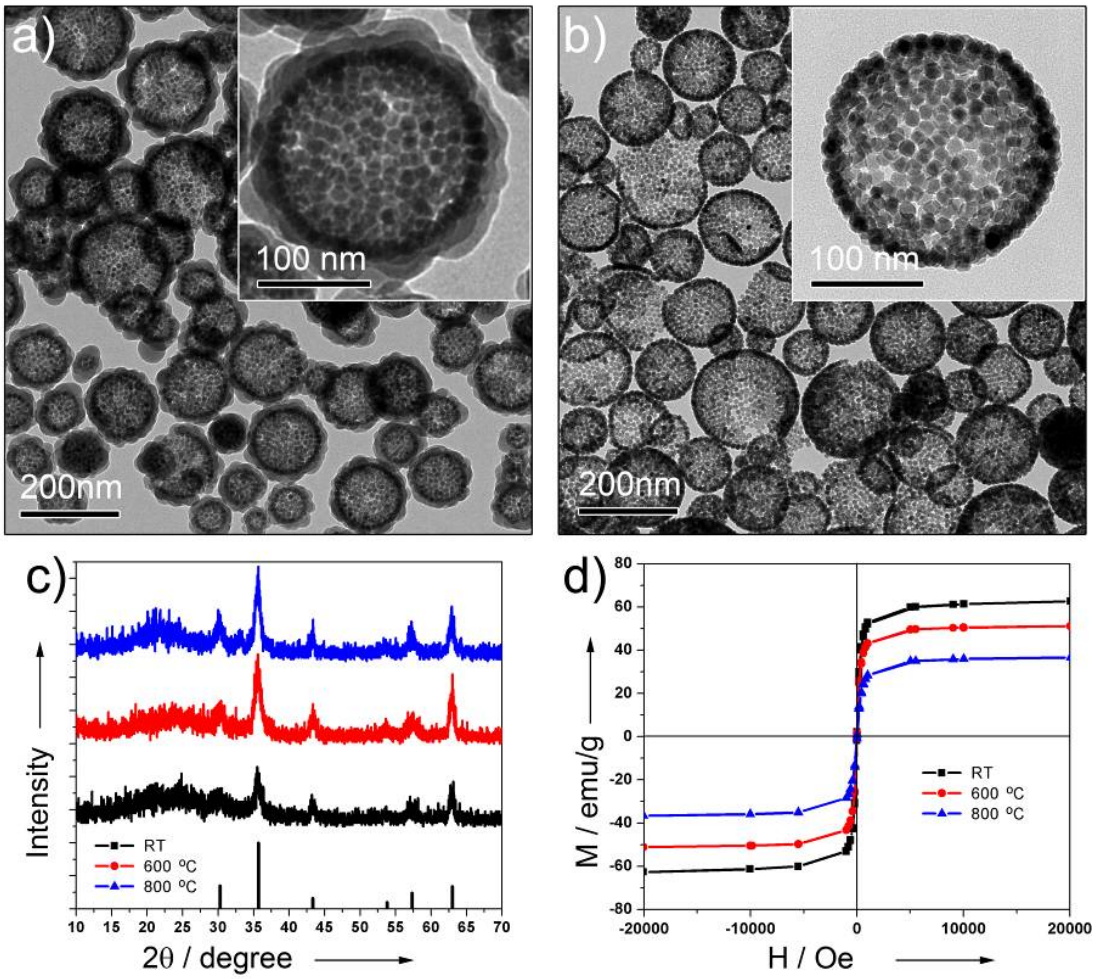

Figure 7.6 (a) TEM images of silica coated γ-Fe_2O_3 HCNCs. (b) TEM images of γ-Fe_2O_3 HCNCs after calcination at 800 ^oC for 2 hour and silica removing. (c, d) X-ray diffraction patterns and magnification hysteretic loops of the three HCNC samples after different calcination temperature. The JCPDS card No. of pure γ-Fe_2O_3 used in (c) is 39-146.

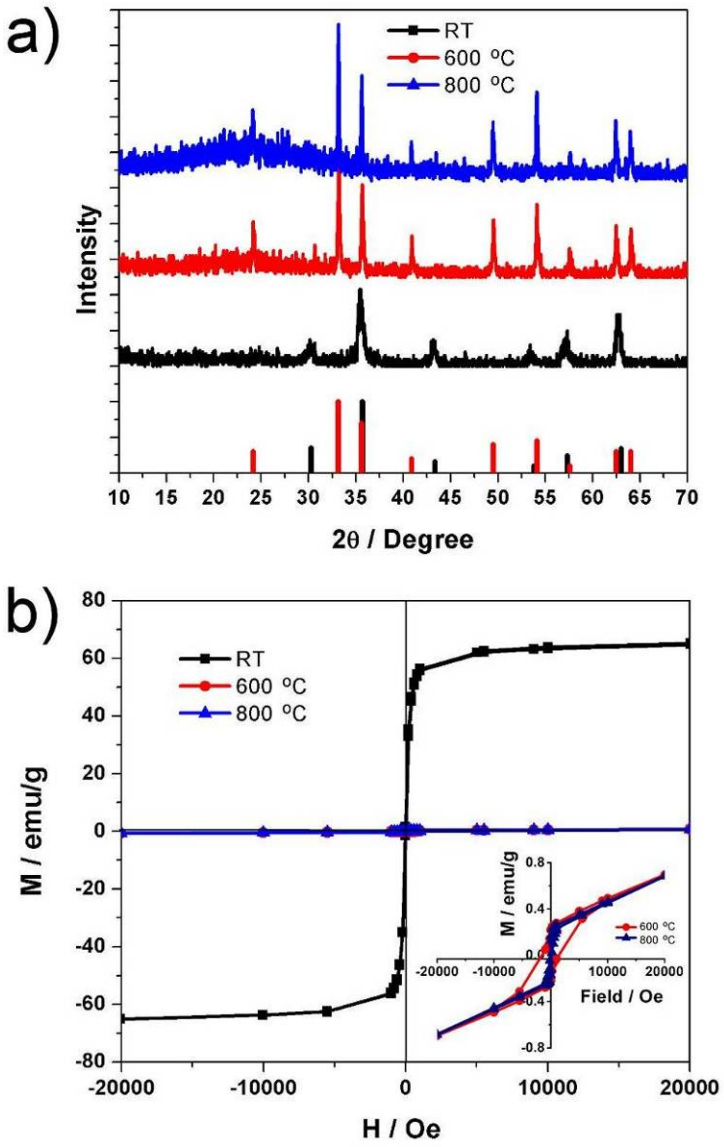

Figure 7.7 (a) X-ray diffraction patterns and (b) magnification hysteretic loops of the initial γ-Fe_2O_3 nanoparticles at different calcination temperature.

temperatures (RT, 600 ^{o}C and 800 ^{o}C) are mainly maghemite γ-Fe_2O_3 phase (JCPDS Card No. 39-1346) nanocrystalline materials with almost identical peak broadening, showing that the primary nanocrystals did not grow significantly during the cluster assembly and calcination. The slight increase in grain size of the calcined samples suggests modest interparticle fusion which contributes to form the nanoparticle shell. Figure 7.6d shows the room-temperature magnetization curves, revealing the superparamagnetic behavior for all the three samples. We note that after calcination at high temperature of 800 ^{o}C, a small peak corresponding to hematite phase appears on XRD pattern and the saturation magnetization value decreases from 63 to 37 emu/g, suggesting the partially transfer from maghemite to hematite phase. However, the as-synthesized HCNCs still perform superparamagnetic properties even after treatment at 800 ^{o}C, which makes them easily isolated from solution using an external magnetic field. All these results imply that the SiO_2 shells not only protect the nanoparticle shells during the calcination, but also are able to prevent the phase transition of γ-Fe_2O_3 to α-Fe_2O_3 and maintain the unique superparamagnetic properties.

This nanoparticle adsorption at polymer/water interface is a general and flexible self-assembly technique, which provides a novel approach for stable HCNCs with different components using nanoparticles as building blocks. To test the versatility of the assembly process, various hydrophobic nanoparticles including trioctylphosphine oxide (TOPO)-capped ZrO_2[44], oleylamine-capped NiO[45], oleic acid-capped QD (CdSe@CdZnS)[46] and oleic acid-capped $NaYF_4$:Yb,Er[47] were assembled at the poly(1-decene)/water interface, as shown in Figure 7.8. From the contrast between the core and

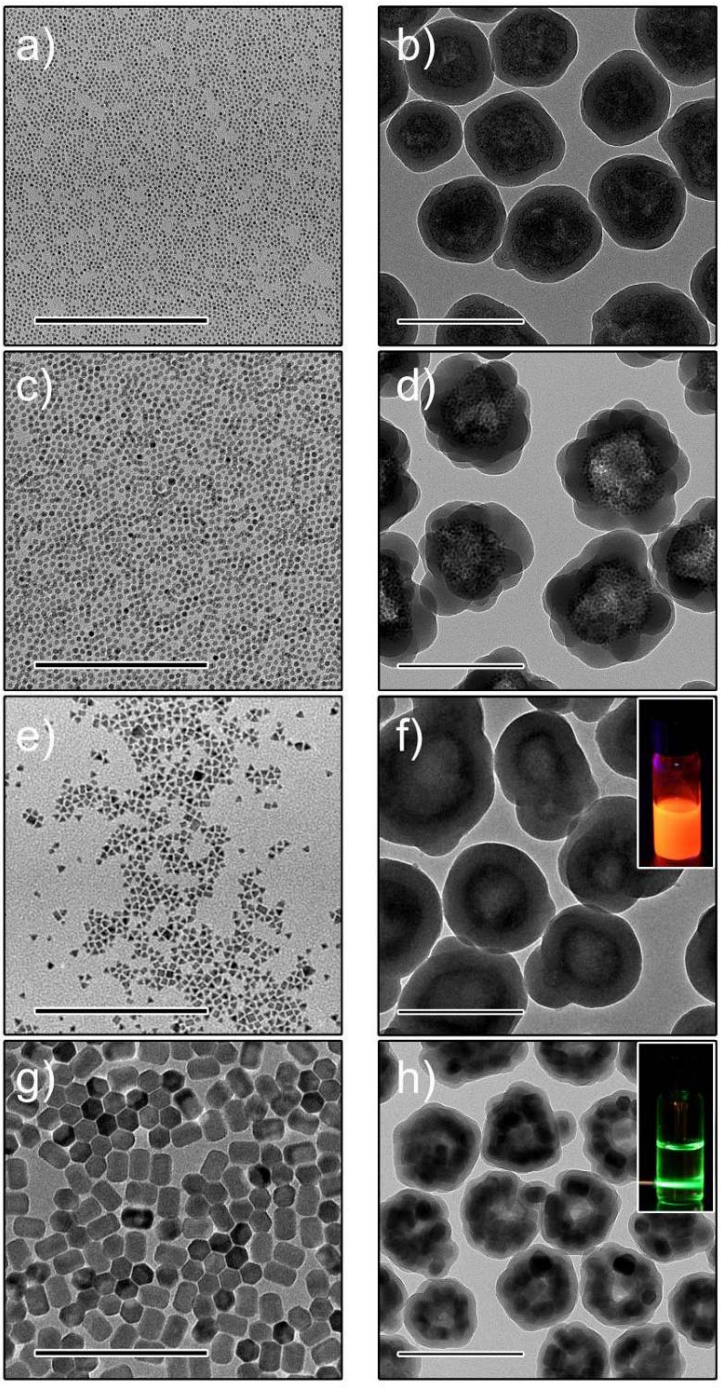

Figure 7.8 TEM images of different nanocrystals and corresponding silica coated HCNCs: (a, b) ZrO_2, (c,d) NiO, (e,f) CdSe@CdZnS (QDs), (g,h) $NaYF_4$:Yb,Er. Scale bar: 200 nm. Insets are digital photos of the aqueous dispersions of QD HCNCs excited by an ultraviolet lamp and $NaYF_4$:Yb,Er HCNCs excited by 980 nm laser.

shell in the TEM images, a layer of nanoparticles without sintering can be easily identified inside the silica layer, indicating the generality of the assembly strategy for hydrophobic nanoparticles at the polymer/water interface. The unique optical properties of QD and $NaYF_4$:Yb,Er can be well maintained after assembly as shown in the insets of Figure 7.8. Still, the small ZrO_2 (~4 nm) and QD (~6 nm) nanoparticles prefer to form multiple layer structures at the interface. The larger ones NiO (~ 8 nm) and $NaYF_4$ (~30×50 nm) can be assembled to produce more stable nanoparticle monolayers. These adsorption behaviors of nanoparticles with different sizes at the interface demonstrate again that assemblies of larger nanoparticles are more stable.

7.4 Conclusion

In summary, we present a general strategy for the fabrication of novel HCNCs with precise control of the size, morphology and surface property. The clusters are prepared by the self-assembly of hydrophobic colloidal nanoparticles at polymer-water interface after evaporation of emulsion droplet solvent. By controlling the original nanoparticle/polymer ratio in the oil droplet, the size of nanoparticles and the type of polymers, the HCNCs with different sizes and morphologies can be conveniently produced. By coating a layer of silica before calcination and removing it afterwards through chemical etching, we have been able to lock the nanoparticle shells, prevent the clusters from aggregating during heating, and enhance the mechanical strength. Such assembly approach, using nanoparticle as building blocks, will provide the research community a highly versatile, configurable, and reproducible process to prepare capsules and membranes with nanoscopic pores for filtering, encapsulation and delivery purpose.

Reference

(1) Boker, A.; He, J.; Emrick, T.; Russell, T. P., *Soft Matter* **2007,** 3, 1231-1248.

(2) Lu, Z.; Gao, C.; Zhang, Q.; Chi, M.; Howe, J. Y.; Yin, Y., *Nano Lett.* **2011,** 11, 3404-3412.

(3) Klajn, R.; Bishop, K. J. M.; Fialkowski, M.; Paszewski, M.; Campbell, C. J.; Gray, T. P.; Grzybowski, B. A., *Science* **2007,** 316, 261-264.

(4) Suh, W. H.; Suh, Y.-H.; Stucky, G. D., *Nano Today* **2009,** 4, 27-36.

(5) Liu, N. G.; Prall, B. S.; Klimov, V. I., *J. Am. Chem. Soc.* **2006,** 128, 15362-15363.

(6) Kulak, A.; Davis, S. A.; Dujardin, E.; Mann, S., *Chem. Mater.* **2003,** 15, 528-535.

(7) Yin, Y.; Alivisatos, A. P., *Nature* **2005,** 437, 664-670.

(8) Murray, C. B.; Norris, D. J.; Bawendi, M. G., *J. Am. Chem. Soc.* **1993,** 115, 8706-15.

(9) Skaff, H.; Lin, Y.; Tangirala, R.; Breitenkamp, K.; Boker, A.; Russell, T. P.; Emrick, T., *Adv. Mater.* **2005,** 17, 2082-2086.

(10) Zhuang, J.; Wu, H.; Yang, Y.; Cao, Y. C., *J. Am. Chem. Soc.* **2007,** 129, 14166-14167.

(11) Bain, C. D.; Troughton, E. B.; Tao, Y. T.; Evall, J.; Whitesides, G. M.; Nuzzo, R. G., *J. Am. Chem. Soc.* **1989,** 111, 321-335.

(12) Murray, C. B.; Kagan, C. R.; Bawendi, M. G., *Annu. Rev. Mater. Sci.* **2000,** 30, 545-610.

(13) Shevchenko, E. V.; Talapin, D. V.; Murray, C. B.; O'Brien, S., *J. Am. Chem. Soc.* **2006,** 128, 3620-3637.

(14) Sun, S.; Zeng, H.; Robinson, D. B.; Raoux, S.; Rice, P. M.; Wang, S. X.; Li, G., *J. Am. Chem. Soc.* **2003,** 126, 273-279.

(15) Lin, Y.; Skaff, H.; Emrick, T.; Dinsmore, A. D.; Russell, T. P., *Science* **2003,** 299, 226-229.

(16) Lin, Y.; Böker, A.; Skaff, H.; Cookson, D.; Dinsmore, A. D.; Emrick, T.; Russell, T. P., *Langmuir* **2004,** 21, 191-194.

(17) Duan, H. W.; Wang, D. Y.; Kurth, D. G.; Mohwald, H., *Angew. Chem. Int. Ed.* **2004,** 43, 5639-5642.

(18) Dai, L. L.; Sharma, R.; Wu, C.-y., *Langmuir* **2005,** 21, 2641-2643.

(19) Pieranski, P., *Phys. Rev. Lett.* **1980,** 45, 569-572.

(20) Duan, H.; Wang, D.; Sobal, N. S.; Giersig, M.; Kurth, D. G.; Möhwald, H., *Nano Lett.* **2005,** 5, 949-952.

(21) Stoeva, S. I.; Huo, F. W.; Lee, J. S.; Mirkin, C. A., *J. Am. Chem. Soc.* **2005,** 127, 15362-15363.

(22) Kotov, N. A.; Dekany, I.; Fendler, J. H., *J. Phys. Chem.* **1995,** 99, 13065-13069.

(23) Caruso, F.; Susha, A. S.; Giersig, M.; Mohwald, H., *Adv. Mater.* **1999,** 11, 950-953.

(24) Caruso, F.; Spasova, M.; Salgueirino-Maceira, V.; Liz-Marzan, L. M., *Adv. Mater.* **2001,** 13, 1090-1094.

(25) Lin, Y.; Skaff, H.; Böker, A.; Dinsmore, A. D.; Emrick, T.; Russell, T. P., *J. Am. Chem. Soc.* **2003,** 125, 12690-12691.

(26) Zhuang, J. Q.; Wu, H. M.; Yang, Y. G.; Cao, Y. C., *Angew. Chem. Int. Ed.* **2008,** 47, 2208-2212.

(27) Bai, F.; Wang, D. S.; Huo, Z. Y.; Chen, W.; Liu, L. P.; Liang, X.; Chen, C.; Wang, X.; Peng, Q.; Li, Y. D., *Angew. Chem. Int. Ed.* **2007,** 46, 6650-6653.

(28) Wang, D. S.; Xie, T.; Peng, Q.; Li, Y. D., *J. Am. Chem. Soc.* **2008,** 130, 4016-4022.

(29) Lu, Z.; Ye, M.; Li, N.; Zhong, W.; Yin, Y., *Angew. Chem. Int. Ed.* **2010,** 49, 1862-1866.

(30) Lu, Z.; Duan, J.; He, L.; Hu, Y.; Yin, Y., *Anal. Chem.* **2010,** 82, 7249-7258.

(31) Zhang, Q.; Joo, J.-B.; Lu, Z.; Dahl, M.; Oliveira, D.; Ye, M.; Yin, Y., *Nano Res.* **2011,** 4, 103-114.

(32) Isojima, T.; Suh, S. K.; Vander Sande, J. B.; Hatton, T. A., *Langmuir* **2009,** 25, 8292-8298.

(33) Dinsmore, A. D.; Hsu, M. F.; Nikolaides, M. G.; Marquez, M.; Bausch, A. R.; Weitz, D. A., *Science* **2002,** 298, 1006-1009.

(34) Schacht, S.; Huo, Q.; Voigt-Martin, I. G.; Stucky, G. D.; Schüth, F., *Science* **1996,** 273, 768-771.

(35) Dinsmore, A. D.; Crocker, J. C.; Yodh, A. G., *Curr. Opin. Colloid. In.* **1998,** 3, 5-11.

(36) Joki, T.; Machluf, M.; Atala, A.; Zhu, J.; Seyfried, N. T.; Dunn, I. F.; Abe, T.; Carroll, R. S.; Black, P. M., *Nat Biotech* **2001,** 19, 35-39.

(37) Russell, J. T.; Lin, Y.; Boker, A.; Su, L.; Carl, P.; Zettl, H.; He, J. B.; Sill, K.; Tangirala, R.; Emrick, T.; Littrell, K.; Thiyagarajan, P.; Cookson, D.; Fery, A.; Wang, Q.; Russell, T. P., *Angew. Chem. Int. Ed.* **2005,** 44, 2420-2426.

(38) Hodneland, C. D.; Lee, Y. S.; Min, D. H.; Mrksich, M., *Proc. Natl. Acad. Sci. USA* **2002,** 99, 5048-5052.

(39) Park, J.; An, K.; Hwang, Y.; Park, J.-G.; Noh, H.-J.; Kim, J.-Y.; Park, J.-H.; Hwang, N.-M.; Hyeon, T., *Nat. Mater.* **2004,** 3, 891-895.

(40) Stober, W.; Fink, A.; Bohn, E., *J. Colloid Interface Sci.* **1968,** 26, 62-69.

(41) Pickering, S. U., *J. Chem. Soc., Trans.,* **1907,** 91, 2001-2021.

(42) Vasile, C., *Handbook of Polyolefins*. CRC Press: 2000.

(43) Yen, F. S.; Chen, W. C.; Yang, J. M.; Hong, C. T., *Nano Lett.* **2002,** 2, 245-252.

(44) Joo, J.; Yu, T.; Kim, Y. W.; Park, H. M.; Wu, F.; Zhang, J. Z.; Hyeon, T., *J. Am. Chem. Soc.* **2003,** 125, 6553-6557.

(45) Park, J.; Kang, E.; Son, S. U.; Park, H. M.; Lee, M. K.; Kim, J.; Kim, K. W.; Noh, H. J.; Park, J. H.; Bae, C. J.; Park, J. G.; Hyeon, T., *Adv. Mater.* **2005,** 17, 429-434.

(46) Carion, O.; Mahler, B.; Pons, T.; Dubertret, B., *Nat. Protocols* **2007,** 2, 2383-2390.

(47) Li, Z. Q.; Zhang, Y.; Jiang, S., *Adv. Mater.* **2008,** 20, 4765-4769.